

**Enhancement of Steel Moment Connections Through Non-Traditional Sections and
Materials**

by

Dan Wei

A dissertation submitted in partial fulfillment
of the requirements for the degree of
Doctor of Philosophy
(Civil Engineering)
in the University of Michigan
2017

Doctoral Committee:

Associate Professor Jason P. McCormick, Chair
Professor Sherif El-Tawil
Professor Jwo Pan
Assistant Professor Seymour M.J. Spence

Dan Wei

danwei@umich.edu

ORCID iD: 0000-0003-2570-0129

© Dan Wei 2017

DEDICATION

To my parents, Changchun and Yueying, and husband, Ruilong, for their endless love and unconditional support.

ACKNOWLEDGEMENT

First and foremost, I would like to express my sincere appreciation to my advisor, Professor McCormick, who has been offering me guidance, mentorship, and inspiration not only in my study, but also in my life. Thanks to his help, I have become a better person and a better researcher. This dissertation would not have been completed without his help.

I also would like to thank my committee members, Professor El-Tawil, Professor Spence, and Professor Pan for their patience and help in solving all the problems that I encountered throughout my research. It is their constructive suggestions and valuable input that allowed me to finish this research project. In addition, I would like to thank all the professors who have taught me during my doctoral study. Without the knowledge I learned from their courses, I would not have been able to make progress on my research project.

Five years of doctoral study at the University of Michigan also allowed me to make valuable friendships that I will cherish forever. I am grateful to my friends and fellow graduate students: Matthew Fadden, Xiaohu Fan, Eric Warner, Malcolm Ammons, Thai Dam, Qian Zhang, Qianru Guo, Jason Martinez, Luis Alfaro, Tasha Tardieu, Carolyn McCann, Nurie Kim, Christian Carreras, Zhijie Wang and Junxing Zheng. Thanks for their consistent support and help which made my life and study in a foreign country so wonderful.

I sincerely appreciate assistance from all the laboratory technicians, Bob Spence, Bob Fisher, Jan Pantolin, and Rick Burch. Without their help and expertise in structural engineering, the experimental work in this dissertation would never be completed so smoothly and on time.

This research could not be finished without the financial support of the National Science Foundation (Grant No. CMMI -1334272). Material donation from Atlas Tube and fabrication of the test specimens provided by Douglas Steel are greatly appreciated. Their contributions made the experimental studies possible.

In the end, I would like to thank my parents, Yueying Lu and Changchun Wei, for their selfless love and support. They cultivated me morally, intellectually, and physically, which prepared me to complete my doctoral study. I also owe my sincere appreciation for my husband, Ruilong Han, for his continuous support, and unconditional love through all the years of my study. I also want to thank my lovely daughter Katherine for all the joy that she brought to me, and thank my mother-in-law for helping me take care of my daughter, so that I could spend more time on this research project.

TABLE OF CONTENTS

DEDICATION	ii
ACKNOWLEDGEMENT	iii
LIST OF TABLES	x
LIST OF FIGURES	xi
ABSTRACT	xxiv
CHAPTER 1 INTRODUCTION	1
1.1 Problem Description	1
1.2 Project Objectives	5
1.3 Dissertation Outline	8
CHAPTER 2 LITERATURE REVIEW	10
2.1 Background	10
2.2 HSS Applications in Steel Structures	13
2.2.1 Background	13
2.2.2 Axial Behavior of HSS	15
2.2.3 Flexural Behavior of HSS	22
2.2.4 Connections	26
2.3 Non-Traditional Civil Engineering Materials for Fill Applications	32

2.3.1 Polymer Foam.....	33
2.3.2 Rubber.....	39
CHAPTER 3 DESIGN AND MODELING OF HSS-TO-HSS COLLAR CONNECTIONS.....	42
3.1 Introduction.....	42
3.2 Experimental Results of Reinforced HSS-to-HSS Moment Connections.....	44
3.3 HSS-to-HSS Collar Connection Concept.....	53
3.4 FEM of HSS Based Collar Connection.....	56
3.4.1 Parametric Study.....	59
3.4.2 Parametric Study Results.....	59
3.4.3 Conclusion of Parametric Study.....	68
3.5 Design Approach for HSS-to-HSS Collar Connection.....	69
3.6 Conclusions.....	75
CHAPTER 4 HSS BASED COLLAR CONNECTION TESTS.....	77
4.1 Introduction.....	77
4.2 HSS Material Properties Test.....	78
4.2.1 Experimental Program.....	79
4.2.2 Experimental Results.....	80
4.2.2.3 HSS Ductility.....	84
4.2.3 Implications of Results.....	85
4.3 Collar Connection Tests.....	86

4.3.1 Introduction.....	86
4.3.2 Experimental Program	87
4.3.3 Experimental Results	99
4.3.4 Plastic Rotation	106
4.3.5 Secant Stiffness Behavior	121
4.3.6 Energy Dissipation Capacity.....	122
4.3.7 Equivalent Viscous Damping Ratio.....	124
4.3.8 Distribution of Strain in the Connections	125
4.3.9 Applications to Design.....	139
4.4 Conclusions.....	140
 CHAPTER 5 FINITE ELEMENT MODELING OF HSS BASED COLLAR CONNECTIONS	
.....	143
5.1 Introduction.....	143
5.2 FE Model Calibration and Validation.....	144
5.2.1 Configuration and Details	144
5.2.2 Material Properties.....	147
5.2.3 Initial Geometric Imperfections.....	148
5.2.4 FE Comparison and Validation.....	149
5.3 FE Model Parametric Study.....	151
5.3.1 Parametric Study Specimens.....	152

5.3.2 Hysteretic Behavior	153
5.3.3 Parameter Effects on the Moment Capacity of the Connections	157
5.3.4 Secant Stiffness	159
5.3.5 Energy Dissipation Capacity.....	162
5.3.6 Cycling Effects.....	164
5.4 Implications for Future Design	165
5.5 Conclusions.....	166
CHAPTER 6 STUDY ON FILL MATERIAL	169
6.1 Introduction.....	169
6.2 Preliminary Evaluation of Fill Materials	170
6.2.1 Monotonic Bending Tests	172
6.2.2 Fill Material Selection.....	177
6.3 Further Details of Selected PU Foam	178
6.4 Compression Test.....	179
6.4.1 Test setup	179
6.4.2 Loading Protocol.....	180
6.4.3 Monotonic Compression Test Result.....	181
6.4.4 Poisson's Ratio Test.....	186
6.4.5 Cyclic Compression Test Result.....	190
6.6 Conclusion	197

CHAPTER 7 STUDY ON CYCLIC BEHAVIOR OF PU FOAM FILLED HSS BEAM	200
7.1 Introduction.....	200
7.2 Parametric Study on Fill HSS Beam via FE Analysis	201
7.2.1 Configuration and Details	201
7.2.2 Material Properties.....	204
7.2.3 FE Model Validation.....	206
7.2.4 Parametric Study Specimens.....	209
7.2.5 FE Study Results.....	211
7.3 Design Implication.....	225
7.4 Conclusions.....	227
CHAPTER 8 SUMMARY AND CONCLUSIONS	229
8.1 Summary.....	229
8.1.1 Summary of HSS based Seismic Moment Connection Study	230
8.1.2 Summary of a Lightweight, Non-Traditional Material Filled HSS Beam Study	231
8.2 Conclusions.....	232
8.3 Research Impact.....	236
8.4 Recommendations for Future Research	238
REFERENCE.....	239

LIST OF TABLES

Table 3.1 Collar Connection Parameters and Values	59
Table 4.1 Material Properties for the HSS 12×8×3/8 Flats	83
Table 4.2 Material Properties of Column HSS 10×10×5/8 Flats.....	83
Table 4.3 Material Properties of Beam HSS 12×8×3/8 Corners	83
Table 4.4 Material Properties of Column HSS 10×10×5/8 Corners.....	83
Table 4.5 Measured Section Properties of HSS Members.....	90
Table 5.1 Configuration of Collar Connections Studied in the FE Parametric Study	153
Table 6.1 Properties of PU Foams	172
Table 6.2 Parameters for the 11 Experimental Beam Specimens.....	176
Table 6.3 Elastic Modulus and Yield Strength of 16 lb PU Foam under Monotonic Compression	186
Table 6.4 Poisson’s Ratio of Each Specimen	189
Table 7.1 HSS Beam Properties and Fill Length.....	210

LIST OF FIGURES

Figure 1.1 First Story Collapse Mechanism of the Steel Moment Frame (Lignos et al., 2013)	2
Figure 1.2 Welded Collar Connection	4
Figure 2.1 Examples of Steel Moment Frame Construction (www.ecs.umass.edu)	10
Figure 2.2 Typical Pre-Northridge Moment Connections (Tremblay et al., 1995)	11
Figure 2.3 Examples of Modified Moment Connection Designs (Engelhardt & Sabol, 1997)	12
Figure 2.4 Examples of Applications of HSS (www.cidect.com)	14
Figure 2.5 HSS Manufacturing Processes (Steel Tube Institute, 2003)	15
Figure 2.6 Typical Hysteresis Behavior of Braces under Symmetric Cyclic Loading (Tremblay, 2002)	17
Figure 2.7 Brace Hysteretic Models (Ikeda & Mahin, 1986) (a) Finite Element Models (b) Physical Theory Models (c) Phenomenological Models	18
Figure 2.8 Interaction Curve for Various β (Sully & Hancock 1996)	21
Figure 2.9 Local Buckling and Fracture of Column Bases (Wang et al., 2008).....	22
Figure 2.10 Dimensionless Curvature Versus Dimensionless Moment (Zhao & Hancock, 1992).....	23
Figure 2.11 Proposal for New Compact Limits for RHS (AS 4100) (Wilkinson & Hancock, 1998).....	24

Figure 2.12 Normalized Moment Versus Rotation Hysteresis Curves and Photographs in HSS Beam Bending Tests (Fadden & McCormick, 2011) (a, b) HSS 203.2 × 152.4 × 9.5 mm at completion of the test; (c, d) HSS 254 × 101.6 × 6.4 mm at completion of the test; (e, f) HSS 304.8 × 152.4 × 6.4 mm during final test cycles.....	25
Figure 2.13 HSS In-Planar Joint Types	27
Figure 2.14 Multi-Planar HSS Connections	28
Figure 2.15 Possible Failure Modes for Brace-to-Chord Joints of Vierendeel Trusses Loaded by Brace In-Plane Bending Moment (Wardenier, 1982).....	29
Figure 2.16 SEM Photograph of (a) PU Open-Cell Foam of Density 28 kg-m ³ ; and (b) Closed-Cell Low Density Polyethylene (LDPE) Foam of Density 24 kg-m ³ (Mills, 2007).....	34
Figure 2.17 Various Applications of Polymer Foam.....	35
Figure 2.18 Schematic Compressive and Tension Stress-Strain Curves for Foams.....	37
Figure 2.19 Cell Deformations under Compressive Loads (Gibson & Ashby, 1999).....	38
Figure 2.20 Applications of Rubber Materials	39
Figure 2.21 Schematics of a Typical Natural Rubber Bearing (Warn & Ryan, 2012).....	41
Figure 3.1 Brittle Failure of Unreinforced HSS based Moment Connections (Fadden et al., 2014).....	44
Figure 3.2 Schematic of the (a) External Diaphragm Plate and (b) Through Plate Connections (units in inch).....	46
Figure 3.3 Photographs of the Test Setup and Through Plate Connection after Testing.....	47
Figure 3.4 Moment-Rotation Hysteresis for the External Diaphragm Plate and Through Plate Connections.....	49

Figure 3.5 Moment-Beam Plastic Rotation Hysteresis for the External Diaphragm Plate and Through Plate Connections.....	50
Figure 3.6 Strain Gage Layout for the Two Reinforced Connections (units in inch).....	51
Figure 3.7 Beam Strain Gage Measurements with respect to Connection Rotation.....	52
Figure 3.8 Strain Values at the Beam Flange Center (be0), Beam Flange Edge (be2), Panel Zone Center (pz1), Column Face(cf1) and Column Back (cb0) for the 2 and 4% Connection Rotation Cycles	53
Figure 3.9 Welded Collar Connections.....	55
Figure 3.10 Elevation View of a Typical Collar Connection (units in inch).....	55
Figure 3.11 Welds in the Collar Connections.....	56
Figure 3.12 Mesh Size for the HSS Beam and Column in the FE Models.....	57
Figure 3.13 Loading Protocol Applied in the FEM	58
Figure 3.14 Normalized Moment versus Connection Rotation Level	61
Figure 3.15 Normalized Moment versus Connection Rotation for 1/2 in. Collar and Endplate Thickness	61
Figure 3.16 Normalized Moment versus Beam Plastic Rotation.....	63
Figure 3.17 Stress Contours for the Collar Connections with and without Stiffeners.....	64
Figure 3.18 Normalized Moment versus Connection Rotation for the Connection with and without Stiffeners when Endplate Thicknesses are 1/2 in.	64
Figure 3.19 Normalized Moment versus Beam Plastic Rotation in for the Connection with and without Stiffeners when Endplate Thicknesses are 1/2 in.	65
Figure 3.20 Contribution of Plastic Rotation.....	66

Figure 3.21 Effect of Beam Endplate Thickness on Max. Moment	67
Figure 3.22 Effect of Collar Thickness on Max. Moment.....	68
Figure 3.23 Effect of Collar Depth on Max. Moment	68
Figure 3.24 Load Path for the HSS Based Collar Connection.....	72
Figure 3.25 Free Body Diagrams of Endplate and Collar	73
Figure 4.1 Tensile Specimen Locations for the HSS 12×8×3/8 Beam and the HSS 10×10×5/8 Column (units in inch).....	80
Figure 4.2 Typical HSS Sub-size Coupon Specimen (units in inch).....	80
Figure 4.3 Engineering Stress-Strain Plots for the Beam Flats	81
Figure 4.4 Engineering Stress-Strain Plots for the Column Flats.....	81
Figure 4.5 Engineering Stress-Strain Plots for the Beam Corners.....	82
Figure 4.6 Engineering Stress-Strain Plots for the Column Corners	82
Figure 4.7 HSS based Collar Connection Test Setup and Configuration.....	88
Figure 4.8 Loading Protocol for the Experimental Test of the Collar Connections.....	89
Figure 4.9 Collar Connection without Stiffeners (units in inch)	91
Figure 4.10 Collar Connection with Stiffeners (units in inch).....	92
Figure 4.11 Optotrak Numbering Scheme for Collar Connection without Stiffeners (units in inch)	93
Figure 4.12 Optotrak Numbering Scheme for Collar Connection with Stiffeners (units in inch)	94
Figure 4.13 Strain Gage Locations for the Connection without Stiffeners (units in inch) ...	96

Figure 4.14 Strain Gage Locations for the Connection with Stiffeners (units in inch)	97
Figure 4.15 Layout of Instrumentation Primarily Used for Secondary Measurements for the Connection without Stiffeners (units in inch).....	98
Figure 4.16 Layout of Instrumentation Primarily Used for Secondary Measurements for the Connection with Stiffeners (units in inch).....	99
Figure 4.17 Normalized Moment versus Connection Rotation for the Collar Connection without Stiffeners.....	102
Figure 4.18 Moment versus Connection Rotation for the Collar Connection without Stiffeners.....	102
Figure 4.19 Local Buckling of Collar Connection without Stiffeners at the First Cycle of 0.06 rad. Rotation Cycle	103
Figure 4.20 Fracture Propagation at Beam Corners of Collar Connection without Stiffeners at the End of the 0.08 rad. Rotation Cycle.....	103
Figure 4.21 Normalized Moment versus Connection Rotation for the Collar Connection with Stiffeners.....	104
Figure 4.22 Moment versus Connection Rotation for the Collar Connection with Stiffeners	104
Figure 4.23 Local Buckling of Collar Connection with Stiffeners at the First 0.06 rad. Cycle	105
Figure 4.24 Fracture Propagation at Beam Corners of Collar Connection with Stiffeners at the End of the 0.08 rad. Rotation Cycle.....	105
Figure 4.25 Backbone Curves for the Collar Connection with and without Stiffeners	106
Figure 4.26 Connection Moment versus Plastic Rotation of the Collar Connections	107

Figure 4.27 Experimental Moment-Plastic Beam Rotation Hysteresis for the Collar Connection without Stiffeners	110
Figure 4.28 Experimental Moment-Plastic Beam Rotation Hysteresis for the Collar Connection with Stiffeners	110
Figure 4.29 Panel Zone Distortion and Parameters	112
Figure 4.30 Experimental Moment-Plastic Panel Zone Rotation Hysteresis for the Collar Connection without Stiffeners	113
Figure 4.31 Experimental Moment-Plastic Panel Zone Rotation Hysteresis for the Collar Connection with Stiffeners	113
Figure 4.32 Experimental Moment-Plastic Column Rotation Hysteresis for the Collar Connection without Stiffeners	115
Figure 4.33 Experimental Moment-Plastic Column Rotation Hysteresis for the Collar Connection with Stiffeners	116
Figure 4.34 Experimental Moment-Plastic Endplate Rotation Hysteresis for the Collar Connection without Stiffeners	118
Figure 4.35 Experimental Moment-Plastic Endplate Rotation Hysteresis for the Collar Connection with Stiffeners	118
Figure 4.36 Sources of Inelastic Rotation at each First Rotation Cycle for the Collar Connection without Stiffeners	120
Figure 4.37 Sources of Inelastic Rotation at each First Rotation Cycle for the Collar Connection with Stiffeners	120
Figure 4.38 Secant Stiffness for the First Cycle at each Rotation Level versus Maximum Positive Cycle Rotation.....	121

Figure 4.39 Energy Dissipation for the First Cycle of Each Rotation Level versus Maximum Positive Cycle Rotation (rad.).....	123
Figure 4.40 Cumulative Energy Dissipation Measured at the First Cycle of Each Rotation Level versus Maximum Positive Cycle Rotation (rad.).....	123
Figure 4.41 Equivalent Viscous Damping Measured at the First Cycle of Each Rotation Level versus Maximum Positive Cycle Rotation.....	125
Figure 4.42 Strain in the Beam versus Connection Rotation Level for the Collar Connection without Stiffeners.....	127
Figure 4.43 Strain in the Beam versus Connection Rotation Level for the Collar Connection with Stiffeners.....	129
Figure 4.44 Strain in the Endplate versus Connection Rotation for the Collar Connection without Stiffeners.....	131
Figure 4.45 Strain in the Endplate versus Connection Rotation for the Collar Connection with Stiffeners.....	131
Figure 4.46 Strain in the Column Face versus Connection Rotation for the Collar Connection without Stiffeners	132
Figure 4.47 Strain in the Column Face versus Connection Rotation for the Collar Connection with Stiffeners	133
Figure 4.48 Strain in the Collar versus Connection Rotation for the Collar Connection without Stiffeners.....	134
Figure 4.49 Strain in the Collars versus Connection Rotation for the Collar Connection with Stiffeners.....	134
Figure 4.50 Strain in the Column Back versus Connection Rotation for the Collar Connection without Stiffeners	136

Figure 4.51 Strain in the Column Back versus Connection Rotation for the Collar Connection with Stiffeners	137
Figure 4.52 Shear Strain versus Connection Rotation for the Collar Connection without Stiffeners.....	138
Figure 4.53 Shear Strain versus Connection Rotation for the Collar Connection with Stiffeners.....	139
Figure 5.1 FE Models of the Collar Connections	145
Figure 5.2 Loading Protocol Applied to the FE Models.....	146
Figure 5.3 Mesh Size of FE Model.....	147
Figure 5.4 True Stress-True Strain Relationship for the Material Models Applied in the FE Analysis.....	148
Figure 5.5 Typical Eigenvalue Buckling Analysis Mode Shape for an HSS Beam	149
Figure 5.6 Comparison of Local Buckling Observed from FE Analyses and Experimental Tests at the Second 0.07 rad. Cycle	150
Figure 5.7 FE Results Comparison with the Experimental Results.....	151
Figure 5.8 Normalized Moment-Rotation Curves for Collar Connections with an HSS 10×10×5/8 Column and Different Beam Sizes (HSS 12×8×3/8, HSS 12×8×5/16 and HSS 12×8×1/2).....	155
Figure 5.9 Normalized Moment-Rotation Curves for Collar Connections with Column HSS 12×12×5/8 and Different Beam Sizes (HSS 12×8×3/8, HSS 12×8×5/16 and HSS 12×8×1/2).....	155
Figure 5.10 Normalized Moment-Rotation Curves for Collar Connections with Varying Collar Thickness ($t_e=1$ in.).....	156

Figure 5.11 Normalized Moment-Rotation Curves for Collar Connections with Varying Beam-to-Column Width Ratio (β) ($t_e=1$ in., $t_c=1/2$ in.)	157
Figure 5.12 Effects of Beam Width to Wall Thickness Ratio (b/t) on Moment Capacity..	158
Figure 5.13 Effects of Beam Depth to Thickness Ratio (d/t) on Moment Capacity.....	159
Figure 5.14 Effects of Endplate Thickness (t_e) on Moment Capacity	159
Figure 5.15 Effects of Beam Width to Thickness Ratio (b/t) on Secant Stiffness.....	160
Figure 5.16 Effects of Beam Depth to Thickness Ratio (d/t) on Secant Stiffness.....	161
Figure 5.17 Effects of Endplate Thickness (t_e) on Secant Stiffness	162
Figure 5.18 Effects of Beam Width to Thickness Ratio (b/t) on Cumulative Energy Dissipation	163
Figure 5.19 Effects of Beam Depth to Thickness Ratio (d/t) on Cumulative Energy Dissipation	163
Figure 5.20 Effects of Endplate Thickness (t_e) on Cumulative Energy Dissipation.....	164
Figure 5.21 Proposed Optimized Weld Configurations.....	166
Figure 6.1 Monotonic Bending Tests.....	171
Figure 6.2 Schematics of Monotonic Bending Test Setup	173
Figure 6.3 Layout of the Optical Tracking Markers.....	173
Figure 6.4 Moment-Rotation Curves for the Four-Point Bending Tests	175
Figure 6.5 Moment-Rotation Curves for HSS 4×4×1/8 in Three-Point Bending Tests	175
Figure 6.6 Picture of the PU Foam Cube and Schematic with Dimensions	179
Figure 6.7 Test setup of PU Foam Cube under Compression.....	180

Figure 6.8 Loading Protocol of PU Foam Cube under Cyclic Compression.....	181
Figure 6.9 Engineering Stress-Strain Curve of PU Foam Cubes under Monotonic Compression Loads at 0.01 in./s.....	182
Figure 6.10 Engineering Stress-Strain Curve of PU Foam Cubes under Monotonic Compression Loads at 0.1 in./s.....	182
Figure 6.11 Engineering Stress-Strain Curve of PU Foam Cubes under Monotonic Compression Loads at 1 in./s.....	183
Figure 6.12 Average Elastic Modulus with Standard Deviation at Different Loading Rates	184
Figure 6.13 Average Yield Stress with Standard Deviation at Different Loading Rates ...	184
Figure 6.14 Stress at Different Strain Levels.....	185
Figure 6.15 Speckle Pattern before and after Compressive Loading (Image size is 3296 by 2472 pixels).....	187
Figure 6.16 Selection of Area of Interest.....	188
Figure 6.17 Strain Contour during Data Analysis	188
Figure 6.18 Displacement Contour during Data Analysis.....	189
Figure 6.19 Poisson’s Ratio at Different Time Points for Five Specimens.....	189
Figure 6.20 Stress Strain Curves at Loading Rate 0.01 in./s under Cyclic Compression Load	191
Figure 6.21 Stress Strain Curves at Loading Rate 0.1 in./s under Cyclic Compression Load	191
Figure 6.22 Stress Strain Curves at Loading Rate 1 in./s under Cyclic Compression Load	192

Figure 6.23 Average Maximum Cycle Stress at the First Cycle of Each Strain Level.....	193
Figure 6.24 Average Maximum Cycle Stress at the Second Cycle of Each Strain Level ..	193
Figure 6.25 Secant Stiffness of the First Cycle at Each Strain Level at Loading Rate of 0.01 in./s.....	194
Figure 6.26 Secant Stiffness of the First Cycle at Each Strain Level at Loading Rate of 0.1 in./s.....	195
Figure 6.27 Secant Stiffness of the First Cycle at Each Strain Level at Loading Rate of 1 in./s.....	195
Figure 6.28 Average Energy Dissipation during the First Cycle at Each Strain Level	196
Figure 6.29 Average Energy Dissipation during the Second Cycle at Each Strain Level..	197
Figure 7.1 Loading History for FE Models	202
Figure 7.2 Energy History for the HSS 8×6×1/4 Beam with Mass Scaling of 100 and Loading Rate of 0.1 in./sec	203
Figure 7.3 Mesh Size for the Cantilever Beam.....	204
Figure 7.4 True Stress-Strain Plots for the Beam Corners and Flats	205
Figure 7.5 True Stress-Strain Curve for the 16 lb PU Foam	206
Figure 7.6 Comparison of Moment-Beam Rotation Relationship of a Cantilevered HSS 8×6×1/4 Beam from FEM and Experimental Testing	207
Figure 7.7 FE Model of the PU Foam Compression Test.....	208
Figure 7.8 Engineering Stress-Strain Relationship from the FE model and Compression Test	208
Figure 7.9 Distribution of Parametric Study Specimens with respect to b/t and d/t Ratios	210

Figure 7.10 Normalized Moment versus Beam Rotation for HSS 12×6×1/2.....	212
Figure 7.11 Normalized Moment versus Beam Rotation for HSS 12×4×5/16.....	213
Figure 7.12 Normalized Moment versus Beam Rotation for HSS 12×10×1/2.....	214
Figure 7.13 Normalized Moment versus Beam Rotation for HSS 12×8×1/4.....	215
Figure 7.14 Secant Stiffness versus Beam Rotation for HSS Beams in Group 1	216
Figure 7.15 Secant Stiffness versus Beam Rotation for HSS Beams in Group 2.....	217
Figure 7.16 Secant Stiffness versus Beam Rotation for HSS Beams in Group 3	218
Figure 7.17 Secant Stiffness versus Beam Rotation for HSS Beams in Group 4.....	219
Figure 7.18 Cumulative Energy Dissipation versus Beam Rotation for HSS Beams in Group 1.....	220
Figure 7.19 Cumulative Energy Dissipation versus Beam Rotation for HSS Beams in Group 2.....	220
Figure 7.20 Cumulative Energy Dissipation versus Beam Rotation for HSS Beams in Group 3.....	221
Figure 7.21 Cumulative Energy Dissipation versus Beam Rotation for HSS Beams in Group 4.....	221
Figure 7.22 Normalized Moment at Each Rotation Level versus Beam Rotation Backbone Curves for Beams in Group 1	222
Figure 7.23 Normalized Moment at Each Rotation Level versus Beam Rotation Backbone Curves for Beams in Group 2	223
Figure 7.24 Normalized Moment at Each Rotation Level versus Beam Rotation Backbone Curves for Beams in Group 3	223

Figure 7.25 Normalized Moment at Each Rotation Level versus Beam Rotation Backbone Curves for Beams in Group 4	224
Figure 7.26 Stress Contour in Empty HSS 12×8×1/4 at the 0.02 rad. Cycle	224
Figure 7.27 Stress Contour in Filled HSS 12×8×1/4 at the 0.02 rad. Cycle.....	225
Figure 7.28 Effect of b/t Ratio on the Percent Degradation of Moment Capacity at 0.04 rad.	226
Figure 7.29 Effect of d/t Ratio on the Percent Degradation of Moment Capacity at 0.04 rad.	227

ABSTRACT

Seismic moment frames have been widely used in earthquake prone areas due to their lightweight and ability to resist lateral forces, while providing high strength and reasonable stiffness. Typically, steel moment frames utilize wide flange beams and columns which leading to alternative structural shapes being overlooked, such as hollow structural sections (HSS). HSS based seismic moment connections have shown potential for good performance during an earthquake, but their detailing requirements require further exploration due to a lack of understanding of their cyclic behavior. Meanwhile, the excessive inelastic deformation concentrated in the HSS beam observed during cyclic tests can lead to the onset of local buckling and early initiation of cracking at the corners of the beam. To mitigate local buckling and increase energy dissipation capacity, a lightweight, non-traditional civil engineering material is explored as a void fill material to increase the resiliency of steel moment frame systems.

An experimental program is undertaken to characterize the cyclic behavior of two reinforced HSS based moment connections whose behavior shows the feasibility of these connections for seismic application. A parametric study of an innovative connection configuration (i.e. welded HSS based collar connection) is conducted to explore detailing requirements for seismic application and the effects of different parameters on the cyclic behavior of the collar connections. These connections provide more feasible field welding requirements and can potential be used in rapid construction. A design approach is derived for the HSS based collar connection based on the assumption that beam plastic hinging will occur prior to weld failure. Experimental testing of two HSS based collar connections is carried out to further characterize their cyclic behavior and explore their potential failure modes and load transfer mechanisms. These experimental test results are used to calibrate finite element models leading to a better understanding of the influences of different parameters on connection performance under cyclic loads and improved design details.

Both experimental and analytical work is conducted toward selection of the most suitable fill material and evaluation of its effects on enhancement of the seismic performance of filled HSS beams. Monotonic bending tests are performed to evaluate the feasibility of four different types of fill materials. Sixteen lb/ft³ polyurethane foam is found to best mitigate local buckling and increase the energy dissipation capacity of the HSS member. Monotonic and cyclic compression tests of the fill materials leads to an understanding of its mechanical properties and provides useful data for development of finite element material models. A parametric study of the empty and filled HSS beams considering different beam width-thickness and depth-thickness ratios is carried out to evaluate the effectiveness of the fill material in terms of postponing local buckling and increasing energy dissipation. Linear regression analysis of the results with respect to width-thickness and depth-thickness ratio limits considering the percent degradation of the moment capacity at 0.04 rad. of rotation, which is the requirement for special moment frames, shows that an expanded range of HSS beams can be used in seismic applications if they are filled with the polyurethane foam. The findings from this work lay the ground work for use of non-traditional civil engineering fill materials more pervasively in structures in order to enhance their damping capabilities and optimize their performance under extreme loads.

CHAPTER 1 INTRODUCTION

1.1 Problem Description

Many steel structures rely on moment frame configurations to resist lateral loads induced by earthquakes or hurricane events. In seismic regions, steel moment frames provide lateral load resistance through the development of plastic hinges at beam ends or column bases to dissipate earthquake input energy as shown in Figure 1.1. The plastic hinges act as fuses limiting inelastic behavior in undesired locations in the structure. During the 1994 Northridge earthquake, no steel buildings collapsed, but fracture was observed at the beam column connections in approximately 120 steel moment frames (Roeder, 2000). These failures often started at the bottom beam flange to column flange weld in the moment connections. Buildings damaged during the Northridge earthquake showed no evidence of plastic deformation before fracturing (Nakashima et al., 2000). Although none of the damaged buildings collapsed or caused significant injuries, economic losses associated with repairs were significantly large (Kircher et al., 1997). The uncertainty about future performance of steel moment frames that arose from this earthquake and the Hyogoken-Nanbu earthquake in Japan the following year led to extensive investigation of their seismic performance (Nakashima et al., 1998). The Structural Engineer Association of California, Applied Technology Council, and Consortium of Universities for Research in Earthquake Engineering made up the SAC Joint Venture which was created in the US to study improvements to connection geometry and configurations of steel moment frames that could reduce demands on critical locations (Nakashima et al., 2000). The resulting research (Anderson et al., 1995; Fisher et al., 1997; Mahin, 1998; Roeder, 2000) combined with parallel research in Japan provided better insight into the nonlinear behavior of steel frames, the need for ductile detailing of these frames and how to accomplish it, and the performance of welds under large cyclic loads. This effort led to improvements in the design of steel moment frame systems and an understanding of their seismic behavior under large cyclic loads (FEMA, 2000a, 2000b; Sabol, 2001).



Figure 1.1 First Story Collapse Mechanism of the Steel Moment Frame (Lignos et al., 2013)

Increased demand for more predictable and reliable performance of structures during extreme loading events expedited the development of performance based seismic design related specifications, which allow engineers to design for different levels of performance objectives. The American Institute of Steel Construction (AISC) Seismic Provisions (2010a) specify three different types of seismic moment frames to meet different expected levels of performance, i.e. special moment frames, intermediate moment frames and ordinary moment frames, which are expected to withstand significant, limited and minimal inelastic deformation, respectively, in the members and connections. A strong column-weak beam mechanism also should be achieved to prevent undesirable soft story mechanisms that can lead to collapse during an earthquake. The vast majority of steel moment frame structures utilize wide flange beams and columns or hollow structural sections (HSS) columns and wide flange beams. The latter is popular in Japan and Europe where the entire frame is utilized to resist lateral loads making the torsional and bidirectional properties of HSS useful. However, limited work has been done to explore alternative, potentially beneficial configurations, particularly those that take better advantages of the properties of HSS.

Recent research on HSS (Wardenier et al., 2010) has shown that cold formed tubes have many advantageous properties with respect to their use in structures, such as a high strength-to-weight ratio, which can reduce the seismic weight of structures; high torsional resistance, which can eliminate or reduce the needs for beam lateral bracing; good axial and bending capacity, which make them suitable as primary load carrying members; and convenience of use in modular construction, which can reduce erection time and costs. A number of experimental and numerical studies on HSS used as truss or bracing members under primarily axial loads have been carried out (Elchalakani et al., 2003; Frater & Packer, 1992; Goggins et al., 2005; Tremblay et al., 2003; Zhao et al., 2007). Other studies of Vierendeel trusses utilizing HSS members have been undertaken, but only focus on members subject to monotonic bending loads or combined monotonic axial and bending loads (Hancock & Rasmussen, 1998; Sully & Hancock, 1996; Zhao & Hancock, 1992). Only a few studies have considered HSS-to-HSS moment connections under cyclic loading conditions to evaluate their seismic performance (Fadden et al., 2014; Fadden, 2013). More commonly, research involving HSS in seismic moment frames focused on moment connection configurations that utilize wide flange beams connected to HSS columns (Chen et al., 2004; Kim et al., 1997; Kurobane, 2004; Miura et al., 2002; Picard & Giroux, 1976; Shanmugam & Ting, 1995; Shanmugam et al., 1991; Wang et al., 2016).

Due to a focus on moment frame configurations that use wide flange beams, potentially beneficial alternative configurations using HSS-to-HSS moment frame systems for low-rise or mid-rise applications have not been considered. Recently, research into the seismic performance of HSS-to-HSS beam column connections has increased which has led to a more comprehensive understanding of their feasibility when subjected to extreme loads. Tests have been performed under cyclic bending loads and design procedures for HSS based moment frame connections have been proposed (Fadden et al., 2014; Kumar & Rao, 2006). Based on their findings, if designed properly, HSS-to-HSS moment connections can exhibit adequate ductility and energy dissipation capacity for seismic applications. During two experimental tests of unreinforced welded HSS-to-HSS beam column connections, excessive inelastic deformation in the column face was observed and brittle fracture initiated at the toe of the weld leading to limited ductility (Fadden et al., 2014). Thus to improve the connection's performance and better limit inelastic deformation to the beam and column panel zone, reinforced HSS based moment connections were developed to evaluate configurations utilizing diaphragm plates (Fadden et al., 2014;

Fadden & McCormick, 2014b). Although these connections showed behavior necessary for use in special moment frame systems, they require significant welding, including complete joint penetration (CJP) welds in the field which incurs a significant cost, require time to do properly and are susceptible to poor quality depending on the conditions in the field. This study will consider alternative configurations and other ways to improve their performance. Thus, the welded HSS based collar connection concept is proposed for constructability as shown in Figure 1.2.

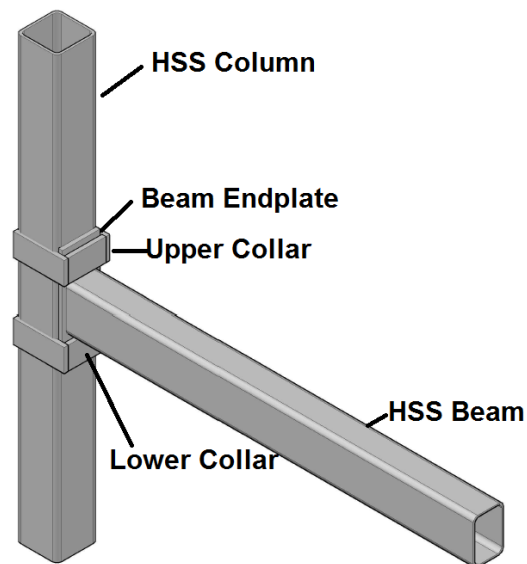


Figure 1.2 Welded Collar Connection

In the previous experimental tests (Fadden et al., 2014), excessive inelastic deformation in the HSS beams led to degradation of moment capacity and eventually resulted in the fracture of the beams. Degradation occurred after sustaining 4% interstory drift, but the ability to better control when and where degradation occurs is an important means of meeting performance based design requirements and limiting damage. To mitigate local buckling, prevent plastic deformation and increase energy dissipation capacity, non-traditional civil engineering materials, such as rubber and urethane foams, are considered as fill materials to investigate their effectiveness in enhancing the seismic performance of HSS beams used in seismic moment frame systems. These materials have been proven to dissipate energy when subject to various loading conditions, but few studies have considered their behavior under cyclic loads. Polymer foams have been widely

used as impact energy absorbing materials in mechanical engineering applications (Gibson & Ashby, 1999). Studies of the behavior of foam cored sandwich structures under impact, bending and compressive loading have been carried out and showed the foam can provide added stiffness and energy dissipation (Compston et al., 2006; Lim et al., 2004; Narayanaswamy et al., 2014; Rizov, 2009; Triantafillou & Gibson, 1987). Rubber materials have been proven effective as elastomeric bearings and dampers in seismic applications (Fan et al., 1991; Fujita, 1992; Fujita et al., 1992; Kelly, 1986; Tani et al., 2009). However, polymer foams and rubber have been rarely used as fill material under cyclic bending loads in civil engineering applications. These light-weight materials have exhibited their potential to increase energy dissipation capacity and mitigate local buckling as fill materials, but still need further study to consider them for seismic applications.

To address the aforementioned concerns and gaps in the state-of-the-art research, the goal of this study is to evaluate the effectiveness of enhancing the seismic performance of HSS-to-HSS moment connections through innovative configurations and the use of non-traditional civil engineering materials which allow for a more controlled, predictable, and resilient system. In doing so, a definitive understanding of connection detailing requirements and limiting parameters for use of filled HSS will be gained.

1.2 Project Objectives

In order to meet the projects overarching goal, the research objectives include: (1) Characterize the behavior of HSS-based welded collar connections experimentally and analytically under increasing cyclic loads and optimize these connections to allow for the utilization of HSS-based moment connections in low-rise or mid-rise steel structures in seismic regions; (2) Identify configuration and detailing requirements for HSS based collar connection and propose potential improvements; (3) Evaluate the ability of non-traditional civil engineering materials as fill materials in HSS beams to enhance the performance of structures under monotonic and cyclic bending loads; (4) Characterize the material properties of select fill material under monotonic and cyclic loads typical of a seismic event; and (5) Characterize the cyclic performance of filled

HSS beams under large cyclic loading conditions through extensive numerical studies while identifying limiting parameters for their use.

These objectives will be accomplished through the following five tasks:

Task 1: Evaluate potential limit states and detailing requirements of reinforced HSS-to-HSS beam column connections through full scale experimental tests and characterize the seismic performance of these reinforced HSS based moment connections through extensive analyses of the load transfer mechanism in the connection, hysteretic behavior, beam plastic rotation and strain distribution.

Task 2: Estimate limit states and determine design parameters through a parametric study of HSS-to-HSS beam column welded collar connections under cyclic loading conditions. Detailing requirements and a design approach are proposed in order to meet strength and ductility requirements. The cyclic performance and failure modes of welded collar connections are then characterized through experimental tests. Specific details of this task include:

- (1) Evaluation of the seismic performance of welded collar HSS based moment connections utilizing finite element analyses with different thicknesses of the beam endplate and collars, collar depth, and use of endplate stiffeners.
- (2) Determination of failure modes of stiffened and unstiffened collar connections, fracture propagation path, plastic deformation sources and strain distribution through experimental tests while evaluating whether HSS-based collar connections have the ability to develop adequate ductility in the plastic hinge region with minimal degradation in moment capacity under earthquake loading conditions.

Task 3: Perform a parametric study to further explore different parameters' influence on cyclic performance of the collar connections. Propose future design recommendations based on experimental tests and parametric study results. The specifics of this task include:

- (1) Calibrate the finite element models of HSS-based collar connections with the experimental results.

- (2) Investigate the influence of different parameters' effects on the connection's behavior via an extensive parametric study considering endplate and collar thickness, beam to column width ratio, beam width thickness ratio and beam depth thickness ratio.
- (3) Propose potential design and detailing improvement for enhancement of seismic performance and constructability of HSS based moment connections.

Task 4: Evaluate the performance of lightweight, non-traditional materials when used as fill in HSS beams under monotonic bending. The specifics of this task include:

- (1) Assess the ability of fill materials to mitigate local buckling through monotonic bending loads. Determine limit states and failure modes of filled HSS beams under monotonically increasing bending loads.
- (2) Select the most suitable type of fill materials among a variety of polymer foam and rubber materials based on their ability to inhibit local buckling and increase the stability of the moment rotation behavior of filled HSS beams.
- (3) Characterize the mechanical properties of the selected fill material through mechanical testing and select the most suitable material model for numerical analysis.
- (4) Characterize the seismic performance of a filled HSS cantilever beam under cyclic bending loads to assess its feasibility in structural applications to control seismic response.

Task 5: Calibrate finite element models with experimental test results and conduct a parametric study on filled HSS beams under cyclic bending loads to evaluate the viability of these lightweight, non-traditional civil engineering materials in structural passive control applications. The specifics of this task include:

- (1) Calibrate finite element models of the filled HSS beam with the experimental test results and measured material properties.
- (2) Assess seismic performance of cantilever beams through detailed finite element analyses and a parametric study considering a variety of material and member parameters.

- (3) Determine whether the fill materials have the ability to prevent local buckling and to increase energy dissipation during a seismic event. Identify changes in the limiting width thickness and depth thickness values for filled HSS beams to ensure they meet AISC (2010a) seismic special moment frame requirements.

1.3 Dissertation Outline

The content of the dissertation is organized into 8 chapters shown as following:

Chapter 2: An introduction on the application of HSS in moment frame systems and their behavior subject to various loading conditions is presented. An overview of previous studies on the mechanical properties and applications of non-traditional, lightweight materials such as polymer foams and rubber materials is also discussed.

Chapter 3: Experimental tests of two reinforced HSS based moment connections are studied which suggests viability of these moment connection in seismic applications. An innovative moment connection, i.e. welded HSS based collar connection, is proposed and a parametric study is conducted through a detailed finite element analyses considering various endplate and collar thicknesses, collar depths and use of stiffeners. A design approach and detailing requirements for the collar connection are developed.

Chapter 4: Two HSS based collar connections are tested experimentally under cyclic loads to further investigate the behavior and failure modes of these connections for seismic applications. These tests provide information on the load path through the connection, moment-rotation behavior, secant stiffness, plastic deformation distribution and energy dissipation capacity.

Chapter 5: A finite element model that can capture the moment capacity, hysteretic global and local behavior of welded collar HSS-to-HSS connections is calibrated and validated with the experimental test results. Then an extensive parametric study is performed which provides an understanding of the influence of design parameters, such as thicknesses of the endplate and collars, beam to column width ratio, beam width thickness ratio and beam depth thickness ratio on the behavior of welded collar connections under earthquake excitations. Future design

implications on HSS based moment connections are presented based on experimental and numerical study results.

Chapter 6: A preliminary study of suitable fill materials is carried out through monotonic bending tests to evaluate their ability to mitigate local buckling and enhance the moment rotation behavior of filled HSS beams. Mechanical properties of the selected material are investigated through monotonic and cyclic mechanical compression tests.

Chapter 7: An finite element model of an empty HSS beam subject to cyclic bending loads is validated against a previously tested cantilever beam (Fadden & McCormick, 2011) and an FE model of the fill material cube is also validated against monotonic compression tests. The validated finite element model that adequately predicts seismic behavior of filled HSS beams is developed and improvement in seismic performance of the HSS beams by incorporation of the lightweight, non-traditional material is evaluated when subject to cyclic loading. Limiting parameters such as beam width thickness ratio and beam depth thickness ratio are studied.

Chapter 8: A summary and conclusions stemming from the research are presented. Assessment of the suitability of HSS based moment connections and the non-traditional civil engineering material for passive control applications under large cyclic loading conditions is discussed. Suggestions for future research on seismic application of HSS based moment connections and innovative fill materials are also presented.

CHAPTER 2 LITERATURE REVIEW

2.1 Background

Columns and beams make up the load bearing components of a moment frame system as shown in Figure 2.1. Columns and beams are connected to one another with fully and/or partially restrained moment connections and are designed to support vertical loads induced by the weight of floors, infill walls, and furniture as well as resist lateral loads due to wind and earthquake loads through shear and bending. During seismic events, input energy is dissipated through a combination of the following mechanisms: plastic hinging of the beams, shear yielding in the panel zone of moment connections, or plastic hinging of the columns. Plastic hinging of the columns is undesirable since this can induce large inter-story drifts and potentially catastrophic soft-story mechanisms. A strong column weak beam approach should be followed in design to ensure safety and satisfy ductility requirements (Roeder et al., 1989).



Figure 2.1 Examples of Steel Moment Frame Construction (www.ecs.umass.edu)

Prior to the 1994 Northridge earthquake, Complete Joint Penetration (CJP) welded flange connections with a bolted or welded shear tab were the most common connection used in seismic moment frame systems as illustrated in Figure 2.2 (Engelhardt & Sabol, 1997; Tremblay et al.,

1995). During the 1994 Northridge earthquake, no fatalities or building collapse associated with steel moment frames were reported (Mahin, 1998; Tremblay et al., 1995). However, unexpected fracture of the beam column connection welds was observed even without the presence of inelastic deformation (Mahin, 1998). The premature, non-ductile fracture required substantial repair which led to significant economic losses. Similar damage was also observed one year later in steel moment frames during the Hyogoken-Nanbu earthquake in Japan (Smolka & Rauch, 1996). The evidence of structural deficiencies and unpredictable seismic performance of steel moment frames resulted in a comprehensive investigation focused on improvement of seismic performance of these moment connections and systems. The SAC Joint Venture was founded by the US Federal Emergency Management Agency (FEMA) to develop repair technologies and new design approaches to ensure improved performance of steel moment frames during future strong earthquakes.

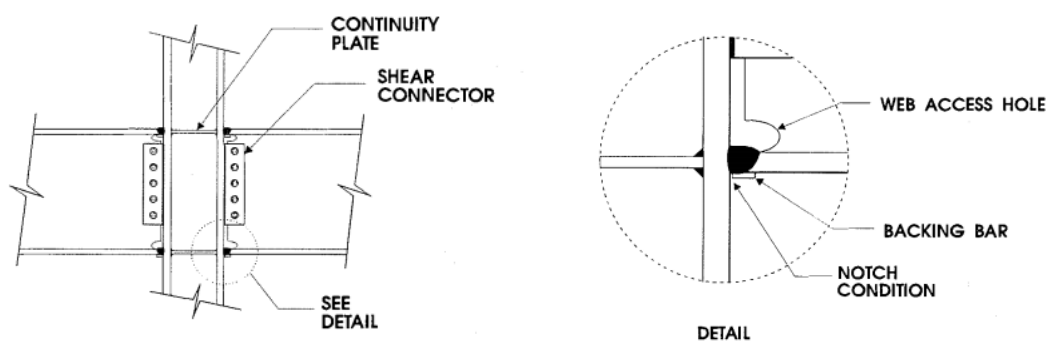


Figure 2.2 Typical Pre-Northridge Moment Connections (Tremblay et al., 1995)

A number of studies and investigations were undertaken which include: field studies of the damaged connections, laboratory testing of pre- and post-Northridge connections, numerical simulations of weld details and fracture failure modes to explore the potential causes contributing to the fracture of these joints (Engelhardt & Sabol, 1997; Miller, 1998; Popov & Blondet, 1996). The studies revealed that low weld metal toughness, groove weld backing bars and web tabs were predominant factors triggering connection fracture failure (Engelhardt & Sabol, 1997). Thus, modifications were made to current design and construction practice. As for the welds, significant changes included the use of weld metal with high toughness, enhancement on welding workmanship and quality control. Connection configurations were modified to utilize cover plates, haunches or ribs to reinforce the joints. Reduced beam sections (i.e. dogbone

shaped beam flanges in the plastic hinge region) were investigated through extensive experimental and analytical tests leading to their prequalification as a seismic connection and the most common connection configuration used today (Chen et al., 2005; Engelhardt & Sabol, 1998; Engelhardt et al., 1996; Kim et al., 2002; Uang et al., 2000; Yu et al., 2000). As illustrated in Figure 2.3, either by reinforcing moment connections or reducing the beam sections, the objective is to move the plastic hinge location away from the column face and ensure the connection is stronger than the beam since the beam flange to column flange weld and surrounding material was shown to be vulnerable to fracture due to weld defects and stress concentrations at the weld access hole (Engelhardt & Sabol, 1997).

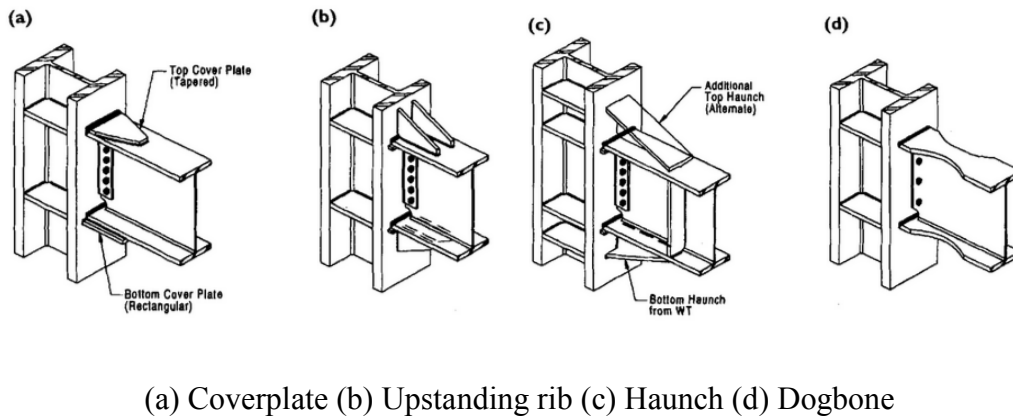


Figure 2.3 Examples of Modified Moment Connection Designs (Engelhardt & Sabol, 1997)

US researchers focused on optimizing the geometry and configuration of seismic moment frame connections to reduce the chance of brittle weld failure at critical joints. Japanese researchers took an alternative approach after the Hyogoken-Nanbu earthquake and focused on improvements in material and weld quality (Nakashima et al., 2000). Work in both countries has led to improvements and modifications to current design of steel moment frame systems.

The need to better understand the performance of structures and ensure their resilience has also led to a focus on performance based design. Performance based design requires a structure to meet specific performance goals, such as maximum inter-story drifts for a given level of shaking. In addition to satisfying different targeted goals, uncertainties in design variables, fabrication and loading are considered in a probabilistic analysis allowing structural reliability indices to be determined to quantify the confidence that the structure will not exceed a targeted performance

level. A focus on performance based design has led to the need to develop means of improving the performance of steel moment frame systems either through new design considerations or incorporation of supplemental systems.

However, studies of steel moment frames have only considered improvements of traditional wide flange beam to column or wide flange beam to HSS column connections without accounting for the potential of other beam sections such as HSS. Innovative materials, such as polymer foams and rubber, also can enhance steel member behavior in the plastic hinge region by limiting local buckling and increasing energy dissipation capacity. The use of alternative beam sections and non-traditional civil engineering materials provides potential solutions that can create more resilient and economical structures.

2.2 HSS Applications in Steel Structures

2.2.1 Background

Hollow structural sections (HSS) commonly refer to cold formed steel members with either round or rectangular cross sections. For the rectangular and square sections, the corners are heavily rounded with a radius approximately twice the wall thickness. HSS also can be hot formed, but hot formed sections are prohibitively expensive thus they are not as popular as cold formed sections (Sun, 2014). Since their introduction in the 1950s, HSS have been widely used in offshore and onshore structures primarily as truss members, braces, barriers, towers, masts, cladding supports and columns (Wardenier et al., 2002).



(a) River tawe south bridge, UK (b) Library and Civic Centre of San Jorge, Spain



(c) The Survanabhumi Airport, Thailand (d) Airport Frankfurt, Germany

Figure 2.4 Examples of Applications of HSS (www.cidect.com)

HSS can be manufactured seamless or from plate with a weld seam. Welded sections are more common where the manufacturing process utilizes either electrical resistance welding or induction welding processes. Round, rectangular or square HSS can be made by deforming a steel plate or strip through forming rollers into a specific section and then welding the seam to create a closed member (Wardenier et al., 2002). The manufacturing process is either: 1) forming a plate into circular tube then rolling it into its final shape; 2) forming the plate directly into its final shape by bending sides through rolling then welding; or 3) welding together the flange tips of two channels. The procedures are provided by the Steel Tube Institute (2003) as illustrated in Figure 2.5.

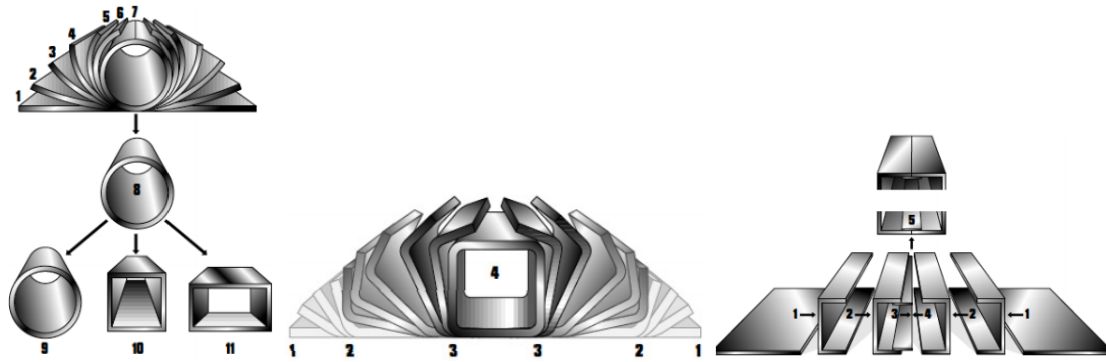


Figure 2.5 HSS Manufacturing Processes (Steel Tube Institute, 2003)

The popularity of HSS has been increasing due to their appealing properties such as a high strength-to-weight ratio, excellent compression, bending and torsional resistance, ease of use in modular construction, aesthetic appeal, and low drag coefficient when exposed to wind or water forces. To better understand the properties of HSS and explore design methods for their applications in seismic moment frame systems, studies on their behavior subject to various loading conditions have been carried out by researchers. Some relevant details of this work are presented below.

2.2.2 Axial Behavior of HSS

2.2.2.1 Brace

The use of HSS as braces in seismic moment frames offers an attractive system for seismic applications because of their high torsional rigidity and excellent compression capacity. However, their applications are typically limited to braced frame systems where they act as the fuse in resisting lateral loads. HSS braces have been proven very efficient in seismic applications through extensive experimental and analytical studies (Bešević, 2014; Elchalakani et al., 2003; Foutch et al., 1987; Fukuta et al., 1989; Goggins et al., 2005; Goggins et al., 2006; Haddad et al., 2010; Lee & Goel, 1987; Nip et al., 2010; Palmer et al., 2012; Pons, 1997; Roeder et al., 1987; Sohal & Chen, 1988; Tang & Goel, 1989; Tremblay, 2002; Tremblay et al., 2003; Tremblay et al., 2008; Zhao et al., 2002). However, experimental tests and post-earthquake observations indicated that tubular braces tended to experience premature fractures after early onset of local buckling during a severe earthquake, which may result in significant degradation in stiffness and

strength of the story (Goggins et al., 2005; Tang & Goel, 1989; Tremblay, 2002). To better understand the inelastic behavior of HSS braces, some research has been conducted to study key parameters that influence post-buckling performance of these braces and braced frames (Goggins et al., 2005; Goggins et al., 2006; Haddad et al., 2010; Sohal & Chen, 1988; Tremblay, 2002; Tremblay et al., 2008); others have tried to predict the fracture life of HSS braces and develop corresponding hysteresis models (Haddad et al., 2010; Tang & Goel, 1989); and methods also have been proposed to mitigate local buckling and delay the occurrence of fracture (Bertero et al., 1989; Lee & Goel, 1987; Liu & Goel, 1988).

Although braces are not used in moment frame systems, studies of HSS axial behavior can provide insight into potential limiting values in moment frame applications. Tremblay (2002) suggested that fracture of RHS bracing members was strongly dependent on the slenderness ratio of the braces, and to a lesser extent, on the width thickness (b/t) ratio of the brace cross section and imposed loading history through 76 cyclic tests of axially loaded HSS bracing members (Figure 2.6). The test results of 15 HSS bracing specimens under cyclic loading tests showed that yield strength, member slenderness and section width thickness (b/t) ratio were three factors that influence ductility capacity of HSS bracing members (Goggins et al., 2005; Goggins et al., 2006). Ten concentric HSS braces were designed based on a weak brace, strong gusset plate principle and tested under cyclic loads which indicated that the initial imperfection, yield strength and gusset plate thickness affects the seismic behavior and occurrence of fracture (Haddad et al., 2010). Tang and Goel (1989) proposed an empirical criterion to predict the fracture of rectangular tubular bracing members in terms of axial deformation. The test results of 34 bracing members, including square tubing, circular tubing and wide flange members, demonstrated that the cross-section shape, slenderness ratio of braces and cross-section size influence the fracture life of brace specimens (Tremblay et al., 2003).

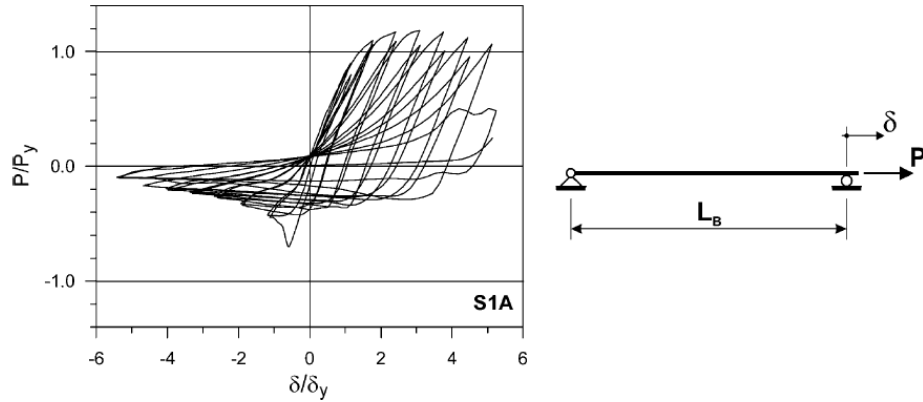


Figure 2.6 Typical Hysteresis Behavior of Braces under Symmetric Cyclic Loading (Tremblay, 2002)

To mitigate local buckling of tubular braces in steel framing systems and thus delay the initiation of fracture, concrete-filled rectangular steel braces were tested under quasi-static cyclic loading (Liu & Goel, 1988). The test results indicated the presence of concrete delayed occurrence of local buckling and dissipated more input energy compared to empty HSS braces especially for braces with larger width thickness ratios and smaller slenderness ratios.

Modeling techniques used for HSS braces provide an insight into numerical simulation of HSS members under large inelastic deformation. As illustrated in Figure 2.7, there are three categories of hysteretic models of brace: finite element model, physical theory and phenomenological models. The latter are simple and computationally efficient, but have been gradually replaced by finite element models with rapid development of finite element programs and a desire to capture the physical behavior. Ikeda and Mahin (1986) proposed an empirical expression for the relationship between axial force and deformation behavior which incorporated several behavioral characteristics for better representation of inelastic behavior of steel braces. Hassan (1991) derived a refined phenomenological model for hysteretic behavior of steel bracing members based on previous experiments to compute dynamic response of concentric braced structures under earthquake excitation. Jin and EI-Tawil (2003) suggested a stress-resultant plasticity model that accounted for gradual spread of plasticity throughout the cross section and brace length as well as deterioration of cross-section stiffness which has been proven capable of yielding relatively accurate inelastic behavior of various braces under cyclic loading conditions. A model for plastic behavior of steel braces with distributed plasticity and fiber discretization of

the brace cross section was developed allowing the response of elements to be computed through integration of the stress-strain relationship (Uriz et al., 2008). The advantage of the model was consideration of kinematic and isotropic hardening as well as accounting for the Bauschinger effect and interaction between axial and bending loads. However, since the model did not consider the effect of local buckling, it is more useful for considering the global response of braces with compact sections whose local buckling would be less severe compared to non-compact braces. Huang (2009) presented a continuum mechanics material model that introduced low cycle fatigue and degradation of mechanical properties when modeling inelastic behavior. The analytical results showed a good agreement with experimental results of braces; however, accuracy of the prediction depends on the material properties specified.

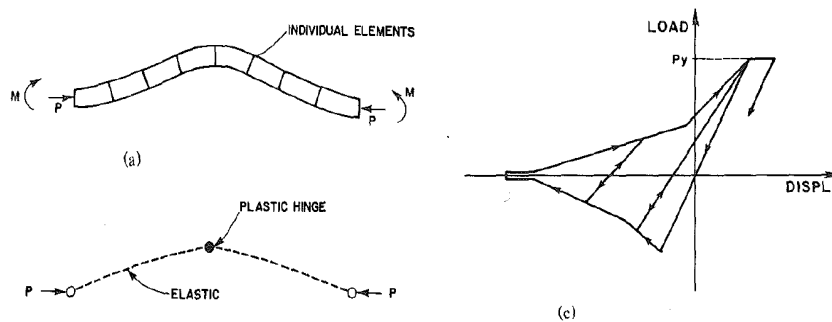


Figure 2.7 Brace Hysteretic Models (Ikeda & Mahin, 1986) (a) Finite Element Models (b) Physical Theory Models (c) Phenomenological Models

2.2.2.2 HSS Columns

HSS columns have been commonly used in steel moment frames in Japan and Europe because of their symmetric biaxial strength, excellent torsional resistance and compression capacity given the reliance of Japanese design on space frame systems. Early studies were performed in Australia, Canada, Japan, Singapore and Europe to explore HSS column inelastic behavior with respect to yield stress and residual stress due to cold forming effects in order to evaluate design procedures (Bjorhovde, 1977; Bjorhovde & Birkemoe, 1979; Chan et al., 1991; Davison & Birkemoe, 1983; Dawe et al., 1985; Hancock & Zhao, 1992; Key & Hancock, 1993; Liew et al., 1989; Sully & Hancock, 1996).

Studies focused on the effects of the cold-forming process and fabrication errors on the local and global behavior of HSS columns. Bjorhovde (1977) first studied the strength and behavior of HSS columns through experimental tests which found heat treatment had little benefit on the overall behavior of columns. Then Bjorhovde and Birkemoe (1979) suggested that material coupon tests alone could not provide enough information for predicting the inelastic behavior of HSS columns. Based on measured residual stress and variant of yield stress around the section, an analytical study accounting for geometric imperfections, residual stress and yield strength distribution was conducted to explore the influence of these key parameters on the behavior of stub and pinned end columns (Davison & Birkemoe, 1983; Key & Hancock, 1993). The results demonstrated that these parameters had minor influence on the ultimate strength of the columns, but did result in a decrease in the axial stiffness or tangent modulus. Key and Hancock (1993) utilized nonlinear finite strip analysis results to demonstrated that residual stress resulted in up to a 10% decrease in axial stiffness from early stages of loading. Another computer aided analytical method similar to the finite strip analysis was performed which provided a relatively accurate result of post buckling behavior of HSS columns (Dawe et al., 1985). The analytical study of HSS columns indicated increased yield strength at the corners had little influence on the local buckling behavior of HSS columns. However, residual stress had significant influence on inelastic behavior of columns in partially yielded areas. With developments in the finite element method, a numerical model which accounted for initial imperfection and residual stress was used to explore the ultimate buckling behavior of HSS columns (Chan et al., 1991). In this method, plate local buckling effects were also considered by adopting a material stress-strain relationship. The analytical results demonstrated this procedure was efficient and accurate enough to predict ultimate capacity of HSS columns.

Other studies considered effects of the slenderness ratio on the post-buckling performance of HSS columns by comparing the ultimate behavior of stub and long column tests under axial compression. To study the ultimate strength of HSS columns subjected to biaxial loads in terms of eccentricity of loading and plate and column slenderness ratios, 28 large scale column tests, including stub and long columns, were conducted (Liew et al., 1989). Hancock and Zhao (1992) also performed tests on long columns to determine a plate slenderness ratio beyond which the section ultimate strength was controlled by local buckling. The test results suggested that an

increase in the plate slenderness ratio could result in a significant drop in the ultimate strength of HSS columns. A set of experimental tests on stub HSS columns and long columns were performed to study strength and collapse behavior of HSS columns. These tests found that the American Iron and Steel Institute (AISI) class A curve was more suitable for concentrically loaded columns than the class B curve (Key et al., 1988). Although these studies focused mainly on the compression behavior of HSS columns, their results provided guidance in the use of HSS for tube based seismic moment frame systems.

Research also has been concentrated on more complex behavior of HSS columns under combined loading conditions. A simplified analysis method to predict collapse behavior of HSS columns under combined axial compression and torsion was proposed based on the plastic mechanism observed in HSS tests under different combinations of compression and torsion (Mahendran & Murray, 1990). Monotonic loading tests of HSS beam columns subject to various combinations of biaxial bending and axial compression loads were undertaken to verify the interaction relationship in the Canadian standard, which was shown to be a conservative and satisfactory approximation (Pillai & Kurian, 1977). Toma and Chen (1983) utilized a deflection method which was validated by experimental test results to explore post buckling behavior of HSS beam columns and found initial imperfections, lateral force at the mid-span, and end moments could lead to a reduction in the ultimate strength under monotonic loading conditions. Chan (1989) proposed an incremental iterative numerical method to trace the load deflection path of HSS beam column nonlinear behavior which had been proven an efficient and accurate method since it eliminated drift off errors. Sully and Hancock (1996) performed pin-ended square HSS beam column tests by applying axial load and two end moments at a specific ratio, β , to investigate interaction design rules. The examples of the interaction curves for different end moments ratios are shown in Figure 2.8. Since the AISC Specification interaction rule at that time did not consider variation of β , it resulted in unconservative designs especially for β equal to negative one. Hancock and Rasmussen (1998) investigated buckling behavior of HSS beam columns under end moment and axial loads which showed axial capacity was better predicted in the Australian Steel Structures Standard, AS4100:1998, Eurocode 3 and the American Institute of Steel Construction Load and Resistance Factor Design Specification than bending capacity

which was reasonably accurate compared to test results. They emphasized that the way the end moment was applied could exert significant influence on the bending capacity of HSS columns.

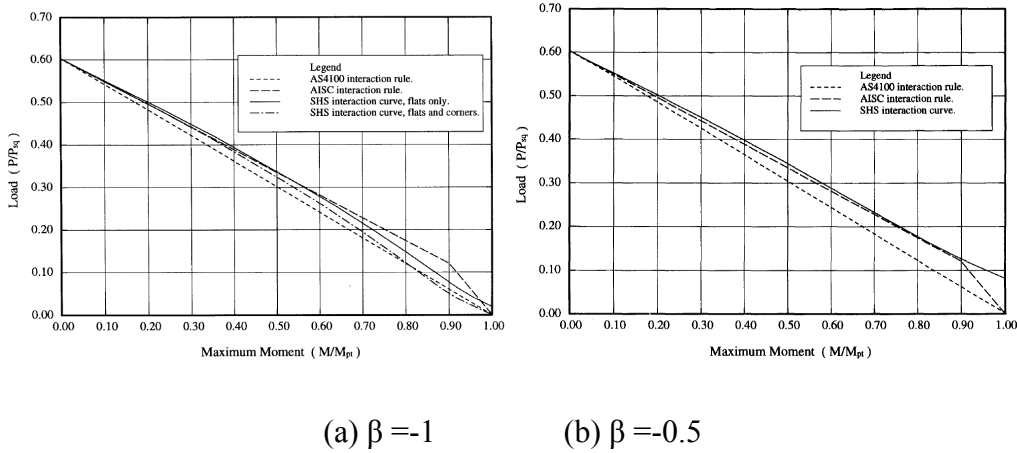


Figure 2.8 Interaction Curve for Various β (Sully & Hancock 1996)

More recently, researchers have started to consider plastic design of HSS columns and conducted full scale tests under seismic loads. Han and Chen (1983) studied buckling and cyclic inelastic behavior of HSS beam columns utilizing a combination of the Finite Segment Method (FSM) and the Influence Coefficient Method (ICM) which had been proven an efficient approximation for post buckling behavior of HSS beam columns without convergence problems. However, to accurately predict cyclic behavior of HSS beam columns, further studies on the generalized stress-strain curve were needed. Wilkinson and Hancock (1998) studied viability of HSS plastic design under bending and compression loads through intensive experimental and numerical analysis which suggested that they could be applied in plastic design, but with stricter element and global slenderness ratios. These slenderness ratio limits needed to be further investigated. Wang et al. (2008) performed collapse simulation of a four-story steel moment frame with HSS columns through an online hybrid test and showed the HSS column base experienced local buckling and fracture (Figure 2.9) at cycles up to 0.1 rad. The fracture resulted in significant deterioration in strength and stiffness of the whole structure. Mamaghani (2010) suggested cyclic biaxial loading effects should be considered in seismic design and ductility evaluation since both experimental tests and numerical analysis showed bidirectional loading could result in much more complex behavior of HSS columns compared to unidirectional loading cases. Lignos and Krawinkler (2010) developed analytical models considering moment rotation relationship and

moment deterioration of a tubular hollow square steel column subject to axial and cyclic moments which has been calibrated against 120 tubular hollow square steel columns tests.

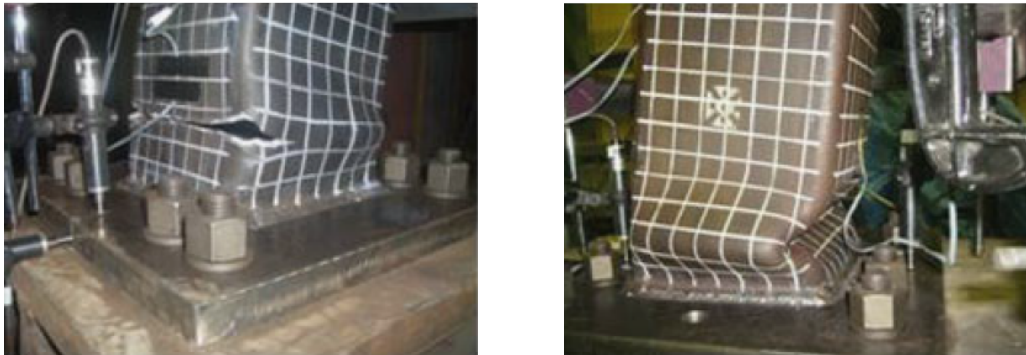


Figure 2.9 Local Buckling and Fracture of Column Bases (Wang et al., 2008)

The application of HSS columns is limited in the United States since few studies have been conducted to explore the feasibility of these column shapes using typical US design methods for moment frame systems. Further investigation on the seismic performance of HSS columns is needed to provide insight into seismic design of HSS columns which could offer an alternative to wide flange shapes that may be susceptible to local and lateral torsional buckling (Fogarty & El-Tawil, 2014).

2.2.3 Flexural Behavior of HSS

As previously mentioned, most research has been focused on HSS beam column behavior subject to bending and compression loads, while only a few studies have considered the flexural behavior of HSS beams. The investigations on performance of HSS beams subject to pure bending could provide insight into the feasibility of HSS beams in steel seismic moment frame systems and offer valuable suggestions on design limitations for these beams.

Work conducted by Hancock and Zhao (1992) revealed flange slenderness limits below which HSS beams could be used in plastic design and determined the ultimate strength of HSS beams under bending loads through experimental tests. In this study, the lower limits on HSS flange slenderness were 25 for C350 rectangular hollow sections (RHS) and 22 for C450 RHS compact sections. Zhao and Hancock (1992) continued to study HSS beam behavior under pure bending tests and found that the actual moment capacities were always greater than the nominal moment

capacities by 18% on average as shown in Figure 2.10. The increase in moment capacity was partly due to material strength enhancement in the cold forming process and partly due to strain hardening effects. However, local buckling could result in a sudden drop of the moment capacity and large degradation in beam strength. To address buckling and collapse behavior of HSS beams under pure bending loads, a set of experimental tests on HSS beams with various depth thickness ratios (d/t) and an analytical study based on the Rayleigh-Ritz method were conducted by Corona and Vaze (1996). Under monotonic increasing loads, HSS beams showed a periodic ripple with increasing curvature of the beams. The amplitude of the ripples also increased for HSS beams with higher d/t values. Wilkinson and Hancock (1998) examined web slenderness limits for plastic design based on experimental test results. They found that the web slenderness limit in specifications derived from wide flange beams was not conservative and influences of web and flange slenderness ratios were not independent. A bilinear limit formula considering interaction of the web and flange slenderness limit was proposed as shown in Equation 2.1. As shown in Figure 2.11, the interaction relationship was drawn at a rotation capacity equal to four regardless of steel material grade. Here the rotation capacity was defined as a measure of rotation between reaching M_p and the point where the moment fell below M_p .

$$\lambda_w \leq 70 - \frac{5\lambda_f}{6}, \lambda_f \leq 30 \quad \text{Equation 2.1}$$

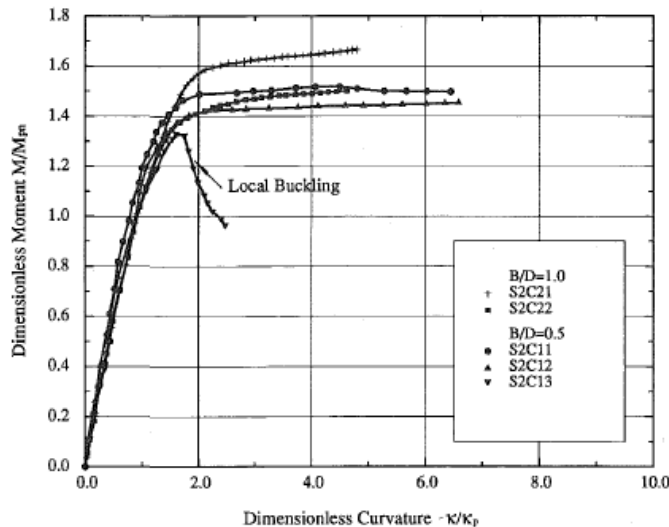


Figure 2.10 Dimensionless Curvature Versus Dimensionless Moment (Zhao & Hancock, 1992)

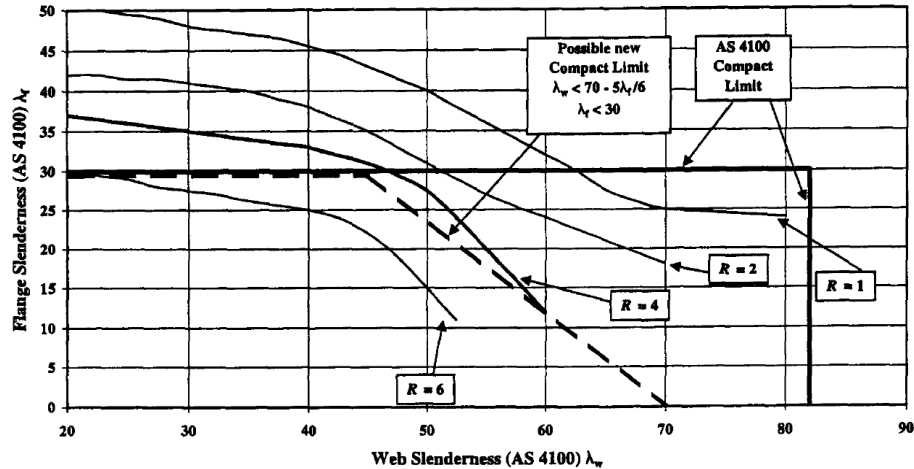


Figure 2.11 Proposal for New Compact Limits for RHS (AS 4100) (Wilkinson & Hancock, 1998)

A model based on lumped damage mechanics and continuum damage mechanics was developed (Guerrero et al., 2007) to study local buckling effects of HSS beams subject to biaxial bending loads. This model had been validated by tests and proven simple and effective in predicting the degree of local buckling of HSS beams under biaxial loads. A new method based on general beam theory was presented to evaluate elastoplastic behavior of HSS beams which was compared with analysis results from the commercial software Abaqus to verify its accuracy and efficiency (Abambres et al., 2012).

In addition to HSS beam tests under monotonic bending loads, cyclic bending tests were performed to address HSS seismic performance. Vaze and Corona (1998) first studied post-buckling behavior and collapse of square HSS beams under cyclic pure bending loads and divided the deformation process into four stages. In the last stage, one of the ripples caused by previous cycling would become unstable and grow faster which led to collapse of the HSS beams and loss of moment capacity. Brescia et al. (2009) compared cyclic behavior and rotation capacity of HSS beams utilizing experimental tests results which verified that the local slenderness ratio had significant influence on seismic performance of HSS beams. HSS beams with lower local slenderness exhibited a stable hysteresis behavior under seismic loads which suggested that HSS were feasible for use in seismic applications if a proper local slenderness ratio was chosen. A comparison of the cyclic performance and ductility capacity between cold-formed and hot-finished HSS beams was carried out which indicated all specimens had

adequate plastic rotation capacities; however, they failed to reach their plastic moment capacities. Fadden and McCormick (2014a) characterized seismic performance of HSS beams and determined the influence of width thickness ratio (b/t) and depth thickness ratio (d/t) through a series of experimental tests and parametric studies under large inelastic cyclic loads. In the experimental tests, most of the HSS beams were able to develop stable hysteresis loops and achieve their plastic moment capacities. However, the beams with larger d/t and b/t ratios led to initiation of local buckling at earlier cycles leading to degradation of the moment capacities and fatigue induced fracture at the corners of the HSS beams as shown in Figure 2.12. Based on the test results, a piecewise function for d/t and b/t interaction relationships was presented to ensure 90% of the moment capacity remains at 0.04 rad. rotation level as seen in Equation 2.2 and Equation 2.3.

$$\frac{d}{t} \leq 55 - 1.05 \frac{b}{t} \text{ for } 14 \leq \frac{b}{t} \leq 22 \quad \text{Equation 2.2}$$

$$\frac{d}{t} \leq 67.1 - 1.6 \frac{b}{t} \text{ for } 22 \leq \frac{b}{t} \leq 26 \quad \text{Equation 2.3}$$

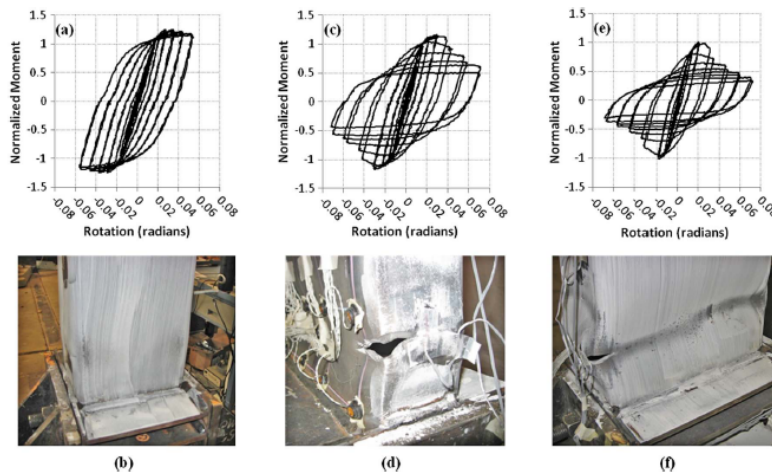


Figure 2.12 Normalized Moment Versus Rotation Hysteresis Curves and Photographs in HSS Beam Bending Tests (Fadden & McCormick, 2011) (a, b) HSS 203.2 × 152.4 × 9.5 mm at completion of the test; (c, d) HSS 254 × 101.6 × 6.4 mm at completion of the test; (e, f) HSS 304.8 × 152.4 × 6.4 mm during final test cycles

Fadden and McCormick (2014a) also suggested that the HSS beams with higher d/t and b/t ratios tend to have larger equivalent viscous damping at low rotation levels, but are less stable at large rotations. With calibrated finite element models, potential limiting parameters to obtain stable

hysteresis behavior and ensure ductility capacity were further explored. The parametric study considered 133 HSS beam sections under cyclic bending loads with d/t and b/t ratios ranging from 7.0 to 31.5 and 16.4 to 52.0 respectively. Based on the finite element simulations, two normalized b/t and d/t limits were presented as shown in Equation 2.4 and Equation 2.5.

$$\frac{b}{t} \leq 0.48 \sqrt{\frac{E}{f_y}} \quad \text{Equation 2.4}$$

$$\frac{d}{t} \leq 1.13 \sqrt{\frac{E}{f_y}} \quad \text{Equation 2.5}$$

These local slenderness ratio limits were more conservative than those specified for compact sections in flexure considering non-seismic applications (AISC, 2010b). If width thickness and depth thickness ratios are properly chosen, HSS beams are capable of developing stable hysteretic behavior with minor degradation in moment capacity, which demonstrates their viability for seismic applications.

2.2.4 Connections

2.2.4.1 Truss Connections

HSS based truss connections have been widely used and the joint types include T, Y and X-joints, Gap K-joints, and Overlap K-joints as seen in Figure 2.13. These joints can even be multi-planar connections as shown in Figure 2.14. Korol and Mirza (1983) performed tests of double chord HSS trusses which exhibited inadequate end joint strength due to joint failures principally by chord shearing at the end of the top chord. Thus design details about improvement of these connections were presented based on experimental test results. Packer and Cassidy (1995) proposed two equations for computation of effective weld length for HSS T, Y and X connections through full scale connection tests. Chiew et al. (2007) investigated square HSS-based T joints under static and fatigue loads and described the failure mode of the fatigue tests: cracking initiated at one of four corners where the branch and chord intersected and then propagated in the direction along the chord sidewall. The fatigue test results provided insight into seismic performance of T joints under cyclic loads. Design guides for rectangular and circular HSS joints under predominately static loads were presented by Packer et al. (2009) and Wardenier et al. (2008) with detailed design procedures for various joint types. These guides

adopted limit state designs considering the ultimate strength of the joint and the load leading to an ultimate deformation limit of the joint. Haque and Packer (2012) studied two methods to predict capacity and the failure mode of welded elliptical hollow section T and X connections which indicated the equivalent rectangular hollow section approach is more accurate.

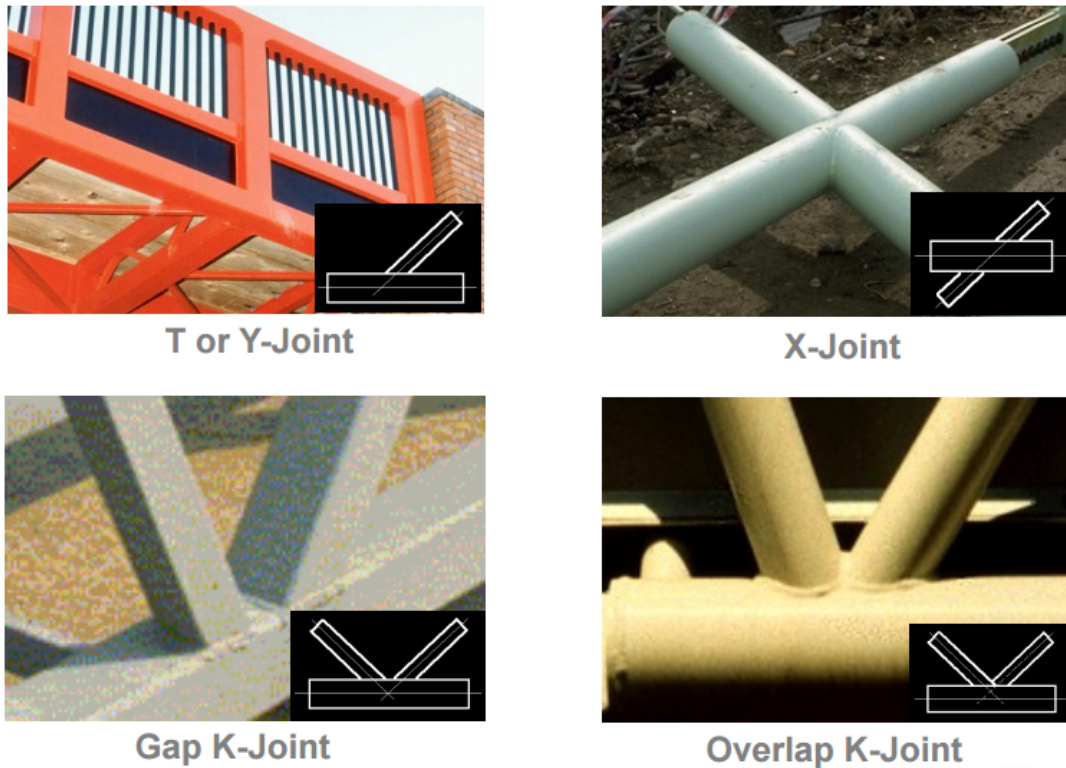


Figure 2.13 HSS In-Planar Joint Types

(Fletcher. Truss Connections-Joint Types. Retrieved from:http://ncsea.confedge.com/asset/confEdge/NCSEA/_warehouse/file/_system/38567dfd_dc40_4c31_b084_4d3dc31402f2/Handout.%204-25-13.B.Fletcher.FullPageColor.pdf)

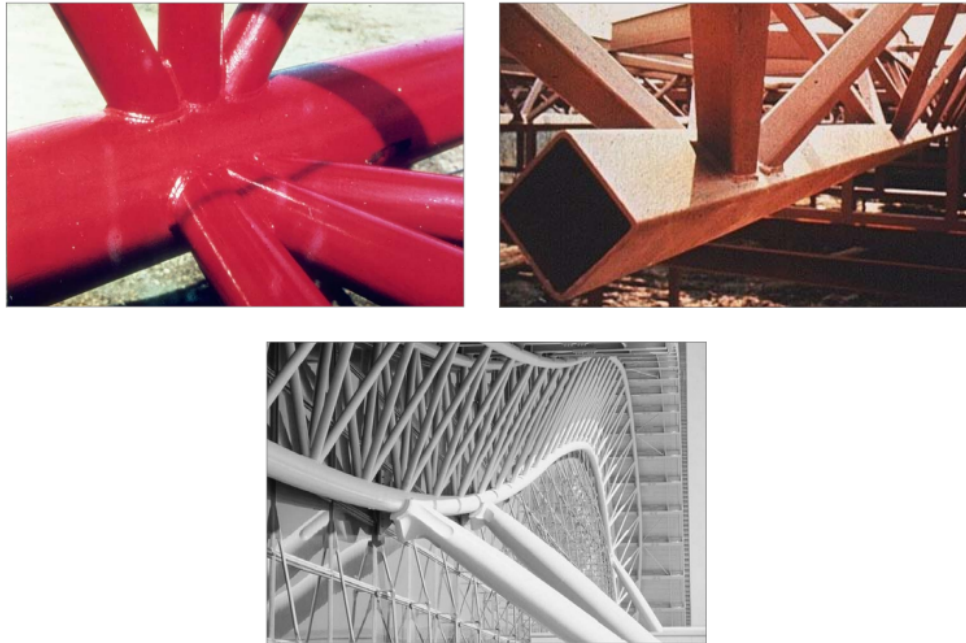


Figure 2.14 Multi-Planar HSS Connections

(Fletcher. Truss Connections-Multi-Planar. Retrieved from:http://ncsea.confedge.com/asset/confEdge/NCSEA/_warehouse/file/_system/38567dfd_dc40_4c31_b084_4d3dc31402f2/Handout.%204-25-13.B.Fletcher.FullPageColor.pdf)

An overview of nonlinear finite element analysis for HSS joints suggested shell elements are accurate enough to simulate behavior of HSS joints under static loads (Vegte et al., 2010). It also indicated that analytical results from implicit and explicit solutions were almost identical and ignoring weld geometry would underestimate ultimate strength of the joints. Woghiren and Brennan (2009) studied weld toe stress concentration in multi-planar HSS KK joints through the finite element method and equations allowing rapid optimization of the joints and identification of the locations of maximum stress were proposed.

2.2.4.2 Vierendeel Truss Connections

Studies on HSS based moment connections are fewer than those on HSS column to wide flange beam connections. However, relevant research on HSS based Vierendeel truss connections can provide useful information in regards to potential limit states of HSS based moment connections since brace-to-chord joints in Vierendeel trusses are designed to resist moment. Braces and chords in a Vierendeel truss are similar to beams and columns in moment frames, respectively

(Jubb & Redwood, 1966). This study also concluded that full moment transfer could be achieved when the column and beams have the same width. Korol et al. (1977) further investigated HSS-to-HSS Vierendeel truss connections with unequal widths and showed that these connections could not achieve full moment transfer unless some reinforcement was applied at the connection. Similar observations were made through finite element analyses performed later (Korol & Mirza, 1982). Wardenier (1982) summarized five potential failure modes for brace-to-chord joints of Vierendeel trusses under in-plane bending. Figure 2.15 illustrates the failure modes:

- (a) Plastic deformation in the chord face;
- (b) Cracking in the chord due to punching shear;
- (c) Cracking in the brace;
- (d) Crippling of the chord sidewalls;
- (e) Shear failure of the chord.

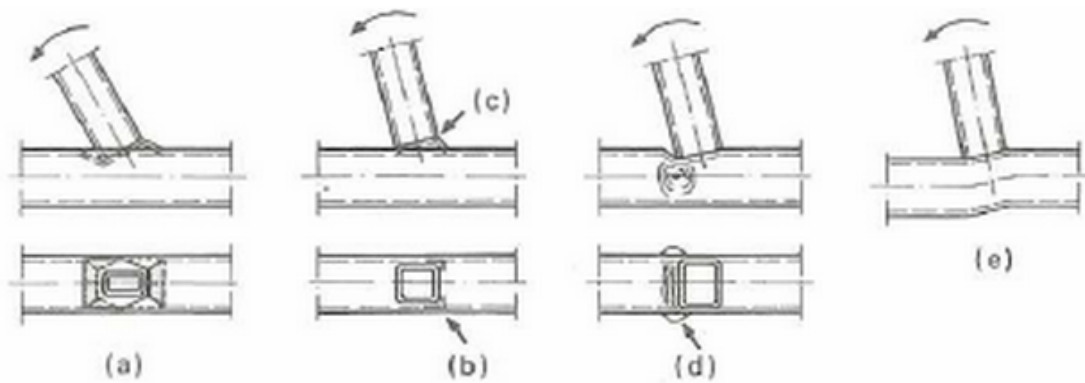


Figure 2.15 Possible Failure Modes for Brace-to-Chord Joints of Vierendeel Trusses Loaded by Brace In-Plane Bending Moment (Wardenier, 1982)

An analytical model to predict ultimate strength of biaxially loaded HSS beam-to-column connections was presented which had been proven accurate through experimental tests (Shanmugam et al., 1993). The results showed the ultimate capacity decreased significantly with increasing axial force subject to biaxial loads for thin walled HSS beam to column connections. Later studies (Packer & Henderson, 1997; Wheeler et al., 1998; Wheeler et al., 2000) further developed bolted HSS based connections with moment resistance. Nevertheless, all of these

bolted connections require additional tees, angles, or plates, which jeopardize their constructability and aesthetic appeal.

2.2.4.3 HSS Column to Wide Flange Beam Connections

Considerable research has been conducted to explore potential wide flange beam to HSS column connection configurations that are able to allow plastic hinging in the beam and meet seismic moment frame requirements. Both experimental tests and numerical analyses have been conducted to characterize the behavior of HSS column to wide flange beam connections. Twenty three moment connections between equal wide flange beams and square HSS columns reinforced by coped strap angles were tested which indicated that these connections were capable of developing the plastic moment capacity of the beam with adequate ductility. However, theoretical results suggested that P- Δ effects should be investigated for large inter-story drifts (Picard & Giroux, 1976). Fifteen moment connections, where the beam flange was narrower than column flange, showed that special attention should be given to the geometric design of the connection to ensure brittle fracture did not occur at the strap angles prior to the development of inelastic deformation. Test results also indicated that these connections could be used in plastic design since they had large rotational capacity (Giroux & Picard, 1977). Ten full scale moment connections between wide flange beams and HSS columns were tested to reveal 8 different failure modes which indicated that increasing the HSS column wall thickness or reinforcing the HSS column flange by using doubler plates was an effective way of achieving beam full plastic moment capacity (Dawe & Grondin, 1990). A blind bolted T-stub connection to an HSS column as an alternative to welded connections was designed and tested under static loads which indicated it behaved as a semi-rigid connection, but would be viable in low rise structures (Lee et al., 2010). A finite element analysis was carried out to study behavior of externally stiffened HSS columns to wide flange beam connections with triangular plates, angles and T-stiffeners. The findings suggested T-stiffeners were most effective in enhancing the rigidity and ultimate strength of the connections (Ting et al., 1991). Tests of 12 full scale double-angle shear connections with HSS columns were carried out which exhibited good rotational and shear resistance subject to monotonic loading (Gong, 2008). Test results also validated the effectiveness of flare bevel welds. A nonlinear analytical model incorporating moment flexibility was developed to predict the moment rotation relationship for extended end plate reinforced

blind bolted connections (Ghobarah et al., 1996). This model was validated by experimental testing and was shown to be reasonably accurate in predicting initial stiffness and ultimate strength at different loading levels.

In addition to investigations focused on static monotonic loading, cyclic loading conditions were also studied to explore these connections' earthquake response. Seven full scale wide flange beam-to-HSS column connections were tested to explore the seismic performance of externally stiffened and internally stiffened connections which found all the connections exhibited stable hysteretic behavior and actual moment capacities exceeded the plastic moment capacities for most connections (Shanmugan et al., 1991). Externally stiffened connections with T-stiffeners showed better ductility and significant increase in ultimate strength when compared to externally stiffened connections with angles and internally stiffened connections. Failure modes observed in the experimental tests were summarized as buckling of the column web, buckling of the beam flange and fracture at either the stiffeners or beam flange. The first mode was undesirable since it was contradictory with the strong column, weak beam philosophy, but this mode could be changed by increasing the column web thickness. They further investigated stress distribution and spread of yielding at various load levels which also indicated T-stiffener reinforced connections were most efficient compared to other types of configurations (Shanmugam et al., 1993). Based on previous studies, Lee et al. (1993) proposed a design guideline for two-way and four-way externally T-stiffened wide flange beam to HSS column connections. They also proposed a Ramberg-Osgood function to characterize moment rotation relationship for externally stiffened moment connections with T-stiffener which showed good agreement with test results. Cyclic tests of RHS column-to-wide flange beam connections reinforced by horizontal haunches were performed which indicated the haunches were effective in forming plastic hinges in the beam and away from the column face (Kurobane et al., 2001). Cyclic performance of high strength blind bolted moment connections with HSS columns was investigated through experimental tests and numerical analysis which suggested the design moment capacity of connections should be equal to 1.3 times those of the beam to minimize degradation of connection stiffness under cyclic loading and connection flexibility should be incorporated into nonlinear dynamic analysis to better predict seismic response of the moment frames (Mourad et al., 1995). Cyclic tests of five large scale reinforced connections and one unreinforced connection between a wide flange beam and HSS column were conducted to evaluate their

seismic performance (Chen et al., 2004). The test results indicated that by reinforcing the connections with vertical rib plates, the failure mode of the connection changed from brittle fracture at the beam flange penetration joint weld and access hole region to ductile plastic hinging away from column face. Two through plates reinforced HSS column to wide flange beam specimens were tested under cyclic loading to investigate their seismic performance which found that ductility and moment capacity degradation did not occur until beam rotation levels of 0.06 rad. (Mirghaderi et al., 2010).

2.2.4.4 HSS based Moment Connections

Limited studies have focused on the cyclic performance of HSS based moment connection, which is critical for these connections to resist earthquake loads. Kumar and Rao (2006) proposed and tested an open web HSS based moment connection by adding a channel at the top and bottom of the beam end. Their results indicated that the strength and stiffness of the proposed connection was related to the dimension of the channel connectors. Good ductility and energy dissipation capacity can be achieved for the connection. Fadden et al. (2014) performed cyclic testing on two fully welded unreinforced HSS-to-HSS beam-to-column moment connections and found these connections were unable to achieve the plastic capacity of the beam prior to fracture of the connection. A finite element parametric study looking to optimize welded HSS based moment connections by reinforcing them with external diaphragm plates and through plates was then conducted (Fadden & McCormick, 2014b). The numerical analysis indicated the reinforced connections could form plastic hinges in the beam with ductile hysteresis behavior and minor moment degradation. Based on previous studies, a design procedure was proposed for HSS-to-HSS moment connections under seismic loads which was instructive for future design work of HSS based moment connections.

2.3 Non-Traditional Civil Engineering Materials for Fill Applications

Structural passive control concepts have been proven effective in controlling structural response, such as enhancing energy dissipation, stiffness and strength of the system or increasing the natural period of the structure thus avoiding resonance under seismic loads. The advantage of passive control has been demonstrated during recent earthquakes (Nagarajaiah & Sun, 2000;

Spencer & Nagarajaiah, 2003). The cost benefits of structures equipped with passive control systems have been proven for retrofitted structures and through the design of a high performance structures such as nuclear plants, emergency response facilities and other critical structures (Buckle, 2000). Although they are effective in enhancing structural performance during an earthquake, passive control systems require additional installation and detailing requirements which complicates construction and increases cost. However, voids associated with HSS members are underutilized locations where innovative materials can be incorporated to provide supplemental energy dissipation capacity which avoids change of design and construction practices of both new and existing steel structures. However, suitable innovative materials need to be chosen and further assessment of the effectiveness of these materials is required through both experimental and analytical techniques (Soong & Spencer, 2002). Polymer foam and rubber as lightweight materials show promise for void fill seismic applications due to their high energy absorption ability and high strength-to-weight ratio. These materials will be discussed as fill materials in the following sections.

2.3.1 Polymer Foam

Polymer foam was first invented in the 1930s as a replacement for rubber and as a coating for protection of other materials (Sivertsen, 2007). A couple of decades later, flexible polyurethane foam was invented and used as cushion material. Polymer foams are made of a polymer and gas phase mixed together and can be either closed cell or open cell based on their microstructure as shown in Figure 2.16. In closed cell foams, the cell walls are intact which can isolate cells from each other. This type of foam is made of a polymer matrix and air bubbles and is generally more rigid and stronger than open cell foams, but with lower permeability. Thus, closed cell foam can be utilized as insulation material that resists leakage of air and water vapor. For closed cell or plastic foams, the deformation of the polymer foam is not recoverable thus energy dissipation mainly depends on cell fracture and crushing. Open cell foam has continuous open passage due to broken cell walls and consists of mainly ribs and struts. The open cell foam is more flexible and provides better absorptive capacity (Lee et al., 2005). Thus, they are good candidates for sound barriers that absorb noise in certain frequency ranges. For open cell or elastomeric foams, some energy is absorbed by hysteresis effects due to viscous flow of air in open cell foams and polymer deformation.

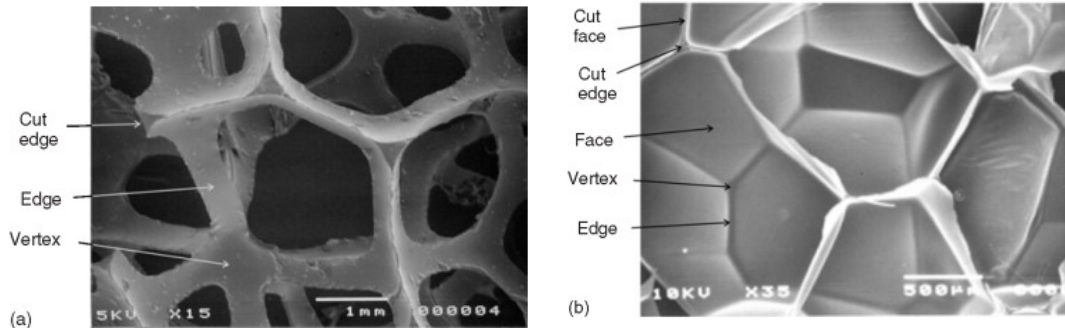
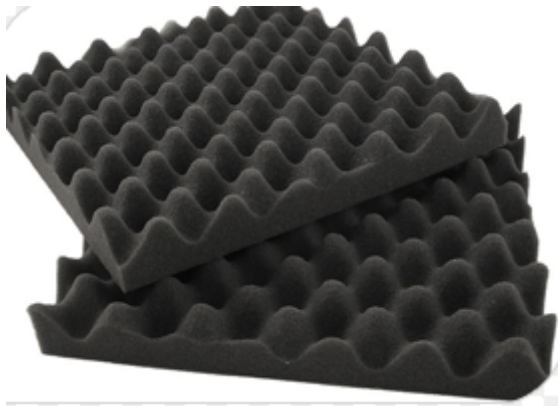


Figure 2.16 SEM Photograph of (a) PU Open-Cell Foam of Density 28 kg-m^3 ; and (b) Closed-Cell Low Density Polyethylene (LDPE) Foam of Density 24 kg-m^3 (Mills, 2007)

According to the composition, cell morphology and mechanical properties of polymer foams, they can be classified as either rigid, semi-flexible or flexible foams. Rigid foam has many applications in construction, building insulation, flotation, cushioning, appliances and packaging. Semi-flexible foams are used in applications such as automotive interiors and upholstery. For instance, seat, armrest and headrests in cars are generally made of semi-flexible foams. Flexible foam can be used as textiles, bedding, carpet underlay, furniture cushions and gaskets. Based on their chemical composition, there are a number of types of polymer foam such as polyurethane (PU), polystyrene (PS), polyolefin (polyethylene (PE) and polypropylene (PP)), poly (vinyl chloride) (PVC), polycarbonate (PC) and some other types in the resin family. Depending on the size of the foam cells, polymer foams can be categorized as macrocellular, microcellular, ultramicrocellular and nanocellular.

Various advantages of polymer foams allow their extensive application in mechanical, marine, aerospace and biomechanical engineering as seen in Figure 2.17. Their low density makes them suitable to be utilized in construction such as ceiling systems and sculptures due to weight reduction benefits. Their low heat transfer ability makes them optimal insulator. Their low permeability allows their use as waterproof materials in roofing system. Their high energy absorption capacity makes them perfect candidate for soundproof material, sports protector equipment and collision energy absorbers in the automobile industry.



(a) Packaging Foam



(b) Helmet



(c) Cushion



(d) Insulator

Figure 2.17 Various Applications of Polymer Foam

Numerous studies focused on their applications due to their range of properties. Rehkopf et al. (1994) studied the dynamic behavior of two densities of semi-rigid PU foam under multiple compression cycles which indicated that the foam undergoes cyclic softening and reduction of stress is greatest at low strain levels. The effects of maximum compression, strain rate and multiple cycles were also investigated which showed correlation with stress amplitude and degradation of each cycle. Ju et al. (2015) tested three types of PU foam under compression loads. The PU foam exhibited a nonlinear hyperelastic and viscoelastic behavior at large deformations that agrees well with Ogden's constitutive model. Triantafillou and Gibson (1987)

suggested a failure mode map for foam core sandwich beams that exhibited good agreement with experimental tests of beams with aluminum faces and rigid polyurethane foam cores. This map is useful for minimum weight design at a specific strength requirement. Pan et al. (2003) investigated sandwich beams with epoxy foam core under three-point bending tests and analyzed their failure modes using finite element simulations. Mills et al. (2007) analytically considered low density polymer foam in three application areas which indicated that the foam is able to provide human protection to avoid injury.

Researchers have also performed extensive studies on the mechanical properties of polymer foam. Warren and Kraynik (1991) formulated a constitutive model for the nonlinear elastic behavior of open cell foams using a micromechanical analysis. Brezny and Green (1990) studied influence of cell size on elastic modulus, fracture toughness, compressive and bending strength. The findings indicated that elastic modulus and fracture toughness were independent of cell size while compressive and bending strength were inversely proportional to cell size. Lakes (1983) suggested that additional degrees of freedom with rotation of microstructure should be considered in a complete continuum model of foamed materials. Zenkert and Burman (2009) tested tension, compression and shear fatigue properties of one type of closed cell foam with three densities. The results showed the fatigue life for different load types exhibited different failure mechanisms. Gibson and Ashby (1999) thoroughly discussed deformation mechanisms and mechanical properties of polymer foam based on a unit cell structure. The schematic compressive stress-strain curve for elastomeric foam includes three regimes: linear elasticity at low stresses, a plastic plateau and densification at high stresses. The linear elasticity is determined by cell wall bending and cell face stretching if the foam is closed celled. In this regime, Young's modulus can be calculated based on the initial slope of the stress-strain curve. The cell wall will collapse by elastic buckling in elastomeric foams that exhibit a plateau in the stress-strain curve under increasing compression load. When the cell walls are completely collapsed and touch each other, the applied load will compress foam and lead to densification. There are few studies on tensile properties of polymer foam since tensile yield strength is negligible compared to its compressive yield strength. However, Gibson and Ashby (1999) investigated microstructure deformation of elastomeric foam and plotted the stress-strain relationship under tensile loads as shown in Figure 2.18. At the lower stress level, linear elasticity is obvious due to cell wall bending and cell face stretching for closed cell foam (Figure

2.19). At large strain levels, the cell wall rotates towards the axis of the tensile load leading to an increase in stiffness. This increase causes the stress-strain behavior to enter the second stage of cell wall alignment. Similar to elastomers, some of the polymer foams are sensitive to loading rates and exhibit time dependent properties (i.e. viscoelasticity). Bergström and Boyce (1998) quantified rate dependent and hysteretic properties due to cyclic loading by proposing a constitutive model of elastomers. Then Bergström and Boyce (2001) modified the constitutive model for applications to soft biological tissues since it is capable of capturing the experimental behavior of elastomers subject to different general multiaxial loading conditions. However, due to complexity of the mechanical properties of polymer foams and wide variety of foams, few models are capable of capturing mechanical behaviors of all the polymer foams.

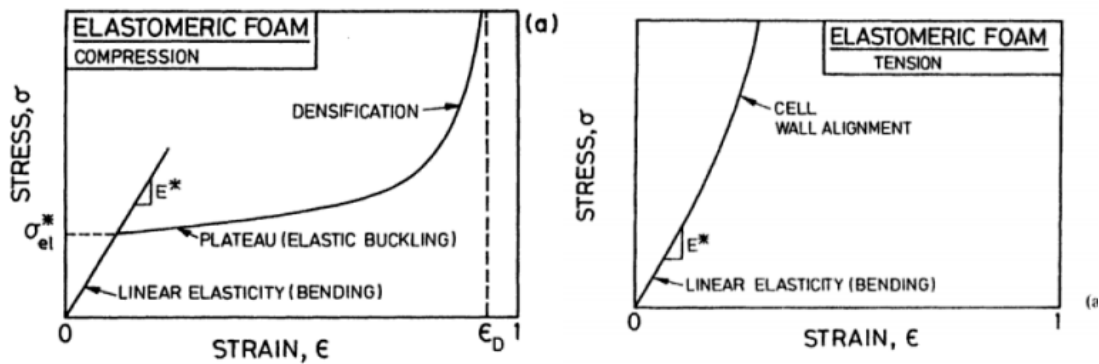
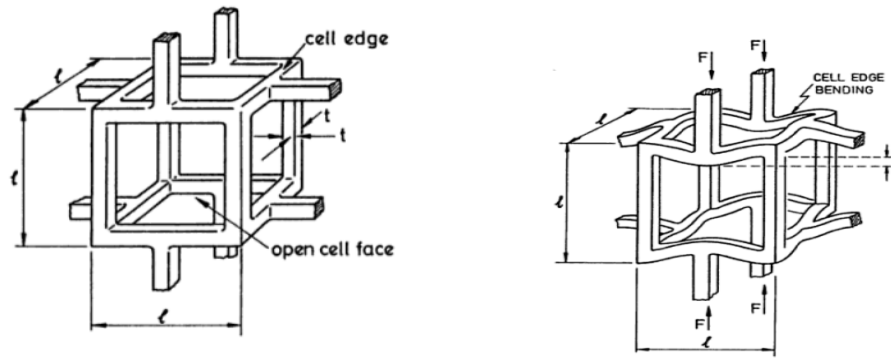
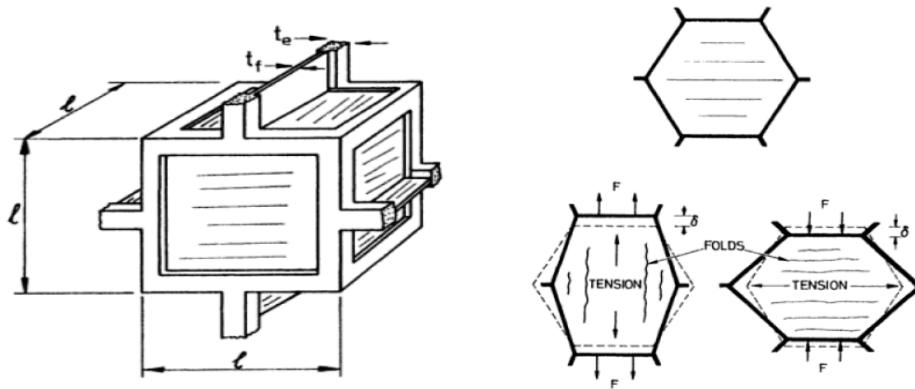


Figure 2.18 Schematic Compressive and Tension Stress-Strain Curves for Foams



(a) Open cell and Its Cell Edge Bending during Linear Elastic Deformation



(b) Closed Cell Polymer Foam and Stretching in Faces under Compression and Tension

Figure 2.19 Cell Deformations under Compressive Loads (Gibson & Ashby, 1999)

For mechanical applications, foams have been widely used as impact energy absorber and in crash protection systems. Many foam core sandwich beams (including metal foam and polymer foam) have been investigated in this field and used in helicopters blades because of their lightweight and damping ability (Lim et al., 2004; McCormack et al., 2001; Pollien et al., 2005; Rizov, 2009; Tan et al., 2013). One of the most important advantages of such sandwich beams is that they can be manufactured into a curved shape compared to a flat honeycomb structures (Ashby et al., 2000). Although polymer foams have many excellent properties, they are rarely utilized in structural engineering due to a lack of knowledge of their viability as fill materials subject to increasing cyclic loads which needs further exploration.

2.3.2 Rubber

Similar to polymer foam materials, there are a variety of rubber materials including natural polymers and synthetic polymers. Even in the same family, different rubber materials can exhibit significantly different characteristics in terms of mechanical properties, thermal properties and chemical stability. They have been widely used in automotive parts, medical apparatus, hardware and even elastomeric laminated bearings in base isolation systems as shown in Figure 2.20.



Figure 2.20 Applications of Rubber Materials

Based on their chemical compositions, types of rubber materials include silicon, polyurethane, nitrile, hydrogenated nitrile, chloroprene, fluorocarbon, styrene-butadiene, ethelyn-propolyn, polyacrylate, ethylene acrylic and natural rubber. Under certain loading conditions, rubber exhibits unique physical and chemical properties has leading to extensive studies on their mechanical properties. Mullins (1948) first discovered stress in the reloading cycle is less than that in the first cycle when unfilled and carbon black reinforced elastomers are subject to cyclic loading. Payne (1962) investigated dynamic properties of carbon black filled rubber and found

the viscoelastic storage modulus was dependent on the amplitude of the applied strain under cyclic loading with small strain amplitude. The Payne effect (also called Fletcher-Gene effect) is attributed to changes in the material's microstructures induced by the loading process.

Multiple constitutive models and finite element models have been developed for rubbers with low and high damping (Amin et al., 2006; Arruda & Boyce, 1993; Yoshida et al., 2004). Ogden and Roxburgh (1999) originally developed a pseudo-elastic model for quasi-static loading-unloading of rubber considering stress softening and residual strain. Dorffman and Ogden (2004) proposed a constitutive model for the Mullins effects with permanent set in particle-reinforced rubber which was validated against uniaxial cyclic loading-unloading tests in tension. However, due to variety of rubber materials and the complexity of their material properties, no constitutive model can universally account for all the physical properties.

For structural passive control, rubber materials are mainly used in elastomeric bearings for seismic isolation and vibration reduction. Early applications of elastomeric bearings in the US can be traced back to three decades ago (Warn & Ryan, 2012). Currently, rubber used in isolation bearings comes in mainly three forms: natural rubber, high damping rubber, and lead-rubber bearings (Morgan & Mahin, 2011). A typical bearing consists of multiple layers of rubber that are laminated to steel shims, as illustrated in Figure 2.21. They have been shown to be effective in reducing base shear, acceleration and overturning moments in a structure through extensive shake table tests (Eidinger & Kelly, 1978; Kelly & Hodder, 1982; Morgan & Mahin, 2011). However, natural rubber bearings can cause excessive lateral deformation due to their insufficient energy dissipation ability. In order to incorporate energy dissipation into the base isolator, high damping rubber bearings and lead-rubber bearings were developed. Carbon black and other fillers are mixed with natural rubber to make high damping rubbers (Naeim & Kelly, 1999). Lead-rubber bearings include a lead core in the central axis of a natural rubber bearing. The lead core is able to dissipate energy through deformation during an earthquake.

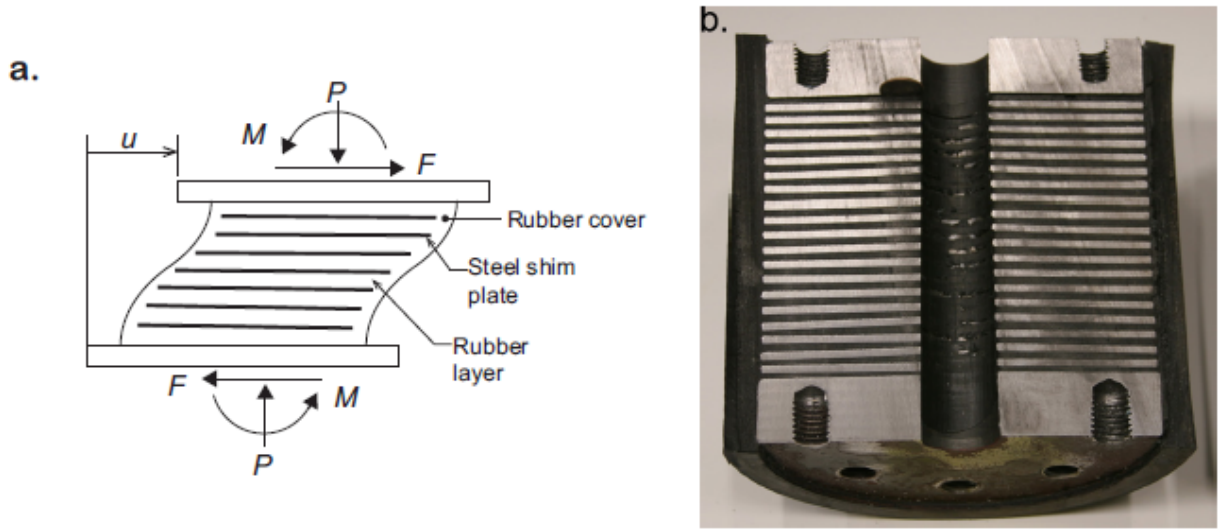


Figure 2.21 Schematics of a Typical Natural Rubber Bearing (Warn & Ryan, 2012)

Other applications of rubber for structural purposes are lacking even though the material has beneficial properties. Infill rubber in HSS members may mitigate local buckling of the HSS member and increase energy dissipation capacity, but work is needed to understand the performance of rubber under large cyclic loading conditions.

CHAPTER 3 DESIGN AND MODELING OF HSS-TO-HSS COLLAR CONNECTIONS

3.1 Introduction

Since the 1970s, use of HSS members in moment frame systems has become popular in Japan, China and Europe (Kurobane et al., 2004) and a number of studies have been focused on HSS column to wide flange beam connections subject to monotonic and cyclic loading. For example, Picard and Giroux (1976) tested 23 coped strap angle reinforced wide flange beam and square tubular column connections subject to monotonic increasing loads and found that properly designed connections of this type were able to achieve the moment capacity of the beam in a rigid frame. Lee and Shanmugam (1993) experimentally and analytically studied effects of various types of stiffeners on the connection behavior under a monotonic loading condition and concluded that the external T-stiffeners are most effective in terms of connection stiffness, strength, ductility and ease in construction. As for the cyclic behavior of wide flange beam to HSS column connections, Shanmugam et al. (1991) performed tests of seven of these connections stiffened by internal continuity plates or external reinforcement (tees or angles). These connections showed good ductility and different failure modes including buckling of column web, buckling of beam flange and fracture at either stiffeners or beam flange. However, the majority of previous research only considered wide flange beam-to-HSS column connections with different reinforcement configurations. The potential for HSS based low-rise moment frames has been overlooked for seismic applications. The studies of wide flange beam-to-HSS column connections provide important information in regards to the development of HSS based seismic moment connections in terms of connection configurations and failure modes as discussed above and in the literature review.

The more prevalent use of HSS-to-HSS moment connections in seismic application has been limited due to lack of understanding of their performance under large cyclic loading conditions.

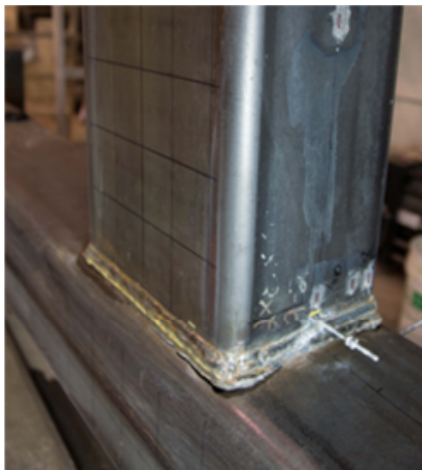
Kumar and Rao (2006) experimentally and analytically investigated rectangular hollow section (RHS) beam to column connections with web openings subject to cyclic loads which exhibited adequate ductility as well as excellent energy dissipation capacity. Then Rao and Kumar (2006) conducted a parametric study on these connections based on the proposed design guidelines and the results suggested the ultimate moment capacity of the connection increased with an increase in the depth of the channel connector but was limited to the capacity of the beam net section. Although these connections were easy to fabricate and convenient for erection, the seismic performance of the connections was affected by strength and stiffness as well as dimensions of the channel connectors which required further investigation. Fadden and McCormick (2011) conducted cyclic bending tests of eleven HSS beams and suggested that the beam width-thickness ratio and depth-thickness ratio affect the cyclic behavior of the HSS beam. However, if these parameters are carefully selected, an HSS beam is able to achieve stable plastic hinging behavior with the maximum moment exceeding the beam plastic moment capacity. Equations associated with these limits can be found in Section 2.2.3. Later Fadden et al. (2014) performed cyclic tests on two fully welded HSS to HSS moment connections and found both connections were not suitable for seismic application due to their brittle failure modes. As a result, a design procedure and finite element parametric study was undertaken focusing on reinforced HSS based seismic moment connections that rely on internal and external diaphragm plates. The numerical study results showed promise of the reinforced connections in earthquake prone zone, but require experimental validation. Other alternative connections that provide fabrication and erection convenience also need to be explored.

This chapter briefly discusses the experimental results of two reinforced HSS based moment connections utilizing either through plates or external diaphragm plates in terms of hysteretic behavior, beam plastic rotation, and strain distribution in each connection component. Then it focuses on improvement of HSS based moment connections by proposing the concept of a welded collar HSS based moment connection. These connections are designed to limit the amount of field welding, and thus increase construction speed and weld quality. The welded HSS based collar connections are then extensively studied through detailed finite element analyses. The effects of different parameters on seismic performance of the collar connections are considered in the FE study to determine design parameters for large-scale experimental specimens, to evaluate the potential of the HSS based collar connection and to explore detailing

requirements of these connections for seismic application. The design approach and detailing requirements for the HSS based collar connection developed through this FE study provide the basis for the experimental tests discussed in the next chapter.

3.2 Experimental Results of Reinforced HSS-to-HSS Moment Connections

As mentioned previously, unreinforced HSS based moment connections experienced brittle failure which should be avoided in seismic design. These connections fractured in the base metal of the HSS column at the toe of the CJP weld with the fracture starting at the corner of the HSS beam regardless of whether the beam was the same width or smaller than the column as shown in Figure 3.1. The findings necessitate reinforcing details to prevent such a failure. The use of external diaphragm and through plates within HSS-based moment connections provides a means of alleviating excessive column face plastification that is often seen when the beam width to column width ratios are less than 0.85 (Packer & Henderson, 1997) and the HSS beam is directly welded to the face of the HSS column. Kamba and Tabuchi (1995) have shown that the use of internal and external diaphragm plates can address the deformation problems associated with the flexibility of an unstiffened HSS column face for HSS column to wide flange beam connections, but consideration of HSS-to-HSS seismic moment connections is limited.



(a) Unmatched Connection

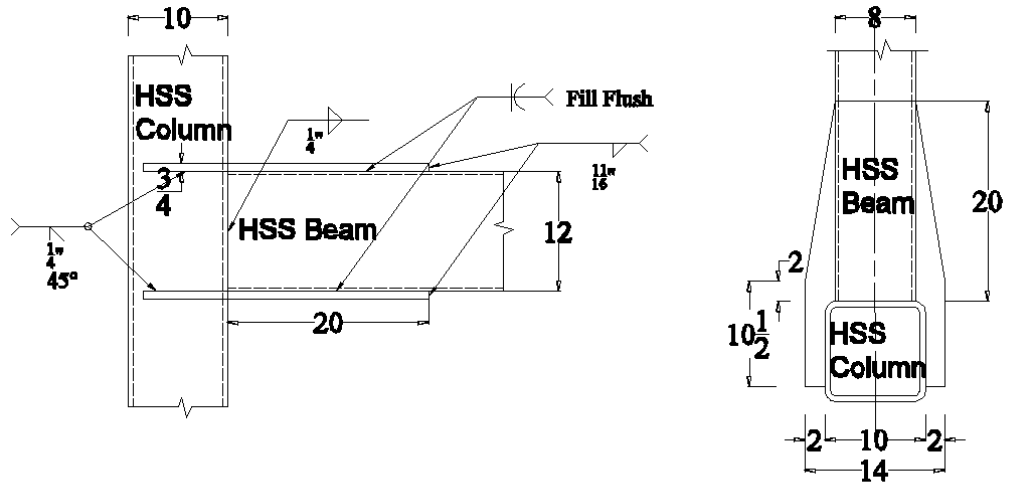


(b) Matched Connection

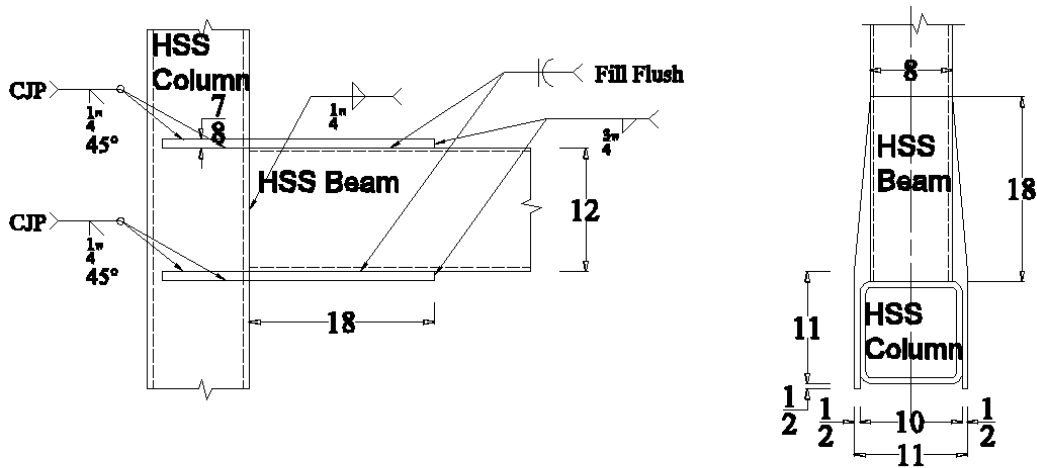
Figure 3.1 Brittle Failure of Unreinforced HSS based Moment Connections (Fadden et al., 2014)

To address this limitation and explore the viability of reinforced HSS-to-HSS seismic moment connections, a design procedure was developed by Fadden and McCormick (2014) considering the limiting parameters of HSS beams in cyclic bending, results from a detailed FE study (Fadden & McCormick, 2014a), and design philosophies outlined in the CIDECT Design Guides (Kurobane et al., 2004; Packer et al., 2009), the AISC Specification 360-10 (2010b), and the AISC Seismic Provisions 341-10 (2010a). The design procedure ensures that either beam plastic hinging or reinforcing plate yielding will occur prior to weld fracture allowing the plastic moment capacity of the beam to be reached. Further details of the design procedure can be found in Fadden and McCormick (2014b).

Two exterior connections are considered both with an HSS 10×10×5/8 column and HSS 12×8×3/8 beam. One connection utilizes an external diaphragm plate which is welded around the column and the second utilizes a through plate in which the HSS column is cut into three segments and then reattached with the through plates in between the segments. A reinforcing plate length of 20 in. for the external diaphragm plate connection and 18 in. for the through plate connection refers to the length of the plate from the column face to its termination point along the length of the beam. Both the external diaphragm plates and through plates are connected to the HSS column using complete joint penetration (CJP) groove welds. A flare bevel groove weld is used along the length of the beam between the reinforcing plates and the beam, while a transverse fillet weld connects the end of the reinforcing plates with the top and bottom of the HSS beam. To ensure that a non-ductile weld failure does not occur based on the developed design and detailing requirements (AISC, 2010b; AWS, 2010), the fillet weld sizes are 3/4 in. and 11/16 in. for the external diaphragm plate and through plate connections, respectively. Figure 3.2 shows the details of the two connections.



(a) External Diaphragm Connection



(b) Through Plate Connection

Figure 3.2 Schematic of the (a) External Diaphragm Plate and (b) Through Plate Connections (units in inch)

The experimental setup is designed to represent a prototype HSS-based seismic moment frame that has 12 ft floor heights and 21 ft bay widths. Two exterior connections are tested where the column is half the floor height above and below the connection and the beam is half the bay width. The ends of the members are pinned to simulate the inflection points in the prototype frame. A photo of the test setup is shown in Figure 3.3 where the column is horizontal and the beam is vertical to allow for ease of testing. A hydraulic actuator is used to apply displacements to the beam tip (vertical member pictured in Figure 3.3) using the loading protocol specified by the American Institute of Steel Construction for prequalification of seismic moment connections

(AISC, 2010a). Tip displacements are applied at a loading rate of 0.05 in./s up to rotations of 0.07 rad.

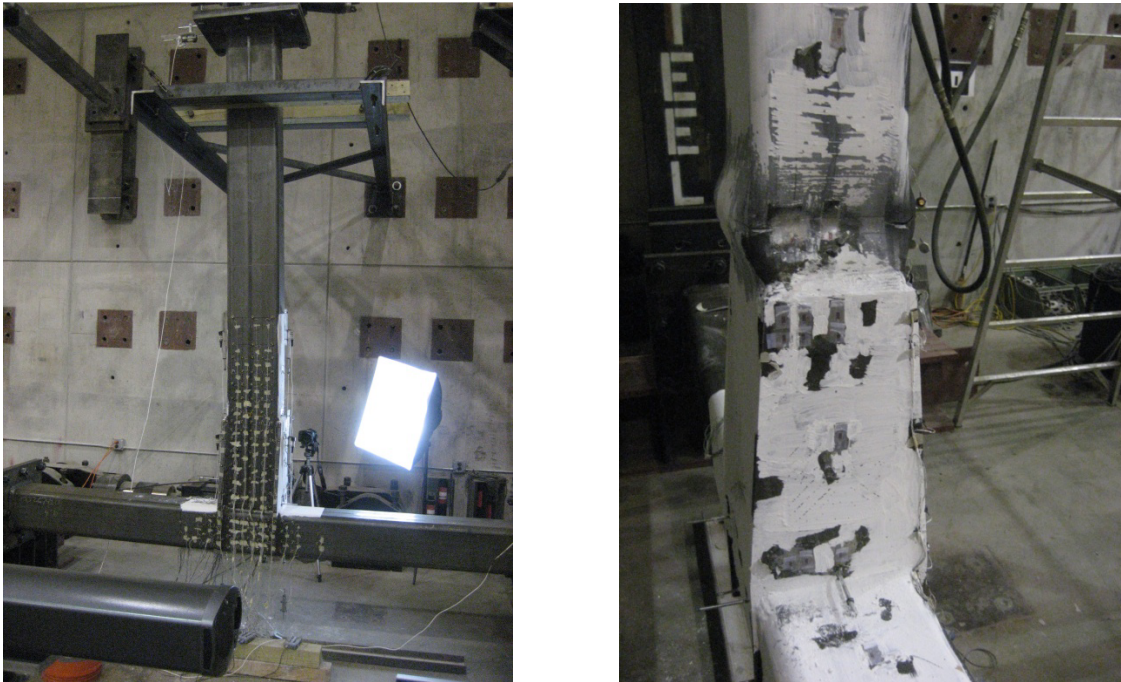


Figure 3.3 Photographs of the Test Setup and Through Plate Connection after Testing

The HSS beams and columns meet ASTM A500 Gr. B. or Gr. B/C standards. Three coupon specimens are taken from the flats of the beam and column of the external diaphragm connection, but not from the through plate connection since its members are from the same batch of material. The average yield strength and tensile strength is measured to be 61.8 ksi and 70.6 ksi for the beam and 61.6 ksi and 67.0 ksi for the column, respectively. The reinforcing plates are made from ASTM A36 steel, which has a minimum specified yield strength of 36 ksi and a minimum ultimate tensile strength of 58 ksi. Materials tests on the plates are not conducted as the plates are not expected to undergo significant yielding. Further details on the experimental testing of the reinforced connections and the results of these tests also can be found in Fadden et al. (2014).

Intermediate and special moment frame system connections are expected to be able to undergo 0.02 rad. and 0.04 rad. of rotation while maintaining at least 80% of their moment capacity (AISC, 2010a). To evaluate the ability of the two reinforced connections to meet these criteria, the moment-rotation behavior of the connections is considered. The moment at the centerline of the column is calculated as the applied load at the beam tip multiplied by the length of the beam

plus half the column depth, while the rotation at the center of the connection is calculated as the horizontal displacement of the beam tip divided by the length of the beam plus half the column depth. The beam plastic moment that is used to normalize the measured moment is calculated as the experimentally measured yield strength of the HSS beam multiplied by the experimentally measured plastic section modulus. The beam plastic moment of the external diaphragm plate and through plate connections are 3240 k-in. and 3270 k-in., respectively.

The moment-rotation plots for the two connections are shown in Figure 3.4. Both connections develop full hysteresis loops with degradation of the moment capacity not occurring until after the first 0.04 rad. cycle. The maximum moments achieved by the external diaphragm plate and through plate connections are 4270 k-in. and 3920 k-in., which are approximately 32% and 20% larger than the plastic moment capacity of the beam. These findings suggest that intermediate and special moment frame requirements can be met using reinforced HSS based moment connections provided that the connection is detailed such that weld fracture does not control. After reaching their maximum moments, both connections show degradation in moment capacity with continued cycling to larger rotation levels. This degradation is the result of local buckling in the beam member, which eventually leads to the initiation of fracture in the HSS beams. Fracture starts at the corner of the HSS beam due to the cold working that is imparted during the HSS manufacturing process (Fadden & McCormick, 2011) and propagates toward the center of the web and flange of the beam. However, the connections are able to reach 0.07 rad. of rotation prior to terminating testing. At this point, the moment capacity of the external diaphragm plate and through plate connections has decreased to 1452 k-in. and 1610 k-in, respectively.

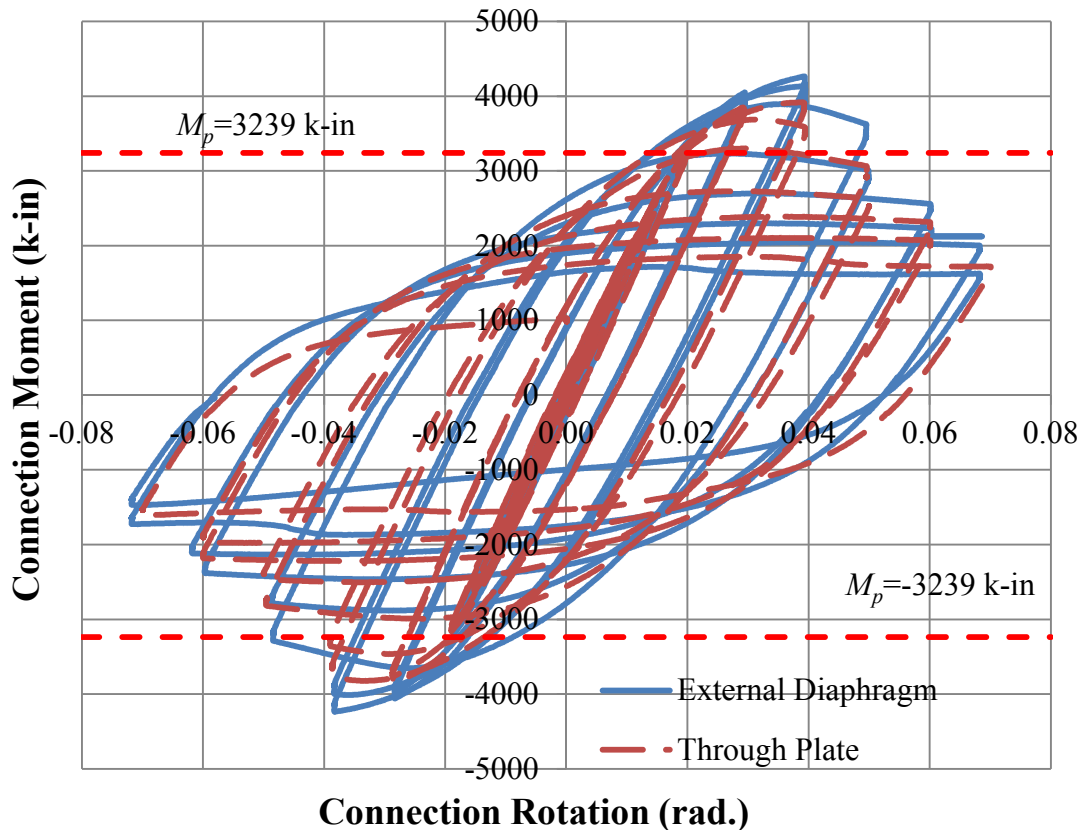


Figure 3.4 Moment-Rotation Hysteresis for the External Diaphragm Plate and Through Plate Connections

The reinforced connections undergo desirable ductile plastic hinging of the HSS beam member prior to local buckling, which is consistent with the current strong column, weak beam design philosophy for moment frame systems. This ductile plastic hinging of the beam can be observed in Figure 3.5 where the normalized moment is plotted with respect to beam plastic rotation. Nearly all of the plastic rotation occurs in the beam member with the external diaphragm connection reaching a maximum beam plastic rotation of 0.053 rad. (i.e. 99% of the measured inelastic rotation) and the through plate connection reaching a maximum beam plastic rotation of 0.056 rad. (i.e. 100% of the measured inelastic rotation) during the 0.07 rad. cycle. However, this large level of plastic deformation in the beam member does lead to local buckling that limits force transfer to other components of the connections. The utilization of a beam member with a lower width-thickness ratio, addition of fill material in the beam, or use of a different connection configuration also will help to inhibit local buckling and promote a more balanced behavior.

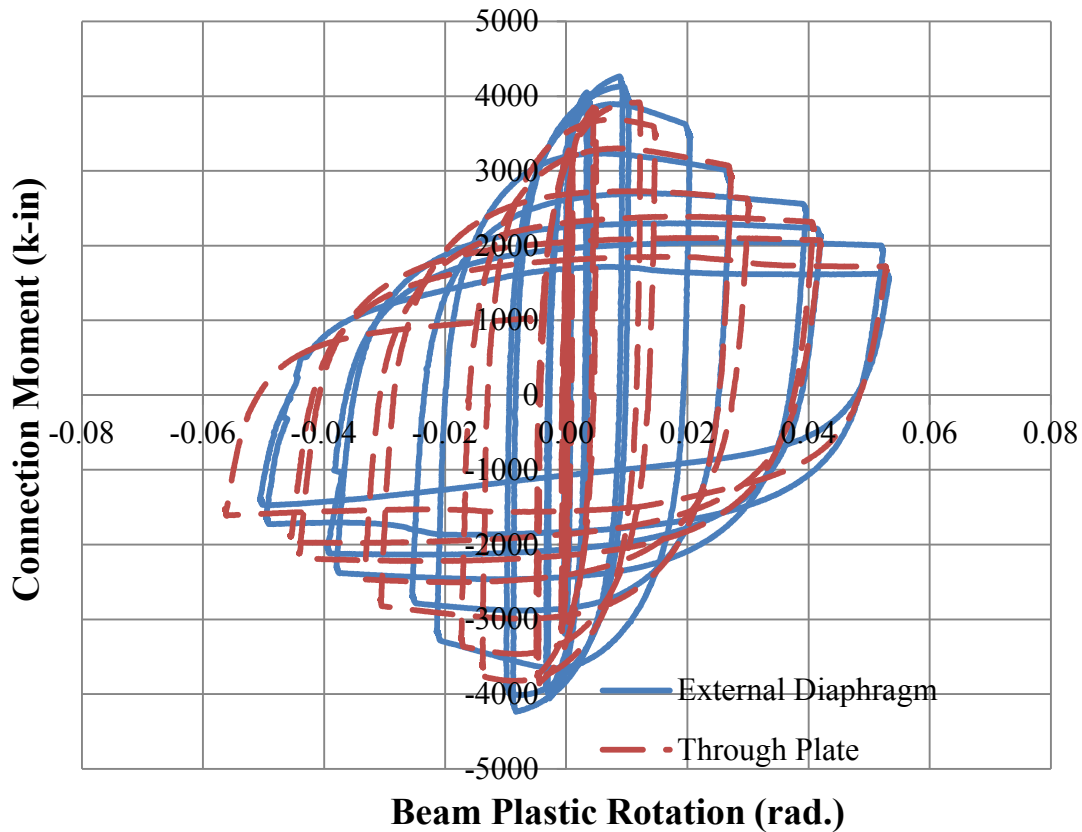


Figure 3.5 Moment-Beam Plastic Rotation Hysteresis for the External Diaphragm Plate and Through Plate Connections

To understand the load path through the HSS beam and into the reinforcing plate, strain gages are placed on the top face of the beam at its center (be0) and 1 in. from its edge (be1); at the center of the column face (cf1); at the center of column back (cb0), which is opposite the side where the beam is connected to the column; and at the center of the panel zone (pz1), as seen in Figure 3.6. Along the length of the beam, the strain gages on the beam (be0 and be1) are located 2 in. away from the end of the reinforcing plate. Along the length of the column, the strain gage on the column face (cf1) is located 2 in. away from beam flange and the strain gage on the column back is located 3 in. away from the beam centerline.

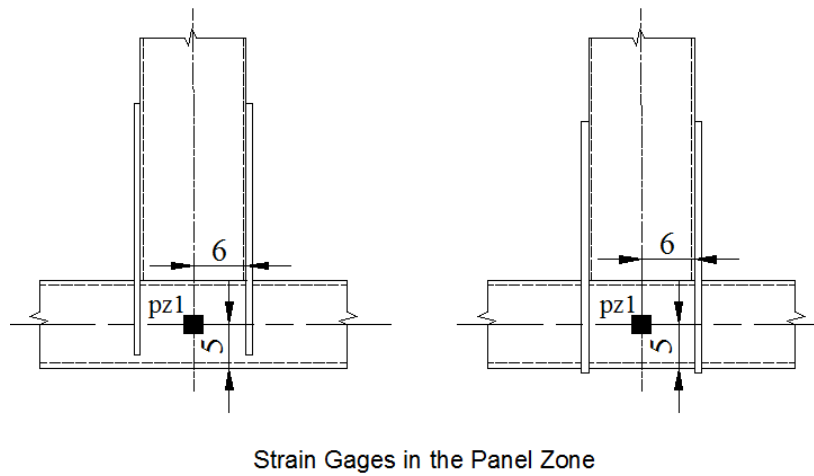
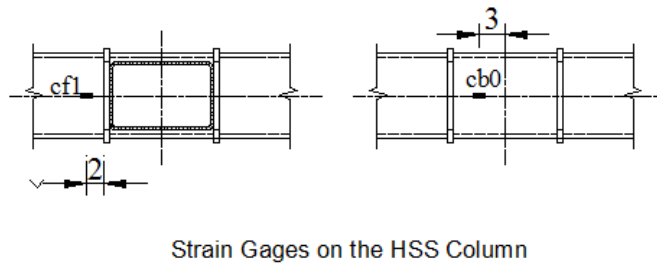
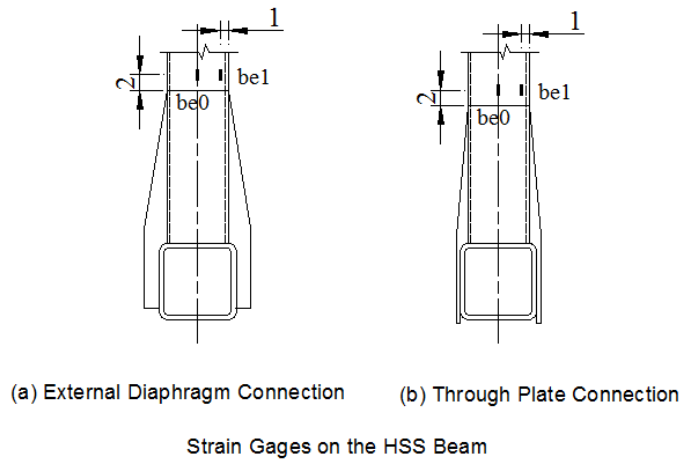


Figure 3.6 Strain Gage Layout for the Two Reinforced Connections (units in inch)

Figure 3.7 provides the measured beam strain values with respect to connection rotation cycle. In general, strains are larger at the center of the beam suggesting that most of the tension and compression force is transmitted through the center of the fillet weld at the end of the reinforcing plate. It is also observed that the yield strain is surpassed during the 0.02 rad. cycle at the center

of the beam and during the 0.03 rad. cycle at the edge of the beam eventually leading to full plastification of the beam section. At rotation levels greater than 0.05 rad., the strain values decrease due to the onset of local buckling further away from the column face than where the strain gages are located.

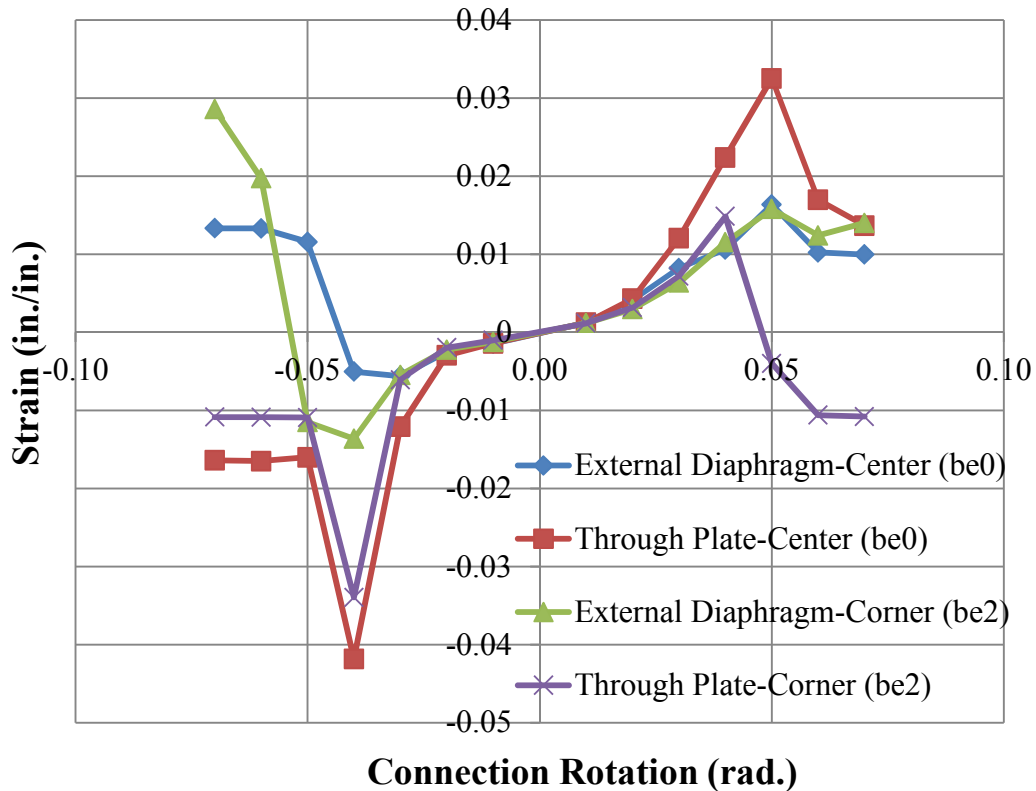


Figure 3.7 Beam Strain Gage Measurements with respect to Connection Rotation

Strain values are large at both the center and edge of the beam flange (be0 and be1) with only minimal column face deformation (cf1). In neither of the connections is a significant amount of strain measured at the back of the HSS column (cb0). Figure 3.8 compares the strain measured in the beam (be0 and be1), panel zone (pz1), column face (cf1), and column back (cb0) at the first positive 0.02 rad. and 0.04 rad. cycles. After 0.02 rad. rotation level, the strain values in the panel zone (pz1) for both connections exhibit the same order of magnitude as that at the beam center (be0) and beam edge (be1). However, during 0.04 rad. cycle, strain values in the beam flanges (be0 and be1) are significantly larger than those in the panel zone (pz1). Strains measured in pz1, cf1 and cb0 generally remain below 0.005 for the two connections, which further shows that almost all of the inelastic deformation occurs in the beam members. In general,

the flow of load through the reinforced connections is advantageous for meeting current seismic design requirements. However, reinforced connections can be labor intensive and require a significant amount of field welding. These connections can be improved through a refined configuration that requires less field welding and obtains better participation of other suitable connection elements in the inelastic deformation.

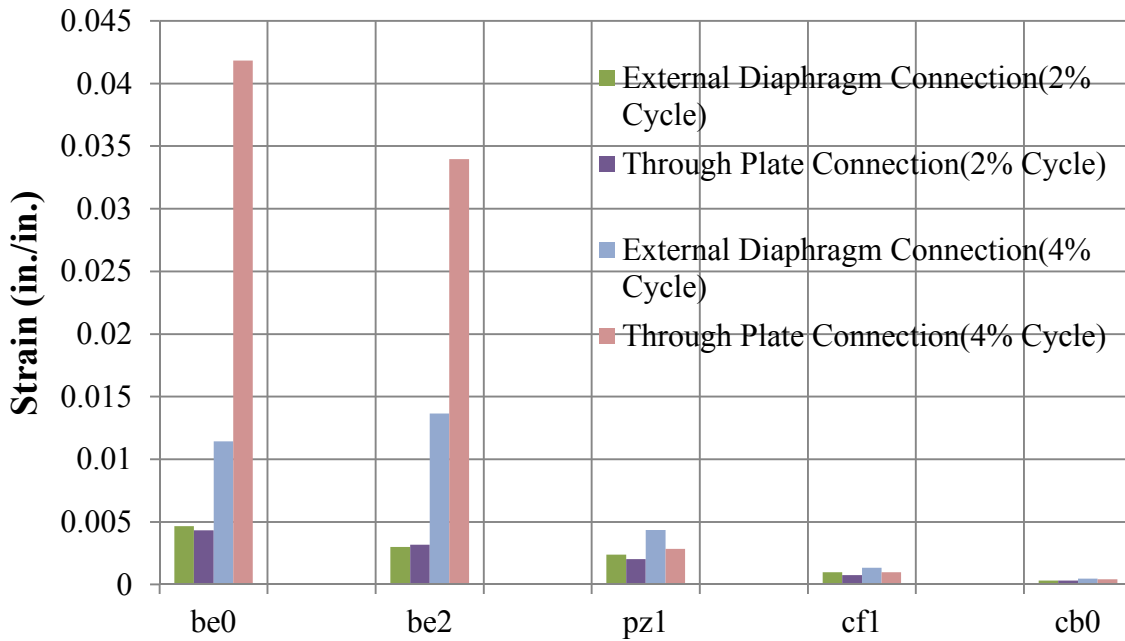


Figure 3.8 Strain Values at the Beam Flange Center (be0), Beam Flange Edge (be2), Panel Zone Center (pz1), Column Face(cf1) and Column Back (cb0) for the 2 and 4% Connection Rotation Cycles

3.3 HSS-to-HSS Collar Connection Concept

Previous studies on HSS-to-HSS welded moment connections, as described in the previous section and chapter, suggest that they are viable for use in seismic moment frame systems. However, these welded connections can be labor intensive to fabricate suggesting that alternative configurations which are more economical and easier to construct need to be considered. Limiting the occurrence of limit states such as column wall plastification and column sidewall crippling should be considered in the development of new HSS based seismic moment connection configurations along with current seismic design requirements (AISC, 2010a) where

the majority of the inelastic deformation must occur in the beam member while also allowing participation of the panel zone. Meanwhile, new connection configurations also provide an opportunity to better distribute the inelastic behavior within the connection compared to what is observed in the previously tested reinforced connections where almost all of the inelastic behavior is confined to the beam member.

To reduce the amount of field welding and expedite construction speed, an innovative collar connection is considered. A schematic and elevation view of the connection configuration is provided in Figure 3.9 and Figure 3.10. The connection configuration utilizes HSS beams and columns to take advantage of their properties. To address field welding concerns and construction speed, the HSS beam member has a stiffened endplate that is shop welded. The beam is attached to the column using two collars that slip over the column and the beam endplate. The lower collar is shop-welded to the column with a gap left between the column face and collar to provide a location for the bottom of the beam endplate to slip into in the field. Once the beam is in place in the field, the upper collar can be slipped down the column and over the top of the beam endplate. As a result of the prior shop welding, only fillet welds or partial groove welds are needed in the field to attach the upper collar to the column and beam endplate and the beam endplate to the column as opposed to complete joint penetration welds that were used in the reinforced HSS based moment connections discussed in the previous section. The required field welds and shop welds are shown in Figure 3.11. Care must be taken to provide proper tolerances to allow the beam endplate to fit into place in the field and proper sizing of welds and members is necessary to limit the occurrence of brittle weld failure and other undesirable limit states associated with localized column deformation.

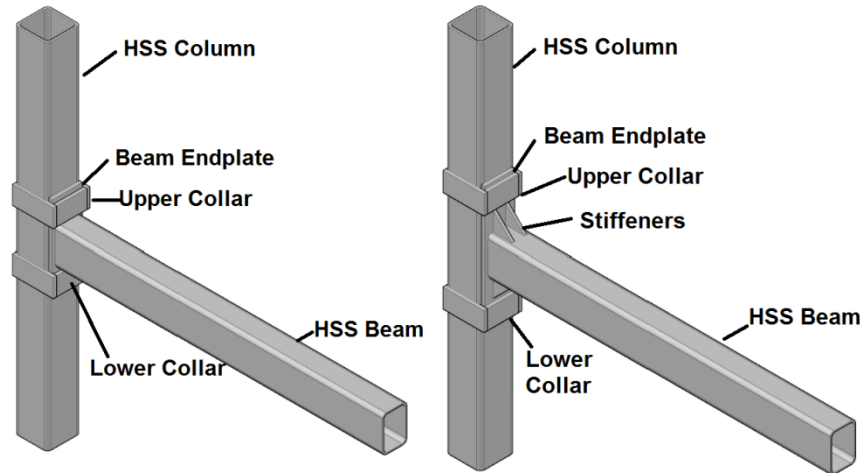


Figure 3.9 Welded Collar Connections

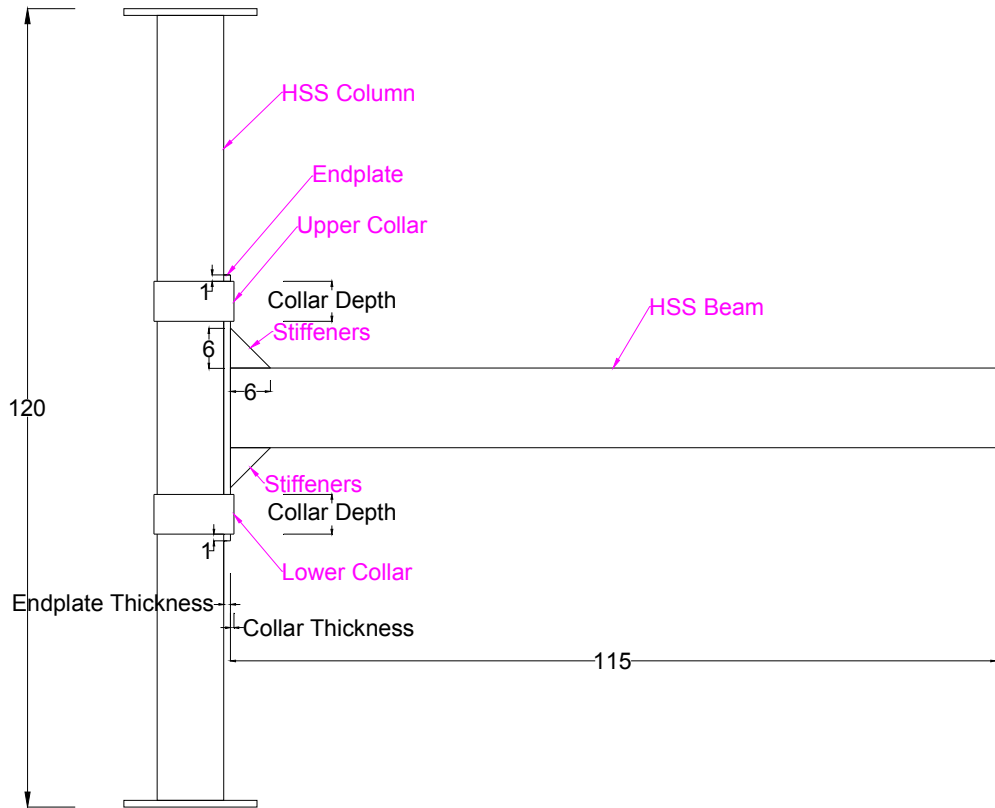


Figure 3.10 Elevation View of a Typical Collar Connection (units in inch)

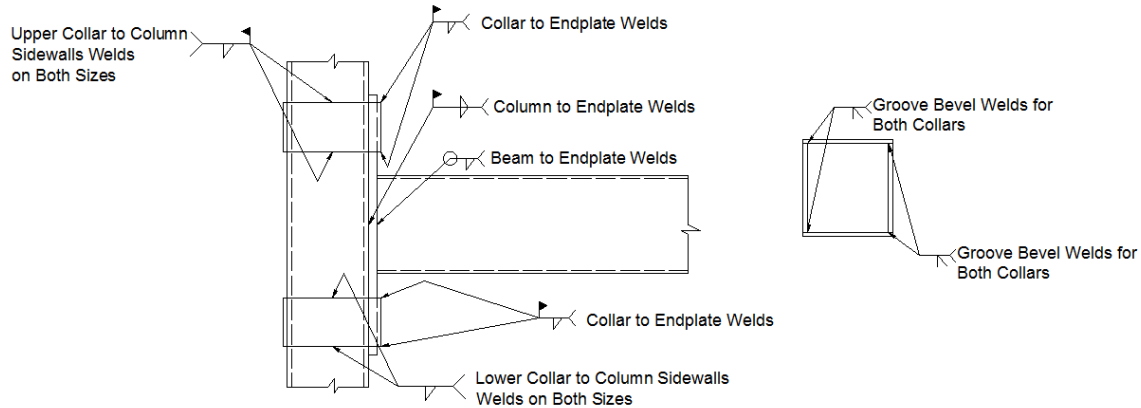


Figure 3.11 Welds in the Collar Connections

3.4 FEM of HSS Based Collar Connection

A FE model is developed to further explore the load path and seismic performance of the HSS based collar connection by considering the effects of beam endplate thickness, collar thickness, collar depth, and stiffeners. The FE model is created in Abaqus CAE (Version 6.14-1) and represents an exterior connection in a seismic moment frame with a bay width of 19 ft and floor height of 10 ft (Figure 3.12). Half the height of the column is modeled above and below the beam and pinned end connections are used to represent the inflection points in the column. Half the span of the beam, 115 in., is modeled with one end connected to the column and the other end free to apply the cyclic displacements to simulate earthquake loading. A single column size, HSS 10×10×5/8, is considered and one beam size, HSS 12×8×3/8, is utilized. The beam section size is selected since it can sustain 80% of plastic moment capacity at 0.04 rad. based on the findings from Fadden and McCormick (2014a). To evaluate the effects of stiffeners on load transfer mechanism and location of inelastic deformation, one connection without stiffeners is studied to contrast with the model with stiffeners as seen Figure 3.9. Further details of the connection can be seen in Figure 3.10 where the beam, column, collars, endplate, and stiffeners are shown. Two stiffeners are used at the top and bottom beam flange to stiffen the beam endplate, respectively. The stiffeners have equal leg lengths of 6 in., a thickness of 3/4 in., and are located 1.5 in. on either side of the centerline of the beam flange.

The beam and column members are modeled with S4R shell elements. To improve the efficiency and accuracy of the analysis, the region adjacent to the column face that spans 40 in. along the beam length utilizes 1/2 in. square elements while for the remaining length of the beam the element size gradually increases from 1/2 in. to 8 in. square elements. The smaller mesh size close the column face is determined based on a convergence study and ensures that the behavior within the plastic hinge region of the beam is accurately captured. The mesh for the column is broken into three segments with the central segment spanning 20 in. above and below the center point of the connection. This region utilizes 1/2 in. square elements due to the potential for panel zone deformation. The other two segments extend to the ends of the column and have a gradually increasing mesh size from 1/2 in. to 6 in. square elements. The collars, beam endplate and stiffeners are modeled with C3D8R solid elements that are 1/4 in. square. Tie constraints are used to simulate the PJP welds between collar plates, the fillet welds across the column side wall, column bottom and beam endplate at the edge of the collars, the fillet welds connecting the HSS beam end to the beam endplate, the fillet welds connecting the stiffeners to the HSS beam endplate, and the fill flush groove weld between the corner of the HSS column and beam endplate. Since tie constraints are used instead of modeling the welds, weld failure is not considered in the models which is justified based on the design approach of avoiding critical weld failure and the focus of this exploratory FEM study on other design parameters.

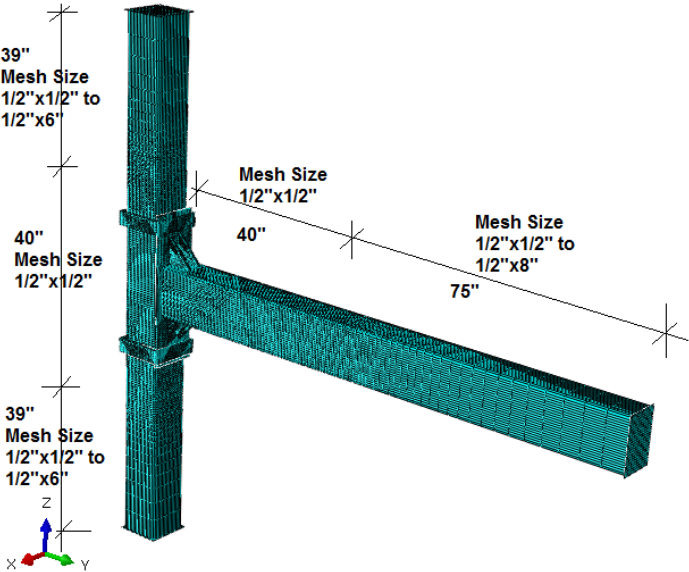


Figure 3.12 Mesh Size for the HSS Beam and Column in the FE Models

Tensile coupon tests of the flat and corner material of an HSS member (Fadden & McCormick, 2011) provide the material properties that are incorporated into the FE models after being converted to true stress-strain values. The measured yield strength and tensile strength of the beam flats are 59.8 ksi and 81.5 ksi and they are 75.3 ksi and 86.2 ksi for the beam corners. Similarly, the same yield strength and tensile strength for the flats and corners of the HSS beam are used for the HSS column. All the material models for the beam and column utilize a combined kinematic and isotropic hardening law to better predict cycling effects. The beam and column models are each partitioned into four flat sections and four corner sections with the material properties corresponding to each being applied to capture the cold working effects associated with the HSS manufacturing process. The corner material is applied up to a distance of twice the wall thickness away from the corner. For the beam endplate, stiffeners and collars, ASTM A36 steel is assumed using an elastic-perfectly plastic model with a yield strength of 36 ksi. A combined isotropic and kinematic hardening rule is used with the plate material model.

To simulate seismic loading, the beam tip is displaced to produce increasing beam rotations from 0.0375 rad. to 0.06 rad. based on modifications to the current loading requirements for prequalification of seismic moment connections (AISC, 2010a). Two cycles are applied at each drift level as shown in Figure 3.13.

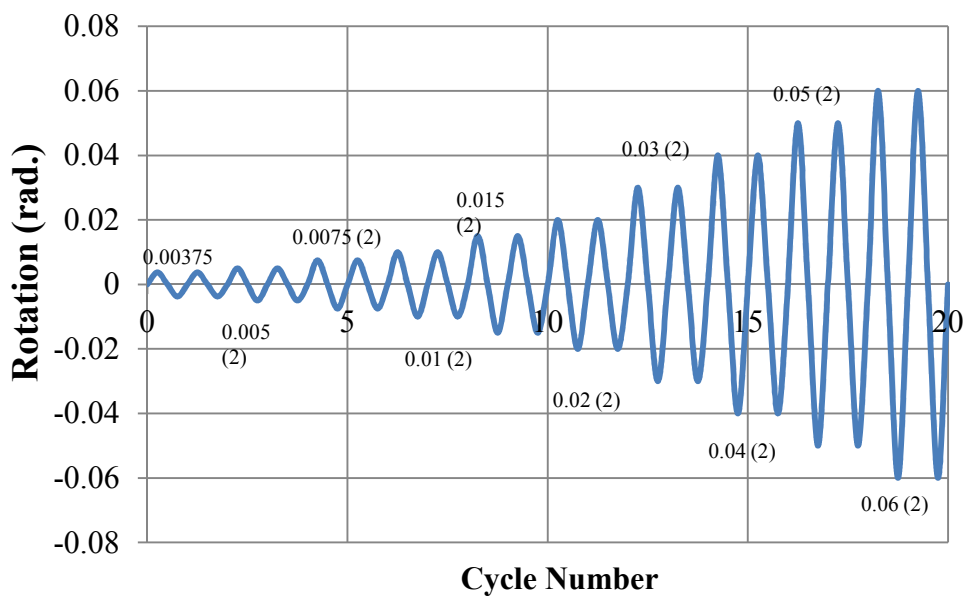


Figure 3.13 Loading Protocol Applied in the FEM

3.4.1 Parametric Study

Given the important role that the collar and beam endplate play in transferring the loads from the beam to the column in the welded collar connection, the effect of changing the collar thickness, t_c , collar depth, d_c , and beam endplate thickness, t_e , are examined to better optimize the connection's performances under seismic loads. The considered values for each of the parameters are listed in Table 3.1 leading to 12 different connection configurations being considered through FE analyses. All combinations of the specified parameters are considered with a collar depth of 6 in. The collar depth is only varied for connections that used 1/2 in. thick collars and endplates. Additionally, one connection without stiffeners has an endplate thickness of 1/2 in., collar thickness of 1/2 in. and collar depth of 6 in. for determination of the influence of stiffeners. For all 12 configurations, the end of the beam endplate extended 1 in. past the collar.

Table 3.1 Collar Connection Parameters and Values

Parameters	Values
Collar thickness, t_c (in.)	1/4, 1/2, 3/4
Collar depth, d_c (in.)	3, 6, 9
Beam endplate thickness, t_e (in.)	1/4, 1/2, 3/4

3.4.2 Parametric Study Results

To study the effect of the specified parameters on the cyclic behavior of the welded collar connections, their moment-rotation behavior is considered. Moment-beam plastic rotation results provide information on whether the majority of the inelastic behavior in the connection occurs in the beam as is currently required by the seismic specifications (AISC, 2010a). The effect of varying the different parameters is also considered with respect to the maximum overall moment capacity of the connection to see which connections are able to develop the beams plastic moment capacity, how stiffeners affect moment capacity and plastic rotation of the beam, and how changing each parameter improves or decreases the connections' ability to do so. These findings are provided in Figures 3.14 through 3.23. For all of these cases, the moment is normalized by the plastic moment capacity of the beam, M_p , which is derived as the yield strength of the beam multiplied by the beams' plastic section modulus provided in the AISC

Steel Construction Manual (AISC, 2010c). Here, the yield strength of the beam is taken as the experimentally observed value for the flat of the HSS member used to develop the FE analyses' material model.

3.4.2.1 Normalized Moment vs. Connection Rotation

The normalized moment-rotation results are shown in Figure 3.14 for the connections with the same beam endplate thickness and collar thickness, 1/4 in., 1/2 in., or 3/4 in. Overall, the plots show large symmetric hysteresis behavior that suggests significant energy dissipation capacity and inelastic deformation. The moment capacity and its degradation with cycling tend to vary with the thickness of the beam endplate and collar. The connections utilizing a larger beam endplate and collar thickness show larger moment capacities. The maximum normalized moments are 0.93 during the 0.06 rad. cycle, 1.03 during the 0.06 rad. cycle, and 1.11 during the 0.05 rad. cycle for the connections with a 1/4 in., 1/2 in., and 3/4 in. thick beam endplate and collar, respectively. The connections with a 1/2 and 3/4 in. beam endplate and collar thickness exhibit a maximum normalized moment greater than unity, which indicates that the beam reached its full moment capacity. However, after reaching its maximum moment, the connection with the thickest endplate and collar shows larger degradation in the maximum moment with continued cycling to 0.06 rad. This observation is mainly due to the fact that the thicker, stiffer endplate allows other structural components to share more inelastic deformation until plastic hinge occurs. As a result of concentration of significant inelastic deformation in the HSS beam, early local buckling of the beam will lead to moment degradation after achieving larger moment capacity.

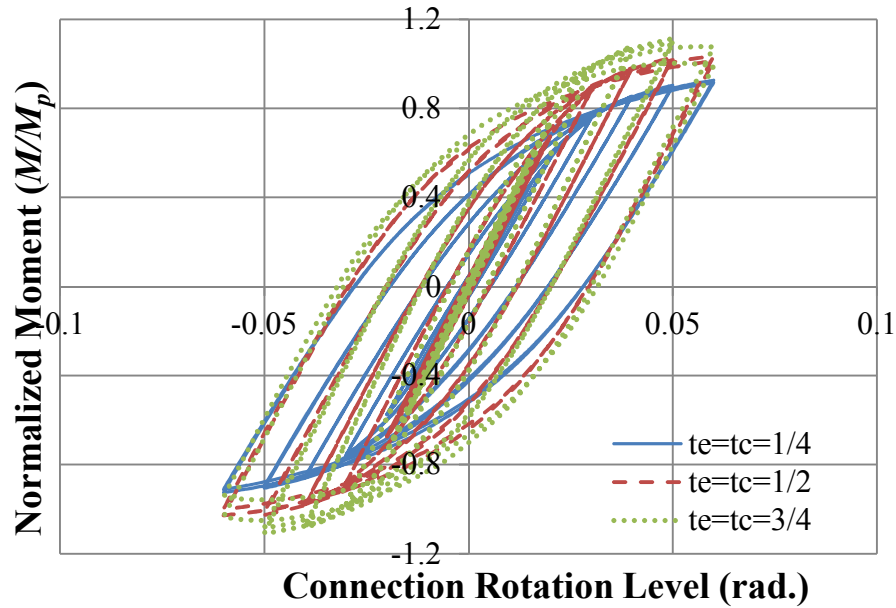


Figure 3.14 Normalized Moment versus Connection Rotation Level

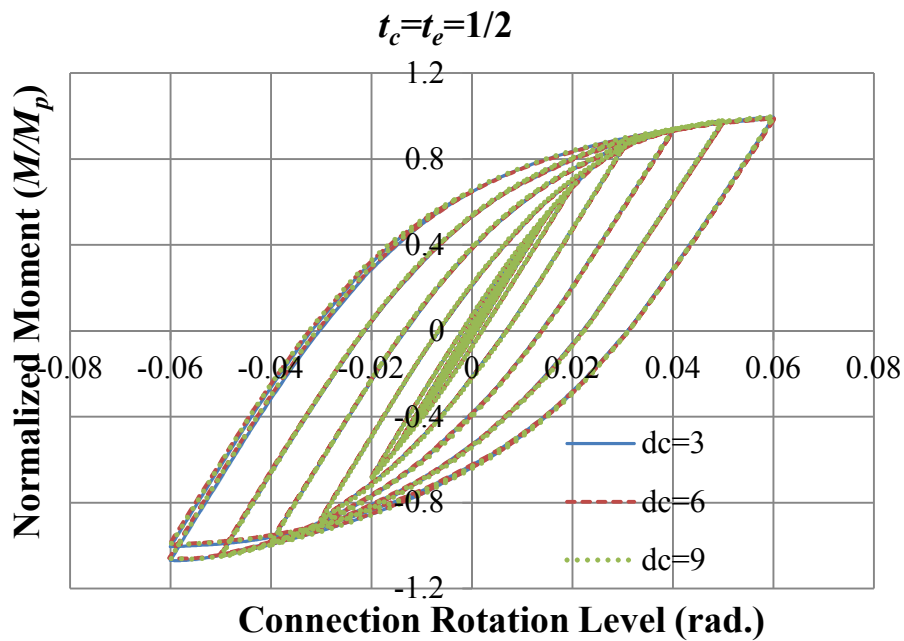


Figure 3.15 Normalized Moment versus Connection Rotation for 1/2 in. Collar and Endplate Thickness

Figure 3.15 provides the normalized moment-rotation plots for the connections with a 1/2 in. thick endplate and collar, and varying collar depths. As the collar depth increases from 3 in. to 9 in., no obvious differences are observed in their moment-rotation behavior. The results suggest

that collar depth has little effects on moment capacity and degradation. The lack of degradation in the moment capacity with cycling suggests local buckling is not significant in these connections.

Overall, the maximum normalized moment increases slightly with an increase in thicknesses of the beam endplate and collar. However, larger endplate thickness leads to more moment degradation during continued cyclic loading. Collar depth has minor effects on maximum moment capacity and moment degradation of the connection.

3.4.2.2 Normalized Moment vs. Beam Plastic Rotation

The plastic rotation of the beam is calculated by subtracting out the elastic rotation from the beam overall rotation as shown in Equation 3.1.

$$\theta_{beam,pl} = \theta_{beam} - \frac{M_{conn}}{K_{beam}} \quad \text{Equation 3.1}$$

where M_{conn} is the connection moment obtained by multiplying the applied force at the beam tip by the horizontal distance from the beam tip to the column centerline; K_{beam} is the secant stiffness of the beam measured when the connection rotation is at the first 0.01 rad. cycle.

The normalized moment-beam plastic rotation behavior (Figure 3.16) shows that with a thicker beam endplate and collar, the beam experiences a larger amount of inelastic deformation. Overall, the maximum beam plastic rotation also decreases from approximately 0.02 rad. to 0.01 rad. to 0.007 rad. with a decrease in the endplate and collar thickness since the thicker endplate stiffens the column face leading to more inelastic deformation concentrated in the beam member which is desirable for seismic applications.

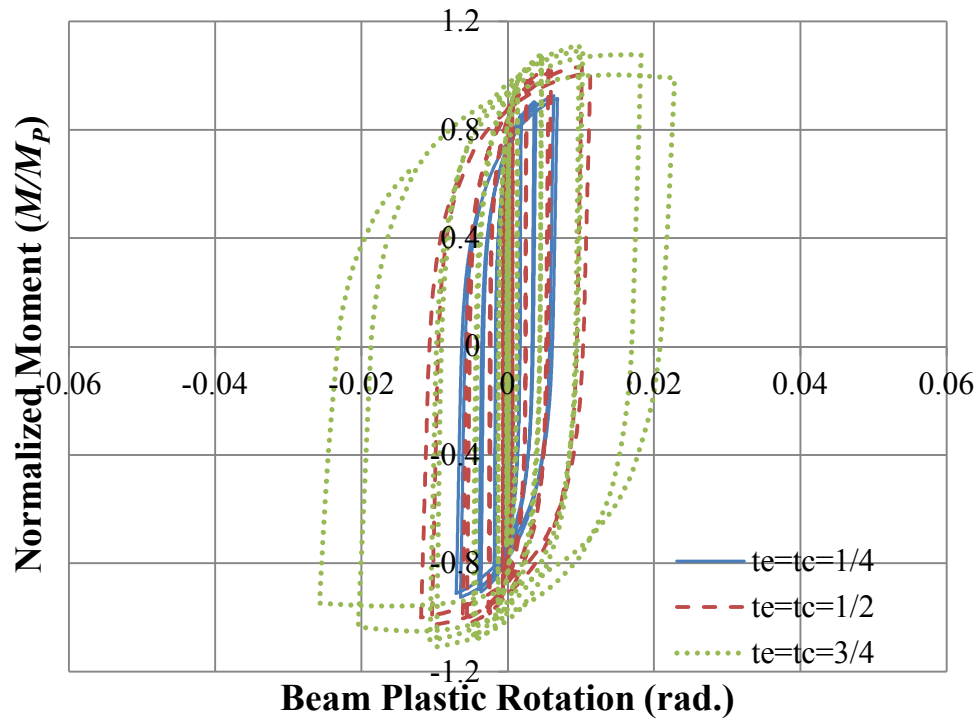
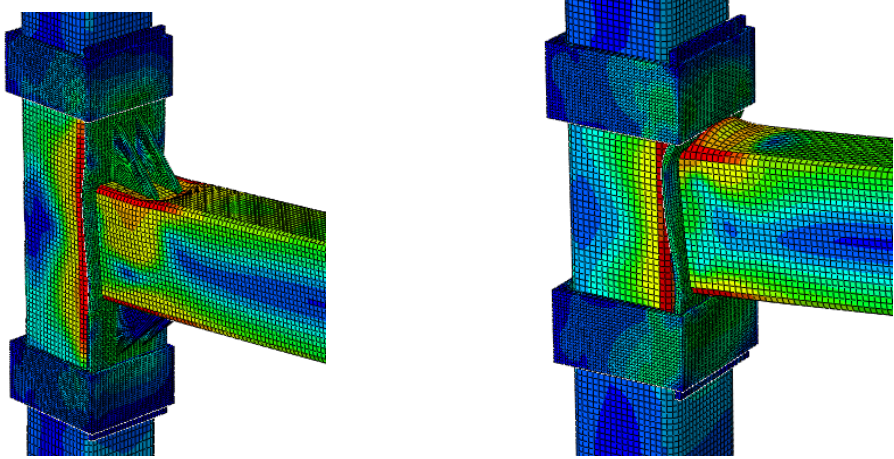


Figure 3.16 Normalized Moment versus Beam Plastic Rotation

3.4.2.4 Effects of Endplate Stiffeners on Cyclic Behavior of the Connection

To evaluate effects of endplate stiffeners on load transfer mechanism and cyclic behavior of the collar connections, FE results of one collar connection with stiffeners and without stiffeners are compared in terms of where local buckling occurs, moment capacity of the connection, and maximum plastic rotation in the beam. As shown in Figure 3.17, at 0.06 rad. cycle, the plastic hinge in the connection with stiffeners forms along the beam where the stiffeners terminate; while plastic hinging of the beam in the unstiffened connection is concentrated adjacent to the endplate. Both connections, with and without stiffeners, exhibit stable hysteretic behavior with little moment capacity degradation as shown in Figure 3.18. However, the connection with stiffeners has a larger initial secant stiffness and maximum normalized moment, which is greater than unity, 1.03, suggesting it is able to reach the plastic moment capacity of the beam. Alternatively, the maximum normalized moment is only 0.96 for the connection without stiffeners. Figure 3.19 shows the normalized moment-beam plastic rotation relationship for these connections. More plastic rotation is concentrated in the beam of the stiffened connection compared to that of the unstiffened connection. The maximum plastic rotations in the beam of

the connections with and without stiffeners are 0.011 rad. and 0.002 rad., respectively. These plastic rotations indicate that the connection with stiffeners is more effective in developing the plastic capacity of the HSS beam and moving the local buckling away from column face which is more feasible for seismic application.



(a) Collar Connection with Stiffeners (b) Collar Connection without Stiffeners

Figure 3.17 Stress Contours for the Collar Connections with and without Stiffeners

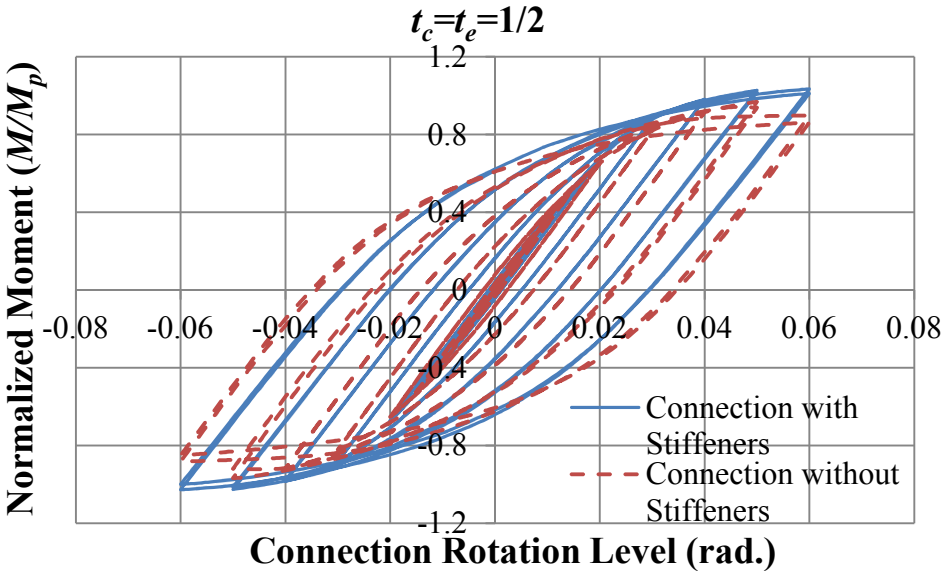


Figure 3.18 Normalized Moment versus Connection Rotation for the Connection with and without Stiffeners when Endplate Thicknesses are 1/2 in.

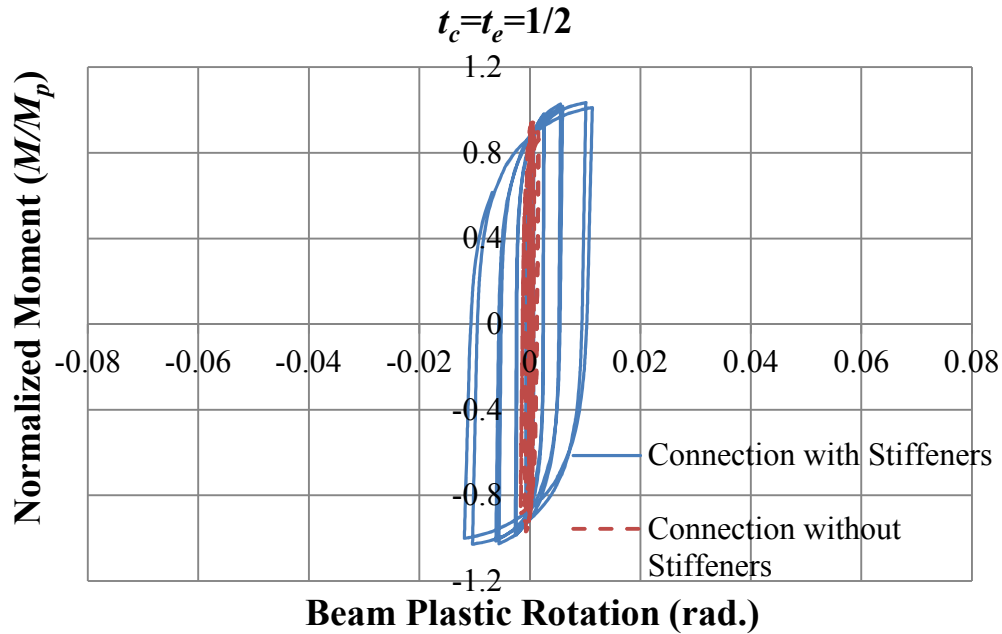
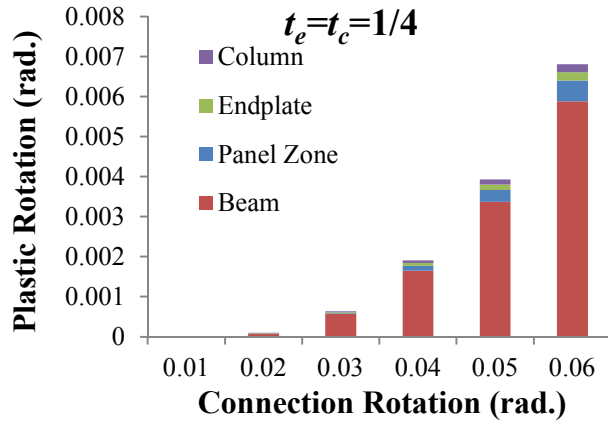


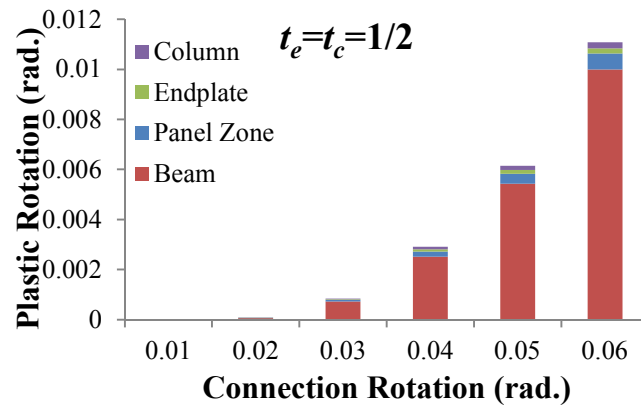
Figure 3.19 Normalized Moment versus Beam Plastic Rotation in for the Connection with and without Stiffeners when Endplate Thicknesses are 1/2 in.

3.4.2.4 Sources of Inelastic Rotation of Connections

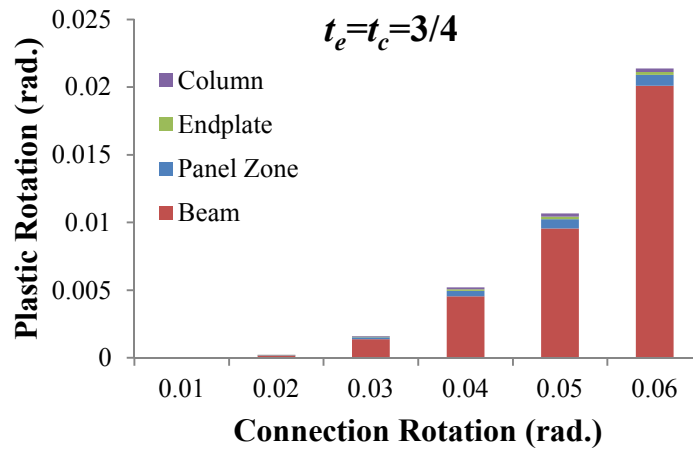
As shown in Figure 3.20, the sources of plastic rotation come from the beam, column, endplate and panel zone. As the thickness of the collar and beam endplate increases, plastic rotation of the connection increases from 0.008 to 0.025 rad. and the contribution of plastic rotation from beam increases as well. This is attributable to the fact that thicker, stiffer endplates allow more inelastic deformation to occur in other structural component. Excessive inelastic deformation is observed in the connections with larger endplate thickness after the formation of beam plastic hinge. Generally, the beam contributes approximately 90% of the total plastic rotation throughout the loading history for the connection with the thickest endplate and collar thickness, which is desirable for a strong column, weak beam design philosophy. The plastic rotation in the panel zone, column and beam increases with an increase of endplate thickness, but contribution of panel zone and column decreases since beam plastic rotation is more dominate in the connection with a thicker endplate and collars.



(a) $t_c = t_e = 1/4$



(b) $t_c = t_e = 1/2$



(c) $t_c = t_e = 3/4$

Figure 3.20 Contribution of Plastic Rotation

3.4.2.5 Parameter Effects on Connection Moment Capacity

To explore the effect of the parameters on the connection moment capacity, the maximum normalized moment is plotted in Figure 3.21 to Figure 3.23 with respect to the given parameter value for all 12 welded collar connections. The results in Figure 3.21 show that as the beam endplate thickness increases, so does the maximum normalized moment. The outlier connection that does not follow this trend has no endplate stiffeners. Excluding this outlier, the maximum normalized moment is approximately 0.93 for the 1/4 in. thick beam endplates, 1.03 for the 1/2 in. thick beam endplates, and 1.11 for the 3/4 in. thick beam end plates. Although the length of the beam endplate is dictated by the collar depth, the collar depth plays little role in the connection's overall behavior due to the fact that yielding of the collar is not observed in these connections. Figure 3.22 and Figure 3.23 show no clear trend in the connection moment capacity with respect to the collar thickness and depth. The results further suggest that the collar plays a more limited role in controlling the capacity of the connection which can be attributed to the fact that the endplate to column face, endplate to collar and collars to column are fully tie together which limits load transmitted to the collar and thus limits the effect of collar parameters on the behavior under large cycling loads.

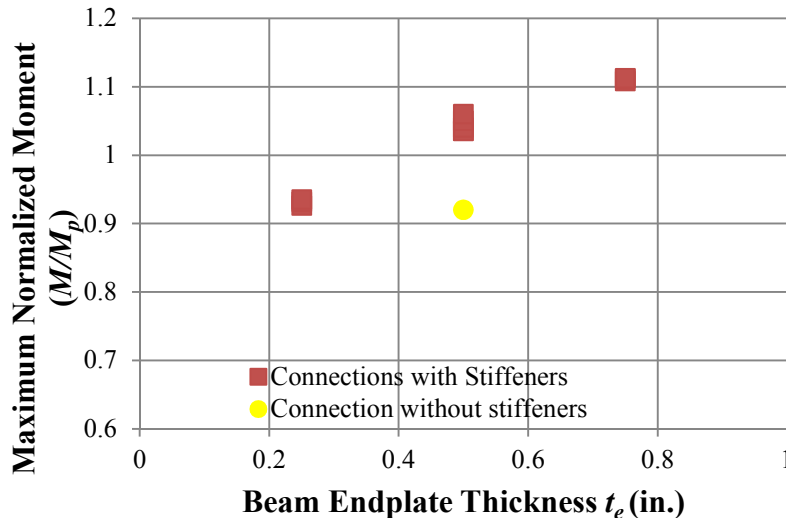


Figure 3.21 Effect of Beam Endplate Thickness on Max. Moment

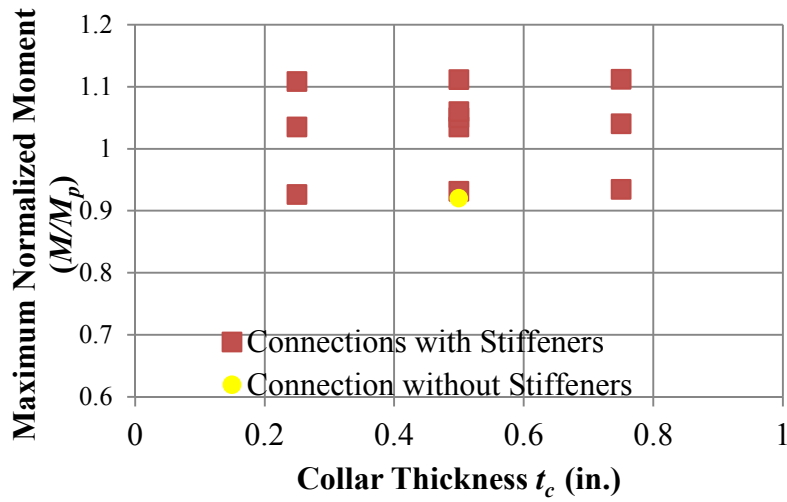


Figure 3.22 Effect of Collar Thickness on Max. Moment

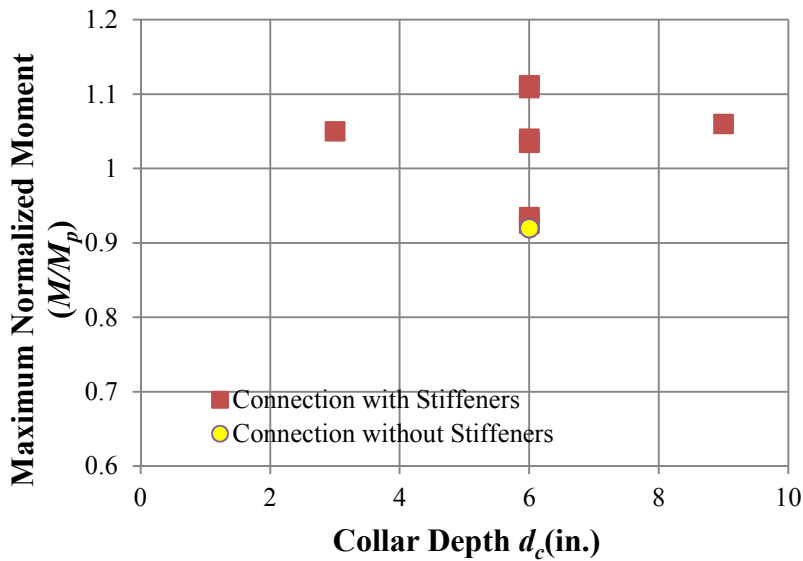


Figure 3.23 Effect of Collar Depth on Max. Moment

3.4.3 Conclusion of Parametric Study

FE analyses are used to explore the effect of various parameters (beam endplate thickness, collar thickness, collar depth, and stiffeners) on the performance of an innovative welded collar HSS-to-HSS seismic moment connection. In total, the behavior of twelve different connection configurations is considered under cyclic loading associated with a seismic event. Ten out of

twelve welded collar connections are able to develop stable plastic hinging of the beam member and reach the beam plastic moment capacity. The beam endplate thickness has more influence on the connection moment capacity than the other parameters and in general the maximum normalized moment can be improved by increasing the thickness of the beam endplate. Collar thickness and depth have little effect on the cyclic behavior of the connections provided collar yielding does not occur prior to the formation of beam plastic hinge. Overall, the welded collar HSS-to-HSS moment connection shows promise for use in low-rise and mid-rise systems. The parametric study results provide substantial insight into parameters that cause significant effects on the overall behavior as well as useful guidance for design and detailing requirements which can lead to more efficient collar connection designs.

3.5 Design Approach for HSS-to-HSS Collar Connection

In this section, an approach is developed to determine the design of HSS-to-HSS collar connections. This approach is not a complete design procedure, but provides a general idea of the assumptions made with respect to connection behavior and requirements of the connection. The assumptions made in this approach provide an initial basis for determining necessary detailing requirements for the collar connections. Final details of the HSS collar connections to be studied experimentally are provided in Chapter 4 and are determined with this approach in mind.

Design of HSS moment connections is covered in AISC 360-10 (2010a) Chapter K, which follows a similar approach to that presented in CIDECT Design Guide 3 (Packer et al., 2009) for rectangular hollow sections under static loading. Potential limit states for welded HSS moment connections are column face plastification, column side wall failure and beam local yielding based on these documents. However, these limit states were determined for static moment connections so they only provide some guidance for seismic HSS-based moment connections. In addition, CIDECT Design Guide 9 (Kurobane et al., 2004) proposes design methods for steel moment connections with HSS members and special requirements for HSS columns under seismic loading. These documents and the following design procedures are considered in developing the design approach for HSS based collar connections, including: American Welding

Society (AWS) D1.1: 2000 (AWS 2000) for prequalified welds connecting HSS members and the Seismic Provision for Structural Steel Buildings (AISC, 2010a).

In order to meet current seismic design requirements, the HSS based collar connection must be designed to ensure that the connection develops the beam's plastic moment capacity without the occurrence of brittle weld failure under large cyclic loads. The objective of the design approach is to achieve a ductile failure mode through beam plastic hinging with possible participation in the inelastic deformation from the collar, endplate and panel zone. Such an approach will allow earthquake energy to be dissipated mainly through beam plastic hinging while potentially having other suitable connection components participate in the inelastic behavior. As such, the plastic moment of the beam can be used as the applied load for the moment connection leading to a capacity based design approach. The design moment and shear force are calculated in Equation 3.2 and Equation 3.3. The plastic moment capacity of the beam under seismic loads is calculated using Equation 3.4 considering the requirements of AISC Seismic Provisions (2010a). Design shear force from the formation of the plastic hinge, V_p , is computed as shown in Equation 3.5.

$$M = M_p + M_G \quad \text{Equation 3.2}$$

$$V = V_p + V_G \quad \text{Equation 3.3}$$

$$M_p = 1.1 R_y F_y Z \quad \text{Equation 3.4}$$

$$V_p = \frac{M_p}{\frac{L_b}{2}} \quad \text{Equation 3.5}$$

where M is the design moment for the collar connection, V is the design shear force, M_G is the moment from gravity loads, V_G is the shear force from the gravity loads, M_p represents the beam plastic moment, R_y is the material overstrength factor equal to 1.4 for ASTM A500 Gr. B steel (AISC 2010a), F_y is the yield strength for HSS beams (46 ksi for ASTM A500 Gr. B steel), Z is the HSS beam plastic modulus and L_b is the beam length in the moment frame..

Free body diagrams for the connection components and the resulting load path are demonstrated in Figure 3.24. The moment and shear loads developed in the beam as a result of the formation of the plastic hinge and gravity loads are transferred to the endplate through fillet welds around HSS beam and stiffeners. It can be assumed that the endplate is rigid due to the use of endplate

stiffeners, the recommended thicknesses from the FE study in Section 3.4 and the fact that its full border is welded to the column except in the locations underneath the collars. The load is then assumed to flow from the endplate to the collar in tension and column face in compression. From here it is assumed that the loads are picked up by the column sidewalls and transferred down through the column.

The fillet welds between beam and endplate and between the stiffeners, endplate, and beam are required to sustain both shear force and bending moment. The elastic method in the AISC Steel Construction Manual Part 8 (2010b) can be used to design these welds. Equation 3.6 and Equation 3.7 provide equations that can be used to size the beam to endplate fillet welds under bending moment and shear. The equations proposed here simplify the calculation by assuming the welds along the web resist the shear forces and welds along the beam flange resist flexure.

$$M \leq \phi_{weld}(d_b b_{b,workable})(1.5t_{wb})\left(\frac{\sqrt{2}}{2}\right)(0.6F_{EXX}) \quad \text{Equation 3.6}$$

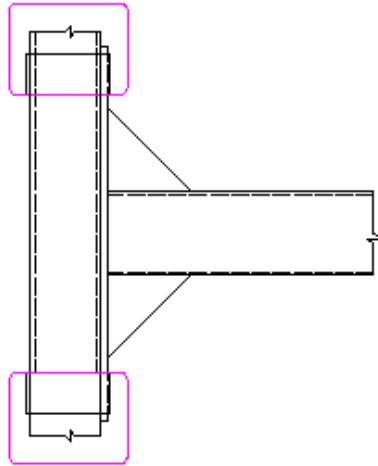
$$V \leq \phi_{weld}R_{n,web} = \phi_{weld}(0.6F_{EXX})\left(\frac{\sqrt{2}}{2}\right)(t_{wb})(2d_{b,workable}) \quad \text{Equation 3.7}$$

where ϕ_{weld} is the resistance factor for welds which has been specified in AISC 360-10 Table J2.5, $d_{b,workable}$ is the workable flat along the beam height, $b_{b,workable}$ is the workable flat along the beam width, t_{wb} is leg size of the beam to endplate weld, F_{EXX} is the weld electrode tensile strength, and d_b is the height of the HSS beam.

For the beam endplate, the preliminary FE study results from Section 3.5 suggest that an endplate thickness of at least 1/2 in. is necessary to develop the plastic capacity of the beam. To limit column face plastification, the width of the endplate should also be greater than 85% the width of the column. The length of the endplate should be chosen so as to extend 1 in. beyond the collars assuming a 1 in. gap also exists between the collar and stiffeners to allow for welding.

Welds connecting the beam endplate to the column face can be used to transfer the shear force to the column. If the endplate width is equal to or less than the workable flat of the column face, then this weld will be a fillet weld, but if the endplate is wider than the workable flat then this weld will be a flare bevel groove weld due to the corner of the HSS column.

Part I: Upper Collar and Column



Part II: Lower Collar and Column

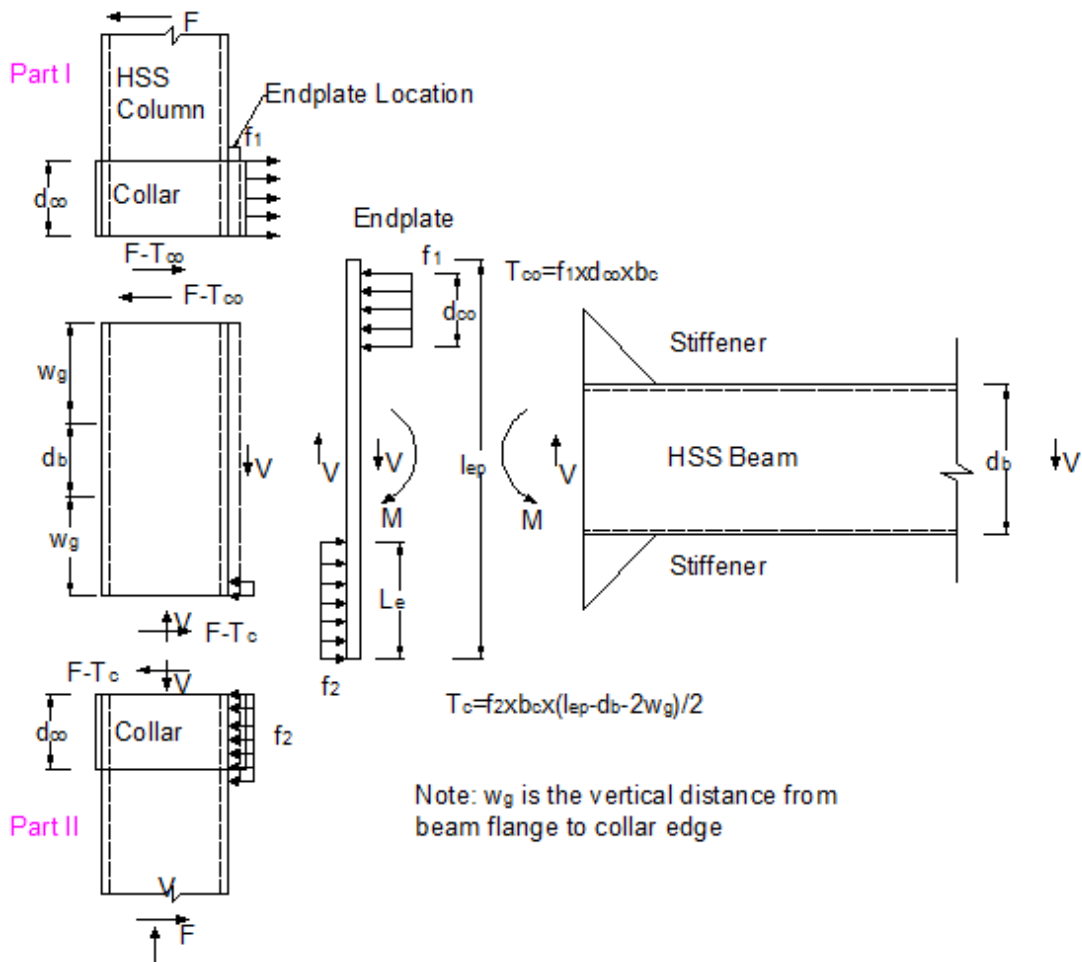


Figure 3.24 Load Path for the HSS Based Collar Connection

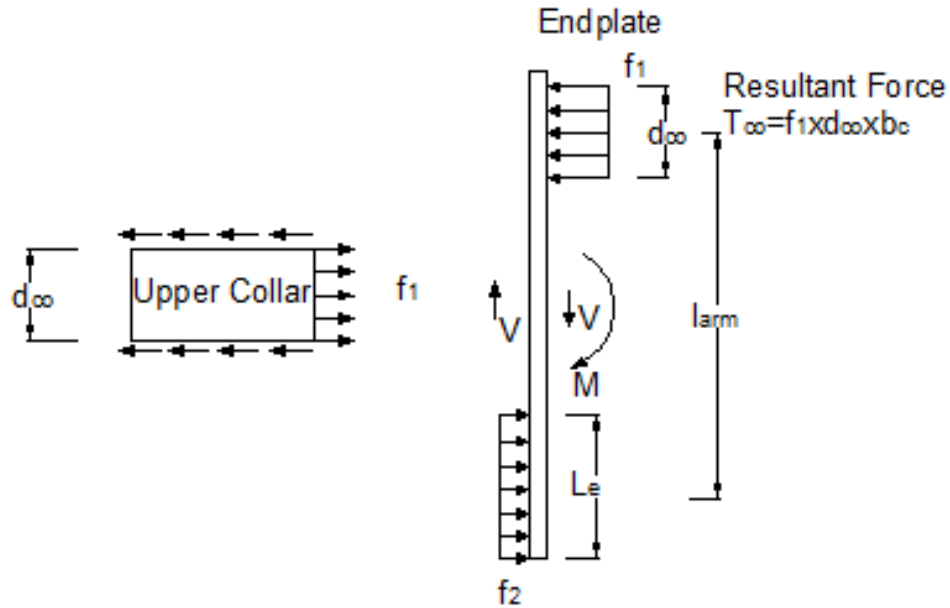


Figure 3.25 Free Body Diagrams of Endplate and Collar

As for the collar design, the most economic design is to assume that the beam reaches its plastic moment capacity and the collar plates yield simultaneously. This design method will provide the minimum requirement for the cross sectional area of the collar, assuming the collar has a consistent cross section all the way around. The free body diagram of the endplate and collar is shown in the Figure 3.25. The design approach is an iterative process where the collar depth (d_{co}) is first assumed and then checked to meet the requirements of the welds along the collar plates attached to the column sidewall since the thickness of the collar plate should be greater than the weld leg size. To determine the required gross section area of the collar, it can be assumed that the collar plates attached to the column sidewall yield as a result of the applied tension. The design tension force in the collar is transmitted by the endplate to the collar. In Equation 3.8, the resultant tension force, T_{co} , in the collar is computed by conservatively assuming the moment arm, l_{arm} , is the vertical distance from the beam's neutral axis to the midpoint of the collar depth. The minimum required gross section area for the collar plates connected to the column sidewalls can be computed based on Equation 3.9 through Equation 3.11 considering limit states of gross section yielding and net section fracture.

$$T_{co} = M/l_{arm} \quad \text{Equation 3.8}$$

$$A_{g,co,yield} = T_{co}/2\phi_{yield}F_y \quad \text{Equation 3.9}$$

$$A_{g,co,fracture} = T_{co}/2\phi_{fracture}F_y \quad \text{Equation 3.10}$$

$$A_{g,co} = \max(A_{g,co,yield}, A_{g,co,fracture}) \quad \text{Equation 3.11}$$

Where l_{arm} is the moment arm which is the vertical distance from resultant tension force in the collar to the resultant compression force in the column face as shown in Figure 3.25, T_{co} is the resultant tension force on the collar, ϕ_{yield} is the resistance factor for gross section yielding which is 0.90, $\phi_{fracture}$ is the resistance factor for the net section fracture which is 0.75, F_y is the yield strength of the collar plate, $A_{g,co,yield}$ is the required collar cross section area based on the limit state of gross section yielding, $A_{g,co,fracture}$ is the required collar cross section area based on the limit state of net section fracture, $A_{g,co}$ is the required collar cross section area based on the two limit state in the collar.

Once the gross section area of the collar sidewall, $A_{g,co}$, is selected, Equation 3.8 and 3.9 must be used to recalculate the tension force, T_{co} , on the collar with a revised moment arm. The collar depth and collar thickness should be carefully selected based on welding requirements since the collar thickness should be larger than the weld leg size connecting the collar to the column.

The welds connecting the individual plates making up the collar should develop the strength of the plates or use a prequalified PJP weld that develops the necessary capacity assuming the welds take all the applied tension.

Welds connecting the collar to column sidewalls can be assumed to resist tension force from beam endplate and each weld segment would sustain a quarter of the tension force on the collar (i.e. T_{co}) as shown in Equation 3.12.

$$\frac{T_{co}}{4} \leq \phi_{weld}R_n = \phi_{weld}(0.6F_{EXX})\left(\frac{\sqrt{2}}{2}\right)(t_{wc})(d_{c,workable}) \quad \text{Equation 3.12}$$

where T_{co} is the tension force in the collar, ϕ_{weld} is resistance factor for the weld which has been specified in AISC 360-10 Table J 2.5, F_{EXX} is the weld metal strength, t_{wc} is the leg size of the collar to column sidewall welds, $d_{c,workable}$ is the workable flat along column height. If the assumed thickness of the collar is greater than 1/4 in., it is required to be at least 1/16 in. thicker than the fillet weld leg size otherwise a thicker collar needs to be chosen.

Following this design approach is expected to ensure proper behavior of the collar connection, but study of an actual connection is needed to fully understand the expected load paths and other parameters affecting the performance of the connection.

3.6 Conclusions

An experimental study is undertaken to evaluate the performance of two reinforced HSS-based connections. The connections consist of HSS-to-HSS members with either an external diaphragm plate or a through plate to more efficiently transfer forces from the beam flanges to the column sidewalls. The connections are designed such that beam plastic hinging or reinforcing plate yielding occurs prior to non-ductile weld fracture. The connections are cycled according to a loading protocol to simulate the expected loading during a far-field earthquake and the results are evaluated in terms of the connection moment rotation behavior, beam plastic hinge behavior, and strain distribution in each structural component. A second set of seismic moment connections is also considered that utilize a beam endplate and collars to connect the HSS members. A total of 12 different HSS-based collar connections are considered through a detailed FE analysis where they are cycled through a similar loading protocol to that of the reinforced connections. The effects of beam endplate thickness, collar thickness, collar depth and stiffeners on the cyclic behavior of the connection along with the distribution of inelastic rotations within the connection are considered in evaluating the connection. In the end, design procedures of HSS based collar connection are proposed.

1. The HSS-based reinforced connections are able to achieve stable plastic hinging of the beam member. The majority of plastic rotation and inelastic deformation is concentrated in the beam which satisfies strong column-weak beam requirements in seismic design philosophy.
2. For the reinforced HSS based moment connections, beam moment capacity is enhanced by 32% and 20% for the external diaphragm reinforced and through plate connections, respectively. Both connections exhibit stable hysteretic behavior with minor moment degradation until local buckling occurs at around the first 0.04 rad. cycle. These reinforced connections are able to satisfy intermediate and special moment frame requirements since

they are capable of maintaining at least 80% of their moment capacity at the 0.02 rad. and 0.04 rad. cycle.

3. For the reinforced connections, adequate width-thickness and depth-thickness ratios of the beam are required to inhibit the onset of local buckling and the occurrence of fracture due to cycling until after the formation of the plastic hinge in the beam member. With the addition of the reinforcing plates, the transfer of forces mainly occurs at the middle of the beam flange where the reinforcing plate terminates along the length of the beam. For this reason, the fillet weld at the end of the reinforcing plate must be properly detailed to prevent non-ductile weld fracture.
4. The HSS based collar connections are proposed and expected to reduce the amount of field welding. FE analyses of on those connections show their ability of development stable plastic hinging in the beam member and achieve its plastic moment capacity. Beam endplate stiffeners ensure that the majority of the inelastic behavior occurs in the beam member and larger endplate thicknesses allow the plastic capacity of the beam to be reached. The beam endplate thickness is shown to control the moment capacity of the connection more than the collar thickness and depth since the stiffer endplate can force yielding to occur in other components, particularly in the HSS beam.
5. Overall, both sets of connections show promise for use in low-rise or mid-rise moment frames.
6. An approach for the design of the welded HSS based collar connection is developed. The approach uses the beam moment capacity to design the connection, requires plastic hinging in the beam member, and avoids non-ductile failure of the connection welds.

CHAPTER 4 HSS BASED COLLAR CONNECTION TESTS

4.1 Introduction

Chapter 3 and Fadden et al. (2014) showed that viability of HSS based seismic moment connections provided through plates or external diaphragm plates are used to move the inelastic behavior away from the column face and to transfer the tension and compression forces due to bending directly into the sidewalls of the HSS columns. However, a significant amount of field welding is needed to construct these joints which can lead to reduced weld quality, slower construction, and increased cost. In order to address these concerns, the HSS based collar connection developed in Chapter 3 is experimentally explored so as to provide an effective HSS based seismic moment connection that requires limited field welding, increased construction speeds and the potential for use in modular construction. Two full scale experimental tests are performed to explore the performance of these collar connections under larger cyclic loads and to understand their potential failure modes.

In experimentally studying the HSS based collar connections, the mechanical behavior of the HSS flats and corners are obtained through tensile coupon tests. Their tensile properties allow for a better understanding of the bending capacity of the beam and provide critical information for numerical models. Cyclic tests of two collar connections, with and without beam endplate stiffeners, are conducted to explore their performance. The experimental test results provide insight into the potential failure modes and load transfer mechanisms of the connections that may not be captured in the previous finite element study in Chapter 3. The experimental study results described herein consider hysteretic behavior, secant stiffness, sources of inelastic rotation, energy dissipation capacity, equivalent viscous damping, and the distribution of strain in the connections. The results also provide the necessary data to validate the finite element models of the connection which can be used to conduct a more detailed parametric study and develop further design recommendations (Chapter 5).

4.2 HSS Material Properties Test

Hollow structural sections are often made from flat steel plate by rolling them into desirable shapes such as round, rectangular or square then welding the seam through electric resistance welding. This manufacturing process results in cold working of the corners and residual stress around the weld seam (Weng & Pekoz, 1988). Thus, the material properties are not consistent around the cross sections. However, the influence of the fabrication process on the properties of the steel around the cross section of an HSS has been studied previously with the results indicating that the influence of the heat affected zone resulting from the seam weld exerts little influence on the mechanical properties of the whole cross section (Fadden, 2013). Based on this research, material test results on HSS flats and corners are able to provide sufficient information to accurately capture the actual properties of the HSS sections and model their behavior.

Most American manufacturers conform to ASTM A500 or the newly adopted ASTM A1085 standards. Since 2013, the new material specification has been extensively utilized in manufacturing HSS members because of its tighter tolerances leading to a more consistent product. It provides more stringent standards such as slightly higher minimum yield strength, tighter tolerance, maximum yield strength and toughness requirements. By adopting the ASTM A1085, the minimum yield strength of HSS members is increased from 46 ksi for rectangular and square HSS and 42 ksi for round HSS to 50 ksi for all shaped HSS. The addition of a maximum yield strength requirement of 70 ksi also reduces capacity design requirements in seismic design. The stringent wall thickness tolerance which is decreased from 10% to 5% and newly introduced mass tolerance of 3.5% allow practitioners to use the nominal wall thickness in structural design instead of 0.93 times the nominal wall thickness that is currently required for ASTM A500 HSS, which makes design with HSS member more efficient. The addition of Charpy notch toughness requirements increases the suitability of HSS members for fatigue applications. Canadian manufacturers produce CSA Standard G40.21 Gr. 50W which essentially has the same requirements of ASTM 1085 without the Charpy notch toughness requirement.

4.2.1 Experimental Program

In the HSS based collar connection tests, the endplate and collars are made of A36 steel plates. Since those plates do not undergo any visible yielding in the test, no coupon tests are carried out for the A36 plates. For both collar connections, HSS members are from the same fabrication batch. The HSS beam is made of ASTM A500 Gr. B steel and the HSS column meets CSA Gr. 40.2150W Class C standards (essentially ASTM 1085 standards). To better understand the properties of the HSS beam and column and provide necessary information for numerical models, tensile coupon specimens are taken from the flats (3) and corners (2) of the HSS beam and column. The test results provide confirmation that the material meets its specified standard and gives a more realistic understanding of the expected capacity and behavior of the connection.

The dimension and cross section location of the coupon specimens are illustrated in Figure 4.1 and 4.2. ASTM A370-17 (2017) protocols provide the standard test methods used in this study for the tensile coupon tests. However, limitations, such as the maximum capacity of the hydraulic test frame, does not allow for strict adherence to these specifications, particularly for the corner specimens. Minor changes have been adopted to accommodate these limitations. The coupon specimens are milled to meet the sub-sized specimen requirement stipulated in ASTM A370-17 (2017) as shown in Figure 4.2. The gage length of each specimen is approximately 2 in. with a 1/2 in. width. All specimens are approximately 3/8 in. thick. Specimens taken from the flanges and webs are designated as F1-F3 for the HSS beam and F6-F8 for the HSS column. Those taken from the corners are defined as C1-C2 for the HSS beam and C3-C4 for the HSS column. The actual dimensions of each specimen are averaged based on the measurements at three points along the gage length. A 22 kip hydraulic uniaxial test frame is used to conduct the test with a 22 kip load cell measuring the load and a 2 in. gage length extensometer (except Specimen F1 which utilized a 1 in. gage length extensometer) measuring strain. The loading rate is 0.01 in./min. The extensometer is removed upon either the occurrence of necking or strain up to 25%, whichever comes first, to prevent damage to the device.

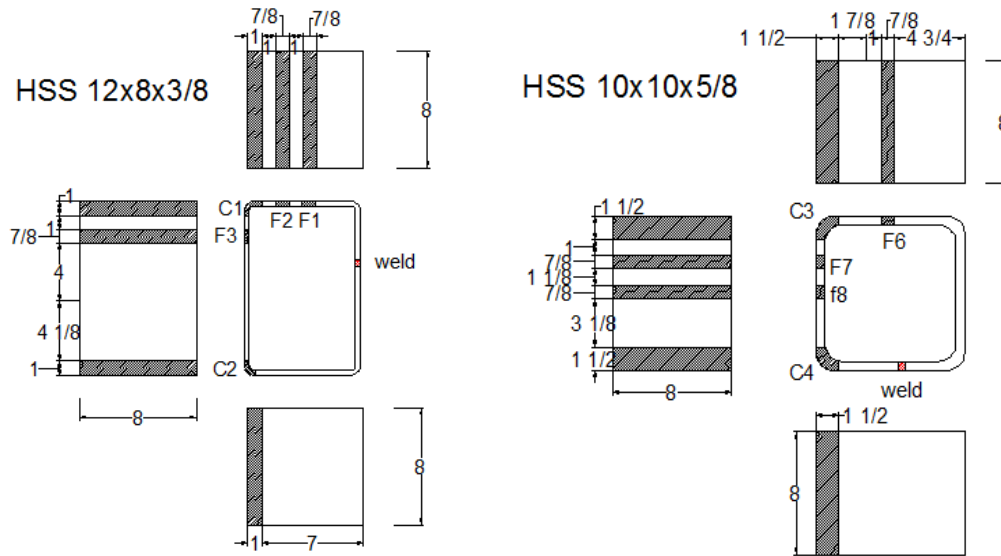


Figure 4.1 Tensile Specimen Locations for the HSS 12×8×3/8 Beam and the HSS 10×10×5/8 Column (units in inch)

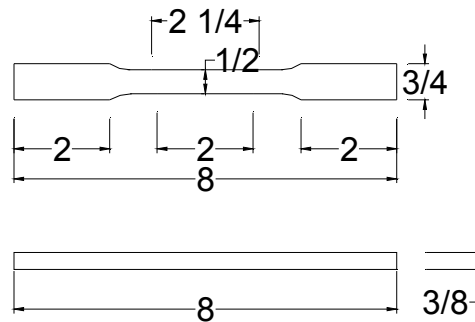


Figure 4.2 Typical HSS Sub-size Coupon Specimen (units in inch)

4.2.2 Experimental Results

The load is converted to stress using the average cross-sectional area from the measured gage dimensions of each specimen. The stress-strain curves are shown in Figure 4.3 to Figure 4.6. A summary of the material properties obtained from the tensile coupon tests is provided in Table 4.1 to Table 4.4 for each specimen which includes tensile yield strength, F_y ; ultimate strength, F_u ; tensile yield strain, e_y ; ultimate strain, e_u ; Young's modulus, E ; ultimate tensile strength to yield strength ratio, F_u/F_y ; and ultimate strain to yield strain ratio, e_u/e_y . The yield strength is calculated by the 0.2% offset method. Since the HSS member has been cold formed, there is no defined plastic plateau. The ultimate tensile strength is calculated as the maximum stress

achieved during loading. The yield strain and ultimate strain correspond to the strain at yield and ultimate strength.

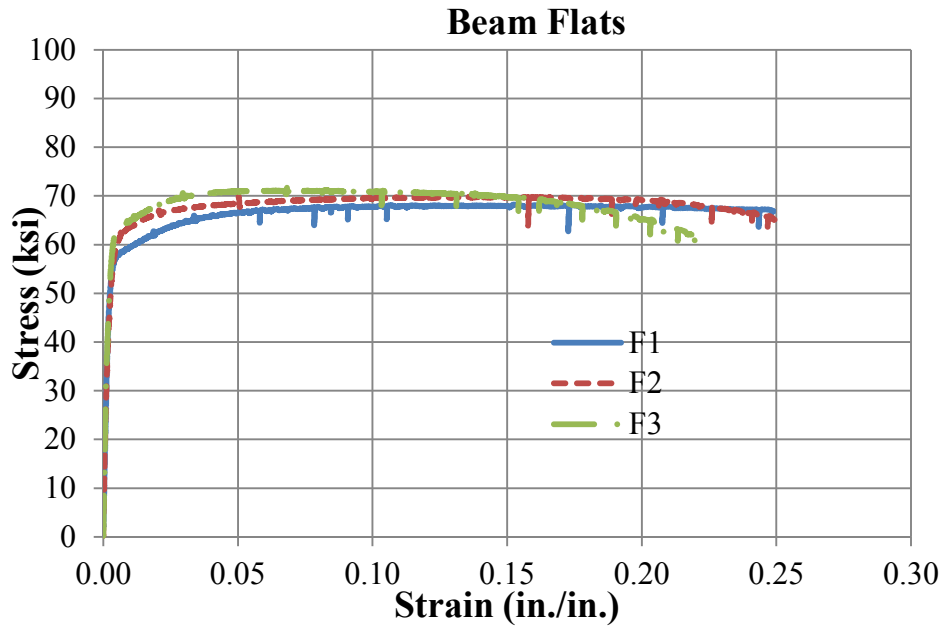


Figure 4.3 Engineering Stress-Strain Plots for the Beam Flats

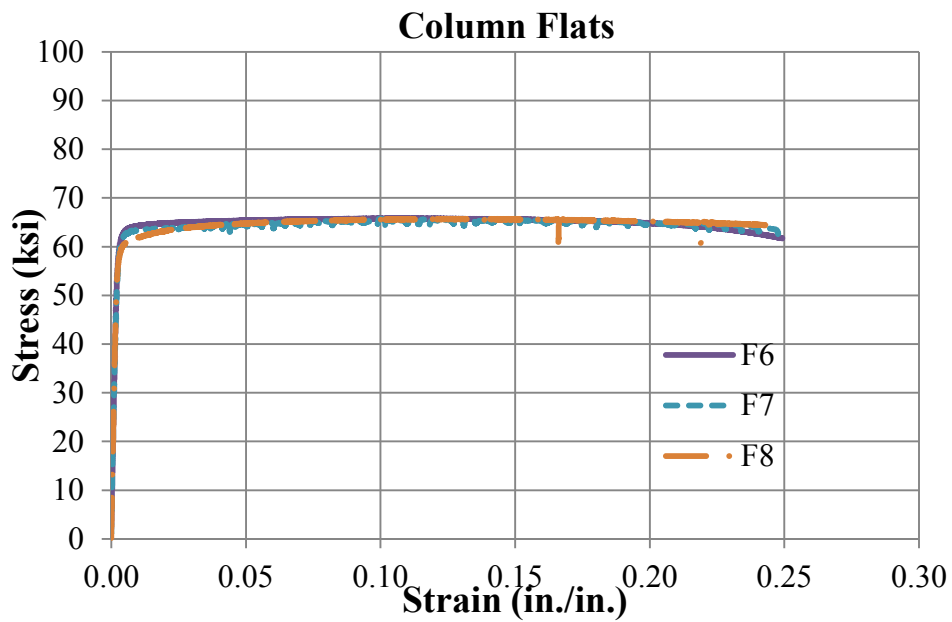


Figure 4.4 Engineering Stress-Strain Plots for the Column Flats

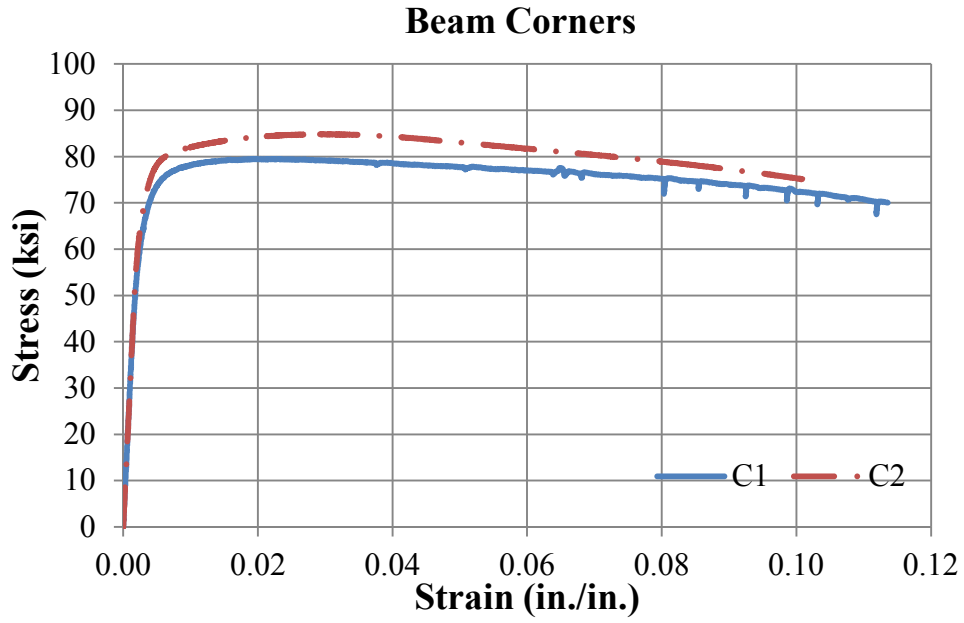


Figure 4.5 Engineering Stress-Strain Plots for the Beam Corners

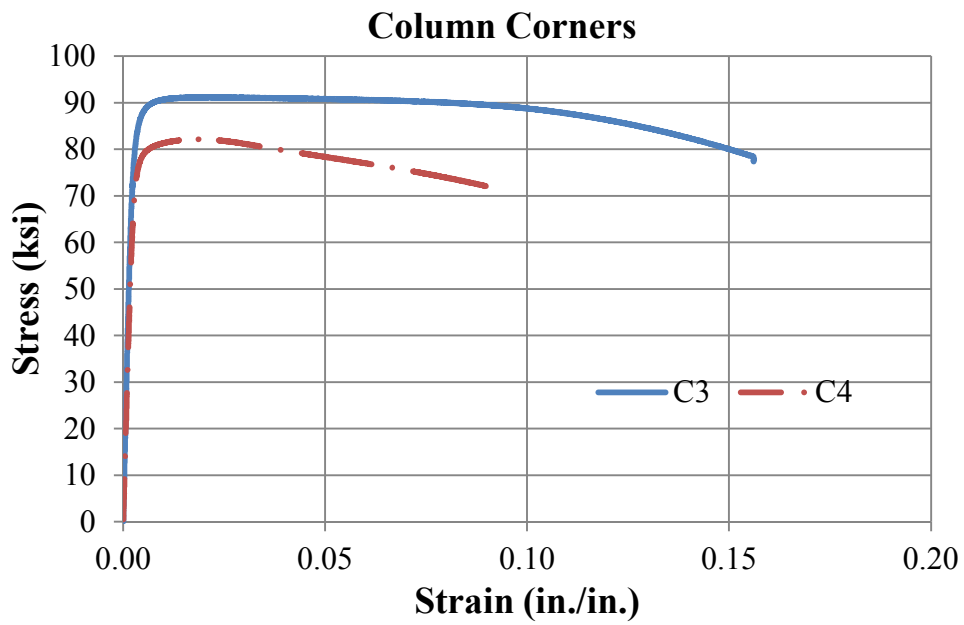


Figure 4.6 Engineering Stress-Strain Plots for the Column Corners

Table 4.1 Material Properties for the HSS 12×8×3/8 Flats

Specimen NO.	F_y (ksi)	F_u (ksi)	E (ksi)	e_y (in./in.) $\times 10^{-3}$	e_u (in./in.)	e_u/e_y	F_u/F_y
F1	56.9	68.2	24700	4.34	0.152	35.1	1.20
F2	57.0	70.0	29300	3.91	0.158	40.5	1.23
F3	61.0	72.2	31800	3.93	0.068	17.4	1.18
Average	58.3	70.1	28600	4.06	0.126	31.1	1.20

Table 4.2 Material Properties of Column HSS 10×10×5/8 Flats

Specimen NO.	F_y (ksi)	F_u (ksi)	E (ksi)	e_y (in./in.) $\times 10^{-3}$	e_u (in./in.)	e_u/e_y	F_u/F_y
F6	62.6	65.8	27300	4.28	0.112	26.1	1.05
F7	62.0	65.8	26500	4.44	0.129	29.0	1.06
F8	60.0	65.7	28600	4.18	0.167	40.0	1.10
Average	61.5	65.8	27500	4.30	0.136	31.5	1.07

Table 4.3 Material Properties of Beam HSS 12×8×3/8 Corners

Specimen NO.	F_y (ksi)	F_u (ksi)	E (ksi)	e_y (in./in.) $\times 10^{-3}$	e_u (in./in.)	e_u/e_y	F_u/F_y
C1	72.0	79.5	30000	4.40	0.196	4.46	1.10
C2	77.0	84.8	30300	4.54	0.294	6.48	1.10
Average	74.5	82.2	30200	4.47	0.245	5.49	1.10

Table 4.4 Material Properties of Column HSS 10×10×5/8 Corners

Specimen NO.	F_y (ksi)	F_u (ksi)	E (ksi)	e_y (in./in.) $\times 10^{-3}$	e_u (in./in.)	e_u/e_y	F_u/F_y
C3	86.8	91.2	37300	4.34	0.199	4.60	1.05
C4	78.3	82.2	30400	4.58	0.184	4.01	1.05
Average	82.6	86.7	33800	4.46	0.192	4.31	1.05

4.2.2.1 HSS Strength

The average yield strengths of the HSS beam flats and corners are 58.3 ksi and 74.5 ksi, respectively. The average ultimate strengths of the HSS beam flats and corners are 70.1 ksi and 82.2 ksi. They both meet the minimum strength requirements for the ASTM A500 specification (2013) which specifies a minimum of 46 ksi for yield strength and 58 ksi for tensile strength for

Grade B steel. The average yield strengths of the HSS column flats and corners are 61.5 ksi and 82.6 ksi, respectively. The average ultimate strengths of the HSS column flats and corners are 65.8 ksi and 86.7 ksi. Both the yield strength and ultimate strength of the HSS column satisfy the requirements specified in the CSA standard which requires a minimum yield strength of 50 ksi and an ultimate strength between 65 ksi to 90 ksi for CSA G40.2150W. In the corners of the HSS beam and column, the yield strength and ultimate strength increase by 30% and 20% due to cold forming effects during fabrication.

As for ultimate strength to yield strength ratio, specimens from the beam flats exhibit the largest value with an average value of 1.20 while the average strength ratios from the beam corners, column flats and column corners are 1.10, 1.07 and 1.05, respectively. To ensure sufficient spread of plasticity in seismic applications after a structure goes inelastic, EuroCode 3 (2005) also provides a suggested value for ultimate tensile strength to yield strength ratio as 1.1. The HSS beam is capable of achieving this suggested value with average values of 1.20 and 1.10 for the beam flats and corners, respectively. The HSS column fails to satisfy this requirement with average values of 1.07 and 1.05 for the column flats and corners, respectively.

4.2.2.2 Young's Modulus

The Young's modulus for specimens taken from the beam flats range from 24,700 to 31,800 ksi with an average of 28,600 ksi as shown in Table 4.1. Meanwhile, the Young's modulus for specimens taken from the column flats varies from 26,500 and 28,600 ksi with an average of 27,500 ksi as shown in Table 4.2. However, the Young's modulus from the corners of both the beam and column show larger stiffness with average values of 30,200 and 33,800 ksi, respectively, as seen in Table 4.3 and Table 4.4.

4.2.2.3 HSS Ductility

The yield strain, e_y , is consistent for all specimens ranging from 3.91×10^{-3} to 4.58×10^{-3} as shown in Table 4.1 to Table 4.4. However, the ultimate strain, e_u , is relatively scattered even when taken from the same cross section location. The values range from 0.0184 to 0.167. The smaller ultimate strain at the corners is attributable to cold forming effects. The ultimate strain to yield

strain ratio varies from 17.4 to 40.5 for flat specimens and from 4.01 to 6.48 for corner specimens.

ASTM A500/A500M-13 (2013) specifies that Gr. B shaped structural tubing must have at least 23% elongation in 2 in. gage length at fracture. This requirement is observed for the coupon specimens taken from the beam flats as shown in the Figure 4.3. The extensometer is removed prior to fracture, but these specimens still exhibit 23% elongation even upon reaching their ultimate tensile strength. However, no specimen from the beam corner reaches the 23% elongation requirement prior to the extensometer being removed. For the column, the CSA 40.2150W specification requires a minimum elongation of 22% in the 2 in. gage be reached prior to fracture. Similar to the HSS beam, all the specimens from the column flats are capable of conforming to the specification requirement even based on their elongation at ultimate strain. None of the specimens from column corners reaches 22% elongation prior to necking.

EuroCode 3 (2005) recommends that elongation at failure not be less than 15% in a gauge length of $5.65\sqrt{A_0}$ where A_0 is the original cross-sectional area. The ratio of ultimate strain to yield strain also shall be at least 15. For the tested HSS, $5.65\sqrt{A_0}$ ranges from 2.16 to 2.50 in. Thus, all specimens from the HSS flats satisfy the 15% elongation requirement before removal of the extensometer. From Table 4.1 and 4.2, these specimens also meet the requirement for the strain ratio 15. However, specimens from HSS corners are unable to conform to the ductility requirement in EuroCode 3(2005).

4.2.3 Implications of Results

The measured material overstrength ratio is smaller than the value specified in AISC 340-10 (2010a) which is 1.4 for ASTM A500 Gr. B steel. The collar connection was designed based on the plastic moment capacity of the HSS beam, with consideration of the overstrength ratio specified in AISC 340-10 (2010a) and minimum yield strength of ASTM A500 Gr. B steel as shown in Equation 3.4. As a result, based on the measured yield strength for the beam flats, the connection's moment capacity tends to be overestimated with such design method.

Cold forming affects materials ductility and elastic stiffness. The findings suggest failure most likely will initiate at the less ductile beam corners in the plastic hinge region. The material

properties obtained here can be utilized to refine and validate finite element models of the HSS collar connections.

4.3 Collar Connection Tests

4.3.1 Introduction

Steel moment frames can be categorized into three types, ordinary moment frames (OMF), intermediate moment frames (IMF) and special moment frames (SMF) with an increasing level of expected performance and ductility capacity. OMF are expected to withstand minimal inelastic story drifts in their members and connections as a result of lateral forces. IMF are designed to sustain limited inelastic story drifts through the flexural yielding of beams and columns as well as shear yielding of beam column panel zones. AISC 341-10 (2010a) specifies that IMF shall be capable of providing $0.80M_p$ at interstory drifts of 0.02 rad. SMF have the strictest ductility requirements in order to be able to provide significant interstory drift capacity through flexural yielding of the beams and shear yielding of panel zone areas. SMF must be capable of sustaining story drifts of 0.04 rad. while still providing moment capacities at least $0.80M_p$. Moment capacity, degradation of moment capacity, and stiffness are important criteria to assess the cyclic behavior of frames under seismic loading.

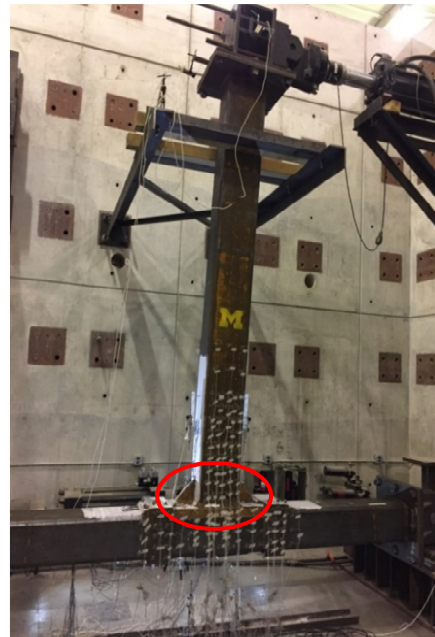
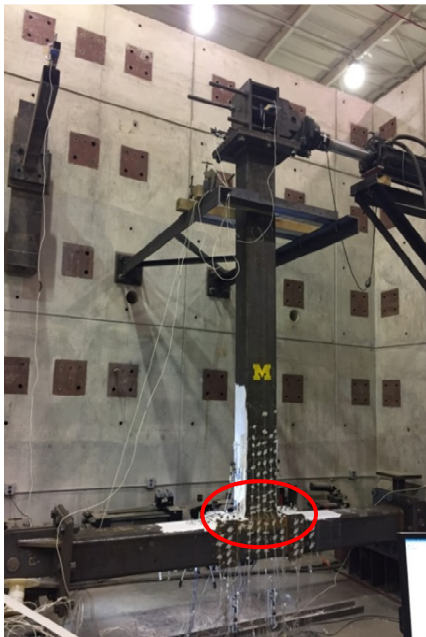
From the perspective of energy, earthquake input energy is balanced by kinematic energy of the structure, energy dissipated by viscous damping and absorbed energy including elastic straining and unrecoverable inelastic deformation of the members. Sources of inelastic deformation and energy dissipation capacity are also indispensable indices to evaluate the seismic performance of the collar connections.

Experimental testing of the two collar connections allows for characterization of their hysteretic behavior, determination of the components involved in the plastic rotation of the connections, measurement of the energy dissipated by the connections during cycling and an understanding of the flow of forces through the connections leading to design and detailing requirements to ensure that the connections meet SMF criteria.

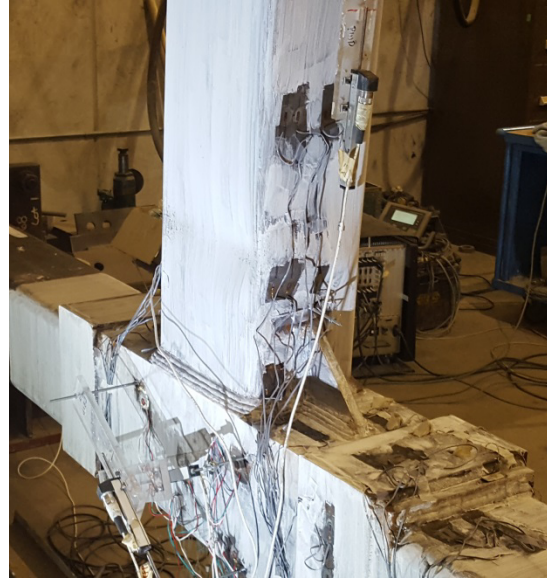
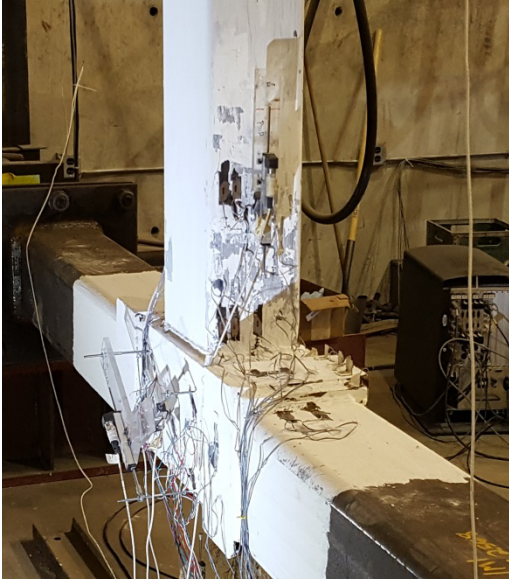
4.3.2 Experimental Program

4.3.2.1 Test Setup and Loading Protocol

The beam-to-column connection subassemblies are rotated 90 degree to meet the laboratory constraints and make loading more convenient. The vertical member is the HSS 12×8×3/8 beam and the horizontal member is the HSS 10×10×5/8 column. The subassembly represents an exterior moment connection in a low-rise steel moment frame with 12 ft floor heights and 21 ft bay widths. Both the beam and column are pinned at their inflection point. The distance from beam tip to column centerline is 127 in. while the distance between the two pins at column inflection points is 144 in. The free end of the beam is pinned and connected to a 150 kip hydraulic actuator with a 30 in. (+/-15 in.) stroke. The actuator is used to apply cyclically increasing displacements that simulate expected inter-story drifts during a far-field type earthquake. The column is bolted to two pin fixtures seated on spreader beams which are connected to the strong floor.



(a) Connection without Stiffeners (b) Connection with Stiffeners



(c) Close Up of Connection without Stiffeners (d) Close Up of Connection with Stiffeners

Figure 4.7 HSS based Collar Connection Test Setup and Configuration

A loading protocol representing a far field earthquake follows that prescribed by AISC for prequalification of seismic moment connections (AISC, 2010a) with minor modifications after fracture propagation following the first two 0.08 rad. cycles. The loading protocol is illustrated in Figure 4.8 with 40 cycles gradually increasing from 0.00375 rad. to 0.08 rad. The quasi-static loading rate is 0.05 in./sec for the first 38 cycles then the displacement is returned to zero. To further explore the failure mechanism and moment capacity after fracture initiation at 0.08 rad. drift, a loading rate of 0.33 in. /sec is applied for the last two cycles.

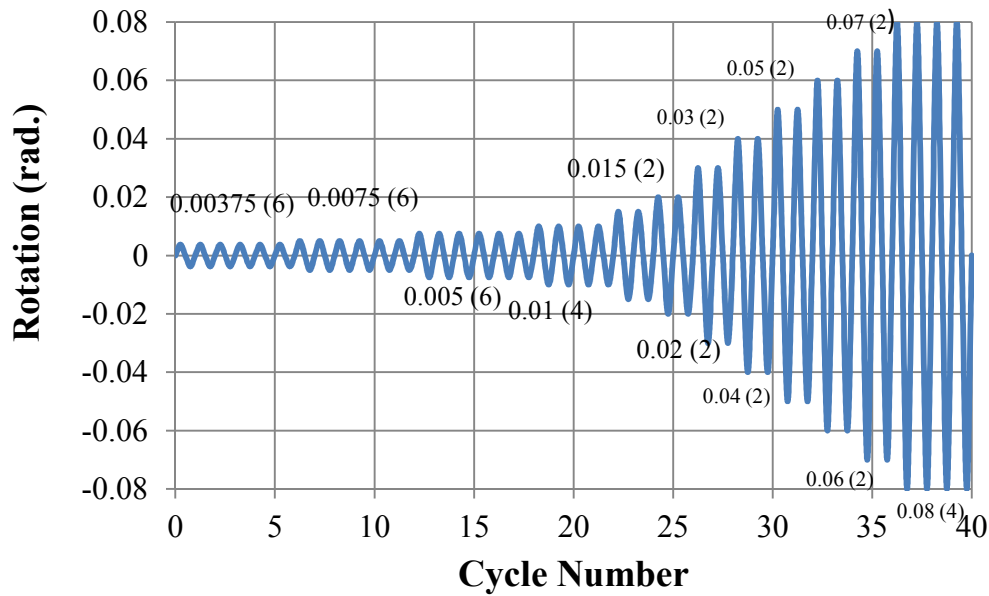


Figure 4.8 Loading Protocol for the Experimental Test of the Collar Connections

4.3.2.2 Test Specimens

The connection tests consist of two full scale HSS based collar connections both with an HSS 12×8×3/8 beam and HSS 10×10×5/8 column. An HSS 10×10×5/8 is chosen for the column since it is the largest section that meets the stringent seismically compact width-thickness limit requirement prescribed by AISC Seismic Provision for Steel Structural Buildings (2010a). The width thickness ratio, b/t , and depth thickness ratio, d/t , for the HSS 10×10×5/8 is 14.2 compared to 16.1 which is the limit for moderately ductile members based on the Equation 4.1 assuming an elastic modulus of 29,000 ksi and yield strength of 46 ksi from AISC 341-10 Table D1.1. An HSS 12×8×3/8 is selected as the beam member since it is capable of developing its plastic moment capacity in a ductile manner with minor moment degradation according to the findings in Chapter 3. Its nominal b/t and d/t ratios meet SMF and IMF ductility criteria based on the previous HSS bending study conducted by Fadden and McCormick (2014a). These two member sizes also match the through plate and external diaphragm plate connections presented in Chapter 3 and allow for comparison of the different connection performances. The actual dimensions of the HSS beam and column are measured for the corner radii, height, width and wall thickness at the flats and corners. The measured b/t , d/t and plastic modulus are calculated and listed in Table 4.5. Yield strength, F_y , utilized for calculation of the plastic moment capacity,

M_p , of the HSS members (Equation 4.2) is the average yield strength from coupon specimens taken from the flats of the separate HSS members.

$$\lambda_{md} = 0.64 \sqrt{\frac{E}{F_y}} \quad \text{Equation 4.1}$$

$$M_p = F_y Z_x \quad \text{Equation 4.2}$$

Table 4.5 Measured Section Properties of HSS Members

Member Section	b/t	d/t	F_y (ksi)	Z_x (in ³)	M_p (k-in)
HSS 12×8×3/8	17.2	27.2	58.3	55.6	3240
HSS 10×10×5/8	12.8	13.2	61.5	73.1	4500

Both collar connections consist of two collars that are slipped over the column member and a beam endplate allowing the beam to be connected to the column. The collars and endplate are made of ASTM A36 steel. The height of the collars is 6 in. and the thickness is 1/2 in. To prevent significant column face plastification, column sidewall crippling and undesired brittle weld failure, a 1 in. thick endplate is welded to the beam. A groove weld filled flush is placed along the length of the endplate between column corner and endplate to carry the shear in the connection. The endplate extends 1 in. beyond the collar and is the same width as the column. Selection of the dimension of the collars and endplate are based on the finite element study results and design approach described in Chapter 3. One collar connection is designed without stiffeners using a prequalified CJP groove weld, as specified in AWS D1.1 (2010), to connect the HSS beam to the endplate. To further control the load transfer mechanism and explore the suitability of fillet welds for the beam endplate connection, stiffeners are added to the second connection between the beam and beam endplate and fillet welds are adopted to weld the beam to the endplate. The thickness of the triangular stiffener plates is 3/4 in. and the length of the side of the triangle is 6 in. The stiffeners are made of ASTM A36 steel. The vertical distance from beam flange and collar in the unstiffened connection is 3 in. and from the stiffener's toe to the collar in the stiffened connection is 1 in. Due to presence of stiffeners, the lengths of the endplates are 32 in. and 40 in. for the connection without stiffeners and with stiffeners, respectively. The transverse welds between the column and collars and endplate and column face are 3/8 in. and 5/8 in. fillet welds, respectively. The welds are designed to prevent weld failure

prior to the development of the beam's plastic moment capacity. Details of the two HSS based collar connections are provided in Figure 4.9 and Figure 4.10.

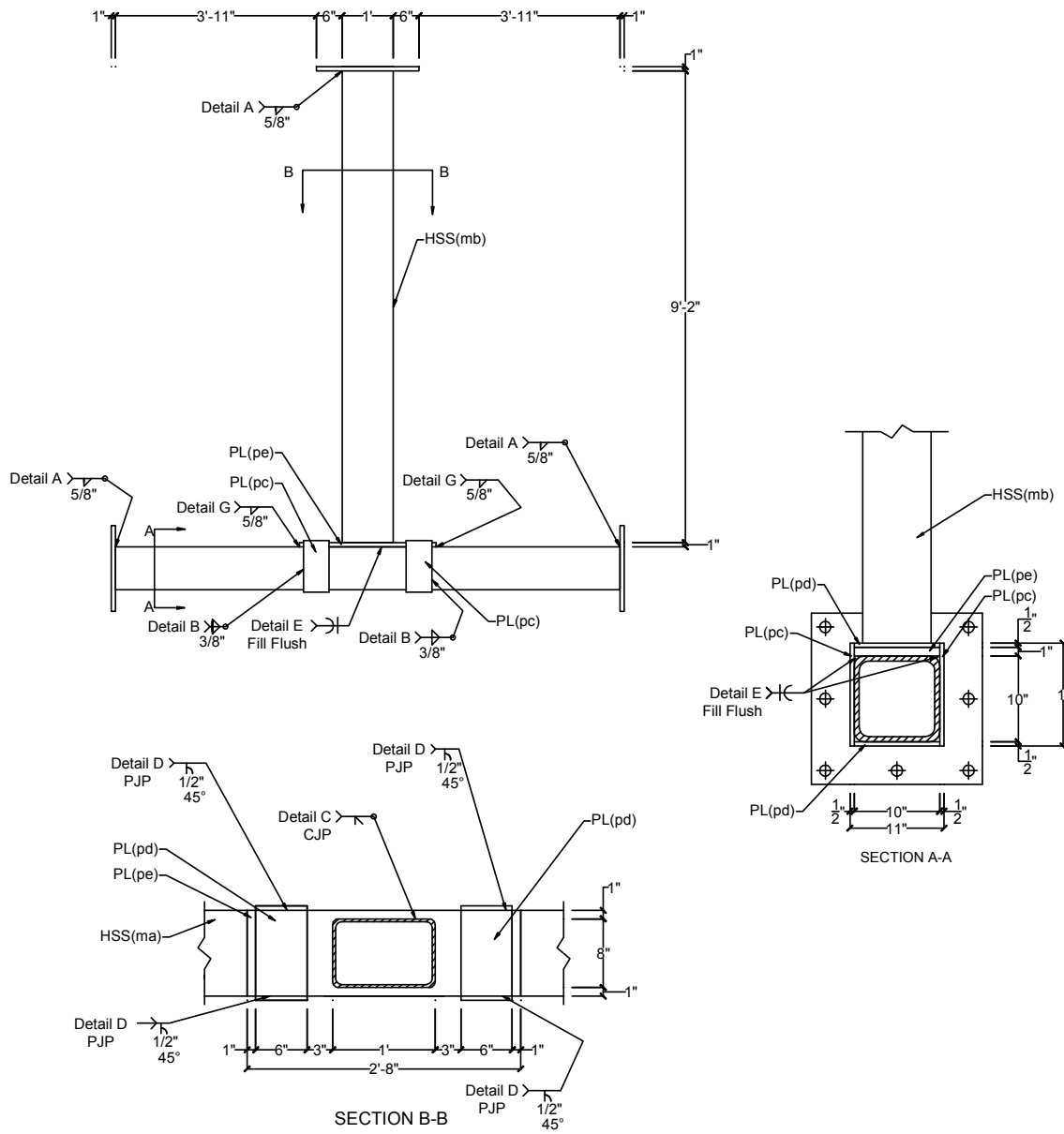


Figure 4.9 Collar Connection without Stiffeners (units in inch)

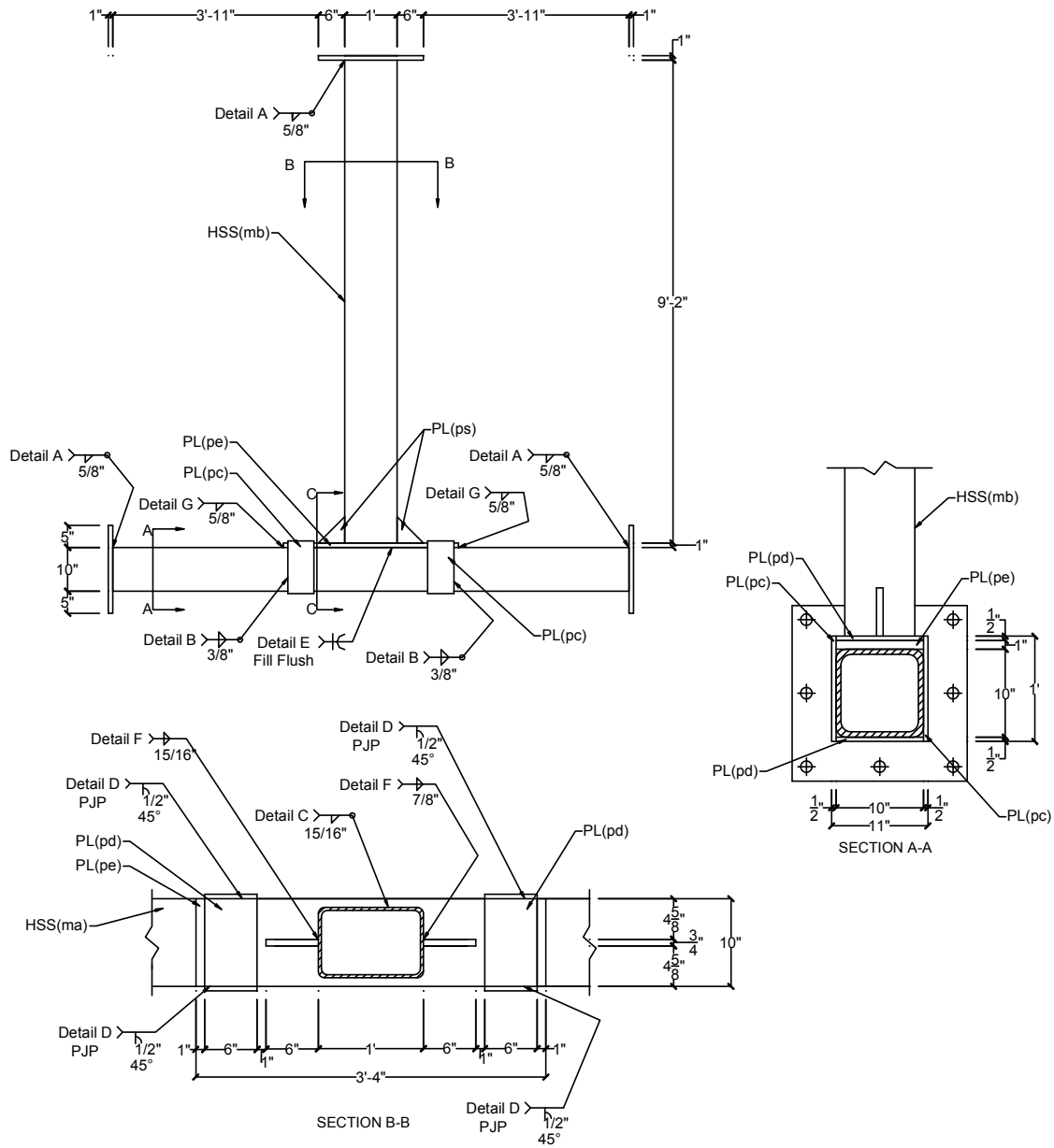


Figure 4.10 Collar Connection with Stiffeners (units in inch)

4.3.2.3 Instrumentation

The two connections are outfitted with Optotrak infrared optical tracking markers, strain gages, a clinometer, linear variable differential transducers (LVDT) and potentiometers. The layout of the instrumentation follows recommendations from the SAC studies considering the performance of pre- and post-Northridge Earthquake connections (SAC, 1997).

The layouts of the tracking markers for the two connections are illustrated in Figure 4.11 and 4.12. A total of 102 and 122 markers are placed on the two connections to map the deformations in the beam, column, column panel zone, beam endplate and collars.

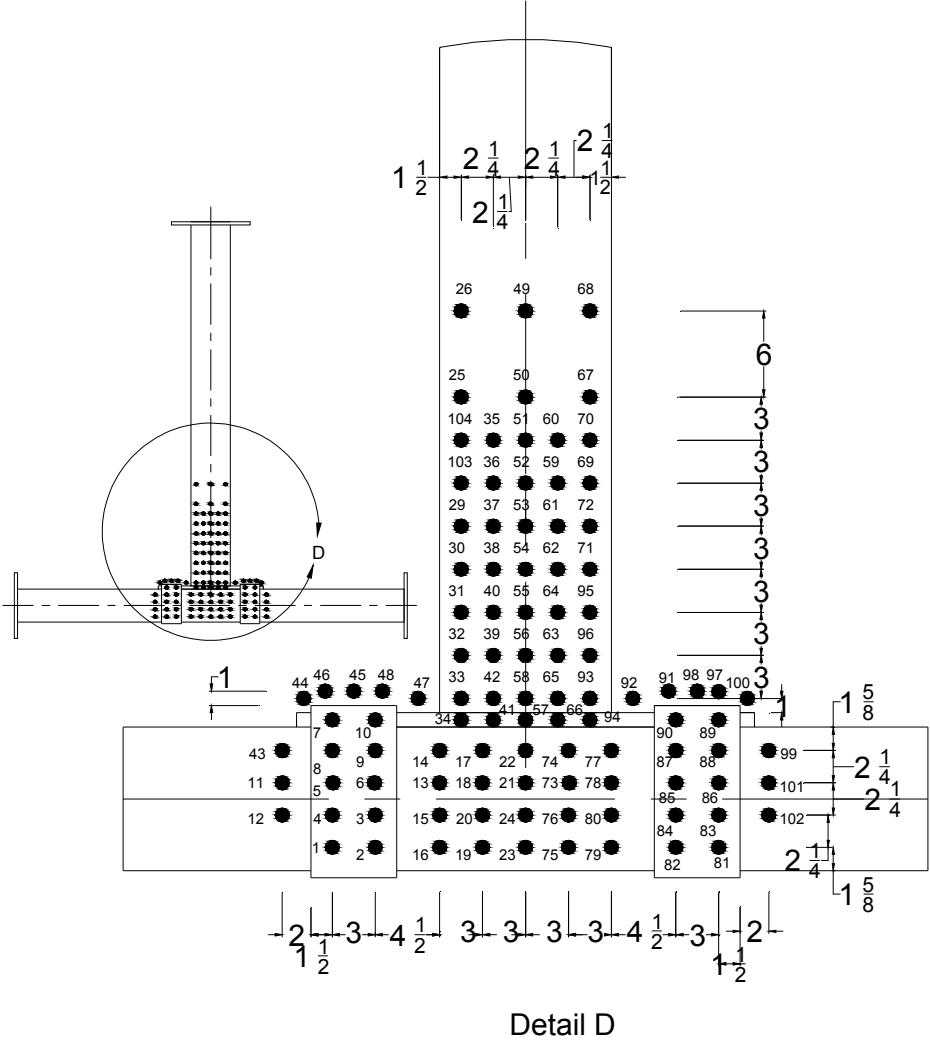


Figure 4.11 Optotrak Numbering Scheme for Collar Connection without Stiffeners (units in inch)

monitor the formation of a plastic hinge in the beam. Two strain gages (cf1-cf2 and ew1-ew2) are used on the column face and beam endplate, respectively, with one strain gage on the centerline of the column and the other one 2.5 in. off the centerline towards the edge of the column face or beam endplate. Seven strain gages (cw1- cw7) are utilized on the west side of the collar to understand the load transfer mechanism. Strain gages cw1-cw3 are on the collar plate connected to the column face, while cw4-cw5 are on the collar plate connected to the column sidewall and cw6-cw7 are on the collar plate welded to the back of the column. Strain gages cw2, cw4-cw5 and cw7 are perpendicular to the column centerline while the other strain gages are parallel to the column centerline. By arranging the strain gages in two perpendicular directions, the flow of forces through collars can be clearly studied. Four (cb1-cb4) and five (cb1-cb5) strain gages are utilized on the back of the column to determine if it plays a role in transferring forces through the connection. In the panel zone, four strain gage rosettes (pz1-pz4) are placed with the 1-1 direction along the column centerline, the 2-2 direction perpendicular to the column centerline, the 3-3 direction 45° to the 1-1 and 2-2 directions in order to measure shear within this region.

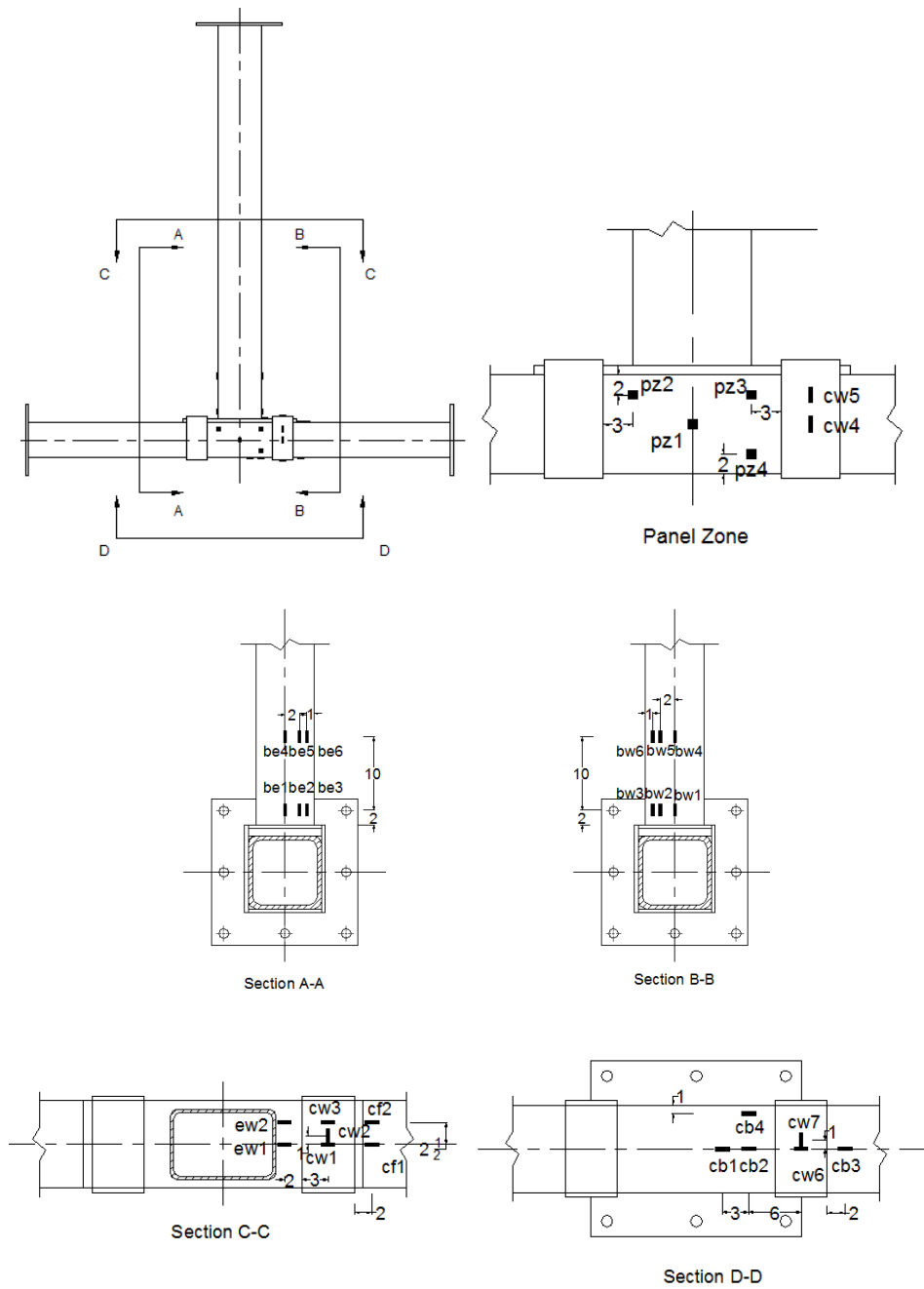


Figure 4.13 Strain Gage Locations for the Connection without Stiffeners (units in inch)

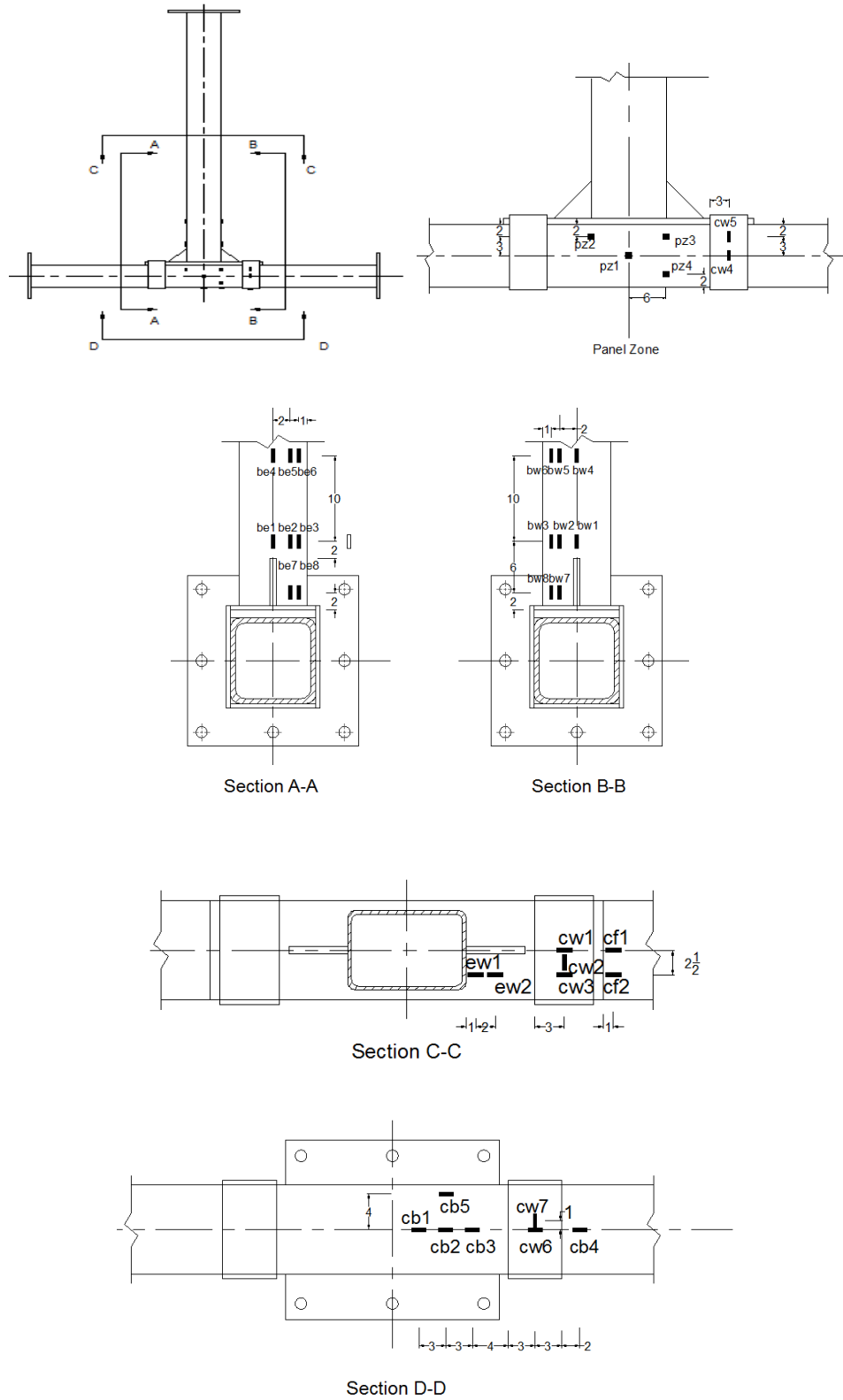


Figure 4.14 Strain Gage Locations for the Connection with Stiffeners (units in inch)

A clinometer is installed on the actuator to measure any change in its angle of inclining from horizontal. Eight LVDTs and two potentiometers are utilized as a secondary system to measure the displacement at different locations during the tests. The specific locations of the LVDTs and potentiometers are shown in the Figure 4.15 and Figure 4.16. LVDT WPS is used to measure any rigid body slip between the pin connection and spreader beam. LVDT TPS is used to measure the relative displacement between the beam fixture connected to the actuator and beam end plate. LVDT PZ0 and PZ1 provide a secondary measurement of panel zone rotation. LVDT BEP and BWP provide the rotation information for the beam in the plastic hinge region. Finally, LVDT CEP and CWP measure column rotations. Potentiometers EP and WP are utilized to measure the displacement

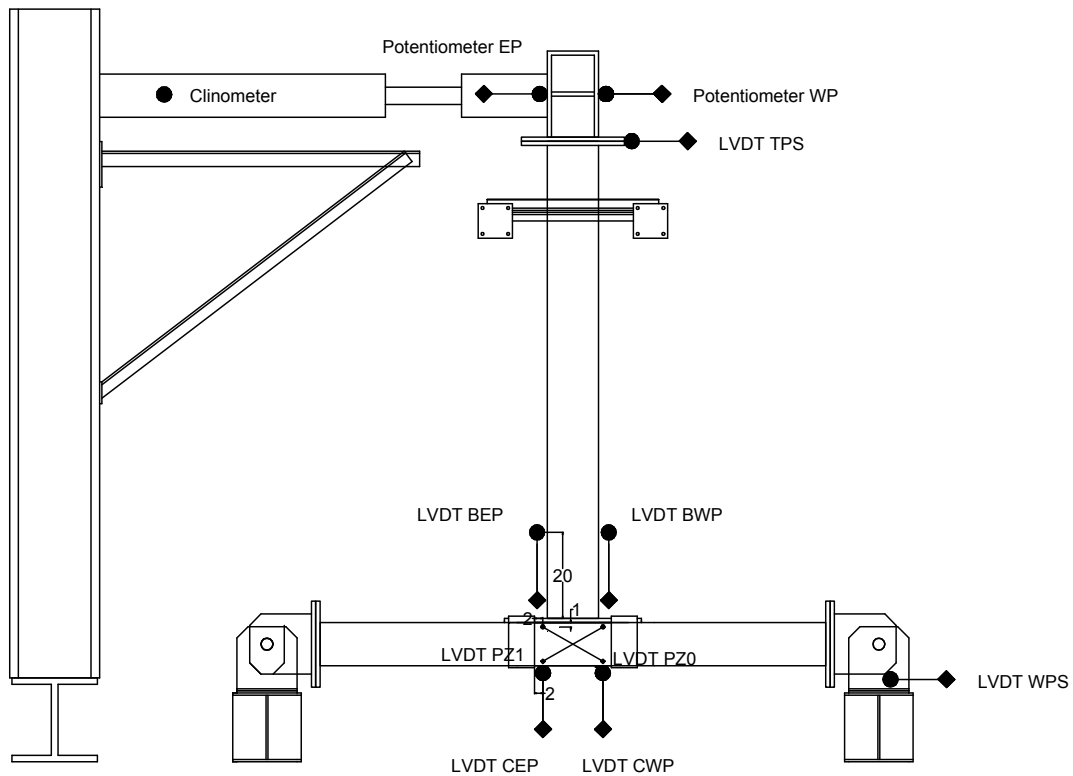


Figure 4.15 Layout of Instrumentation Primarily Used for Secondary Measurements for the Connection without Stiffeners (units in inch)

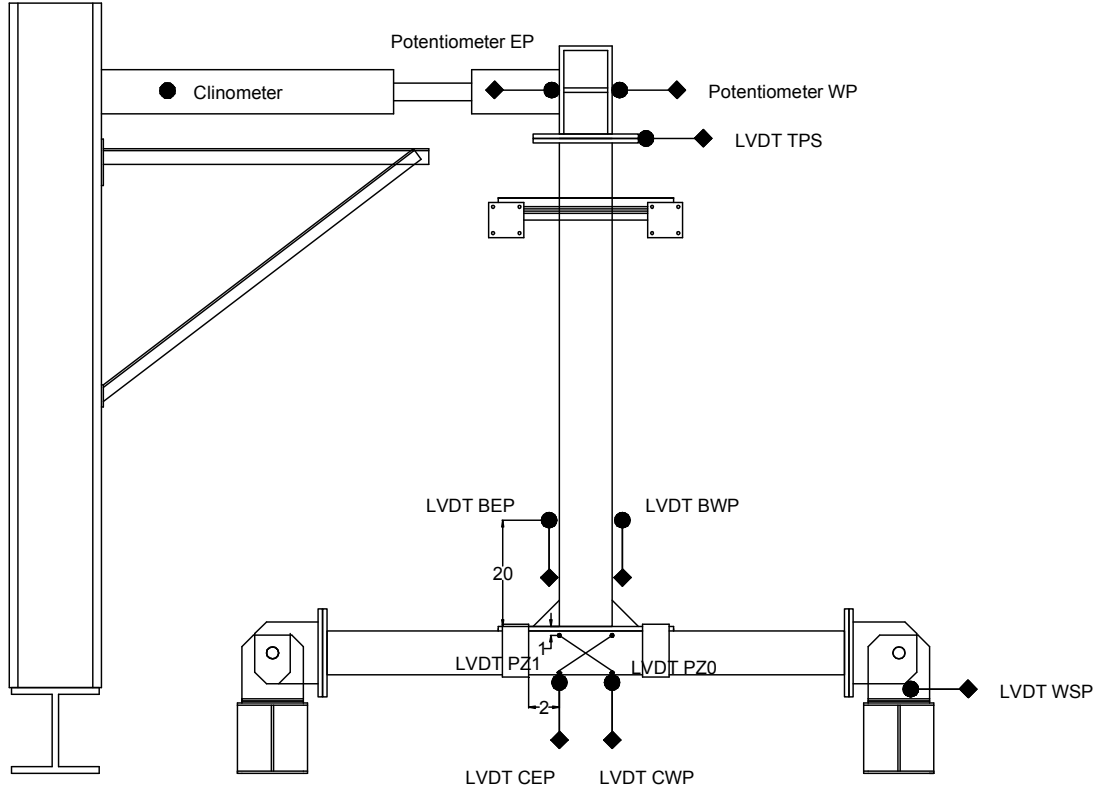


Figure 4.16 Layout of Instrumentation Primarily Used for Secondary Measurements for the Connection with Stiffeners (units in inch)

4.3.3 Experimental Results

The clinometer installed on the actuator indicates that the actuator's maximum inclined angle is less than 2 degree which is negligible and will be ignored in subsequent calculations. The absolute displacement of the beam tip is calculated utilizing the actuator displacement by removing any displacement measured by LVDT WPS which stems from undesired rigid body displacement of the whole connection. The plastic rotation calculations are based on Optotrak markers rather than displacements measured with the LVDTs to better capture individual connection components' response.

4.3.3.1 Hysteretic Behavior

The hysteresis behavior of the collar beam–column connections is evaluated in terms of moment capacity and moment degradation under large cyclic loads. Both collar connections are cycled up to the 0.08 rad. cycles with 40 full cycles according to the prescribed loading protocol (Figure

4.8). The connection moment is calculated using the load from the actuator multiplied by the length of the beam plus the thickness of endplate and half the depth of the column as seen in Equation 4.3.

$$M_{conn} = L \times (l_b + t_e + 0.5d_c) \quad \text{Equation 4.3}$$

Where M_{conn} is the connection moment, L is the load measured from actuator, l_b is the length of the beam, t_e is the thickness of the endplate, d_c is the height of the column. The interstory drift or rotation of the connection is calculated from the displacement of the actuator divided by the length of the beam plus the thickness of endplate and half the depth of column.

The measured elastic stiffness of the unstiffened collar connection is 9.1 k/in. compared to the theoretical stiffness 12.7 k/in. which indicates the connection is relatively flexible. The connection moment is also normalized by the measured plastic moment capacity of the beam based the member dimension measurements and material properties previously presented. The normalized moment clearly shows if the connection is able to achieve the plastic moment of the beam as shown in Figure 4.17. The maximum normalized moment is 1.23 indicating the connection is able to develop the plastic moment capacity of the beam and suggests its feasibility in seismic applications from the perspective of strength. The connection moment versus story drift is also plotted in the Figure 4.18. The connection reaches a maximum moment of 3990 k-in. at the 0.05 rad. cycle and local buckling of the beam flange is not observed until the first 0.06 rad. cycle as shown in Figure 4.19. Fracture initiates at the corner of the HSS beam during the second 0.07 rad. cycle as a result of onset of local buckling in the plastic hinge region. However, this rotation is above that expected during a typical earthquake. In the subsequent cycles with increasing rotation level, fracture propagates slowly away from the corners toward the center of the webs and flanges. After reaching its maximum moment capacity, the maximum moment capacity of each subsequent cycle decreases by 12% and 28% for the second 0.06 rad. and first 0.07 rad. cycles. As a result of beam fracture, the moment capacity decreased rapidly during the following cycles. In the first cycle to 0.08 rad., the maximum moment decreases to 2500 k-in. which corresponds to a 49% decrease in moment capacity from the maximum overall moment. In the final cycle, which is the fourth cycle to 0.08 rad., the maximum moment is only 1370 k-in. or a 70% moment degradation compared to the maximum moment at 0.05 rad. The extent of the fracture at the end of the test is shown in Figure 4.20.

The measured elastic stiffness of the stiffened collar connection is 9.7 k/in. which is stiffer than the unstiffened connection, but still fairly flexible compared to theoretical stiffness of 12.7 k/in. The maximum normalized moment is 1.25 suggesting this configuration can also achieve the plastic moment capacity of the beam as shown in Figure 4.21. The connection moment versus rotation relationship is plotted in Figure 4.22. The connection reaches its maximum moment of 4060 k-in. at the 0.05 rad. cycle and local buckling of the beam near the top of the stiffeners is not observed until the second cycle at 0.05 rad. seen in Figure 4.23. In the first cycle to 0.06 rad., bulging is observed in the beam web. Initiation of fracture at the beam corner does not start until the first 0.08 rad. cycle owing to the large cyclic inelastic deformations resulting from local buckling and less ductile material in the HSS beam corner. The fracture quickly propagates in the subsequent cycles and maximum moment starts to decrease as a result of fracture opening. The moment capacity of the connection drops quickly to 2300 k-in. at the first cycle to 0.08 rad. which is a 40% decrease compared to the maximum overall moment capacity of the connection. In the final cycle, the maximum moment is 1710 k-in. which represents a 58% moment degradation compared to the maximum moment reached. The extent of the fracture at the end of testing is shown in Figure 4.24.

Both collar connections exhibit similar hysteretic behavior under large cyclic loads with maximum normalized moments around 1.2 at the 0.05 rad. cycle as shown in Figure 4.25. Thus both connections are able to achieve the beam plastic moment capacity and sustain $0.80M_p$ at the 0.04 rad. rotation level satisfying the requirement for SMF. The stiffened connection shows a slightly larger elastic stiffness, 9.7 k/in., compared to 9.1 k/in. for the unstiffened connection and less moment degradation (i.e. 58% compared with 64% in the unstiffened connection during the second 0.06 rad. cycles) after initiation of fracture. The stiffeners are effective in moving the plastic hinge region away from column face.

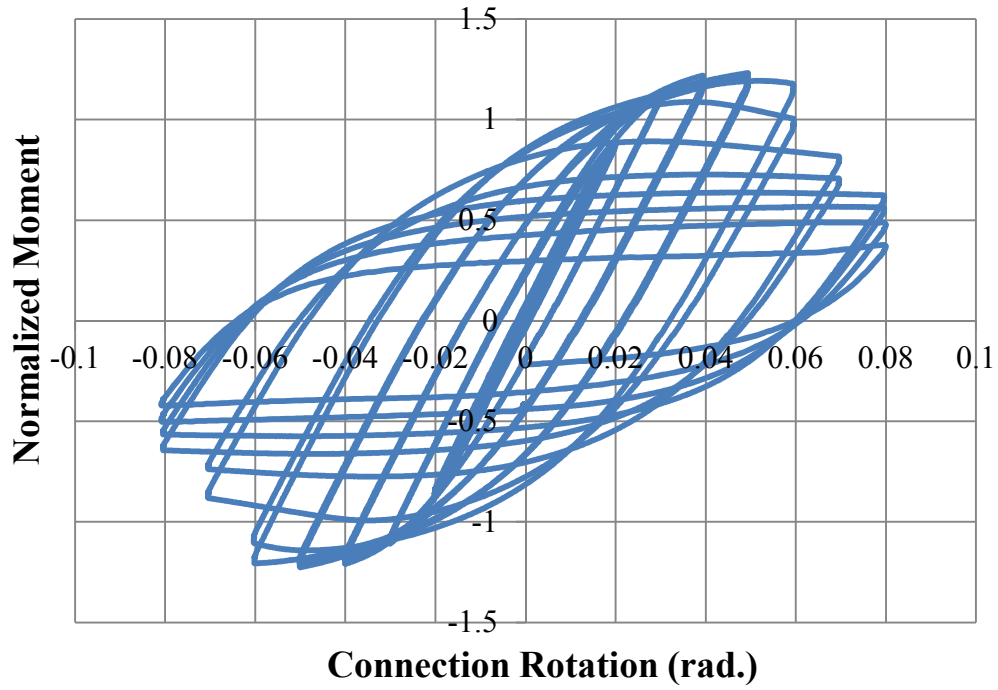


Figure 4.17 Normalized Moment versus Connection Rotation for the Collar Connection without Stiffeners

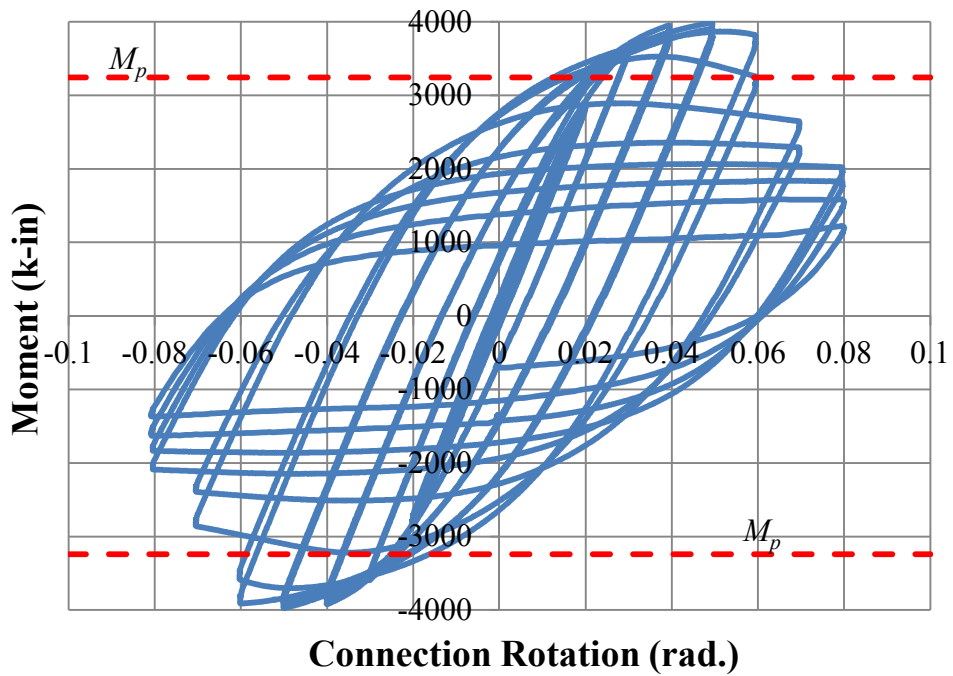


Figure 4.18 Moment versus Connection Rotation for the Collar Connection without Stiffeners



Figure 4.19 Local Buckling of Collar Connection without Stiffeners at the First Cycle of 0.06 rad. Rotation Cycle



Figure 4.20 Fracture Propagation at Beam Corners of Collar Connection without Stiffeners at the End of the 0.08 rad. Rotation Cycle

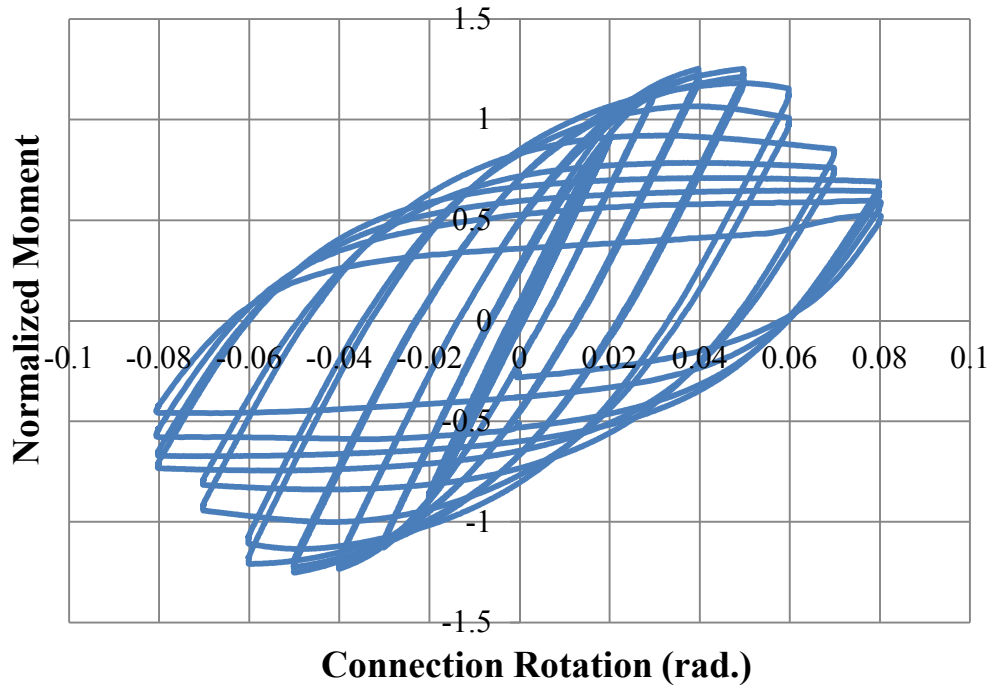


Figure 4.21 Normalized Moment versus Connection Rotation for the Collar Connection with Stiffeners

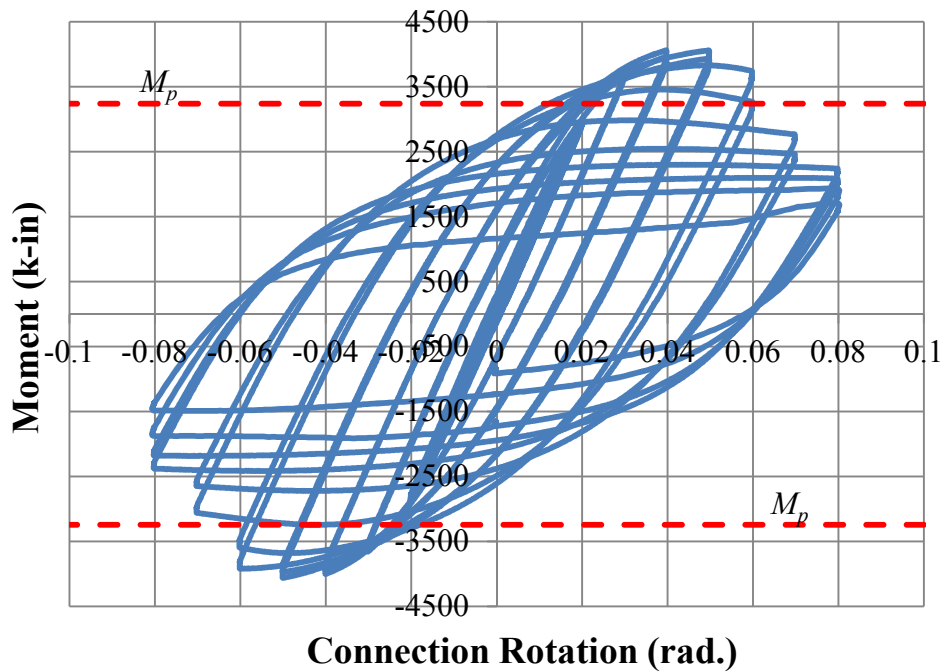


Figure 4.22 Moment versus Connection Rotation for the Collar Connection with Stiffeners

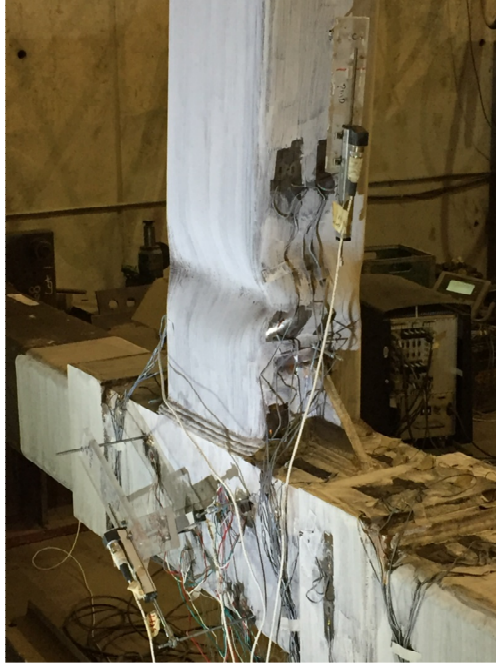


Figure 4.23 Local Buckling of Collar Connection with Stiffeners at the First 0.06 rad. Cycle



Figure 4.24 Fracture Propagation at Beam Corners of Collar Connection with Stiffeners at the End of the 0.08 rad. Rotation Cycle

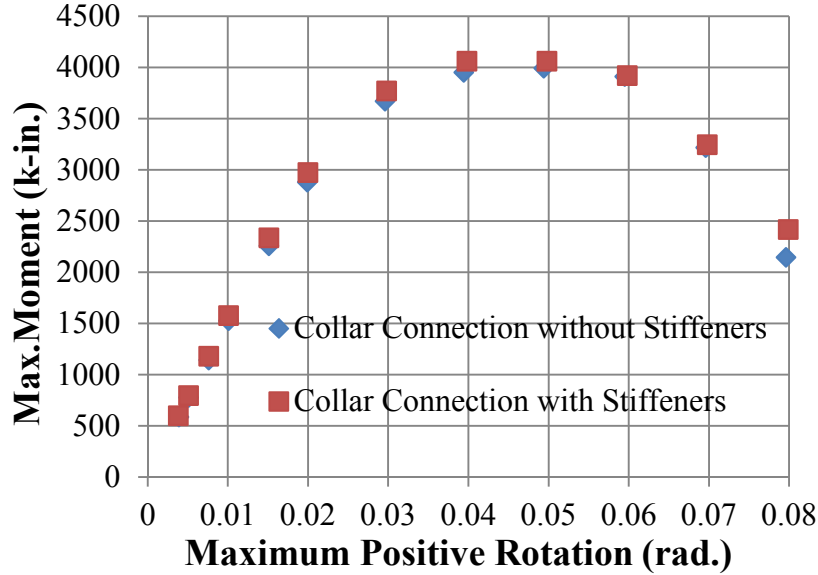


Figure 4.25 Backbone Curves for the Collar Connection with and without Stiffeners

4.3.4 Plastic Rotation

The extent of plastic rotation in each connection component has been analyzed to better understand the distribution of inelasticity within the connections under large cyclic loads. The collars are fully welded to the column, thus plastic rotation of the collars is essentially the same as the HSS column. The potential sources of inelastic deformation include the beam, beam column panel zone, column, and endplate as shown in Equation 4.4.

$$\theta_{conn,pl} = \theta_{beam,pl}^{CL} + \theta_{pz,pl} + \theta_{col,pl} + \theta_{ep,pl}^{CL} \quad \text{Equation 4.4}$$

Where $\theta_{beam,pl}^{CL}$ is the beam plastic rotation about the column centerline, $\theta_{pz,pl}$ is the panel zone plastic rotation, $\theta_{col,pl}$ is the column plastic rotation, and $\theta_{ep,pl}^{CL}$ is the endplate plastic rotation about the column centerline.

The plastic rotation of each component is computed utilizing the Optotrak displacement markers. Connection moment versus connection plastic rotation for both connections are plotted in the Figure 4.26. The plastic rotation calculations are only valid prior to fracture initiation since once fracture occurs deformations become large and concentrated in the fracture region.

In the collar connection without stiffeners, the maximum moment occurs at a plastic rotation of 0.024 rad. accounting for approximately 49% of overall connection rotation. The fracture at the beam corners initiates at the second 0.07 rad. cycle at a plastic rotation of 0.052 rad., which is approximately 74% of the 0.07 rad. connection rotation. In the collar connection with stiffeners, at the maximum moment, the plastic rotation is approximately 0.023 rad. resulting in 46% of the overall connection rotation. The fracture at the beam corners initiates at the second 0.08 rad. cycle with a plastic rotation of 0.065 rad., which is approximately 81% of the 0.08 rad. connection rotation. Given the ability to reach large plastic deformation levels, it is clear that connections undergo stable ductile behavior until fracture initiates which further suggest their applicability to seismic moment frame systems.

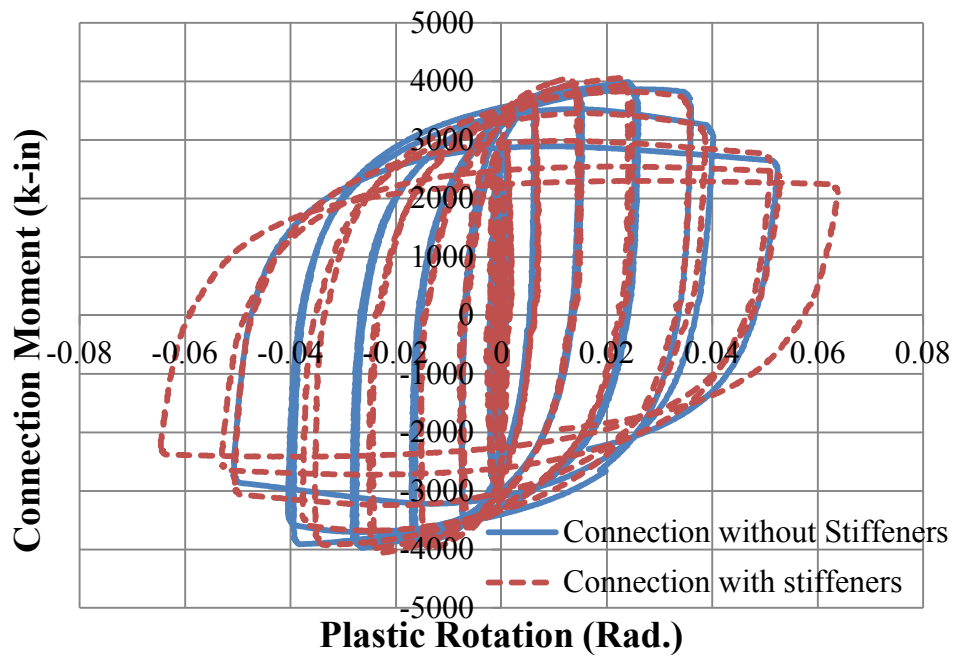


Figure 4.26 Connection Moment versus Plastic Rotation of the Collar Connections

4.3.4.1 Beam Plastic Rotation

Beam rotation based on the optical tracking system is calculated by subtracting out the beam rigid rotation measured at the beam base adjacent to the endplate from the beam overall rotation. The numbering schemes for the optical tracking markers for the collar connection without and with stiffeners are shown in Figure 4.11 and Figure 4.12.

For the unstiffened collar connection, the beam overall rotation is based on Equation 4.5 by using the row of markers furthest from the column face and the second row closet to the column face since the beam is rotating about the beam base. Beam rigid rotation is calculated by Equation 4.6 which should be eliminated to obtain the absolute beam rotation. The displacement of the markers at a given time is calculated by subtracting out the initial coordinates measured at the beginning of the test from the coordinates at that instant which is depicted as the symbol starting with d in the following equations.

$$\theta_{beam,overall} = \frac{d49_x - d56_x}{49_y - 56_y} \quad \text{Equation 4.5}$$

$$\theta_{beam,rigid} = \frac{d33_y - d93_y}{33_x - 93_x} \quad \text{Equation 4.6}$$

where $d33_y$ and $d93_y$ correspond to the markers displacement in the vertical direction, $d49_x$, $d56_x$ and $d58_x$ correspond to the markers' displacement in the horizontal direction, 33_x and 93_x correspond to the markers' coordinates throughout the loading history in the horizontal direction (the difference between 33_x and 93_x represents the horizontal distance between marker 33 and 93); and 49_y and 56_y correspond to the markers' coordinates throughout the loading history in the vertical directions (the difference between 49_y and 56_y represents the vertical distance between the marker 49 and 56).

For the connection with stiffeners, the beam overall rotation is based on Equation 4.7 since throughout the loading protocol, the beam rotates about an axis that aligns with the top of the stiffeners. As a result, the markers closest to the top of the stiffeners along the beam are used to calculate the beam rotation. The rigid rotation is calculated in a similar manner to the unstiffened collar connection based on Equation 4.8.

$$\theta_{beam,overall} = \frac{d70_x - d78_x}{70_y - 78_y} \quad \text{Equation 4.7}$$

$$\theta_{beam,rigid} = \frac{d40_y - d16_y}{40_x - 16_x} \quad \text{Equation 4.8}$$

where $d40_y$ and $d16_y$ correspond to the markers' displacement in the vertical direction, $d70_x$ and $d78_x$ correspond to the markers' displacement in the horizontal direction, 40_x , 16_x , 70_y and 78_y correspond to the markers coordinates in the horizontal and the vertical directions, respectively.

The two sets of equations above can then be used to calculate the actual beam rotation using Equation 4.9.

$$\theta_{beam} = \theta_{beam,overall} - \theta_{beam,rigid} \quad \text{Equation 4.9}$$

Assuming all plasticity occurred within the instrumented area, beam plastic rotation is calculated based on Equation 4.10,

$$\theta_{beam,pl} = \theta_{beam} - \frac{M_{conn}}{K_{beam}} \quad \text{Equation 4.10}$$

where M_{conn} is the connection moment, K_{beam} is the beam stiffness measured from the beam moment-rotation hysteresis during the first 0.01 rad. drift level. The ratio of the connection moment to the stiffness of the beam is the elastic rotation which is subtracted out from the beam rotation to calculate the beam plastic rotation.

The beam rotation is converted to beam plastic rotation about the column centerline using Equation 4.11.

$$\theta_{beam,pl}^{CL} = \theta_{beam,pl} \left(\frac{l_b}{l_b + t_e + 0.5d_c} \right) \quad \text{Equation 4.11}$$

where l_b is the length of the HSS beam, d_c is the depth of the column, and t_e is the thickness of the endplate.

For the collar connection without stiffeners, plastic rotation of the beam is only 0.023 rad. when the maximum moment is reached. During the last cycle prior to fracture, the beam reaches its maximum plastic rotation of 0.052 rad. representing almost 100% of the total plastic rotation in the connection as shown in Figure 4.27. For the collar connection with stiffeners, plastic rotation in the beam is only 0.021 rad. at the maximum moment. A maximum beam plastic rotation of 0.059 rad. is reached prior to fracture resulting in almost 100% plastic rotation concentrated in the beam as seen in Figure 4.28. The vast majority of plastic rotation is concentrated in the beam for both collar connections which is desirable based on current seismic design requirements (AISC, 2010a) that ensure a strong column-weak beam mechanism to avoid soft story collapse. This result indicates both collar connection configurations are feasible for seismic applications in

terms of their ability to have the majority of the inelastic behavior occur in the beam. Both connections show excellent behavior in terms of largely limiting inelasticity to the HSS beam.

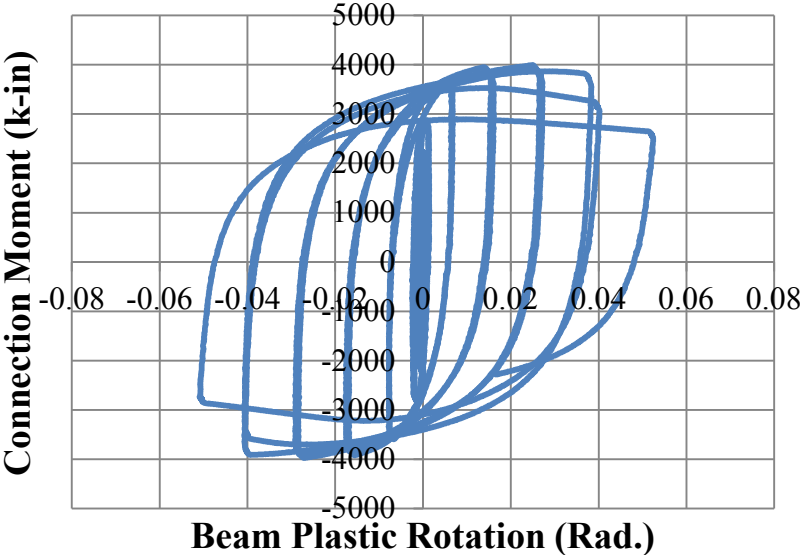


Figure 4.27 Experimental Moment-Plastic Beam Rotation Hysteresis for the Collar Connection without Stiffeners

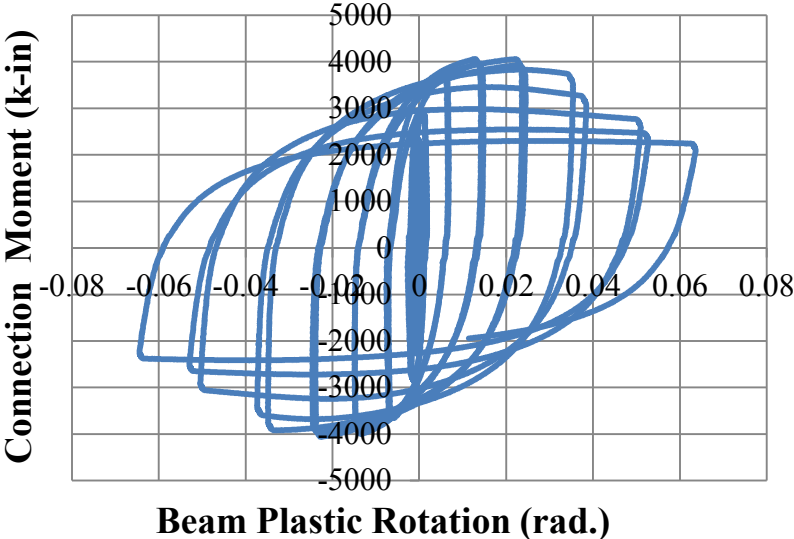


Figure 4.28 Experimental Moment-Plastic Beam Rotation Hysteresis for the Collar Connection with Stiffeners

4.3.4.2 Panel Zone Plastic Rotation

During loading, the panel zone experiences shear forces due to the forces transferred from the beam to the column. Shear deformation in the panel zone is also an important parameter to evaluate seismic performance of the connection since excessive deformation may affect the connection's ductility and lead to large lateral deformation in the moment frame. However, a balanced panel zone design allows for some participation of the panel zone in dissipating energy through inelastic deformation and shear yielding thus alleviating some of the demands on the beam plastic hinge region provided beam plastic hinging remains the primary mechanism.

Both connections show a larger shear capacity than the shear force demands placed on the panel zone. The panel zone shear force demands are calculated based on Equation 4.12 where M_p is calculated as the applied force multiplied by the beam length. The measured shear demands for the unstiffened and stiffened connections are 303 kips and 308 kips, respectively. The actual moment arm utilized in calculating M_p in the stiffened connection is slightly smaller than the beam length which leads to a slightly larger M_p and larger demands on the panel zone.

$$V_{u,pz} = \frac{M_p}{0.95d_b} \quad \text{Equation 4.12}$$

The panel zone capacity can be calculated based on Equation 4.13 which is derived based on AISC 360-10 (2010b) Equation J10-9.

$$V_{n,pz} = 2(0.6\Phi F_y d_c t_c) \quad \text{Equation 4.13}$$

where $V_{n,pz}$ is the panel zone shear capacity, F_y is the measured material yield strength of the column flats, t_c is measured thickness of the column and Φ is the resistance factor, 0.90 for this case. For both connections, the shear capacity of the panel zone is 386 kips which indicates that the panel zone is capable of elastically resisting the shear forces transferred from the beam to the column and failure of the panel zone is unlikely to occur.

The panel zone rotation is computed utilizing the four Optotrak markers at the corners of the panel zone. The location of those markers, as indicated in Figure 4.29, is utilized to capture the change in geometry using the law of cosines. The rotation angles calculated at the back of the

connection, γ_1 , and at the front of the connection near the beam, γ_2 , is averaged allowing plastic rotation to be calculated. The calculations are provided in Equation 4.14 to Equation 4.17.

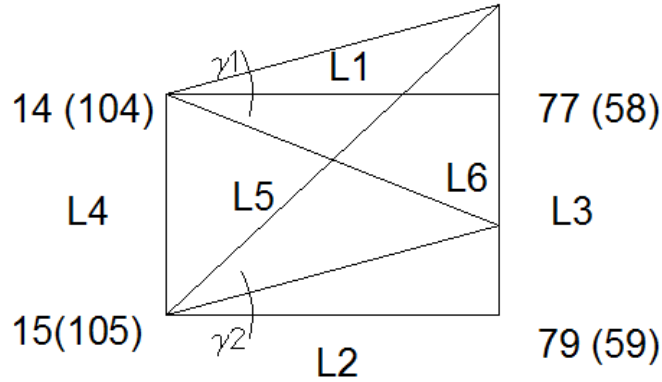


Figure 4.29 Panel Zone Distortion and Parameters

$$\gamma_1 = \frac{\pi}{2} - \arccos\left(\frac{L_1^2 + L_4^2 - L_5^2}{2L_1L_4}\right) \quad \text{Equation 4.14}$$

$$\gamma_2 = -\frac{\pi}{2} + \arccos\left(\frac{L_2^2 + L_4^2 - L_6^2}{2L_2L_4}\right) \quad \text{Equation 4.15}$$

$$\theta_{pz} = \frac{\gamma_1 + \gamma_2}{2} \quad \text{Equation 4.16}$$

$$\theta_{pz,pl} = \theta_{pz} - \frac{M_{conn}}{K_{pz}} \quad \text{Equation 4.17}$$

where K_{pz} is the elastic stiffness of the panel zone measured during the first 0.01 rad. cycle.

Figure 4.30 and Figure 4.31 provide plots of connection moment versus panel zone plastic rotation. The maximum plastic rotation of the panel zone in the connection without stiffeners is 8×10^{-4} rad. prior to fracture initiation. At the maximum moment, the plastic rotation in the panel zone is only 5×10^{-4} rad. which indicates that the panel zone region has little inelastic deformation and almost remains elastic. In the collar connection with stiffeners, the plastic rotation in the panel zone is also insignificant with a maximum value of 7×10^{-4} rad. prior to fracture initiation. At the maximum moment, the plastic rotation in the panel zone is 4×10^{-4} rad. which is inconsequential compared to that of the beam. Both connections exhibit negligible rotation associated with plastic shear deformation and no local buckling or failure of the panel zone indicating a strong panel zone connection behavior. The collar connection without stiffeners

shows slightly larger plastic rotation in the panel zone suggesting that the unstiffened connection is more effective in engaging the panel zone in the plastic deformation to provide some of the inelastic behavior. In general, a more balanced panel zone design may be more optimal in the future.

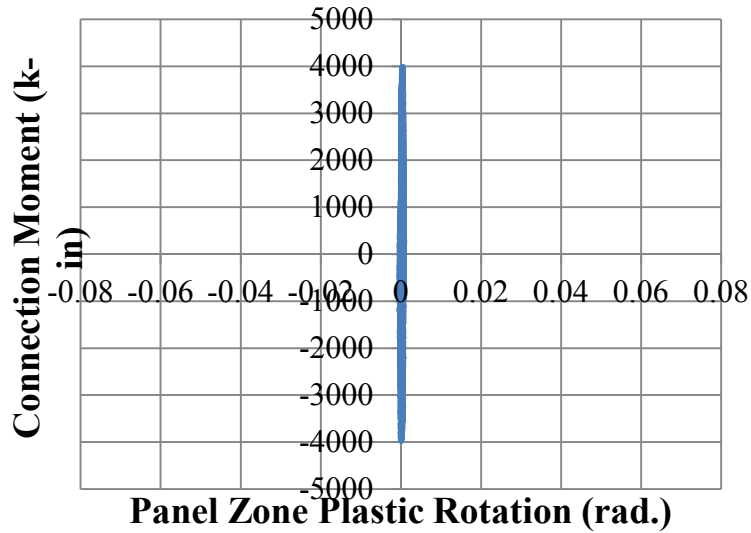


Figure 4.30 Experimental Moment-Plastic Panel Zone Rotation Hysteresis for the Collar Connection without Stiffeners

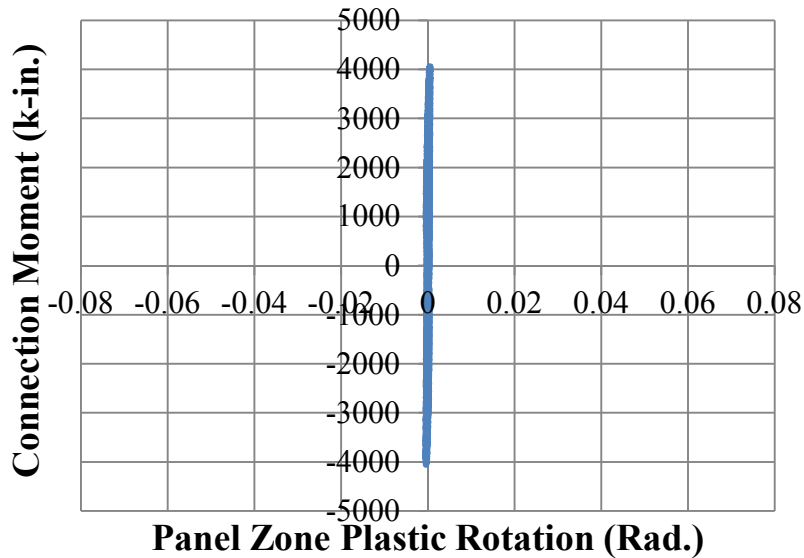


Figure 4.31 Experimental Moment-Plastic Panel Zone Rotation Hysteresis for the Collar Connection with Stiffeners

4.3.4.3 Column Rotation

To prevent the formation of a soft story and collapse during seismic loading, analysis of the plastic rotation of the column is necessary to avoid excessive deformation concentrated in the column.

The column rotation is measured based on four Optotrak markers attached to the column. Rotation is calculated twice and then averaged about the column centerline. For the collar connection without stiffeners, Equation 4.18, Equation 4.19 and Equation 4.22 are utilized based on its markers numbering scheme, while Equation 4.20 to Equation 4.22 are used for the collar connection with stiffeners.

$$\theta_{col,1} = \frac{d78_y - d13_y}{78_x - 13_x} \quad \text{Equation 4.18}$$

$$\theta_{col,2} = \frac{d80_y - d16_y}{80_x - 16_x} \quad \text{Equation 4.19}$$

$$\theta_{col,1} = \frac{d37_y - d133_y}{37_x - 133_x} \quad \text{Equation 4.20}$$

$$\theta_{col,2} = \frac{d39_y - d134_y}{39_x - 134_x} \quad \text{Equation 4.21}$$

where $d78_y$, $d13_y$, $d80_y$ and $d16_y$ correspond to the markers' vertical displacement in the collar connection without stiffeners; 78_x , 13_x , 80_x and 16_x correspond to the marker coordinates in the horizontal direction for the collar connection without stiffeners; $d37_y$, $d133_y$, $d39_y$ and $d134_y$ correspond to the markers' vertical displacement in the collar connection with stiffeners; and 37_x , 133_x , 39_x and 134_x correspond to the marker coordinates in the horizontal direction for the collar connection with stiffeners.

$$\theta_{col} = \frac{\theta_{col,1} + \theta_{col,2}}{2} \quad \text{Equation 4.22}$$

The plastic rotation is then calculated by removing the elastic portion, connection moment, M_{conn} , divided by the stiffness of column based on the column moment hysteresis during the first 0.01 rad. cycle, K_{col} , as shown in Equation 4.23.

$$\theta_{col,pl} = \theta_{col} - \frac{M_{conn}}{K_{col}} \quad \text{Equation 4.23}$$

For the collar connection without stiffeners, the maximum plastic rotation observed in the column is 7×10^{-4} rad. prior to fracture. At the maximum moment, plastic rotation of the column is only 5×10^{-5} rad. indicating that the column has little inelastic deformation under large cyclic loads. For the collar connection with stiffeners, prior to fracture initiation, the maximum plastic rotation measured in the column is only 4×10^{-4} rad. When the maximum moment is reached, the plastic rotation of the column is only 9×10^{-5} rad. Columns in both connections experience little plastic rotation and no local buckling which indicates that the strong column-weak beam requirement is satisfied by these connections.

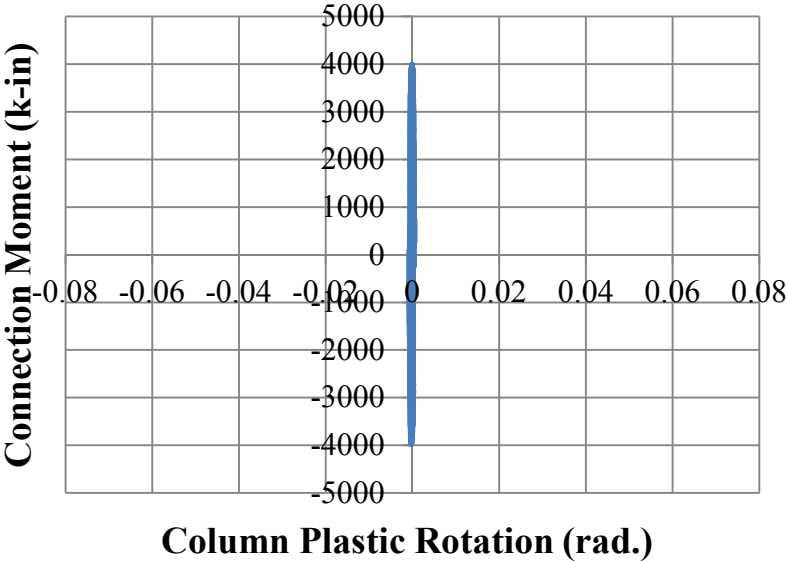


Figure 4.32 Experimental Moment-Plastic Column Rotation Hysteresis for the Collar Connection without Stiffeners

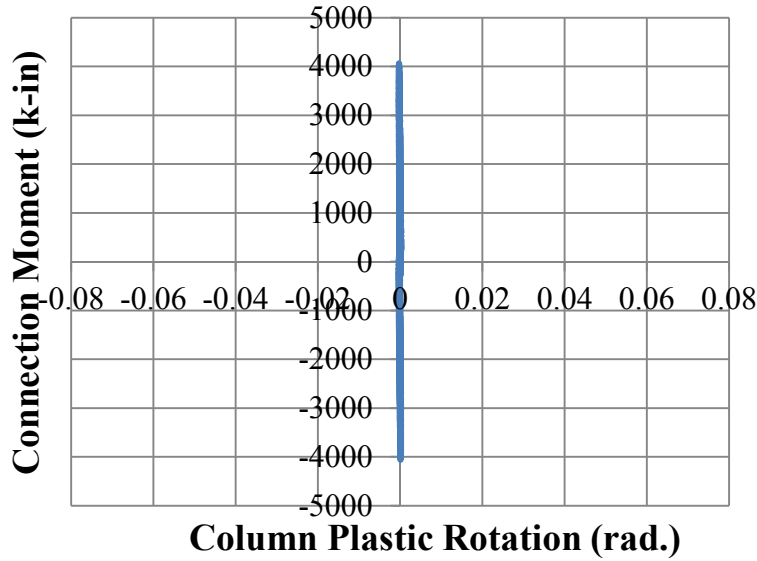


Figure 4.33 Experimental Moment-Plastic Column Rotation Hysteresis for the Collar Connection with Stiffeners

4.3.4.4 Beam Endplate Rotation

The magnitude of the plastic rotation in the beam endplate is an important index to determine the extent of deformation in the endplate and column face. Excessive plastic deformation of the endplate and column face should be avoided to reduce susceptibility of failure of the column. The amount of endplate rotation is calculated by subtracting the column edge rotation from the beam endplate rotation as shown in Equation 4.24 for the unstiffened connection and Equation 4.25 for the stiffened connection.

$$\theta_{ep} = \frac{d34_y - d94_y}{34_x - 94_x} - \frac{d77_y - d14_y}{77_x - 14_x} \quad \text{Equation 4.24}$$

$$\theta_{ep} = \frac{d55_y - d102_y}{55_x - 102_x} - \frac{d58_y - d104_y}{58_x - 104_x} \quad \text{Equation 4.25}$$

where $d34_y$, $d94_y$, $d77_y$ and $d14_y$ correspond to the markers' vertical displacement for the collar connection without stiffeners; 34_x , 94_x , 77_x and 14_x correspond to the markers' coordinates in the horizontal direction for the collar connection without stiffeners; $d55_y$, $d102_y$, $d58_y$ and $d104_y$ correspond to the markers' vertical displacement for the collar connection with stiffeners; and 55_x , 102_x , 58_x and 104_x correspond to the markers' coordinates in the horizontal direction for the collar connection with stiffeners.

$$\theta_{ep,pl} = \theta_{ep} - \frac{M_{conn}}{K_{ep}} \quad \text{Equation 4.26}$$

The plastic rotation then is measured by endplate rotation, θ_{ep} , minus the elastic rotation, which is calculated by the connection moment, M_{conn} , divided by elastic stiffness, K_{ep} , of the endplate during the first 0.01 rad. cycle as seen in Equation 4.26. Plastic rotation should be converted to the rotation about the column centerline by utilizing Equation 4.27.

$$\theta_{ep,pl}^{CL} = \theta_{ep,pl} \left(\frac{l_b}{l_b + t_e + 0.5d_c} \right) \quad \text{Equation 4.27}$$

where $\theta_{ep,pl}^{CL}$ is the beam endplate rotation about the column centerline, $\theta_{ep,pl}$ is the beam endplate rotation, l_b is the length of the beam, t_e is the thickness of the beam endplate, d_c is the depth of the column.

Maximum plastic rotation in the endplate is 2.6×10^{-3} rad. and 3×10^{-4} rad. for the collar connections without and with stiffeners. At the maximum moment, plastic rotation in the endplate is 1.4×10^{-3} rad. and 1×10^{-4} rad. for the unstiffened and stiffened connections, respectively. Plastic rotation of the beam endplate in the collar connection without stiffeners is larger than that of the collar connection with stiffeners indicating stiffeners can effectively restrain inelastic rotation from occurring in the endplate and column face with almost all plastic deformation concentrated in the beam. Both connections show relatively small plastic rotations of the endplate compared to that of the beam as a result of the endplate thickness. This performance of both connections is desirable for seismic application since excessive deformation of the endplate and column face will lead to significantly reduced capacity.

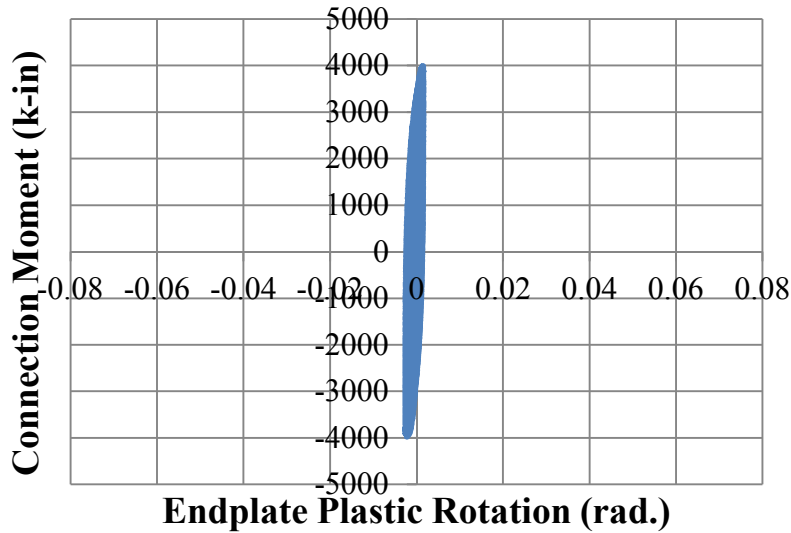


Figure 4.34 Experimental Moment-Plastic Endplate Rotation Hysteresis for the Collar Connection without Stiffeners

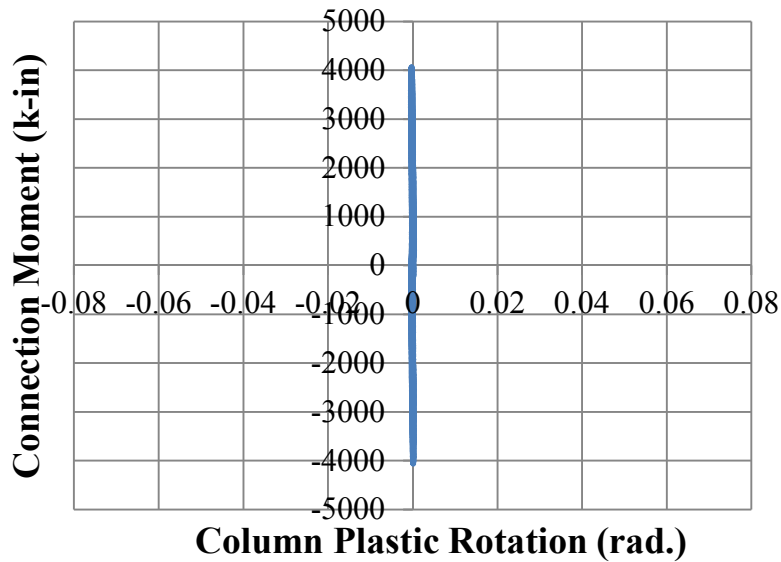


Figure 4.35 Experimental Moment-Plastic Endplate Rotation Hysteresis for the Collar Connection with Stiffeners

4.3.4.5 Sources of Inelastic Rotation

Sources of inelastic rotation with respect to each structural component making up the two connections have been considered to reveal the distribution of inelasticity and a better understanding of the limit states and ultimate behavior of the connections. Plastic rotation of

each component (i.e. beam, column, column panel zone and endplate) at the first cycle of each story drift level prior to failure versus connection rotation is plotted in Figure 4.36 and Figure 4.37 for the unstiffened and stiffened collar connection, respectively. For both collar connections, beam plastic rotation increases rapidly with increasing cyclic rotation and dominates the connection behavior contributing the majority of the total plastic rotation at every drift level. In the collar connection without stiffeners, when the maximum moment is reached at the 0.05 rad. rotation level, beam plastic rotation takes up 87% of the total plastic rotation. The endplate rotation primarily contributes the next largest rotations to the inelastic behavior. The beam member contributes approximately 96% of the overall plastic rotations at the 0.07 rad. story drift immediately prior to fracture. The collar connection with stiffeners shows a similar behavior better limits inelasticity to the beam member. When the maximum moment is achieved at the 0.05 rad. cycle, the beam plastic rotation accounts for 96% of the total plastic rotation while only 3% plastic rotation stems from the panel zone as a secondary source of inelasticity. In the last cycle prior to failure, all the plastic rotation outside the beam equals less than 1%. This analysis shows that both connections exhibit desirable seismic performance with the vast majority of inelastic deformation limited to the beam member. The stiffened collar connection is more efficient in limiting plastic hinging in the beam and preventing inelastic deformation outside the beam region. It also moves the location of the beam plastic hinge further away from the connection.

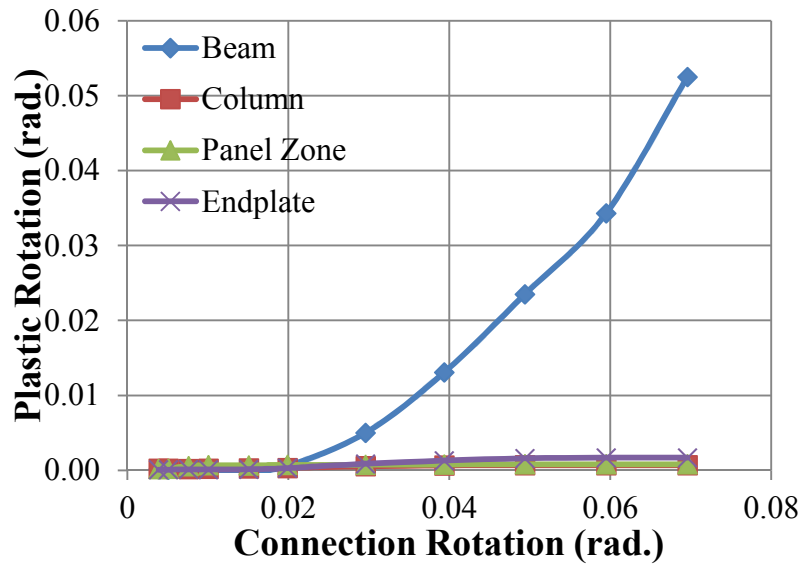


Figure 4.36 Sources of Inelastic Rotation at each First Rotation Cycle for the Collar Connection without Stiffeners

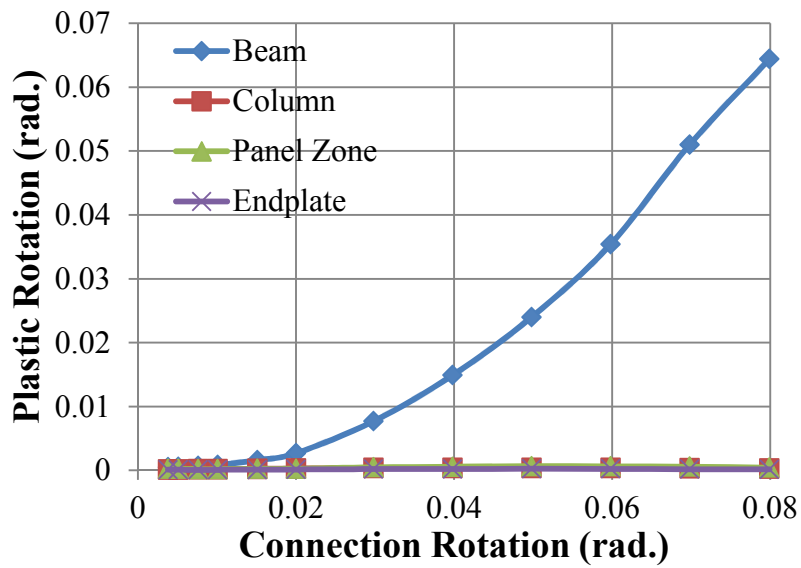


Figure 4.37 Sources of Inelastic Rotation at each First Rotation Cycle for the Collar Connection with Stiffeners

4.3.5 Secant Stiffness Behavior

Secant stiffness of each cycle is measured by using the load at the peak displacement divided by the peak displacement. It provides an additional index to evaluate capacity deterioration due to increasing inelastic deformation and the initiation of fracture in the connections. Secant stiffness at the first cycle of each rotation level for both connections is plotted in Figure 4.38. During the small story drift cycles (i.e. story drift not larger than 0.02 rad.), the two connections' stiffnesses remain constant and almost identical with values of 9.1 k/in. and 9.7 k/in. for the unstiffened and stiffened collar connections since the connections remain elastic. The secant stiffness decreases to 4.0 k/in. at the 0.06 rad. and 4.9 k/in. at 0.05 rad. for unstiffened and stiffened collar connections when local buckling occurs. These values correspond to a 57% and 50% stiffness degradation from initial values. Upon fracture initiation, secant stiffness is 2.5 k/in. and 1.8 k/in. which is approximately a 73% stiffness degradation at 0.07 rad. and a 80% stiffness degradation at 0.08 rad. for the collar connection without and with stiffeners, respectively. The collar connection with stiffeners has a slightly larger secant stiffness throughout the loading protocol which results from the fact that the plastic hinge forms away from the column face. Both connections exhibit similar secant stiffness degradation under increasing cyclic loads.

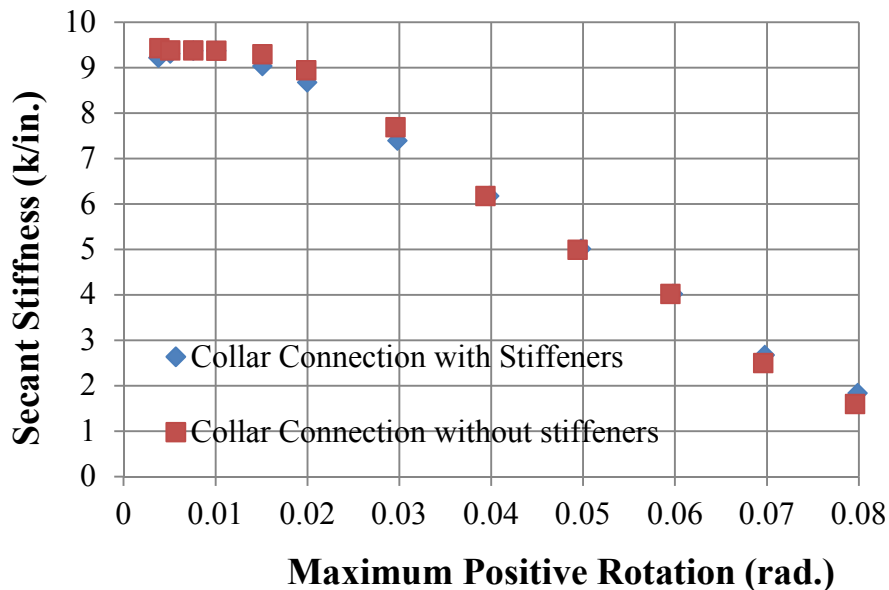


Figure 4.38 Secant Stiffness for the First Cycle at each Rotation Level versus Maximum Positive Cycle Rotation

4.3.6 Energy Dissipation Capacity

Input earthquake energy transmitted to the steel moment frame can be dissipated through viscous damping and hysteretic energy due to inelastic deformation of structural components. Thus energy dissipation capacity is an important factor in evaluating seismic performance of the connections. Energy dissipation at each drift level can be calculated as the area enclosed by load-displacement hysteresis curve for that cycle. The cumulative energy is the sum of these values for each cycle and provides an understanding of the level of damage sustained by the connection.

Dissipated energy measured at the first cycle at each rotation level is plotted in Figure 4.39. When the story drift is less than 0.02 rad., the dissipated energy is less than 10 k-in. for each cycle for both collar connections since the connections have no inelastic deformation. Energy dissipated in each cycle increases gradually after the connections reach the 0.03 rad. cycle. For the collar connection without stiffeners, the maximum dissipated energy per cycle is 500 k-in. at the 0.07 rad. cycle. After this cycle, the energy dissipated drops to 448 k-in. for the first 0.08 rad. cycle. As a result of failure, the dissipated energy in the last cycle is only 243 k-in. Similar energy dissipation behavior is observed in the collar connection with stiffeners, but with slightly large energy dissipated in each cycle. Energy dissipated in the stiffened connection reaches its maximum value of 507 k-in. at the 0.07 rad. cycle and then drops to 492 k-in. at the 0.08 rad. drift level. After crack opening, the energy dissipated in the final cycle is only 287 k-in. Fracture initiation and propagation leads to reduced energy dissipation capacity for both connections indicating eventual failure of the connection. However, the decreasing rate of energy dissipation is slower in the stiffened connection compared to the unstiffened.

Cumulative dissipated energy based on the first cycle to each story drift level is plotted in Figure 4.40. Both connections exhibit similar cumulative energy dissipation capacities. During the smaller cycles where rotation levels are less than 0.02 rad., cumulative energy is less than 30 k-in. for both connections. With increasing drift levels, the cumulative energy increases rapidly with values of 2350 k-in. and 2390 k-in. at the first 0.07 rad. cycle for the collar connection without and with stiffeners, respectively. In the final cycle, cumulative energy dissipation reaches 4190 k-in. and 4460 k-in. for the unstiffened and stiffened connections, respectively, which indicates

that the collar connection with stiffeners dissipates only slightly more energy. The results are not surprising given that both connections undergo beam plastic hinging which is where the majority of inelastic behavior occurs.

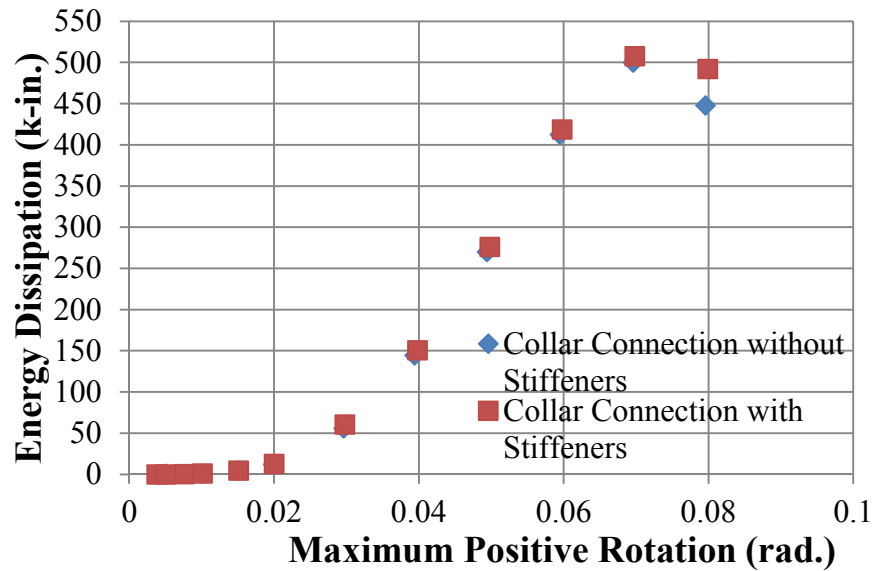


Figure 4.39 Energy Dissipation for the First Cycle of Each Rotation Level versus Maximum Positive Cycle Rotation (rad.)

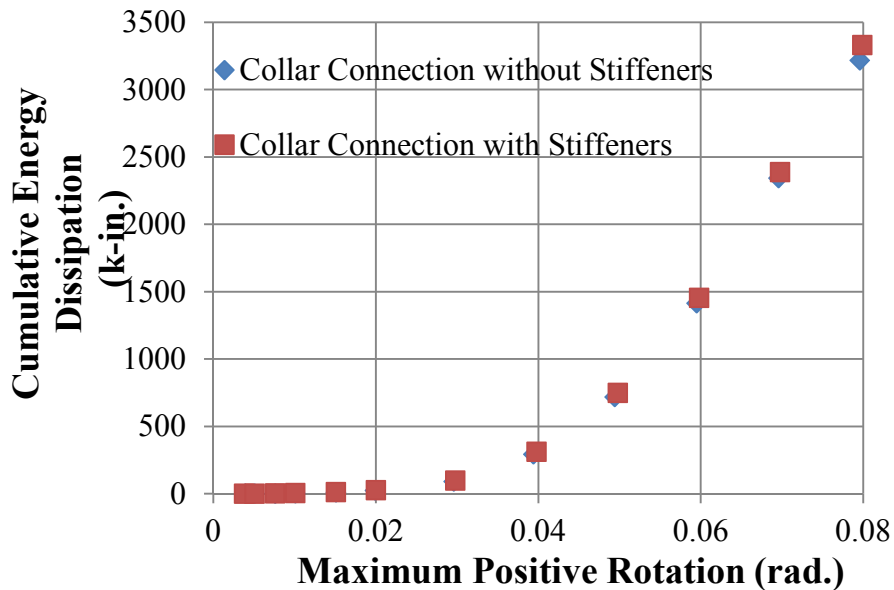


Figure 4.40 Cumulative Energy Dissipation Measured at the First Cycle of Each Rotation Level versus Maximum Positive Cycle Rotation (rad.)

4.3.7 Equivalent Viscous Damping Ratio

Viscous damping is a key indicator to characterize energy dissipation capacity of a structure or a structural component which provides a normalized index of energy dissipation capacity when comparing with other structural components. The equivalent viscous damping ratio is calculated as the energy dissipated per cycle, E_D , normalized by the elastic strain energy, E_{s0} , and 4π .

$$\varepsilon_{eq} = \frac{1}{4\pi} \frac{E_D}{E_{s0}} \quad \text{Equation 4.28}$$

Figure 4.41 plots the equivalent viscous damping at the first cycle of each rotation level. In the elastic region, the viscous damping is relatively small with 3.3% and 3.4% at the 0.02 rad. cycle for unstiffened and stiffened connections, respectively. In the following cycles, viscous damping increases gradually achieving 41% at the 0.07 rad. cycle for the collar connection without stiffeners and 39% at the 0.07 rad. cycle for connection with stiffeners upon initiation of fracture. At the first 0.08 rad. drift level, viscous damping reaches its maximum value of 44% and 42% for the stiffened and unstiffened connections, respectively. In the final cycle, viscous damping drops to 36% and 39% for the connection without and with stiffeners, respectively, owing to fracture propagation and connection failure. The unstiffened connection exhibits higher equivalent viscous damping suggesting it is more efficient in dissipating energy compared with the stiffened connection although its dissipated energy in each cycle is slightly less than that of the stiffened connection.

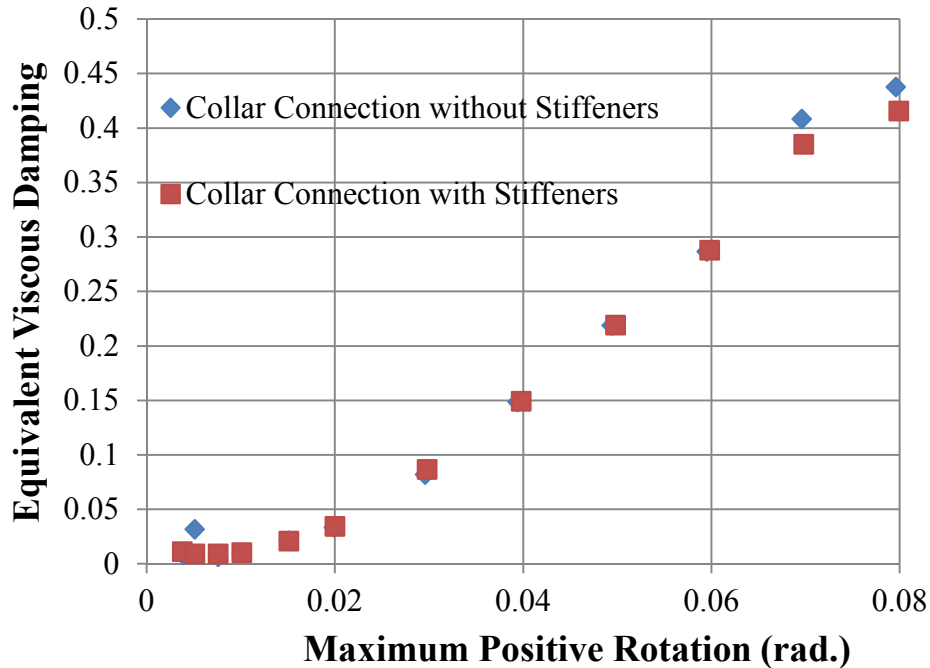


Figure 4.41 Equivalent Viscous Damping Measured at the First Cycle of Each Rotation Level versus Maximum Positive Cycle Rotation

4.3.8 Distribution of Strain in the Connections

4.3.8.1 Strain in the Beam

Strain gages are placed on the beam flange to better understand the strain distribution and force transfer path in the HSS beam member. In the collar connection without stiffeners, six strain gages (be1-be6 and bw1-bw6) are located on each side of the beam flanges in the plastic hinge region as seen in Figure 4.13. Strain gage be1, be4, bw1 and bw4 are on the centerline of the beam. In the collar connection with stiffeners, eight strain gages (be1-be8 and bw1-bw8) are placed on each side of the beam flanges in the plastic hinge region as shown in Figure 4.14. Strain gages be1, be4, bw1 and bw4 are on the centerline of the beam. The strain gages on the east side beam flange are mirrored on the west side beam flange. The strains at the completion of the first cycle to each rotation level are plotted in the Figure 4.42 and Figure 4.43.

In the collar connection without stiffeners, the maximum strain at each location ranges from -0.018 for be1 at 0.07 rad. to 0.026 for be6 at 0.08 rad. on the east side while it varies from -0.015 for bw1 at 0.07 rad. to 0.043 for bw4 at 0.08 rad. on the west side of the beam. When the

rotation of the beam is less than 0.04 rad., strain does not exceed the yield strain and the maximum strain is observed in strain gage be6 and bw5 indicating initial load transfer is from the beam corners to the center of the beam flange then into the connection. In the following cycles prior to local buckling of the beam flange at 0.06 rad., strain gage be3 on the east side and bw3 on the west side reach their maximum strain values of 0.009 and 0.009 which are larger than the measured yield strain from the beam flats. Strain levels at the corners also exceed that at the beam centerline during the 0.05 rad. cycle. When local buckling occurs, strain gages be1 and bw1 exhibit maximum strain of 0.018 and 0.015 at the 0.06 rad. cycle, respectively, which reveals that loads flow from the beam corner to beam center with yielding spreading to the whole flange. However, after local buckling and fracture initiation at the 0.06 rad. cycle, strain values decrease which is attributable to the discontinuity in the beam flange induced by fracture.

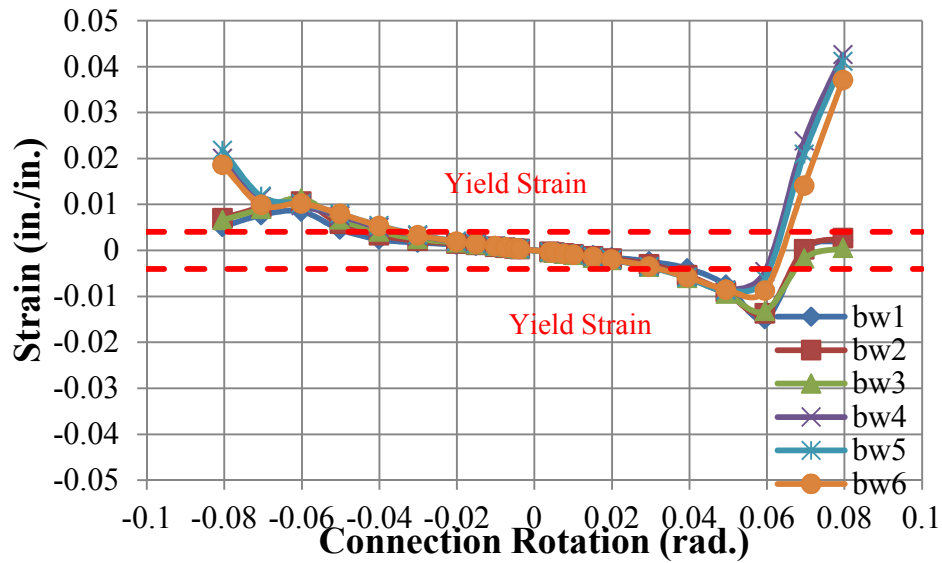
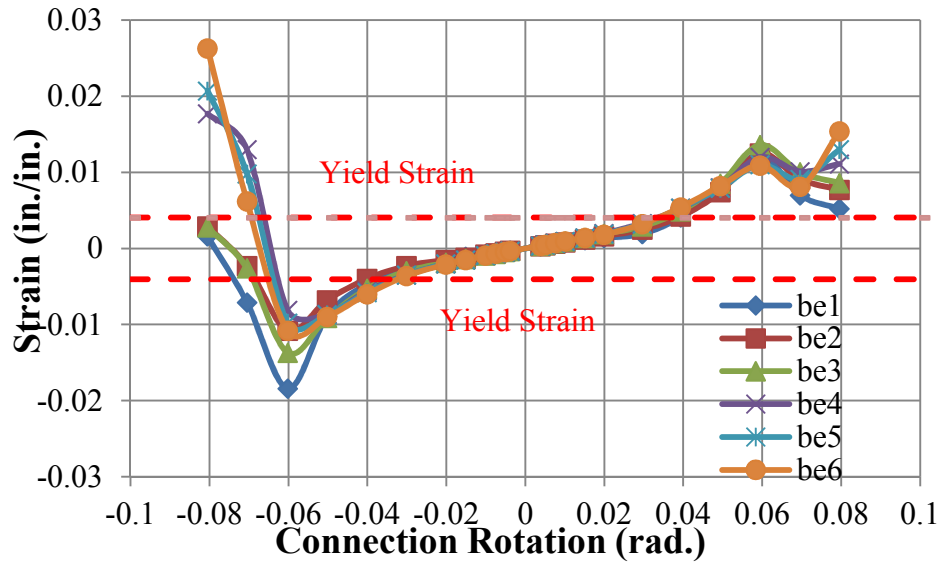


Figure 4.42 Strain in the Beam versus Connection Rotation Level for the Collar Connection without Stiffeners

In the collar connection with stiffeners, the maximum strain in the beam strain gages ranges from to 0.002 in be7 to 0.003 in be1 at the 0.06 rad. cycle on the east side of the beam while it varies from 0.003 in bw7 at 0.06 rad. to 0.040 in bw1 at the 0.07 rad. story drift. When the rotation level of the beam is less than 0.03 rad., strain is smaller than the yield strain and the maximum strain is observed in strain gage be2 and bw2 both reaching a strain of 0.003. Prior to local buckling of

the beam flange at 0.05 rad., strains in the strain gages be1 to be3 and bw1 to bw3 increase rapidly, reaching maximum strain values of 0.011 and 0.010 for be2 and bw2 at 0.04 rad., which suggests load concentrates at the top of the stiffeners. This location is coincident with where local buckling occurs in later cycles. When the onset of local buckling occurs in the beam plastic hinge region, strain gages be1 and bw1 reach their maximum strain of 0.020 and 0.018 at 0.05 rad., respectively. Strain values in be1 to be3 and bw1 to bw3 are largest compared to other strain gages which reveals flexural yielding occurs first at the top of the stiffeners in the beam flange. At the 0.08 rad. drift level, strains drop as a result of the initiation of fracture at the beam corners. Overall, strain gages be4 to be6 and bw4 to bw6 exhibit almost identical strain values indicating load distributes uniformly along the beam flange 12 in. away from the stiffener. Strain gages be1 to be3 and bw1 to bw3 show the same order of magnitude strain levels and similar trends during the 40 full cycles. Strains in be1 to be3 and bw1 to bw3 are always greatest compared to other strain gages which suggests load concentrated in the beam flange aligns with the top of the stiffeners and distributed uniformly over the beam flange region. Strain gages be7, bw7, be8 and bw8 typically do not reach their yield strain suggesting the majority of deformation occurs beyond the stiffeners along the beam flange.

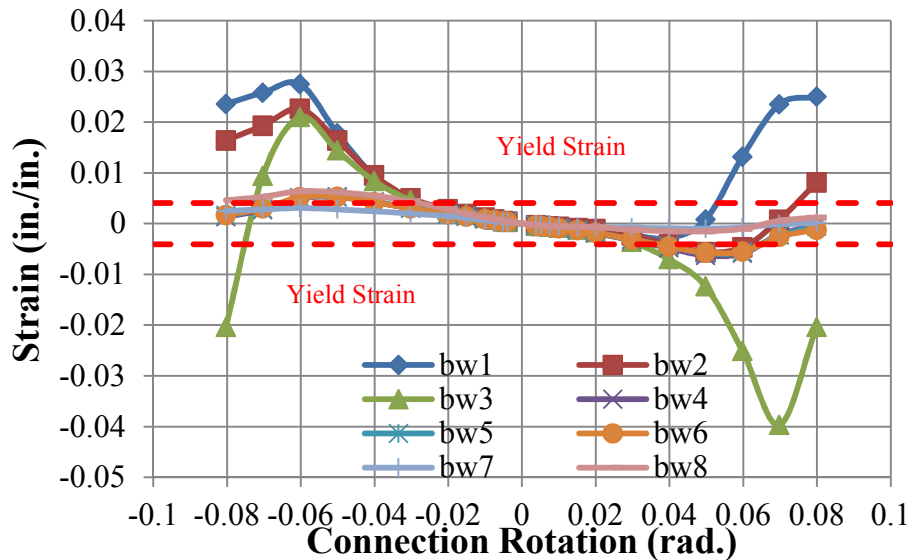
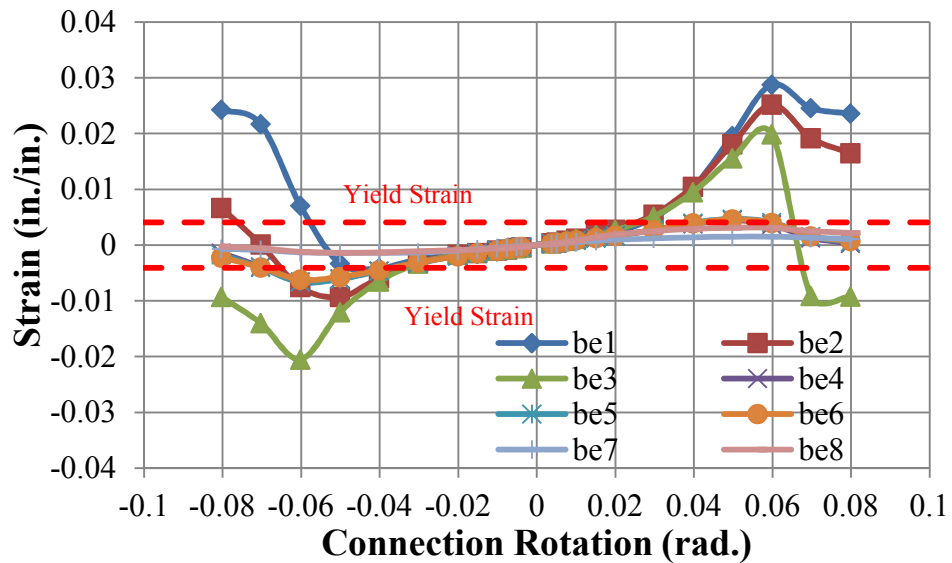


Figure 4.43 Strain in the Beam versus Connection Rotation Level for the Collar Connection with Stiffeners

4.3.8.2 Strain in the Beam Endplate

Strain in the endplate is considered to explore the load transfer path and to evaluate whether excessive deformation occurs either in the endplate or column face. In the collar connection without stiffeners, two strain gages (ew1 and ew2) are located on west side of the endplate as

seen in Figure 4.13. Strain gage ew1 is on the centerline of the endplate and ew2 is located at 2.5 in. off the centerline towards the edge of the endplate. For the collar connection with stiffeners, two strain gages (ew1 and ew2) are placed on the west side of the endplate as shown in Figure 4.14. Strain gages ew1 and ew2 are 2.5 in. off the centerline of the endplate. Strain gage ew1 and ew2 are 1 in. and 3 in. away from the beam flange on the west side of the connection, respectively. For both connections, the strains at the peak rotation of the first cycle of each rotation level are plotted in Figure 4.44 and Figure 4.45.

For the connection without stiffeners, strain at the centerline of the column is almost identical with that near the column corners indicating forces are uniform across the width of the endplate. Strain gages ew1 and ew2 reach their peak values at approximately the 0.04 rad. cycle with strains of 0.007 and then plateau at this level through the 0.06 rad. cycle. During the last cycle, strain in ew1 and ew2 decreases after fracture of the beam. Strain values surpass the yield strain for both strain gages in the connection without stiffeners showing yielding occurs in the endplate.

Strains in strain gage ew1 and ew2 for the connection with stiffeners remain below the yield strain throughout the loading. These results suggest that the stiffeners move deformations in the endplate away from the beam endplate interface. However, slightly larger strains are seen closer to the beam endplate weld. As with the collar connection without stiffeners, strains decrease after the 0.06 rad. cycle due to deformation concentrating in the local buckle of the beam and fracture point.

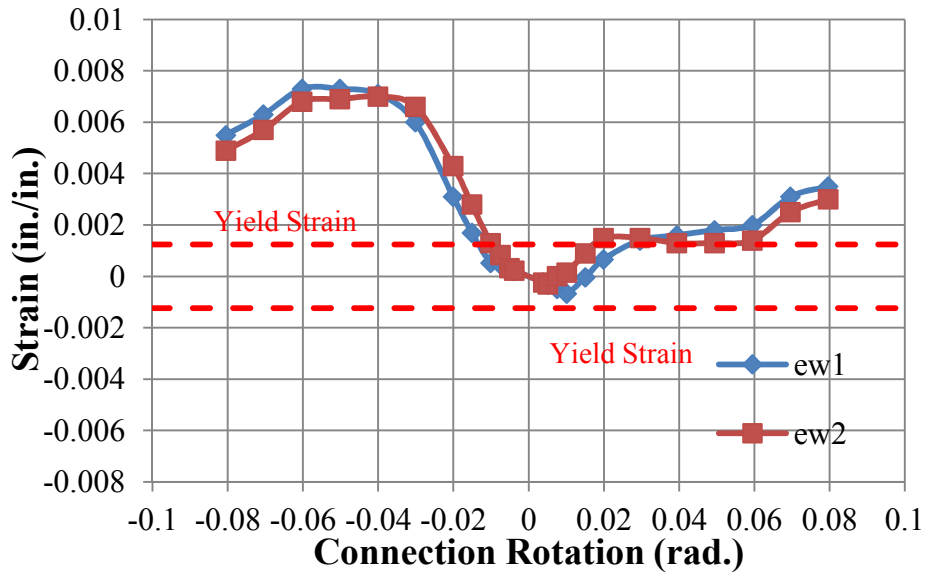


Figure 4.44 Strain in the Endplate versus Connection Rotation for the Collar Connection without Stiffeners

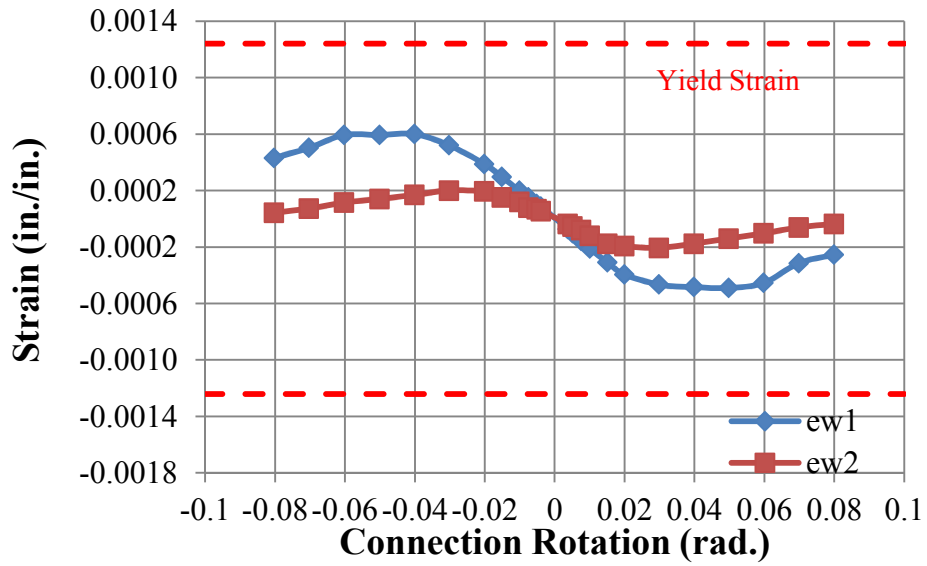


Figure 4.45 Strain in the Endplate versus Connection Rotation for the Collar Connection with Stiffeners

4.3.8.3 Strain in the Column Face

Strains in the column face just past the end of the endplate are studied to analyze any load transfer path from the endplate to column face. Two strain gages (cf1-cf2) located on the column face 1 in. away from the end of the endplate on the west side of the connection as shown in Figure 4.13 and Figure 4.14 for the collar connection without and with stiffeners, respectively. Strain gage cf1 is located on the centerline of the column and strain gage cf2 is 2.5 in. off the centerline towards the edge of the column.

Both connections show similar strain results for gages cf1 and cf2 with strains remaining small with maximum values of around 0.0013. The results suggest very little load is transferred through the end of the endplate to the column face. As a result, the weld at the end of the endplate may not be necessary for the collar connections to be effective. The similar strain values in both gages suggest a uniform distribution of load across the column face.

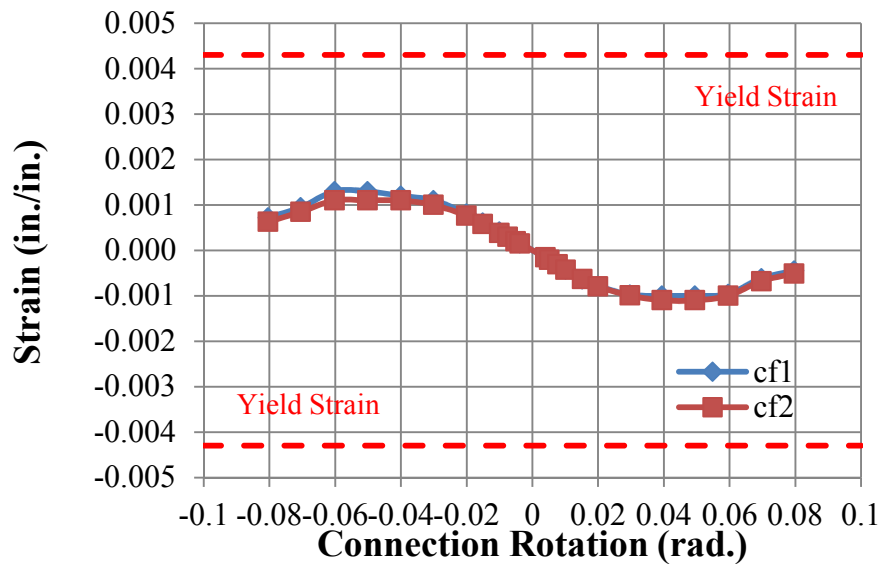


Figure 4.46 Strain in the Column Face versus Connection Rotation for the Collar Connection without Stiffeners

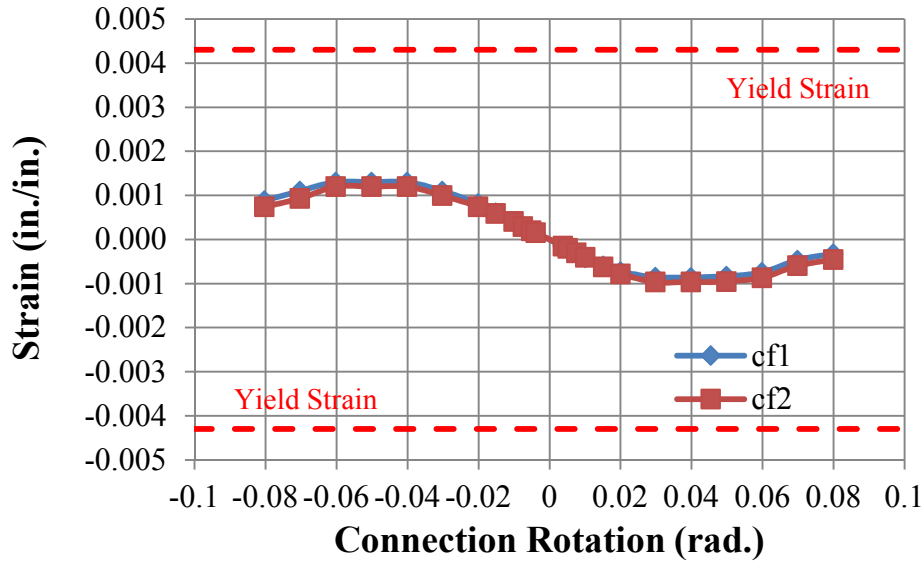


Figure 4.47 Strain in the Column Face versus Connection Rotation for the Collar Connection with Stiffeners

4.3.8.4 Strain in the Collar

Seven strain gages are placed on the collar to monitor the load through the collars as shown in Figure 4.13 and Figure 4.14. Strain gage cw1, cw3 and cw6 are in the direction parallel to the column centerline, while cw2, cw4, cw5 and cw7 are in the direction perpendicular to the column centerline to better study the stress flow in the collars. Strain gages cw1 to cw3 are on the collar plate connected with the top column face, cw4 and cw5 are on the collar plate welded to column sidewall, cw6 and cw7 are on the collar plate attached to the column bottom. The strain level versus connection rotation are shown in Figure 4.48 and Figure 4.49 for the collar connection without and with stiffeners, respectively. The sign of the measured strain in cw6 has been changed for comparison with gages cw1 and cw3.

For the collar connection without stiffeners, in the direction parallel to the column centerline, the strains in strain gages cw1, cw3 and cw6 reach maximum values of 0.0002, 0.0001 and 0.0003 at 0.06 rad. prior to the onset of local buckling. After local buckling is observed in the beam flange, strain in cw1, cw3 and cw6 starts to decrease quickly. In the direction perpendicular to the column centerline, strains in strain gages cw2, cw4, cw5 and cw7 reach maximum values of 0.0004, 0.0002, 0.0003 and 0.0004, respectively at the 0.06 rad. rotation level. Strains then decrease after this point with continuing cycling. Given that the strains are larger in the gages

perpendicular to the column longitudinal axis, it can be inferred that the collars resist more of the load through a hoop like action and bending load is transferred through tension induced by the endplate. The magnitude of strains is small compared to the yield strain of the collar plates indicating the collars experience elastic deformation throughout the entire loading protocol. The results also suggest that the collars can be more efficiently designed. Strain in the collar of the connection with stiffeners are smaller than those observed in the connection without stiffeners. However, the overall observation and trends are similar.

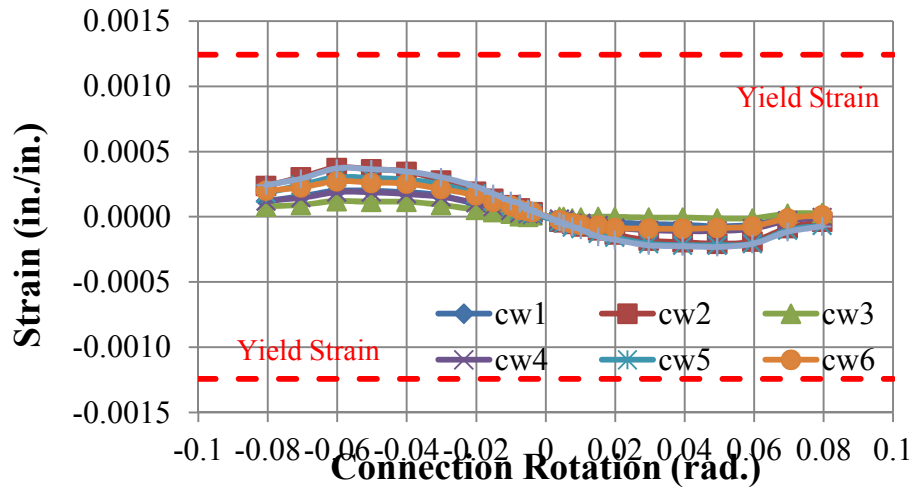


Figure 4.48 Strain in the Collar versus Connection Rotation for the Collar Connection without Stiffeners

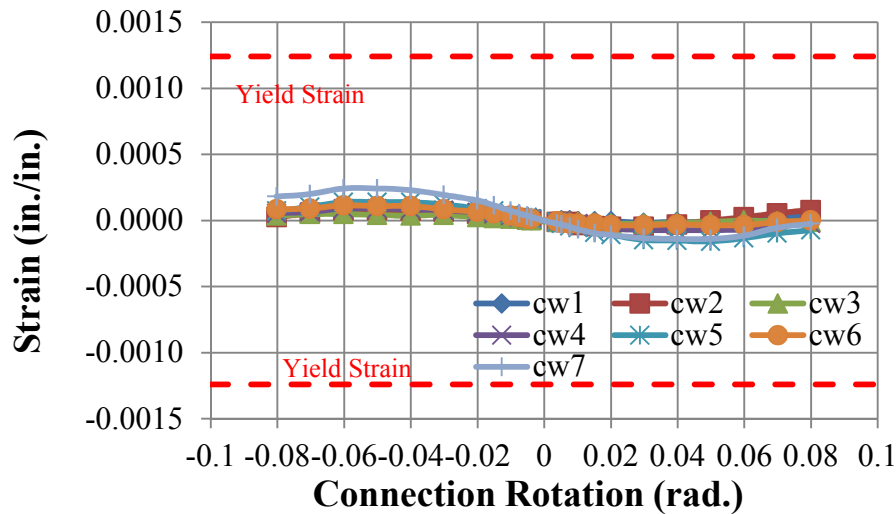


Figure 4.49 Strain in the Collars versus Connection Rotation for the Collar Connection with Stiffeners

In general, the collar strain results suggest that a more efficient collar design is possible as yielding in the collar is considered acceptable. The results also suggest that more load than anticipated may be transferring directly from the endplate to the column face through the longitudinal welds along the length of the endplate between the endplate and column.

4.3.8.5 Strain in the Back of the Column

The back of the column is defined as the face opposite the column face connected with the beam. To monitor load flow path from the collars and column sidewalls to the column back, four (cb1-cb4) and five (cb1-cb5) strain gages are utilized on the west side of the column back for the collar connection without and with stiffeners, respectively, as seen in Figure 4.13 and Figure 4.14. In the collar connection without stiffeners, strain gages cb1 to cb3 are located on the column centerline an increasing distance away from the beam centerline and cb4 is located 4 in. from the column centerline towards the edge of the column back. In the collar connection with stiffeners, strain gages cb1 to cb4 are located on the column centerline an increasing distance away from the beam centerline and cb5 is located at 4 in. off from the column centerline towards the edge of the column.

Strain in the column back is much smaller than that measured on the column face which suggests the column back only experiences small deformation and no yielding. In the collar connection without stiffeners, strain in cb3 is largest with a maximum value of 0.0009 at 0.05 rad. The maximum strain in cb1, cb2 and cb4 are only 0.0004, 0.0007 and 0.0008 at the 0.05 drift level. In the following cycles, strain decreases. Strain in the corner (cb4) is larger than that at the center of the column back (cb2).

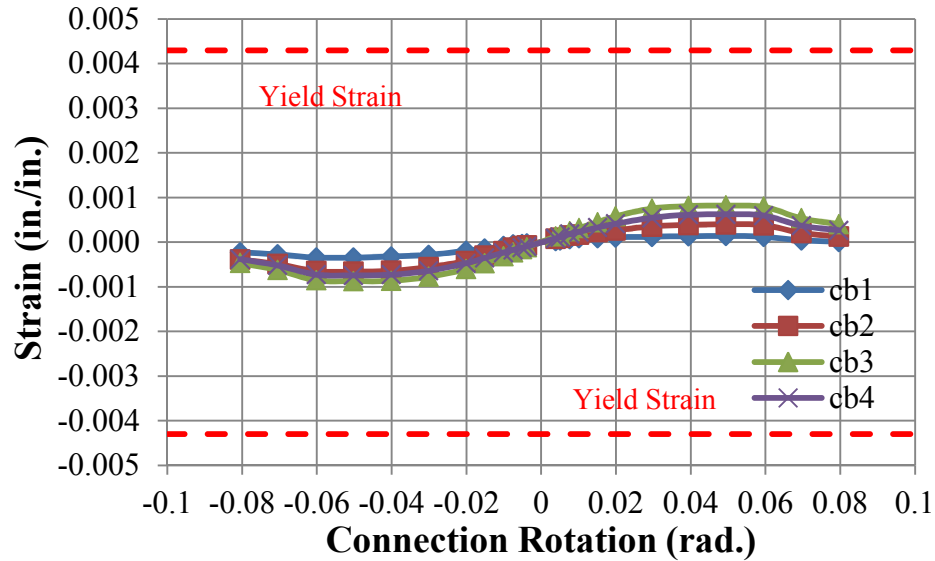


Figure 4.50 Strain in the Column Back versus Connection Rotation for the Collar Connection without Stiffeners

In the collar connection with stiffeners, strain levels in all strain gages located on the column back do not exceed the yield strain of the column member indicating the column back only undergoes elastic deformation. The magnitude of the strain level increases from cb1 to cb4, suggesting that at the column back, the further from the beam neutral axis the higher strain level is measured. At the smaller rotation level, the strain level in cb1 to cb4 monotonically increases. Strain in cb4 is largest with a maximum value of 0.0010 at 0.06 rad. The maximum strain in cb1 to cb3 and cb5 are only 0.0003, 0.0005, 0.0007 and 0.0007 at the 0.05 rad. drift level, respectively. Upon fracture initiation at first 0.08 rad. rotation level, strain decreases. Similar behavior to that seen with the stiffened connection is observed where closer to the corners has larger values.

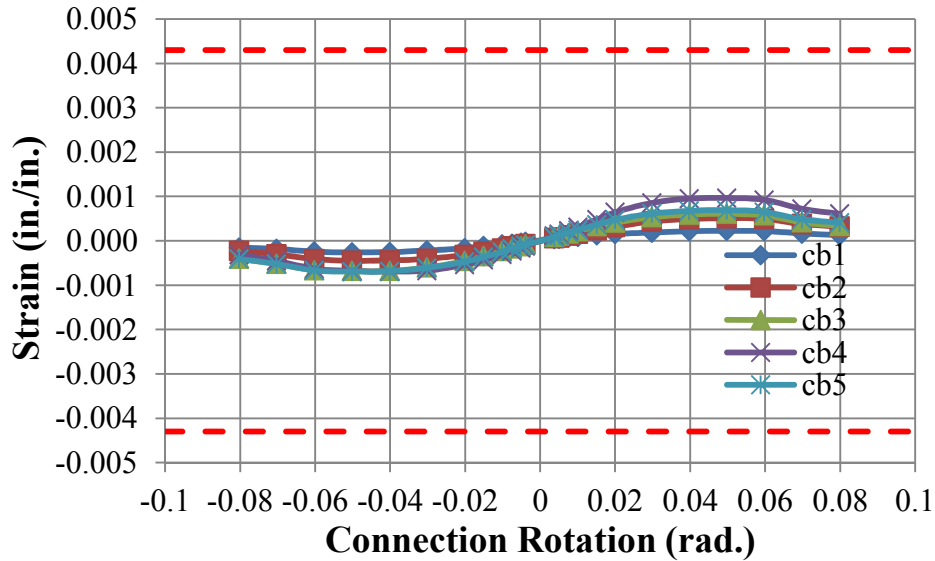


Figure 4.51 Strain in the Column Back versus Connection Rotation for the Collar Connection with Stiffeners

4.3.8.6 Strain in the Panel Zone

Shear strain in the panel zone is analyzed to study its stress state using four strain gage rosettes as seen in Figure 4.13 and Figure 4.14. In both collar connections, strain rosette pz1 is located at the center of the panel zone, pz2 and pz3 are at the corners of the panel zone towards the column face, and pz4 is at the corner of the panel zone towards the column back on the west side of the connection. The strain gage rosettes consist of three strain gages in three direction, direction one is perpendicular to the HSS beam member, direction two is parallel to the HSS beam member, direction three is at a 45° angle with the beam member. Thus shear strain is calculated based on Equation 4.29.

$$\gamma_{12} = 2\varepsilon_3 - \varepsilon_1 - \varepsilon_2 \quad \text{Equation 4.29}$$

where γ_{12} is the shear strain. ε_1 , ε_2 and ε_3 are the strain measured in direction one, two and three, respectively. The shear strains in strain rosettes pz1 to pz4 are plotted in Figure 4.52 for the collar connection without stiffeners and in Figure 4.53 for the connection with stiffeners in terms of each rotation level.

In the collar connection without stiffeners, for rotation levels smaller than 0.02 rad., strains in pz1 to pz4 are linearly proportional to the drift ratio which indicates the panel zone only

undergoes elastic deformation. Strain in the center of the panel zone (i.e. strain rosette pz1) is the largest reaching a maximum value of 0.0036 at 0.05 rad. and exceeding the yield strain before local buckling is observed in the beam. The shear strains in pz2 to pz4 show similar strain levels throughout the entire loading history with maximum values of 0.0013, 0.0013 and 0.0012 at 0.06 rad. cycle. Strain in pz1 decreases rapidly after local buckling and fracture. After fracture, the panel zone no longer sees significant forces. A similar behavior is seen in the panel zone for the connection with stiffeners.

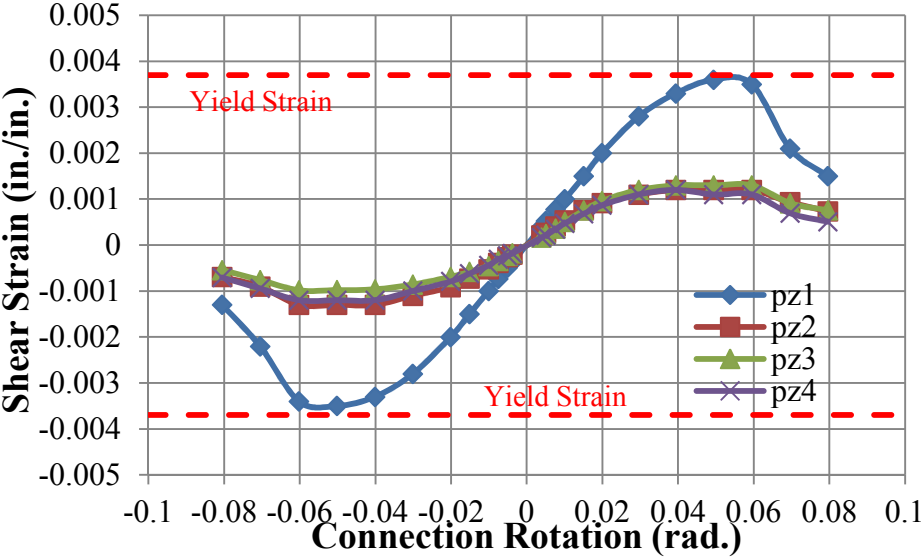


Figure 4.52 Shear Strain versus Connection Rotation for the Collar Connection without Stiffeners

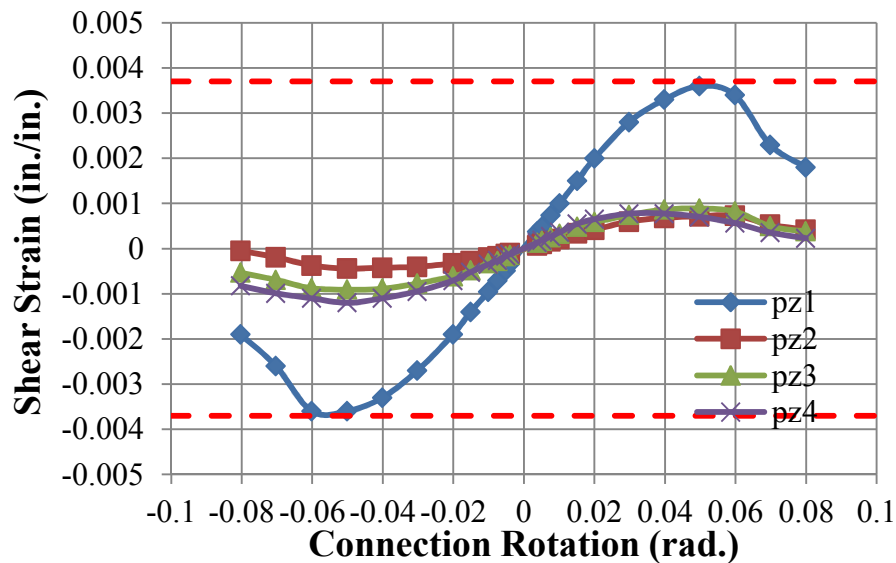


Figure 4.53 Shear Strain versus Connection Rotation for the Collar Connection with Stiffeners

Shear strain in the panel zone is an order of magnitude smaller than that on the beam flanges, but still larger than the strain at other locations indicating the panel zone experienced limited deformation. Formation of compression and tension struts causes shear strain on pz1 to be the greatest compared to that in strain rosette pz2 to pz4. The shear strain in pz2 to pz4 exhibits similar trend and almost identical values throughout the loading history in the connection without and with stiffeners. Overall, the maximum shear strain at the center of the panel zone (pz1) is close to the shear yield strain of the column, while strain on pz2 to pz4 is much smaller than the yield strain indicating the panel zone experiences limited inelastic deformation for both connections. The lack of significant inelastic behavior in the panel zone of both connections suggests that they are strong panel zone designs and the panel zone can be better utilized in future design.

4.3.9 Applications to Design

Based on experimental test results from the collar connection without stiffeners and with stiffeners under seismic loads, both collar connections exhibit stable hysteresis behavior with minor moment capacity degradation, suggesting they are feasible for the seismic moment frames. The inelastic deformation is concentrated in the beam which conforms to a strong column-weak

beam seismic design philosophy and the need for a majority of the inelastic deformation to occur in the beam. Both connections are able to develop the beam plastic moment capacity in a ductile manner.

These tests provide useful data to allow better insight into seismic performance of welded HSS based collar connections in terms of hysteretic behavior, sources of plastic rotation, secant stiffness, energy dissipation capacity and distribution of strain in the connection. The measured connection stiffness is smaller than the theoretical elastic stiffness for both connections. The low elastic stiffness of the connection can lead to larger story drifts than anticipated so care should be given to member selection to ensure proper stiffness. Both connections eventual failure at large drift levels with fracture initiating at the beam corners attributable to the onset of local buckling and cycling in the plastic hinge region. These connections exhibit similar cyclic behavior regarding moment capacity, moment degradation, secant stiffness and energy dissipation capacity suggesting stiffeners only have a minor effect on the overall performance of the collar connection. However, the stiffeners are able to effectively move the location of inelasticity away from the column face since local buckling of the beam is observed at the top of the stiffeners instead of adjacent to beam to endplate welds. As a result, the strain in the endplate, collars and column face of the connection with stiffeners is smaller than that of the connection without stiffeners. For the collar connection with stiffeners, almost all the inelastic rotation is concentrated in the beam, while inelastic deformation observed outside the beam is negligible. Both connections show desirable behavior for developing a strong column-weak beam behavior as required in seismic design with nearly all the plastic rotation occurring in the beam members. However, sharing inelastic deformation with other structural components might lead to a more efficient design and requires further exploration.

4.4 Conclusions

Material coupon tests of HSS members provide a better understanding of the specimens' mechanical properties in terms of strength and ductility. An experimental study of HSS based collar connections is conducted to evaluate their ability to resist lateral forces induced by seismic loads and understand their seismic performance under large cyclic loading conditions. The cyclic

performance is assessed in terms of hysteretic behavior, energy dissipation, secant stiffness and magnitude of plastic rotation in each structural component. The distribution of strain in the connection region is considered to determine the load transfer mechanism and potential failure mode. Several conclusions are summarized as follows:

1. All the subsize coupon specimens satisfy the strength requirement prescribed in the ASTM standards. However, only coupon specimens from the beam flats are capable of meeting all specification requirements from EuroCode 3.
2. Both the unstiffened and stiffened collar connection exhibit stable hysteretic behavior up to the 0.06 rad. story drift with moment degradation less than 10% and they are both able to develop the plastic moment capacity of the beam. At around the 0.06 rad. rotation level for the collar connection without stiffeners and the 0.05 rad. cycle for the connection with stiffeners, local buckling of the beam flange is observed followed by fracture initiation. Once fracture starts to propagate, moment capacity decreases quickly up to 70% and 58% for the unstiffened and stiffened connections, respectively, in the fourth 0.08 rad. cycle.
3. The vast majority of the plastic rotation is concentrated in the HSS beam throughout the loading history for both connections. The presence of stiffeners is effective in moving the plastic deformation away from the column face which leads to slightly earlier onset of local buckling and less plastic rotation outside the HSS beam compared to the unstiffened connection.
4. The degradation of the secant stiffness gradually increases after the 0.02 rad. drift level. Both connections show similar trends and magnitudes in the loss of secant stiffness at increasing rotation levels.
5. The cumulative energy dissipation for the unstiffened and stiffened connections are 2344 k-in and 2390 k-in at the 0.07 rad. story drift, which corresponds to 41% and 38% equivalent viscous damping, respectively. The results indicate that the collar connection without stiffeners is slightly more efficient at dissipating energy.
6. The stiffened connection is less effective in spreading strain to other structural components (i.e. endplate, collars and column) with a smaller magnitude of strain distributed outside the HSS beam compared to that of the unstiffened connection. The strain in the beam surpasses the yield strain indicating inelasticity concentrated in the beam member.

7. As cyclic loads increase, the panel zone experiences limited yielding which initiates at its center for both connections. No local buckling or failure is observed in the panel zone with only negligible rotation associated with inelastic deformation indicating a strong panel zone design.
8. The endplate yielding is only observed in the connection without stiffeners which further indicates that stiffeners can effectively move the inelastic deformation away from column face. Collar yielding does not occur for both connections due to the fact that the weld configurations restrain deformation of the endplate thus limit the function of the collars.
9. Both connections show seismic performance that is acceptable for IMF and SMF systems. However, the performance could be improved by engaging other structural components in accommodating the inelastic deformation.

CHAPTER 5 FINITE ELEMENT MODELING OF HSS BASED COLLAR CONNECTIONS

5.1 Introduction

Many early finite element (FE) studies of HSS members and connections focused on their application in axial loaded truss members. For example, Korol et al. (1989) performed nonlinear FE analysis of twelve rectangular hollow sections (RHS) double chord K-joints which exhibited good agreement with experimental test results. Kozy (2005) investigated chord bearing capacity in a long span tubular truss through experimental and analytical studies. Some other numerical simulations of HSS columns to wide flange beams (Shanmugam et al., 1994; Ting et al., 1991) in steel moment frames were conducted and results indicated the FE results were in good correlation with the experimental test results.

Only a few FE studies considered HSS based moment connections. Korol and Mirza (1982) performed FE analysis on rectangular hollow section T-joints to study how different geometric parameters influence ultimate branch moment and punching shear forces developed in the connection. More recently, Fadden and McCormick (2014b) developed 39 FE models of unreinforced HSS based moment connections subject to cyclic loads which showed these connections were unable to achieve the beam plastic moment capacity. They later proposed two reinforced HSS based moment connections and 24 FE models of each reinforced connections were studied and shown viable for seismic application (Fadden & McCormick, 2014b). However, their proposed reinforced HSS based moment connections can be further improved to reduce the demand for field welding and hence construction.

Chapter 4 showed the viability of the HSS based collar connection as an improvement approach, but more work is needed to optimize the configuration and detailing requirements to ensure a safe, reliable and economic connection. FE analyses provide an opportunity to further explore

parameters associated with these connections. Vegte et al. (2010) summarized nonlinear finite element (FE) analysis for welded HSS joints and bolted joints and found that shell elements are accurate for most studies of tubular joints. They also suggested that FE analyses are capable of simulating load-deformation behavior satisfactorily if joints failed by plastification rather than fracture. Therefore, shell element based FE analysis is adopted in this study for the HSS based collar connection which also showed plastification of the joint occurred prior to fracture.

The objectives of this chapter is to further explore the behavior of HSS based collar connections under large cyclic loads through a comprehensive FE study and to provide more insight into their viability for seismic applications. FE models developed in Abaqus 6.14-1 (2014) are first calibrated to experimental test results of the collar connections to ensure the model can accurately characterize the global and local behavior under large cyclic loads. A parametric study of twenty-eight HSS based collar connections considers various parameters including: endplate thickness (t_e), collar thickness (t_c), beam width thickness ratio (b/t), beam depth thickness ratio (d/t), and beam to column width ratio (β). FE analyses provide a means of evaluating different parameters that influence the performance of the collar connection and provide insight with respect to detailing requirements. Based on the experimental results from Chapter 4 and the parametric study, implications for the design of HSS based welded collar connections are provided.

5.2 FE Model Calibration and Validation

To validate whether the FE models are able to accurately simulate the cyclic behavior of HSS based collar connections under large cyclic loads, two models of HSS based collar connections, one without stiffeners and the other with stiffeners, are developed to compare with the experimental test results.

5.2.1 Configuration and Details

To compare the numerical results with the experimental findings from Chapter 4, the same connection configurations are applied through FE modeling with a beam length of 110 in. and column length of 118 in. These dimensions represent the same exterior moment connections as

the previously presented experimental tests. A gap of 1 in. is left between the toe of the stiffener and collar edge for the collar connection with stiffeners whereas a gap of 3 in. is used between the beam flange and collar edge for the collar connection without stiffeners. The beam endplate extends 1 in. beyond the collar resulting in a total length of 32 in. and 40 in. for the connections without and with stiffeners, respectively. In order to simulate the pin connectors at the end of the column and the fixture connecting the beam to the actuator, discrete rigid plates are utilized since in the experimental tests, those connectors are rigid compared to the HSS members. As shown in Figure 5.1, the horizontal HSS member is the HSS beam and vertical member is the HSS column. Boundary conditions are applied at the reference points of the rigid plates to represent the pinned connections at the column ends. The measured geometry of the HSS section, including section height, width, corner radius and wall thickness, are used in the models. Vertical displacements are applied at the beam tip following the loading protocol shown in Figure 5.2. The loading history increases from 0.00375 rad. to 0.07 rad. which follows loading requirements for beam-to-column moment connections specified by AISC 341-10 (2010a).

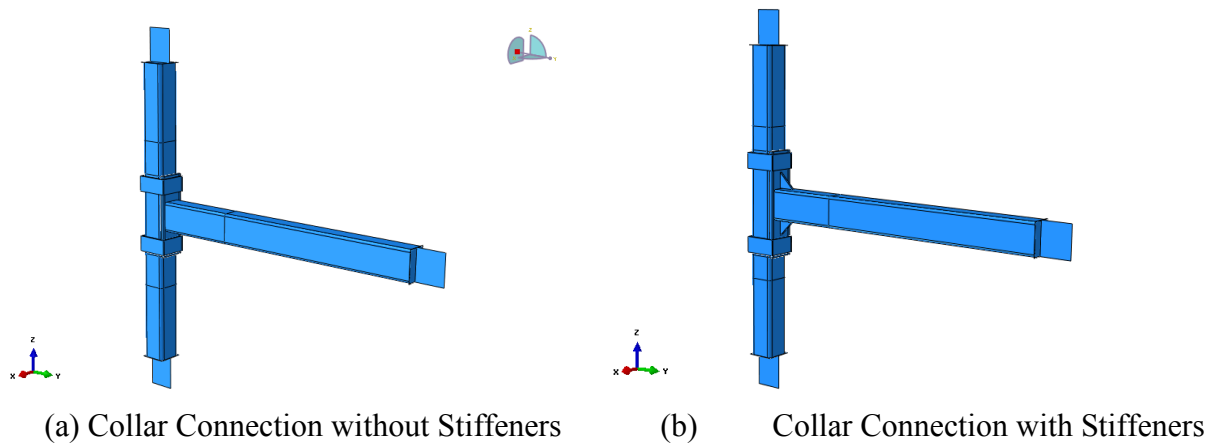


Figure 5.1 FE Models of the Collar Connections

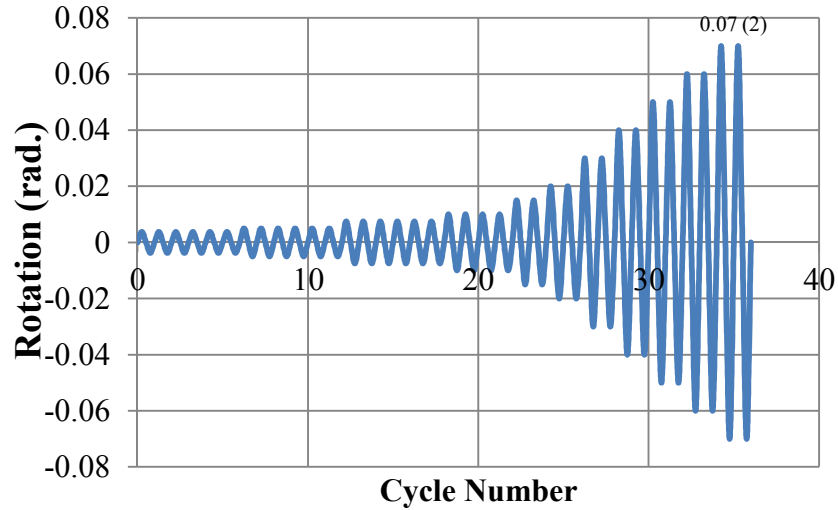


Figure 5.2 Loading Protocol Applied to the FE Models

In the FE models, the HSS beams and HSS columns are modeled with S4R shell elements while the collar plates, endplate, and stiffeners are all modeled using C3D8R solid elements. Similar to the FE models developed in Chapter 3, the HSS beams and HSS columns have been divided into different portions with different mesh sizes for computational efficiency and accuracy. A convergence study is conducted to ensure the mesh sizes provide accurate results. For the HSS beam, the portion adjacent to the endplate, which spans 30 in. along the beam length, is meshed with 1/2 in. square elements, while for the remaining length of the beam the mesh size gradually increases from 1/2 in. by 1/2 in. square to 1/2 in. by 10 in. rectangular elements. For the HSS columns, the central portion spanning 58 in. in length is meshed with 1/2 in. square elements, while the remaining length is meshed with 1/2 in. by 1/2 in. square to 1/2 in. by 10 in. rectangular elements as shown in Figure 5.3. The solid elements are all 1/4 in. square elements considering potential inelastic deformation may occur in the collars, endplate and stiffeners. Tie constraints are used to simulate the welds based on welds specified in the experimental tests which include fillet welds across the column side wall, fillet welds on the column back and beam endplate at the edge of collars, fillet welds across the HSS beam end at the beam endplate, fillet welds around the stiffeners at the beam flange and beam endplate and the fill flush groove weld between the HSS column corners and the beam endplate. Thus, weld failure is not considered in the models which is justified based on the design approach of avoiding critical weld failure and the findings from the experimental study, and monitoring of stress levels.

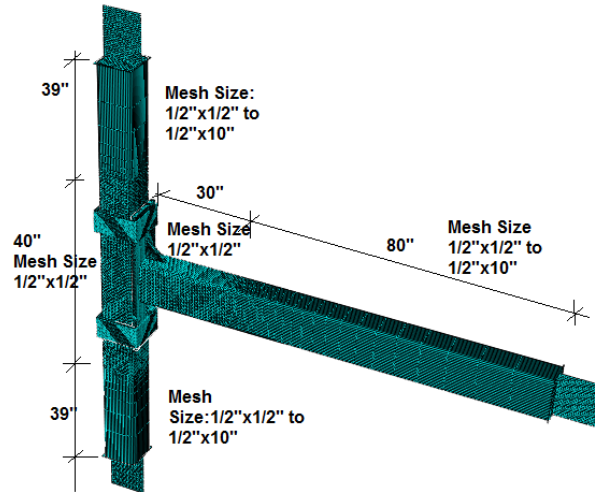


Figure 5.3 Mesh Size of FE Model

5.2.2 Material Properties

Tensile coupon tests of the flat and corner material of the HSS members in the welded HSS based collar connections discussed in Chapter 4 provide the material properties that are incorporated into the FE models. The measured engineering stress-strain curves are converted to true stress-strain values utilizing Equation 5.1 and Equation 5.2.

$$\sigma = s(1 + e) \quad \text{Equation 5.1}$$

$$\varepsilon = \ln(1 + e) \quad \text{Equation 5.2}$$

where e and s are the engineering strain and engineering stress, respectively, and ε and σ are true strain and true stress, respectively.

For the HSS beam, the stress-strain relationships from coupon specimens F2 and C1 are selected for the beam flat and corner material behavior. Details of these material properties can be found in Table 4.1 and Table 4.3. For the HSS column, specimens F6 and C4 are utilized for the column flat and corner material model where detailed discussion of these can also be found in Chapter 4, Table 4.2 and Table 4.4. The stress-strain relationships of these coupon specimens are utilized since they are representative of the materials used in the HSS connections.

The measured yield and tensile strength of the beam flats are 57.0 ksi and 70.0 ksi and for the beam corners they are 72.0 ksi and 79.5 ksi, respectively. Similarly, the measured yield and

tensile strength of the column flats are 62.6 ksi and 65.8 ksi and for the column corners they are 78.3 ksi and 82.2 ksi. All the material models for the beam and column utilize a combined kinematic and isotropic hardening law to better predict cycling effects. The beam and column models are each partitioned into four flat sections and four corner sections with the material properties corresponding to each being applied to capture the cold working effects associated with the HSS manufacturing process. The corner material is applied up to a distance of twice the wall thickness away from the corner. For the diaphragm plate, ASTM A36 steel was assumed using an elastic-perfectly plastic model with a yield strength of 36 ksi. A combined kinematic and isotropic hardening rule is used with the plate material model.

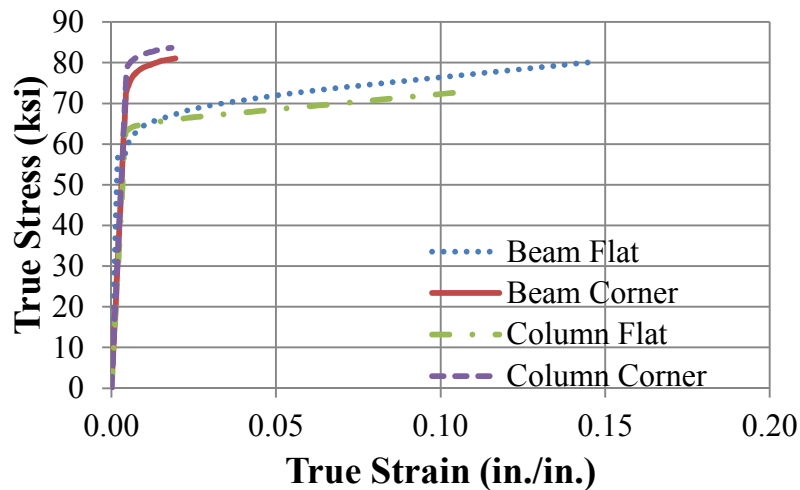
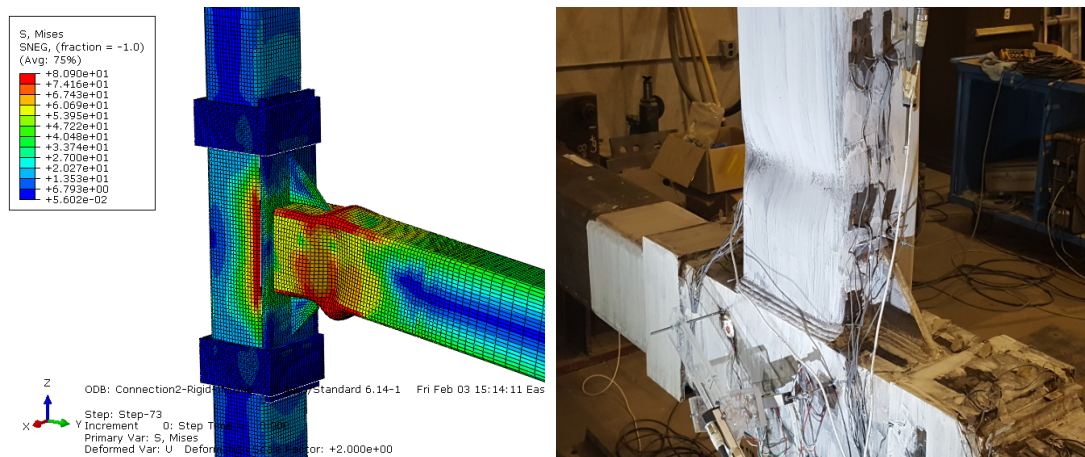


Figure 5.4 True Stress-True Strain Relationship for the Material Models Applied in the FE Analysis

5.2.3 Initial Geometric Imperfections

To accurately simulate the hysteretic behavior observed during the experimental test and capture local and global buckling behavior, an initial geometric imperfection in the beam is applied by introducing the mode shape obtained from an eigenvalue buckling analysis of the beam as shown in Figure 5.5. The eigenvalue buckling analysis provided the shape of the perturbation with a maximum nodal value of unity. Although larger initial imperfections tend to induce earlier local buckling and larger moment degradation, it is reasonable to utilize an imperfection of 1% of the smaller dimension of the HSS beam as this value corresponds to the maximum allowable out-of-plane tolerance for ASTM 500 steel (AISC, 2010b).



(b) Collar Connection with Stiffeners

Figure 5.6 Comparison of Local Buckling Observed from FE Analyses and Experimental Tests at the Second 0.07 rad. Cycle

The resulting moment-rotation hysteretic curves are compared with test results in Figure 5.7. For the collar connection without stiffeners at the small and intermediate rotation levels, the FE model slightly under predicts the moment capacity of the connection until the onset of local buckling. Once rotations reach 0.07 rad., the FE hysteresis curve is almost coincident with the test results which indicates that the FE model is able to provide an accurate representation of what was observed during the experimental tests. In the FE model, the maximum moment achieved by the connection without stiffeners is 3640 k-in. which conservatively predicts the moment capacity of the connection measured during the experiment by approximately 9%. Secant stiffness measured at the first 0.01 rad. cycle is 8.6 k/in. obtained with the FE analysis which underestimates the connection stiffness by 7% compared to the test result.

In the collar connection with stiffeners, the overall behavior shows a good correlation with the test result throughout the loading history. The maximum moment of the connection with stiffeners obtained with the FE analysis is 3910 k-in. which underestimates the moment capacity of the connection during the experiment by only 4%. The secant stiffness of the connection model is 8.8 k/in. which is 7% less than that measured during the experimental test. The prediction of local buckling and moment degradation matches well with the tests as shown in Figure 5.7

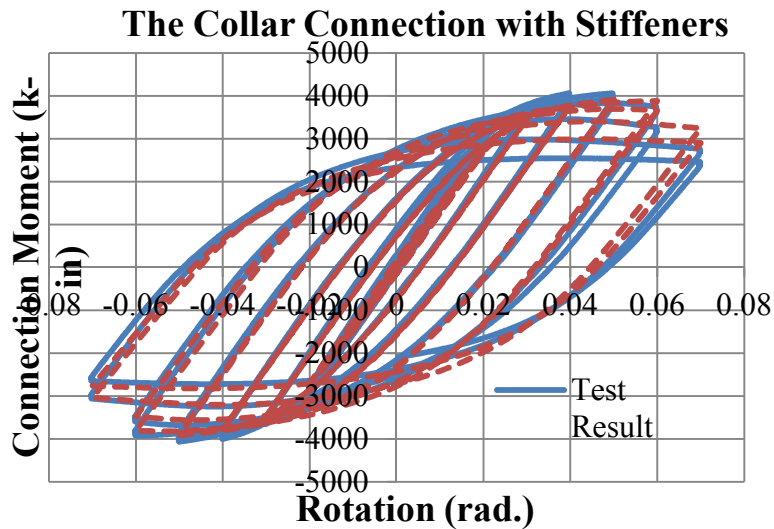
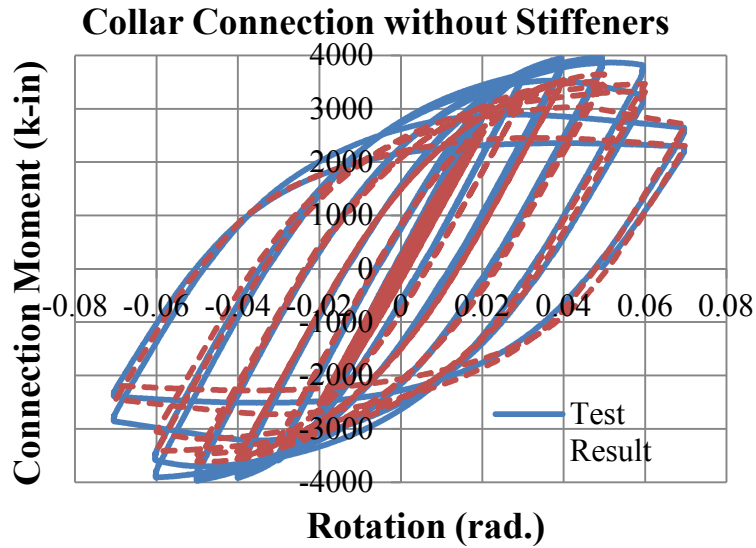


Figure 5.7 FE Results Comparison with the Experimental Results

In general, comparison between the experimental and FE analysis shows that the FE models are capable of accurately predicting the cyclic behavior of the connections and they are suitable for applications in a parametric study of the collar connections.

5.3 FE Model Parametric Study

The seismic moment frame configuration used in the experimental test of the collar connection without stiffeners is used as the starting point for developing the HSS-based collar connection

parametric study. Since the experimental results in Chapter 4 show little influence of the stiffeners on the overall behavior and performance of the connection, all collar connection models in the parametric study are without endplate stiffeners.

5.3.1 Parametric Study Specimens

Given the important role that the collar and beam endplate play in transferring the forces from the beam to the column in the welded collar connection, the effect of changing the collar thickness (t_c) and beam endplate thickness (t_e) are considered in order to better optimize the connection's performances under seismic loads. The role that the beam and beam to column width ratio (β) play in the performance of the connection are also explored by considering beams with various width-thickness ratios (b/t), 10.8 to 24.5, depth-thickness ratios (d/t), 14.2 to 48.5, and beam to column width ratios (β), 0.5 to 0.8. As a result, the beam section sizes span those that would produce stable plastic hinges and those that would likely buckle locally prior to reaching their full moment capacity under bending loads. The considered values for each of the parameters are listed in Table 5.1 leading to 28 different connection configurations being considered. For each of the beam section sizes, all combinations of the specified parameters were considered with a collar depth of 6 in.

Two columns sizes (HSS 10×10×5/8 and HSS 12×12×5/8) and eight different beam sizes are considered (HSS 12×8×5/16, HSS 12×8×3/8, HSS 12×8×1/2, HSS 12×8×5/8, HSS 12×6×1/4, HSS 12×6×3/8, HSS 10×8×3/8 and HSS 10×8×5/8). To isolate the effects of b/t , d/t and β , the thickness of the collars and beam endplate are kept at 1/2 in. and 1 in. for the first 16 connections as shown in Table 5.1. The connections with HSS 12×8×3/8 and HSS 12×6×3/8 beams are selected as baseline models to evaluate the effect of endplate (t_e) and collar thickness (t_c) on the cyclic performance of the collar connections. Based on the experimental test results in Chapter 4, endplate thickness of 1 in. and collar thickness of 1/2 in. are adequate for development of the plastic moment capacity of an HSS 12×8×3/8 beam. To evaluate the feasibility of the collar connections with thinner endplate and collars, endplate thicknesses of 3/4 in. and 1/2 in. and a collar thickness of 1/4 in. are also considered in the parametric study leading to the last 12 connections in Table 5.1.

Table 5.1 Configuration of Collar Connections Studied in the FE Parametric Study

Connection No.	Beam	Column	b/t	d/t	β	t_e (in.)	t_c (in.)	Z_p (in ³)	M_p (k-in)
1	12×8×3/8	10×10×5/8	19.9	31.4	0.80	1	1/2	53.00	3026.83
2	12×8×5/16	10×10×5/8	24.5	38.2	0.80	1	1/2	44.90	2564.24
3	12×8×1/2	10×10×5/8	14.2	22.8	0.80	1	1/2	68.10	3889.19
4	12×8×5/8	10×10×5/8	10.8	17.7	0.80	1	1/2	82.10	4688.73
5	12×6×3/8	10×10×5/8	14.2	31.4	0.60	1	1/2	44.80	2558.53
6	12×6×1/4	10×10×5/8	22.8	48.5	0.60	1	1/2	31.10	1776.12
7	10×8×3/8	10×10×5/8	19.9	25.7	0.80	1	1/2	40.50	2312.96
8	10×8×5/8	10×10×5/8	10.8	14.2	0.80	1	1/2	62.20	3552.24
9	12×8×3/8	12×12×5/8	19.9	31.4	0.67	1	1/2	53.00	3026.83
10	12×8×5/16	12×12×5/8	24.5	38.2	0.67	1	1/2	44.90	2564.24
11	12×8×1/2	12×12×5/8	14.2	22.8	0.67	1	1/2	68.10	3889.19
12	12×8×5/8	12×12×5/8	10.8	17.7	0.67	1	1/2	82.10	4688.73
13	12×6×3/8	12×12×5/8	14.2	31.4	0.50	1	1/2	44.80	2558.53
14	12×6×1/4	12×12×5/8	22.8	48.5	0.50	1	1/2	31.10	1776.12
15	10×8×3/8	12×12×5/8	19.9	25.7	0.67	1	1/2	40.50	2312.96
16	10×8×5/8	12×12×5/8	10.8	14.2	0.67	1	1/2	62.20	3552.24
17	12×8×3/8	10×10×5/8	19.9	31.4	0.80	1	1/4	53.00	3026.83
18	12×8×3/8	10×10×5/8	19.9	31.4	0.80	3/4	1/2	53.00	3026.83
19	12×8×3/8	10×10×5/8	19.9	31.4	0.80	1/2	1/2	53.00	3026.83
20	12×8×3/8	12×12×5/8	19.9	31.4	0.67	1	1/4	53.00	3026.83
21	12×8×3/8	12×12×5/8	19.9	31.4	0.67	3/4	1/2	53.00	3026.83
22	12×8×3/8	12×12×5/8	19.9	31.4	0.67	1/2	1/2	53.00	3026.83
23	12×6×3/8	10×10×5/8	14.2	31.4	0.60	1	1/4	44.80	2558.53
24	12×6×3/8	10×10×5/8	14.2	31.4	0.60	3/4	1/2	44.80	2558.53
25	12×6×3/8	10×10×5/8	14.2	31.4	0.60	1/2	1/2	44.80	2558.53
26	12×6×3/8	12×12×5/8	14.2	31.4	0.50	1	1/4	44.80	2558.53
27	12×6×3/8	12×12×5/8	14.2	31.4	0.50	3/4	1/2	44.80	2558.53
28	12×6×3/8	12×12×5/8	14.2	31.4	0.50	1/2	1/2	44.80	2558.53

The loading protocol used for the parametric study follows the AISC (2010a) specified loading history for qualification of beam-to-column connections in intermediate and special moment frames as described in Figure 5.2. Element type, mesh size, interface tie constraints and material behaviors applied in this parametric study are the same as the FE model used in validation study (Section 5.2). Similarly, a 1% initial imperfection is utilized to more accurately capture global and local buckling behavior of the HSS beam subject to large cyclic loads.

5.3.2 Hysteretic Behavior

All of the HSS based collar connections have symmetric hysteretic behavior as shown in Figure 5.8 to Figure 5.11. In all the plots, the moment sustained by the collar connection is normalized

by the plastic moment capacity of the beam (M_p) which is computed by multiplying the yield strength of the HSS flat (based on the experimental coupon data) by the beam theoretical plastic modulus (AISC, 2010b).

To compare the effects of b/t and d/t on the cyclic behavior of the collar connections, the column size, endplate thickness and collar thickness are constant in the Figure 5.8 and Figure 5.9. With smaller b/t values, the hysteresis loops are much fuller and show less moment capacity degradation. Connection No. 3 and Connection No. 11 which have the lowest b/t ratio, 14.2, and a fairly small d/t ratio, 22.8, show little moment degradation, while Connection No. 2 and Connection No. 10 with highest b/t and d/t , 24.5 and 38.2, exhibit significant moment degradation after reaching their maximum moment capacity at approximately the 0.03 rad. rotation cycle. Connection No. 1 and Connection No. 9 have moderate moment capacity degradation at the 0.05 rad. rotation level which is associated with the onset of beam local buckling. The connections with higher b/t and d/t ratios show larger moment degradation. The initiation and degree of local buckling is highly dependent on the b/t and d/t ratios which is demonstrated by previous studies (Fadden & McCormick, 2014a; Wilkinson & Hancock, 1998). The maximum normalized moments achieved for Connection No. 1 to Connection No. 3 are almost identical which are all greater than unity. Similarly, the maximum normalized moments are 1.18, 1.15 and 1.17 for Connection No. 9 to Connection No. 11, respectively. These findings suggest that these collar connections are capable of developing the beam's plastic moment capacity and thus suitable for seismic applications from the perspective of an acceptable yield mechanism and strength. However, b/t and d/t ratios should be carefully selected to ensure the collar connection behaves in a ductile manner with minor moment degradation under cyclic loads.

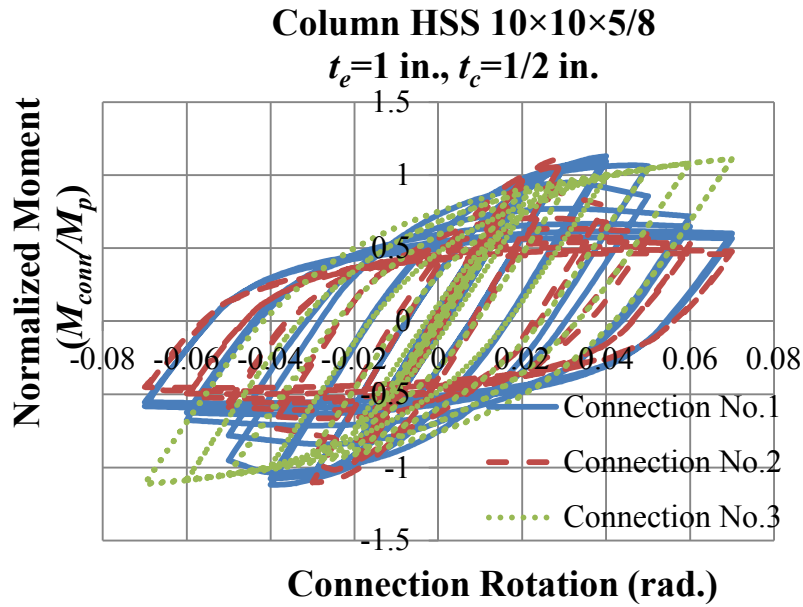


Figure 5.8 Normalized Moment-Rotation Curves for Collar Connections with an HSS 10×10×5/8 Column and Different Beam Sizes (HSS 12×8×3/8, HSS 12×8×5/16 and HSS 12×8×1/2)

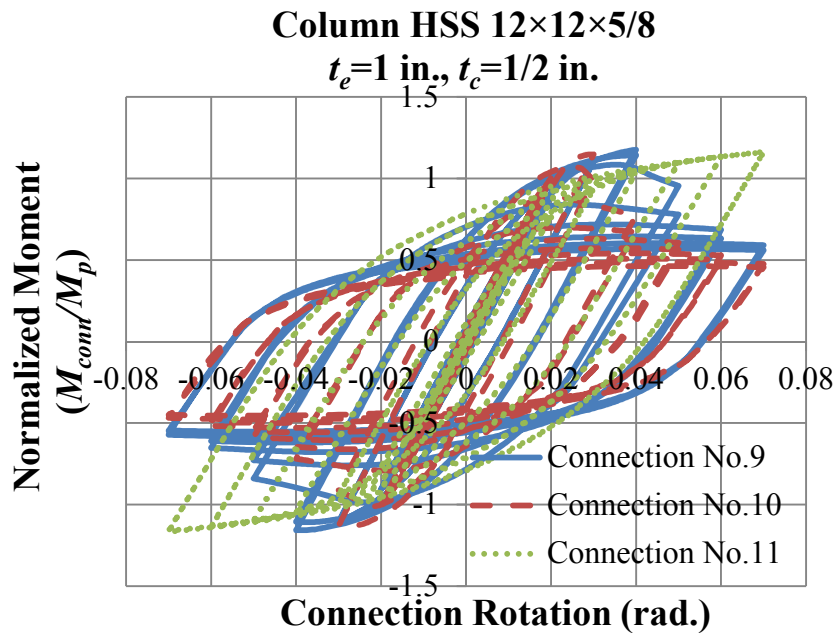


Figure 5.9 Normalized Moment-Rotation Curves for Collar Connections with Column HSS 12×12×5/8 and Different Beam Sizes (HSS 12×8×3/8, HSS 12×8×5/16 and HSS 12×8×1/2)

To evaluate the effects of collar thickness on the cyclic performance of the collar connection, the hysteretic behavior of Connection No. 5 and Connection No. 23 are plotted in Figure 5.10. The

similarity between the behaviors of the two connections suggests that the collar thickness does not play a significant role in the behavior provided the collars do not yield. The limited effect of the collar thickness' limited effect is due to the fact that the weld configuration restrains the endplate and limits the function of the collars as was partially seen in the experimental results. The maximum normalized moment for both connections is 1.22, which also indicates that the moment capacity of the beam is able to be achieved. After reaching the maximum moment of the connections at around 0.05 rad., the moment capacity starts to deteriorate due to inelastic deformation concentrated in the HSS beam and the occurrence of local buckling.

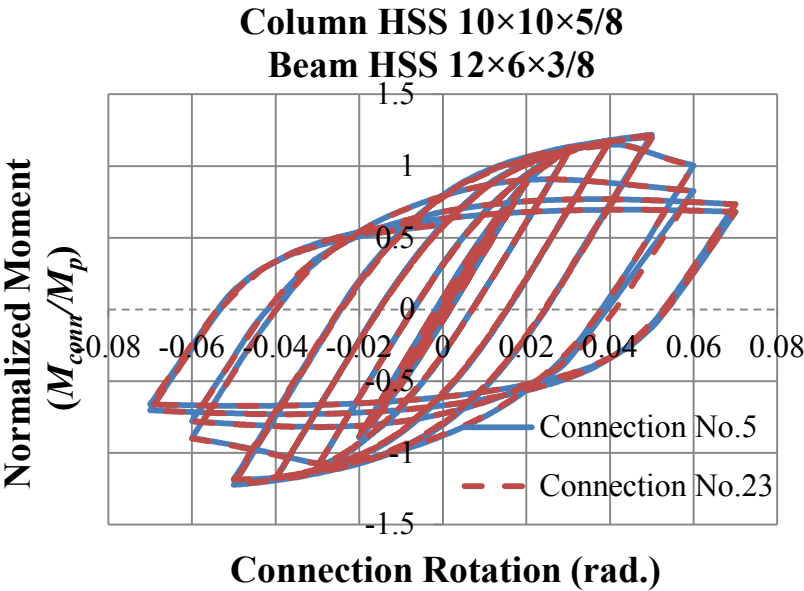


Figure 5.10 Normalized Moment-Rotation Curves for Collar Connections with Varying Collar Thickness ($t_c=1$ in.)

Figure 5.11 provides the hysteresis loops of Connection No. 4 and Connection No. 12 in order to compare the effect of β on the collar connection performance. The plots show similar stable hysteresis behavior with little moment degradation with increasing cyclic loads. The almost coincident hysteresis loops suggest minimal effect of β on the seismic performance of the collar connection owing to the fact that the force from the beam is transmitted to the endplate and then to the column face and sidewalls. Even though β varies, the beam endplate width to column width ratio is constant for both connections and thus the influence of β is minimal. The results clearly show that the end plate dimensions play a more significant role than β . The maximum normalized moments are 0.95 and 0.97 for Connection No. 4 and Connection No. 12,

respectively, suggesting that these connections with the HSS 12×8×5/8 beam also fail to develop the plastic moment capacity of the beam. This is attributable to the fact that collar yielding occurs prior to development of the beam plastic moment capacity. Even though the beams have smaller b/t ratios, the maximum normalized moment capacity never reaches unity.

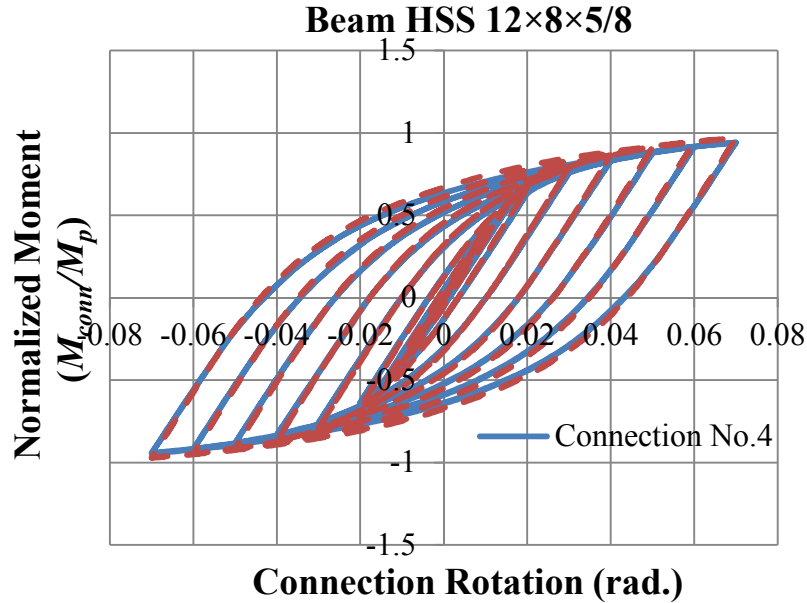


Figure 5.11 Normalized Moment-Rotation Curves for Collar Connections with Varying Beam-to-Column Width Ratio (β) ($t_e=1$ in., $t_c=1/2$ in.)

Twenty four out of 28 collar connections are able to achieve the beam plastic moment capacity except for the connections with HSS 12×8×5/8 and HSS 10×8×5/8 beams due to the fact that yielding of the collar is observed prior to the development of the beam plastic hinge. The findings from the hysteretic behavior of the collar connections suggest that the collar connections are suitable for seismic applications and yielding of the collar can inhibit the formation of the beam plastic hinge if not properly considered in design.

5.3.3 Parameter Effects on the Moment Capacity of the Connections

To isolate the effect of b/t , the first 16 connections with t_e of 1 in. and t_c of 1/2 in. are plotted in Figure 5.12. With an increasing b/t ratio, the maximum normalized moment of the connections slightly decrease due to the earlier onset of local buckling. For the connections with the smallest

b/t ratios as seen in Figure 5.12, the normalized moment is smaller than unity as a result of the collar yielding first suggesting care must be taken in designing the collar for compact sections.

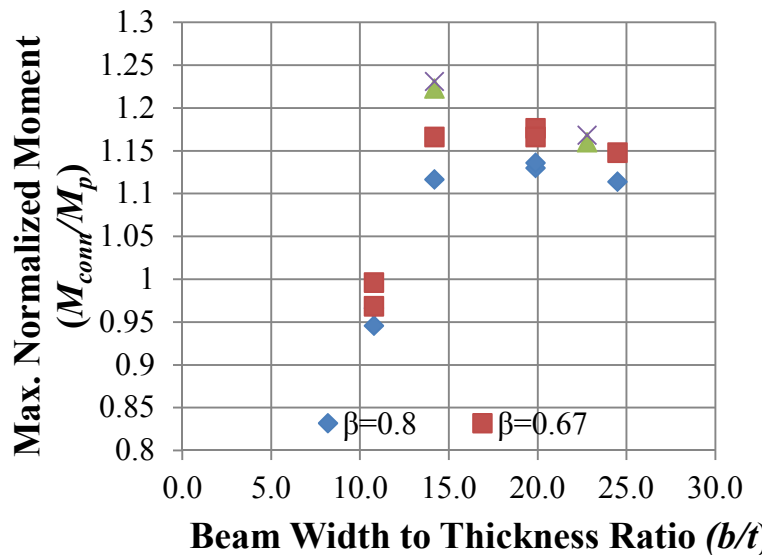


Figure 5.12 Effects of Beam Width to Wall Thickness Ratio (b/t) on Moment Capacity

The relationship of maximum normalized moment and beam depth thickness ratio is plotted in Figure 5.13 for the first 16 collar connections to evaluate the effects of beam depth thickness ratio (d/t) on the connection capacity. Except for the connections with d/t ratios of 14.2 and 17.7, all normalized moments are approximately 1.20. The outliers are the connections with lower d/t ratios that show maximum normalized moment capacity less than unity. Since the seismic performance of the connections with lower d/t ratios are controlled by collar yielding instead of beam flexural yielding, the connection is unable to develop the beam plastic capacity.

In Figure 5.14, the maximum normalized moment for the whole loading protocol versus the thickness of endplate is plotted for the last 12 connections to better isolate the effects of varying the endplate thickness, t_e , on the moment capacity of the connection since there are only two HSS beam sizes (i.e. HSS 12×8×3/8 and HSS 12×6×3/8) considered in this set of connections. The results show that the normalized moment capacity increases with increasing endplate thickness (t_e) owing to the fact that a thicker endplate allows other components to be more involved in the providing capacity and inelastic deformation.

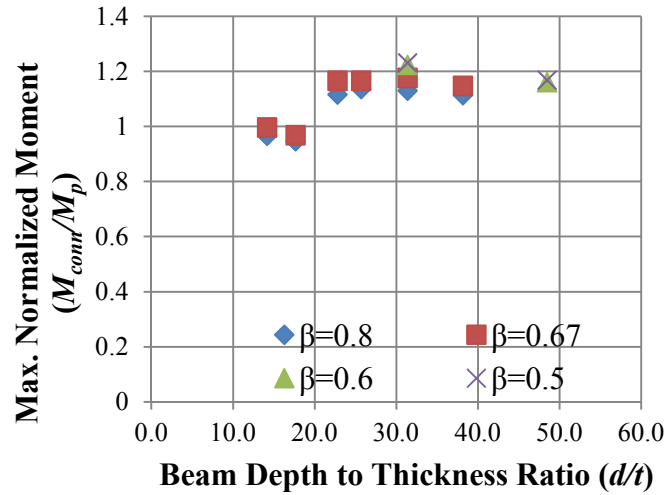


Figure 5.13 Effects of Beam Depth to Thickness Ratio (d/t) on Moment Capacity

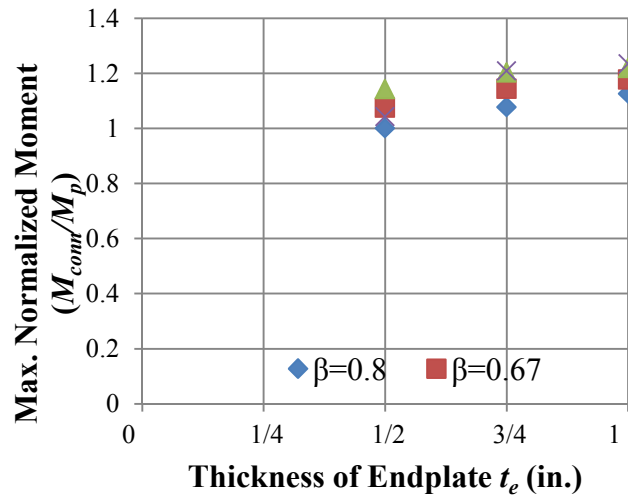


Figure 5.14 Effects of Endplate Thickness (t_e) on Moment Capacity

5.3.4 Secant Stiffness

The secant stiffness of the collar connection is obtained by utilizing the applied force at the maximum cycle displacement divided by the maximum cycle displacement at the first 0.01 rad., 0.04 rad. and 0.06 rad. cycles. The effects of the beam b/t and d/t are evaluated by utilizing the first 16 connections so that the endplate and collar thicknesses are constant as shown in Figure 5.15 and Figure 5.16.

The secant stiffnesses of the collar connections range from 7.14 k/in. to 13.61 k/in at the first 0.01 rad. cycle. The secant stiffness at the 0.01 rad. rotation level generally decreases with larger b/t and d/t . However, the outliers in Figure 5.15 and Figure 5.16 are the connections with smaller beam sections (i.e. HSS 12×6×3/8, HSS 12×6×1/4, HSS 10×8×5/8 and HSS 10×8×3/8) which owes to the fact that the smaller beam section theoretically require lower reaction force to reach the same level of displacement in the elastic region. At the 0.04 rad. cycle, the connections with b/t smaller than 20 and d/t smaller than 32 exhibit uniform degradation of secant stiffness suggesting their stable and ductile behavior under cyclic loads. Upon the 0.06 rad. cycle, for the connections with b/t larger than 15 and d/t larger than 25, the secant stiffness decreases rapidly due to the onset of local buckling. Overall, secant stiffness of the collar connections is highly dependent on the b/t and d/t ratios. The findings suggest that the beam width-thickness and depth-thickness ratios should remain below these values to limit moment degradation and ensure ductile behavior.

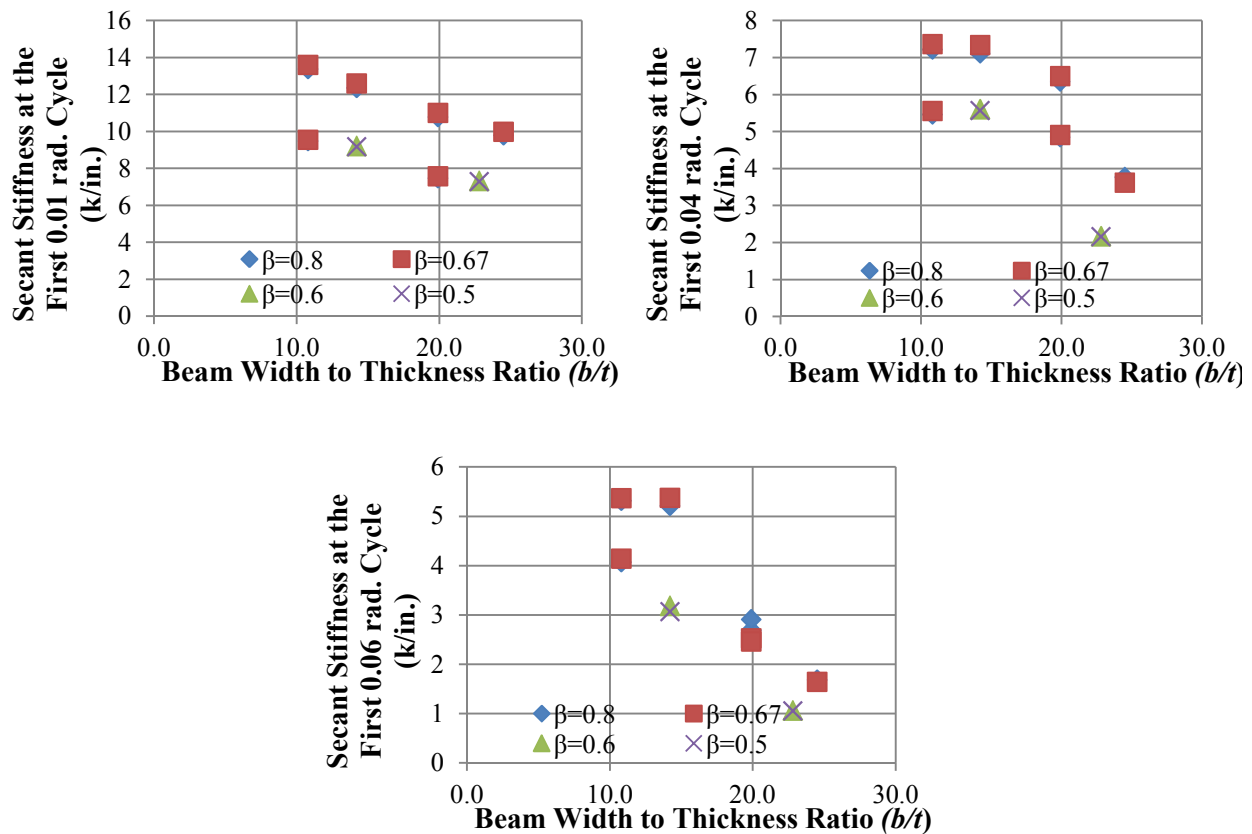


Figure 5.15 Effects of Beam Width to Thickness Ratio (b/t) on Secant Stiffness

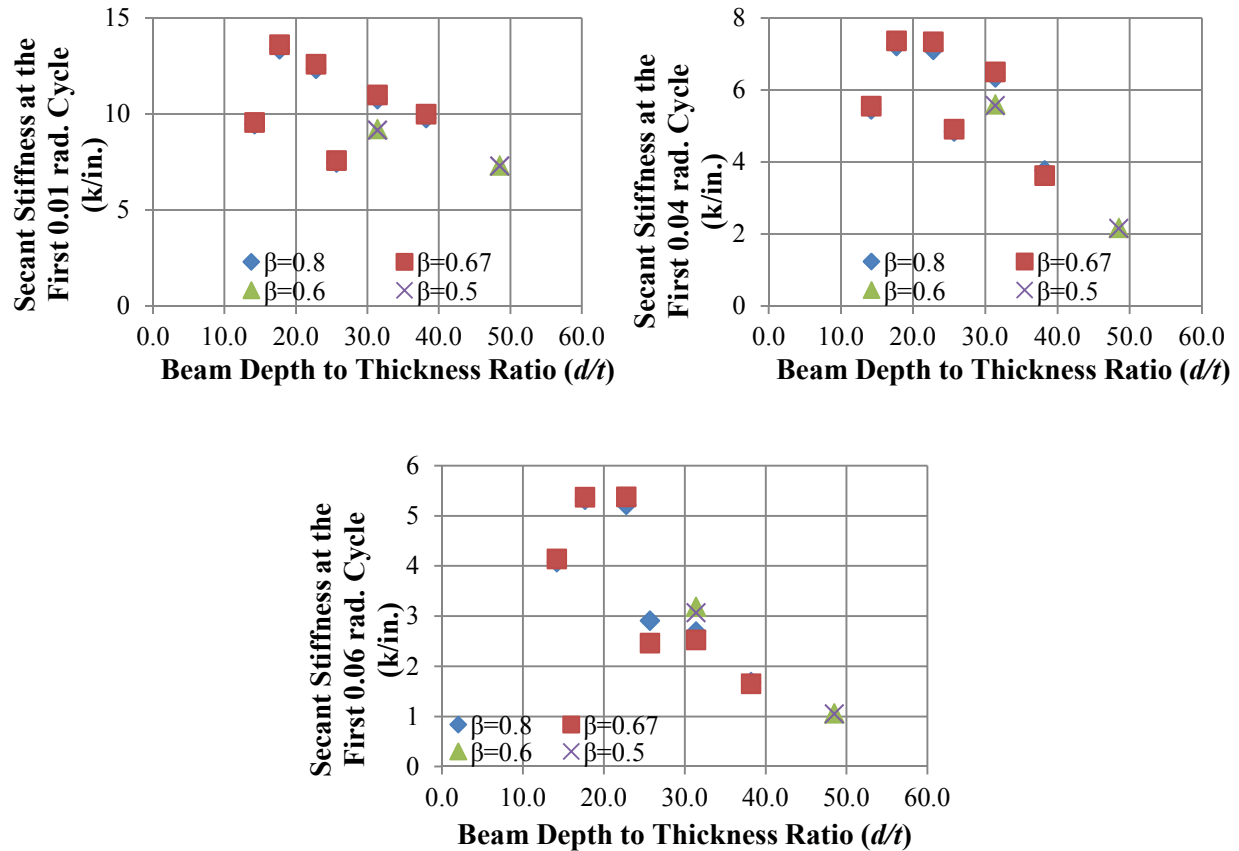


Figure 5.16 Effects of Beam Depth to Thickness Ratio (d/t) on Secant Stiffness

In Figure 5.17, the connections with β of 0.8 and 0.67 have an HSS 12×8×3/8 beam and those with a β of 0.6 and 0.5 have an HSS 12×6×3/8 beam. At the 0.01 rad. cycle, for the collar connections with the same beam size, the secant stiffness is almost identical with respect to a given endplate thickness. The connections with the larger beam size require a larger reaction force to achieve the same displacement level. This is the reason why the secant stiffness of the connections with an HSS 12×6×3/8 beam is smaller than those with an HSS 12×8×3/8 beam.

At the small and intermediate level of rotation (0.01 rad. and 0.04 rad. rotation level), the secant stiffness of the collar connections increase with increasing endplate thickness due to the fact that a thicker endplate allows more inelastic deformation to occur outside the endplate. At the largest rotation level, the secant stiffness of the connections with a thicker beam endplate decreases rapidly. In the connections with a thicker endplate, the excessive inelastic deformation observed in the HSS beam leads to earlier onset of local buckling after the formation of a plastic hinge in the HSS beam. As a result, larger secant stiffness degradation is observed in the connections with

a thicker endplate at larger rotation level. This finding suggests that an increase in endplate thickness may lead to stiffness degradation at a slightly earlier cycle as a result of earlier onset of local buckling.

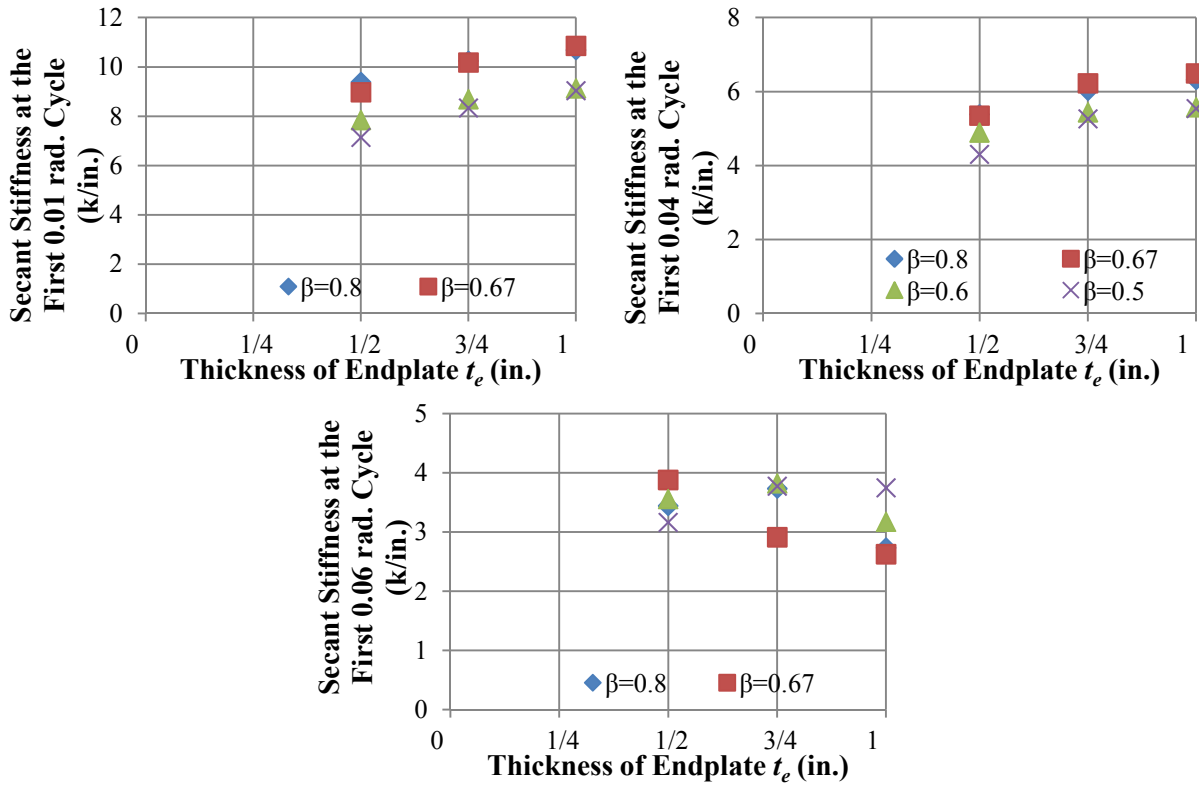


Figure 5.17 Effects of Endplate Thickness (t_e) on Secant Stiffness

5.3.5 Energy Dissipation Capacity

The dissipated energy is calculated based on the area enclosed under the displacement and load hysteretic curves considering effects of b/t , d/t and endplate thickness, t_e , as shown in Figure 5.18 to Figure 5.20. The cumulative energy dissipated throughout the loading history ranges from 1170 k-in to 3520 k-in.

Figure 5.18 and Figure 5.19 plot the relationship of beam width thickness ratio (b/t) and depth thickness ratio (d/t) versus cumulative dissipated energy. With higher b/t and d/t , the cumulative energy dissipated decreases due to early initiation of local buckling of the HSS beam. In Figure 5.18, with the same b/t ratio, the outliers are the connections with smaller beam sections since the moment-rotation hysteresis loops are smaller due to the smaller moment capacity of these

beams. Similarly, the outliners in Figure 5.19 are the connections with HSS 10×8×5/8 and HSS 10×8×3/8 beams which are smaller beam sections compared to those connections with the same d/t ratios. The effect of β is minimal on energy dissipation capacity as shown in Figure 5.19 and Figure 5.20 due to the fact that force from the beam can be transferred to the column sidewalls directly through the endplate. These findings suggest cumulative energy dissipation capacity is not only affected by the compactness of the HSS beam, but also influenced by the beam section sizes. The collar connections with larger HSS beams, which have smaller b/t and d/t ratios, tend to dissipate more energy under cyclic loads.

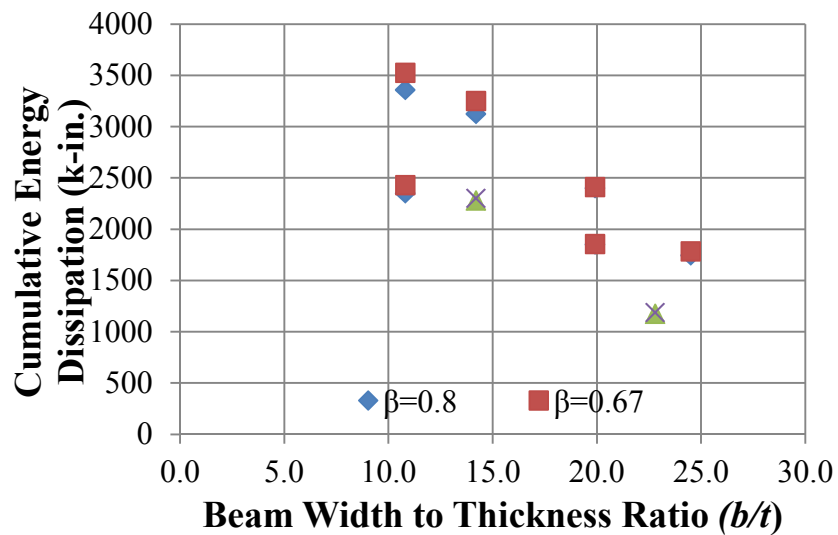


Figure 5.18 Effects of Beam Width to Thickness Ratio (b/t) on Cumulative Energy Dissipation

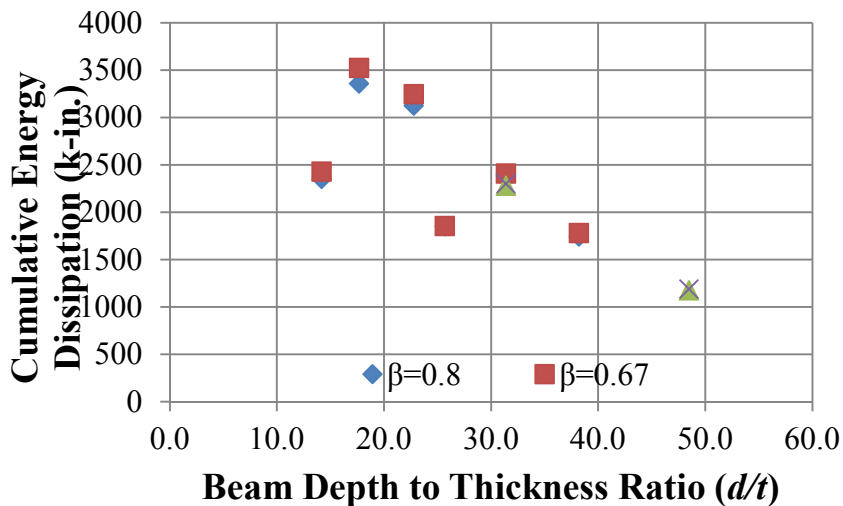


Figure 5.19 Effects of Beam Depth to Thickness Ratio (d/t) on Cumulative Energy Dissipation

The cumulative energy dissipated throughout the loading history increases slightly with increasing endplate thickness (t_e). This finding is attributable to the fact that the moment capacity of the connections increases with an increase in t_e and the enclosed area for connections with the same beam sections and thicker endplate is larger.

Compared to the beam section sizes and beam compactness in the collar connections, the influences of the endplate thickness, t_e , and beam to column width ratio, β are insubstantial on the energy dissipation capacity.

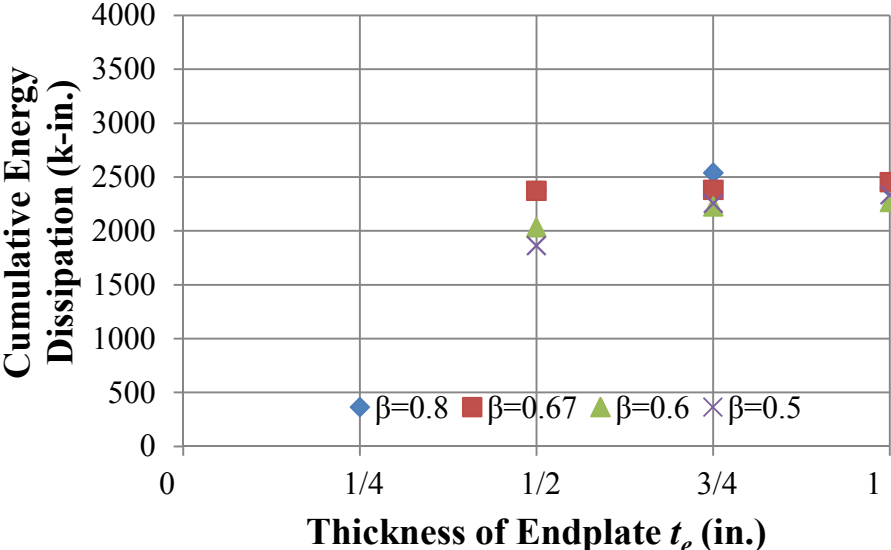


Figure 5.20 Effects of Endplate Thickness (t_e) on Cumulative Energy Dissipation

5.3.6 Cycling Effects

To consider HSS based collar connections in seismic moment frames, their cyclic behavior must be stable when subject to continued cycling with only minor moment capacity degradation. The hysteretic behavior obtained from 28 collar connections in the parametric study suggests that beam width thickness ratio, b/t ; depth thickness ratio, d/t ; beam endplate thickness, t_e ; and collar thickness, t_c , are the most important factors to determine whether the connections can develop the plastic moment capacity of the beam and their degree of moment degradation under cyclic loads. The collar connections with smaller b/t and d/t ratios exhibit fuller hysteresis loops with minor moment degradation observed under continued cyclic loads. Collar plate yielding or

endplate yielding prior to the formation of the beam plastic hinge will limit the development of the plastic moment capacity of the beam which is undesirable for seismic application.

AISC (2010a) specifies that in special moment frames (SMF), the flexural resistance of the connection should be at least 0.80 times the plastic moment capacity of the beam at an interstory drift angle of the 0.04 rad. Thus the moment capacity at the 0.04 rotation level is an important criteria for consideration of the use of collar connections in SMF. Twenty four out of 28 HSS based collar connections achieve their maximum moment at or after 0.04 rad. cycle showing their suitability in SMF under seismic loads. The collar connections with the largest b/t and d/t ratios (i.e. the connections with HSS 12×8×5/16 and HSS 12×6×1/4 beams) exhibit the largest moment degradation under continued increasing cyclic loads. Due to the earlier onset of local buckling in the HSS beam, these connections are unable to sustain 80% of their plastic moment capacity up to the 0.04 rad. drift level after reaching their maximum moment at around the 0.03 rad drift level.

5.4 Implications for Future Design

The HSS based collar connections are capable of developing plastic hinges in HSS beams with stable hysteretic behavior and minor moment degradation which is desirable for seismic application. Both the experimental tests and numerical study show promise for their application in seismic moment frames. However, since almost all of the inelastic deformation is concentrated in the HSS beam member, the panel zone of the connection is underutilized which leads to an inefficient design for the moment connections. At the same time, the welding configurations also limit the function of the collars since deformation of the endplate is constrained by the fillet welds on the column face and groove welds along the endplate edges. These welds are the reason why collar yielding only controls in the connections with the largest HSS beams as described in the parametric studies in Chapter 3 and Chapter 5. Thus to improve the seismic performance of the HSS based collar connections, sharing of the inelastic deformation with other structural components needs to be considered.

One improvement is to eliminate fillet welds on the top surface of endplate along the edge of the collars as well as the fillet welds on the column face along the end of the endplate. The revised

weld configuration is provided in Figure 3.11. The welds along the length of the endplate are expected to transfer only shear force from the HSS beam while bending moment is transferred to the collars as tension and compression loads from the endplate. As a result, the collar plates can more efficiently transfer loads and share inelastic deformation with other structural component.

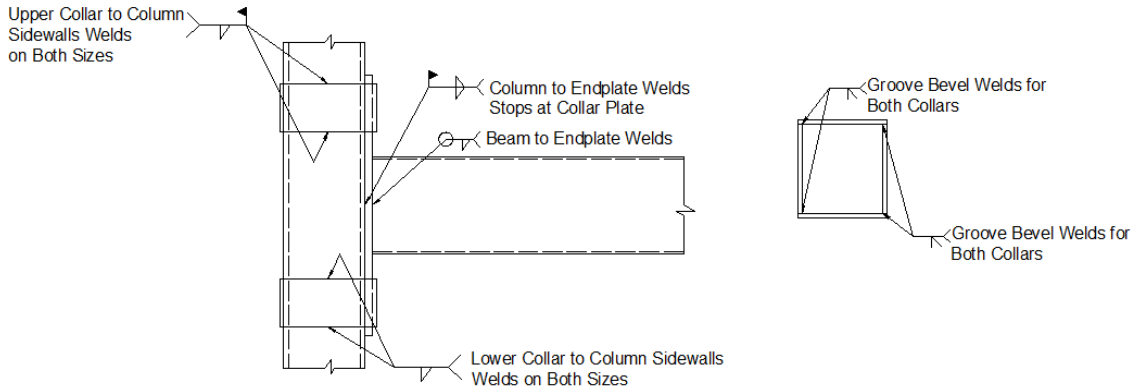


Figure 5.21 Proposed Optimized Weld Configurations

5.5 Conclusions

The calibration and validation of two FE models to experimental test results of the HSS based collar connections are conducted leading to a parametric study of HSS based collar connections subject to increasing cyclic loads. The parametric study consists of 28 collar connections with b/t from 10.8 to 24.5, d/t from 14.2 to 48.5, t_e from 1/2 in. to 1 in. and t_c from 1/4 in. to 1/2 in. All of the collar connection FE models incorporate 1% geometric imperfections of the beam section geometry and experimentally measured material properties. The parametric study results have been evaluated in terms of hysteretic behavior, secant stiffness and energy dissipation capacity with respect to t_e , t_c , b/t and d/t . The cycling effects on the behavior of the collar connections are also considered with a focus on the degradation of moment capacity at 0.04 rad. Based on the test and parametric study results, future design recommendations are proposed with improvements on the weld configuration. The key conclusions are summarized as follows:

1. FE models developed in Abaqus utilizing shell elements for HSS members, solid elements for endplate and collars, experimentally measured material properties and 1%

geometric imperfections are sufficiently accurate to simulate cyclic performance of the collar connections subject to seismic loads. The FE models of collar connections without and with stiffeners underestimate the moment capacity of the connection by 9% and 4%, respectively, and under predict secant stiffness by 7% for both connection models.

2. Among the 28 HSS based collar connections, beam width to column width ratio, β , exhibits little effect on the seismic performance of the collar connections since forces can be more efficiently transferred to the column sidewalls through the endplate. The effect of the collars is limited due to the weld configurations applied in the parametric study. However, in the connections with the largest beam plastic modulus, collar yielding controls the seismic performance leading to a failure to develop the beam plastic moment capacity.
3. For all but four of the 28 collar connections, the moment capacities are greater than the beam plastic moment capacity. Increasing t_e leads to increases in moment capacity since more inelastic deformation is observed outside the endplate for the connections with a thicker endplate. With increasing b/t , moment capacity of the collar connection decreases due to early initiation of local buckling. However, the normalized moment capacity is less than unity for beams with the smallest b/t attributable to the fact that collar plates yielding results in limited increases in maximum moment.
4. Secant stiffness increases with increasing endplate thickness, t_e , at small and intermediate rotation levels due to the fact that a thicker, stiffer endplate allows the HSS beam to be more involved in inelastic deformation. The larger moment achieved in the connections with a thicker endplate at the intermediate level may lead to excessive deformation in the HSS beam as rotations increase. As a result, larger moment degradation observed in the connections with a thicker endplate will lead to a decrease in secant stiffness at larger rotation levels.
5. A decrease in b/t and d/t ratio will lead to a larger secant stiffness since the HSS beam with smaller b/t and d/t is less susceptible to local buckling. The collar connections with larger beam sections tend to be much stiffer at the early cycles.

6. Cumulative energy dissipated throughout the loading history decreases with increasing b/t and d/t . The collar connections with larger beam sections tend to dissipate more energy due to the larger hysteresis loops exhibited under cyclic loads.
7. For all except four of the 28 collar connections, moments sustained at 0.04 rad. are larger than 80% of the beam plastic moment capacity indicating their feasibility in SMF. All the collar connections can sustain 80% of the beam plastic moment capacity at the 0.02 rad. cycle showing their viability in IMF.
8. Optimization of the weld configuration based on experimental and numerical studies has been proposed, but needs further exploration.

CHAPTER 6 STUDY ON FILL MATERIAL

6.1 Introduction

Steel structures have been designed to absorb earthquake input energy through formation of localized plastic hinges resulting in damage accumulation and significant economic losses (AISC, 2010a). Supplemental energy dissipation systems were devised to provide alternative methods to mitigate structural response and hence reduce or even eliminate structural damage during an earthquake (Christopoulos et al., 2006). These supplemental systems can be used in the construction of new high performance structures or for retrofit of existing buildings. Although they have been proven effective in enhancing the overall performance of structures (Soong & Spencer, 2002), the additional installation of a damping device or base isolation system and detailing requirements associated with these can require additional space that needs special architectural attention. Alternatively, the voids associated with HSS beams are underutilized locations where materials can be incorporated to provide supplemental energy dissipation while also stabilizing the inelastic bending behavior through mitigation of local buckling. Use of the voids in HSS for the fill material also does not require special space demands in the structure or vastly different detailing requirements.

Filling the voids of HSS opens up opportunities for the use of non-traditional civil engineering materials. Potential innovative materials considered include polymer foam and rubber materials which are lightweight compared to other structural materials. Thus, they add little seismic mass in a void fill application, which is beneficial in seismic applications. Polymer foam is well known for its high strength-to-weight ratio and its energy absorption capacity provides beneficial impact protection (Gibson & Ashby, 1999). These properties have led to its use in the aerospace field, mechanical industry, military and other engineering disciplines (Lim et al., 2004; Rizov, 2009). Nevertheless, they have rarely been used in structural engineering and earthquake engineering since few studies have systematically characterized polymer foams under cyclic

loadings. On the other hand, rubber materials have been mainly used in isolation bearings for seismic application in structural engineering. By using rubber, the effectiveness of the base isolation system in enhancing of seismic performance through period elongation has been proven (Morgan & Mahin, 2011). Similar to polymer foam, few studies have considered their viability as fill material in seismic applications. Although both polymer foam and rubber show promise in a void fill application, further exploration is needed to study their performance under cyclic loading conditions.

The objective of this study is to select a suitable fill material for HSS beams undergoing large cyclic loads and to perform extensive mechanical tests on this material to provide better insight into its seismic performance. In this chapter, feasibility of various fill materials such as polyurethane (PU) foam and urethane rubber materials are evaluated based on preliminary monotonic test results and the ability to inhibit local buckling. Upon selection of a viable fill material, a series of mechanical behavior tests are conducted on cube specimens to capture its yield strength, elastic modulus, stress degradation under cyclic loading conditions and Poisson's ratio to better evaluate its suitability for applications in structural and earthquake engineering. The findings from the material tests provide essential data to more accurately model these materials in detailed finite element studies of the filled HSS beams under cyclic bending loads.

6.2 Preliminary Evaluation of Fill Materials

Structural passive control provides an effective way to minimize structural component damage. At the same time, the underutilized voids of HSS provide a suitable location to locate these innovative and non-traditional civil engineering materials which do not require extra space in the structure or special detailing requirements. Some good examples of such innovative materials are polymer foams and rubber. Since they are light-weight materials which add little seismic mass and have high energy absorption properties, they show promise for use in seismic applications. However, few studies have systematically characterized their performance subject to similar loads as seismic loads and further investigation is needed. Thus, their performance under monotonic bending loads is evaluated in the fill application in terms of moment capacity and ability to postpone local buckling. Comparative tests between empty and filled HSS beams to

quantify the benefit of the fill material are considered. Both three point and four point bending tests of filled beams with different fill materials are conducted where the same fill length is used for all the beams. The results provide an understanding of the expected behavior under pure bending and combined bending and shear as illustrated in Figure 6.1. The experimental results provide insight into the seismic performance of the fill materials and their effectiveness to control seismic response in terms of local buckling mitigation and energy dissipation capacity enhancement. The findings also allow for selection of the candidate material to explore more thoroughly for the void fill application.

For the monotonic tests, two sizes of HSS members are considered: HSS 4×4×1/8 and HSS 5×5×1/8 because of their large width-thickness and depth-thickness ratios, which are 31.5 and 40.1, respectively. These ratios suggest that local buckling will occur under bending and provide feasibility of evaluating whether local buckling is inhibited by the presence of the fill materials. Each of the HSS specimens is cold formed and made of ASTM A500 Gr. B steel that has a specified minimum yield strength of 46 ksi and a specified minimum tensile strength of 58 ksi. The theoretical plastic moment strengths are 118 k-in and 187 k-in when calculated using the specified minimum yield strength multiplied by the theoretical plastic section modulus for the section.

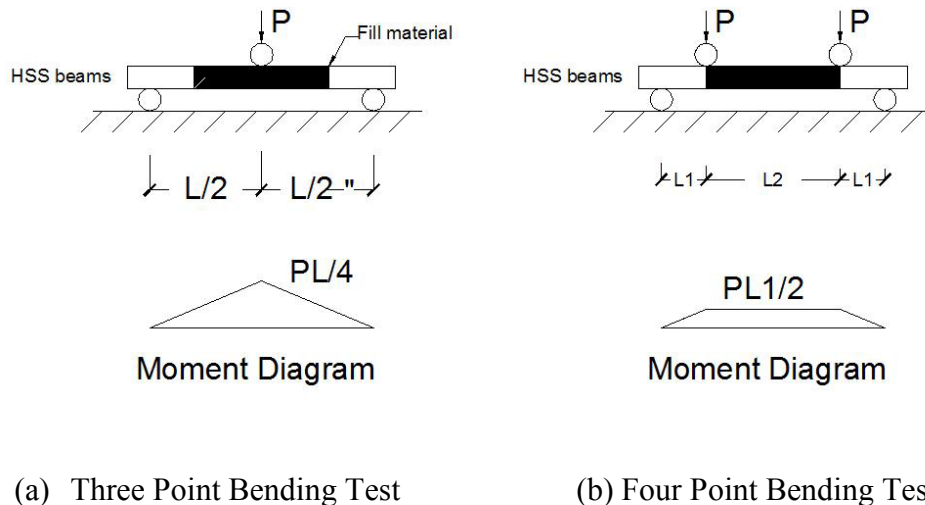


Figure 6.1 Monotonic Bending Tests

6.2.1 Monotonic Bending Tests

6.2.1.1 Fill Materials

Three expanding PU foams and one urethane rubber material are selected as fill materials. All of those materials are made from a two part pourable liquid mix. When cured, the PU foam is a closed cell foam whose density depends on its expansion during curing. To consider the effect of the PU foam's density on its use as a fill material in HSS, three densities of PU foam are considered, 4 lb, 8 lb and 16 lb which indicates the weight per cubic foot. Manufacturer stated properties for the three types of foams are listed in Table 6.1.

Table 6.1 Properties of PU Foams

	4lb Foam	8lb Foam	16lb Foam
Parallel Compressive Strength	90 psi	250 psi	580 psi
Tensile Strength	110 psi	225 psi	450 psi
Shear Strength	70 psi	130 psi	230 psi
Flexural Strength	120 psi	350 psi	750 psi

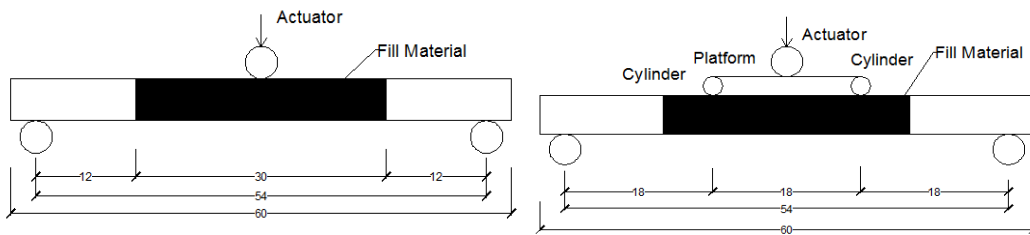
*properties from <http://www.uscomposites.com/foam.html>

Rubber is also considered because of its ability to sustain large deformations while continuing to remain elastic. Among potential rubber materials, urethane rubber exhibits good wear resistance and is easy to use in a fill application since it can be poured, brushed on or sprayed on a surface or into a void. After curing, there is little shrinkage which means no undesirable voids will form within the HSS. The selected urethane rubber for evaluation is one type of concrete molding and stamping urethane rubber with a reported tensile strength of 650 psi and tensile elongation of 150%.

The fact that the PU foam and rubber materials are initially liquid and the shape of their solid form is dependent on the mold into which they are poured makes them an excellent candidate for HSS void fill applications. Manufacturer recommended mixing procedures are used for all four fill materials. The intent of these materials is to increase energy dissipation of the HSS during bending and postpone local buckling leading to the potential use of HSS with larger width-thickness and depth-thickness ratios, while not significantly increasing the strength and weight as is seen with concrete filled HSS.

6.2.1.2 Test Setup and Loading Protocol

Eleven HSS beams with different section sizes and fill materials are tested under monotonic increasing bending loads (Table 6.2). The length of each beam is 60 in. and the fill length is 30 in. at the center of the beam. The clear span between the two supports is 54 in. for all of the HSS beams as shown in Figure 6.2. For the four-point bending tests, the load is applied through a platform which is supported by two cylinders that rest on the beam toward the end of the fill region. The loading beam spans one third of the beam's length at the center of the beam dividing the beam into three segments of equal length. As for the three-point bending tests, the load is applied at the center of the beam. The loading is displacement controlled with a loading rate is 0.001 in./s. The test is terminated when the deflection of the beam is approximately 1.1 in. representing a rotation of 0.04 rad. provided the bending capacity of the beam has been reached. Instrumentation utilized for these tests include a grid of optical tracking markers on the web of the HSS beams to measure displacement (Figure 6.3) and a 100 kips load cell to record load applied by the actuator.



(a) Three-Point Bending Tests

(b) Four-Point Bending Tests

Figure 6.2 Schematics of Monotonic Bending Test Setup

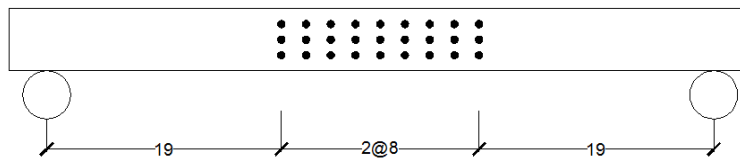


Figure 6.3 Layout of the Optical Tracking Markers

6.2.1.3 Test Results

The preliminary results of the foam filled HSS beams are compared with empty beams under monotonic loading. Moment is computed as shown in Equation 6.1 and Equation 6.2 for the beam in the three-point and four-point bending, respectively. Rotation of the beam is derived utilizing Equation 6.3 which takes the deflection at the center of the beam divided by half the beam span.

$$M = PL/4 \quad \text{Equation 6.1}$$

$$M = PL/6 \quad \text{Equation 6.2}$$

$$\theta = 2\delta/L \quad \text{Equation 6.3}$$

P is the load applied by the actuator; L is the full span of the beam; M is the measured moment; δ is the measured deflection at the center of beam and θ is the rotation at the center of the beam.

During the tests, local buckling is observed near the center of all the beams except for beam No. 4. In beam No. 4, localized damage is observed where load is applied which negatively affects its performance. The smaller HSS beams achieve their maximum moment capacity at later cycles which is attributable to the later onset of local buckling provided they have smaller width thickness and depth thickness ratios.

Figure 6.4 and Figure 6.5 provide the moment-rotation curves for the three-point and four-point monotonic loading tests. All of the filled beams show an increase in moment compared to the empty HSS members under the same loading condition, except for Beam No. 4. In Beam No. 4, moment capacity is almost the same as the empty HSS beam, whereas in Beam 2, the moment capacity is 13% larger than that of the empty HSS beam. In the three-point bending tests, the 8 lb, 16 lb PU foam and urethane rubber fill materials increase moment capacity by 18%, 37% and 4.4% compared to the empty HSS. Compared to the urethane foam, PU foams are more effective in enhancement of moment capacity of the HSS beams. An increase in moment capacity is advantageous for structural application, although it is not anticipated due to the fact that the strength of the foam is negligible compared to that of steel.

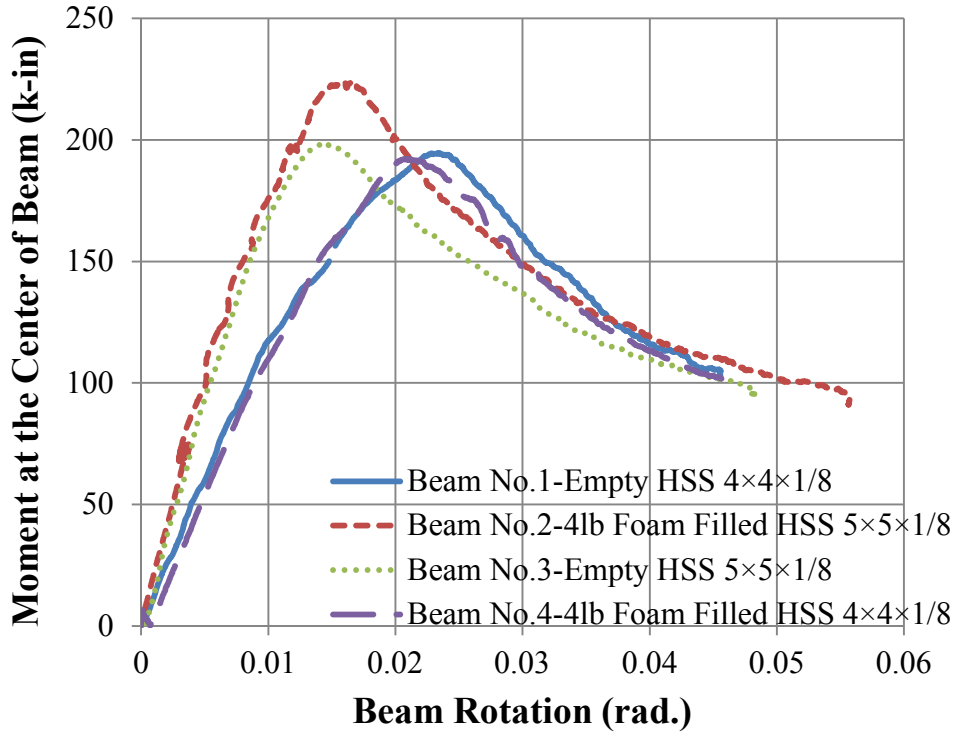


Figure 6.4 Moment-Rotation Curves for the Four-Point Bending Tests

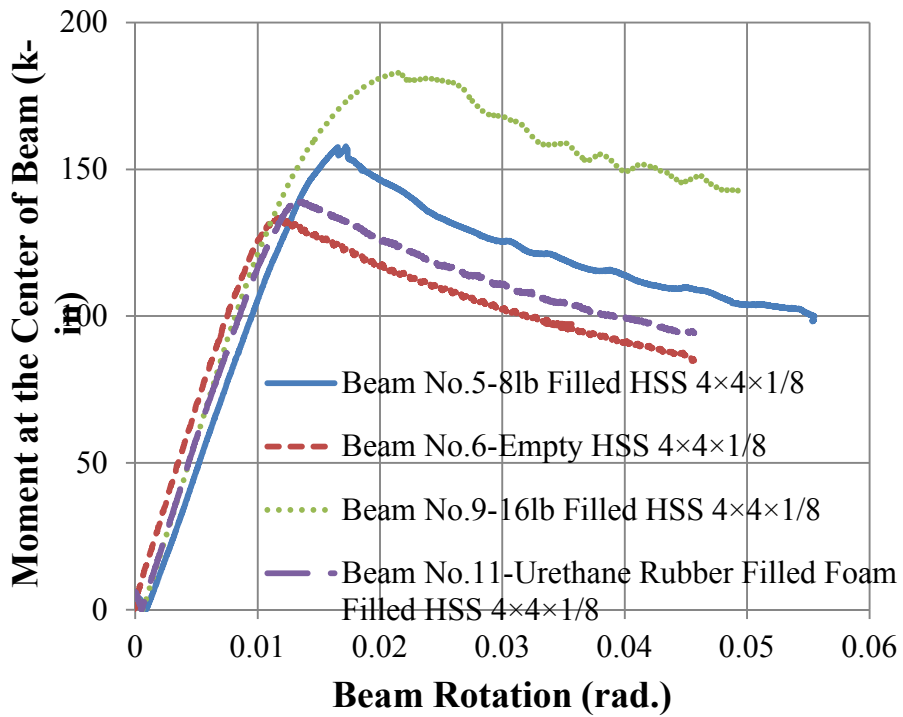


Figure 6.5 Moment-Rotation Curves for HSS 4×4×1/8 in Three-Point Bending Tests

The 4 lb, 8 lb, 16 lb PU foams and the urethane rubber postpone local buckling by up to 0.005 rad., 0.005 rad., 0.01 rad. and 0.002 rad., respectively. Upon the onset of local buckling, the moment starts to decrease suggesting the beam lose its ability to sustain larger loads. The PU foams are more effectively compared to the urethane rubber in terms of mitigation of local buckling given that the moment decreases at a slightly larger rotation level. Thus the application of PU foams as fill materials can alleviate local buckling of HSS beams which potentially allows for consideration of wider range of HSS beams especially for those with a larger width thickness and depth thickness ratios.

Table 6.2 Parameters for the 11 Experimental Beam Specimens

Beam No.	Beam Size (in.)	Fill Material	Test Type	Maximum Moment (k-in)	Cumulative Energy Dissipation at 0.03 rad. (k-in.)
1	HSS 4×4×1/8	Empty	4 point	195	11.5
2	HSS 5×5×1/8	4 lb foam	4 point	224	14.3
3	HSS 5×5×1/8	Empty	4 point	198	12.9
4	HSS 4×4×1/8	4 lb foam	4 point	192	11.5
5	HSS 4×4×1/8	8 lb foam	3 point	158	6.5
6	HSS 4×4×1/8	Empty	3 point	133	6.1
7	HSS 5×5×1/8	Empty	3 point	132	5.8
8	HSS 5×5×1/8	8 lb foam	3 point	180	7.7
9	HSS 4×4×1/8	16 lb foam	3 point	183	7.9
10	HSS 5×5×1/8	16 lb foam	3 point	139	5.9
11	HSS 4×4×1/8	rubber	3 point	139	6.1

The initial stiffness of the HSS beams is the same regardless of the presence of the fill materials and the type of fill materials suggesting no enhancement in the beam's elastic stiffness. This finding is expected since the stiffness of the fill material is negligible compared to the stiffness of the steel. The secant stiffnesses of the filled and empty beam at 0.03 rad. are also computed by using the applied loads divided by the displacement at 0.03 rad. Since all of the beams reach their moment capacity prior to the 0.03 rad. rotation level, secant stiffness at 0.03 rad. provides a means of evaluating the post-buckling behavior of the HSS beams. For the four-point bending tests, the 4 lb PU foam improves the secant stiffness by 9% based on a comparison of beam No. 2 and beam No. 3 at the 0.03 rad. rotation level. In the three-point bending tests, 8 lb PU foam, 16 lb PU foam and the urethane rubber can enhance the secant stiffness of the beam by up to

37%, 64% and 8%, respectively. This finding indicates the presence of the fill material can effectively mitigate secant stiffness degradation. The 16 lb foam filled HSS beam exhibit the most significant improvement in terms of alleviation of stiffness degradation.

The cumulative energy dissipated at 0.03 rad. is computed as the enclosed area of the load-displacement curves to provide better understanding of energy dissipation capacity of each fill material (Table 6.2). In the three-point bending tests, the cumulative energy is 9% larger for the 4 lb PU foam filled HSS beam compared with the same size empty beam. In the four-point bending tests, the HSS beams filled with 8 lb PU foam, 16 lb PU foam and the urethane rubber dissipate 34%, 30% and 1% more energy at the 0.03 rad. rotation level, respectively. The 16 lb PU foam exhibits the second largest energy dissipation capacity compared to other PU foam and the urethane rubber showing promise for seismic application.

6.2.2 Fill Material Selection

The monotonic bending tests of the empty and filled HSS beams provide better insight into the effects of these lightweight, non-traditional materials on mitigation of local buckling, alleviation of post buckling stiffness degradation and enhancement of energy dissipation capacity. As a result, the most suitable fill material is selected for further exploration of its feasibility as fill material in seismic applications.

PU foams exhibit better ability to stabilize post buckling behavior and dissipate input energy compared to the urethane rubber. Previous study showed that elastic modulus and yield stress of the closed cell PU foam increases with increasing density (Linul et al., 2013), which is consistent with the monotonic test results.

During the monotonic tests, 16 lb PU foam is the most effective material in postponing the occurrence of local buckling given the 16 lb PU foam filled beam reaches its maximum moment at approximately 0.01 rad. later than the empty HSS beam, whereas the other fill materials only postpone it by 0.005 rad. at most. Although the initial secant stiffness of the filled HSS beams is not improved by the 16 lb PU foam, the post-buckling secant stiffness of the filled beam at 0.03 rad. is increased by 64% which is the largest improvement among all the fill materials. Cumulative energy dissipated at 0.03 rad. is also increased by 30% due to the presence of the 16

lb PU foam. Meanwhile, a slight increase in the moment capacity of the 16 lb PU foam filled HSS beam can be expected based on the monotonic test results. The overall excellent performance achieved by the presence of 16 lb foam suggests that it is the most suitable fill material among four types of lightweight materials studied.

6.3 Further Details of Selected PU Foam

PU foam is one of the most widely used polymer foams among a highly diverse family of polymer or plastic foams. PU foam refers to a type of polymer foam made of urethane linked molecular chains. Research on the microstructure of PU foam has shown that its mechanical properties are affected by the manufacturing process. The flexible and rigid PU foams differ in mechanical properties due to different microstructure although they both have low density. The 16 lb PU foam is a closed cell and rigid PU foam.

Various standards developed by ASTM stipulate test methods for PU foams under different loading conditions. ASTM D1621 (2010) and ASTM D1623 (2009) describe standard test methods for compressive properties of rigid cellular plastics and tensile and tensile adhesion properties of rigid cellular plastics, respectively. ASTM D3039 (2014) proposes standard test method for tensile properties of polymer matrix composite materials, but these materials are reinforced by high-modulus fibers. ASTM D3574 (2016) specifies standard test methods for flexible cellular materials which apply to slab, bonded and molded urethane foam.

The PU foam used in this study is an expanding PU foam typically used in marine flotation (low density foams) and architectural casting support application (high density foams). It is selected as fill candidate due to its superior strength and energy dissipation capacity as demonstrated in the previous section. The foam is made from a two-part pourable liquid. The two liquid components are combined with a mix ratio of 1:1 and allowed to cure. The resulting PU foam is a closed cell foam with an approximate density of 16 lb per cubic foot after expansion. The expansion volume is approximately 4:1. The manufacturer specified properties are provided in Table 6.1. All of the mechanical properties in Table 6.1 represent typical values and may vary due to variables associated with creating the foam (temperature, mold size, mixing time, confinement, etc.).

To further characterize the mechanical properties of the 16 lb PU foam and provide better insight into its feasibility to inhibit local buckling and increase energy dissipation capacity as a fill materials in HSS members under large cyclic loads, two liquids are combined in equal parts and thoroughly mixed together to initiate the chemical expansion and curing process. The mixed liquid is poured into a five sided mold which allows the foam to expand in the vertical direction. After 24 hours curing, the mold is removed and the cured slab of foam is cut into 1.5 in. cubes (Figure 6.6) in such a way that the majority of the foam material is from the interior portion of the foam slab. The cubes are prepared to evaluate the foam's mechanical properties under both monotonic and cyclic compression tests. ASTM D1621 (2010) requires at least five specimens be tested to obtain reliable mechanical properties under compression.



Figure 6.6 Picture of the PU Foam Cube and Schematic with Dimensions

6.4 Compression Test

6.4.1 Test setup

To evaluate the behavior of the PU foam under compression, both monotonic and cyclic compression tests are performed to simulate loadings expected during an earthquake. Loads are applied in displacement control using a 22 kip hydraulic uniaxial testing apparatus. Two flat, horizontal steel platforms are used to apply the load to the top and bottom of the foam while the four sides of the foam are unconstrained as shown in Figure 6.7. The crosshead displacement is found to provide an accurate measurement of the foams deformation based on comparison to measurements taken using a linear variable displacement transducer. Given the expected variability, a large number of specimens from multiple batches of material are tested in order to

better understand and evaluate the variation and non-homogeneous nature of the compressive properties of the PU foam.

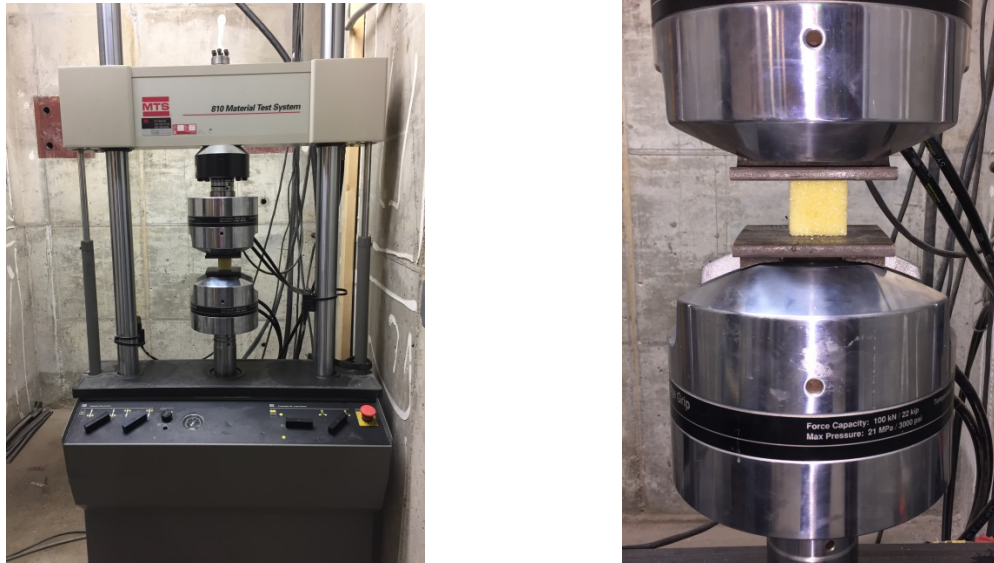


Figure 6.7 Test setup of PU Foam Cube under Compression

6.4.2 Loading Protocol

To investigate whether this foam is sensitive to loading rate, three different loading rates, 0.01 in./s, 0.1 in./s and 1 in./s, are considered here which are equivalent to strain rates of 0.007/s, 0.07/s and 0.7/s, respectively. For the monotonic tests, the cubes are compressed up to 80% of their original height and a constant displacement is applied at the three specified loading rate. For the cyclic compression tests, the loading protocol consists of two cycles at each deformation level with deformation cycles increasing from 10% to 40% in increments of 10% followed by four cycles to 50% of the PU cubes original height. The loading protocol is plotted in Figure 6.8. In terms of the applied crosshead displacement, like the monotonic test, the cyclic tests are run at the three specified loading rates.

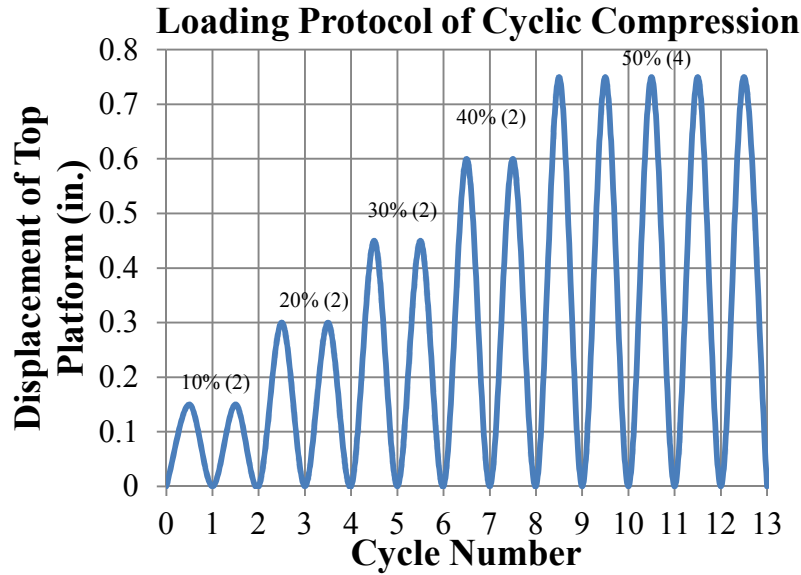


Figure 6.8 Loading Protocol of PU Foam Cube under Cyclic Compression

6.4.3 Monotonic Compression Test Result

Monotonic compression tests of the PU foam provide some basic mechanical properties for structural applications, variation of those properties between samples and important data for developing material models for numerical studies. Three batches of the PU foam are created from the same two part liquid except at different times. The compression stress-strain relationship is shown in Figure 6.9 through Figure 6.11 for the different loading rates. The blue dotted lines represent the stress-strain curves for the first batch of material designated as Group 1, the green solid lines represent the second batch of material designated as Group 2 and the red dashed lines represent the last batch designated as Group 3. Stress is calculated as the load measured by the load cell divided by the average cross-sectional area of the specimen measured at three different locations along its height. The strain is calculated as the crosshead displacement divided by the original height of the specimen. Twenty-seven specimens are tested at each of the three loading rates, 0.01 in./s, 0.1 in./s and 1 in./s, respectively. The stress-strain curve is similar to the schematic stress-strain relationship of polymer foam shown in Figure 2.19 and can be divided into three regions, which include initial linear elastic behavior, followed by a plastic plateau with much lower stiffness due to foam crushing, and at the end an increase in stiffness at larger deformations due to foam consolidation. The initial elastic modulus, yield strength based

on the 0.2% offset method, and stress at 10%, 20%, 30%,40%, 50% and 60% strain levels are analyzed.

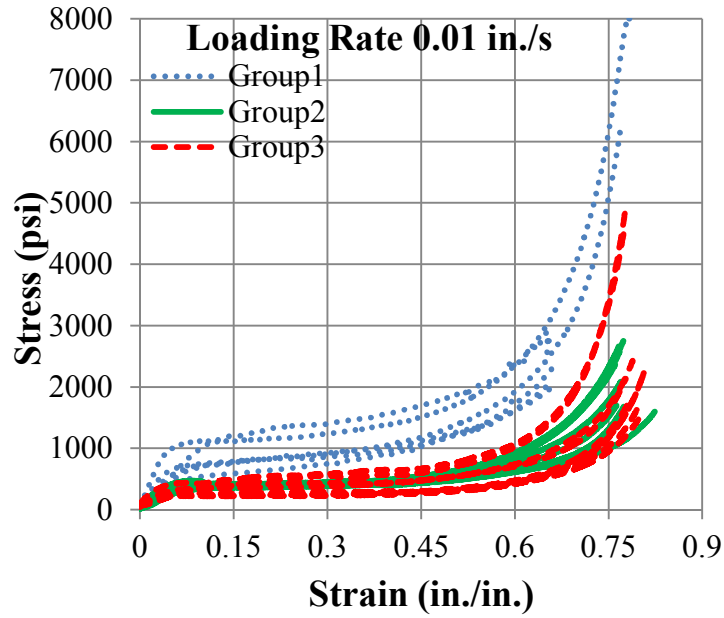


Figure 6.9 Engineering Stress-Strain Curve of PU Foam Cubes under Monotonic Compression Loads at 0.01 in./s

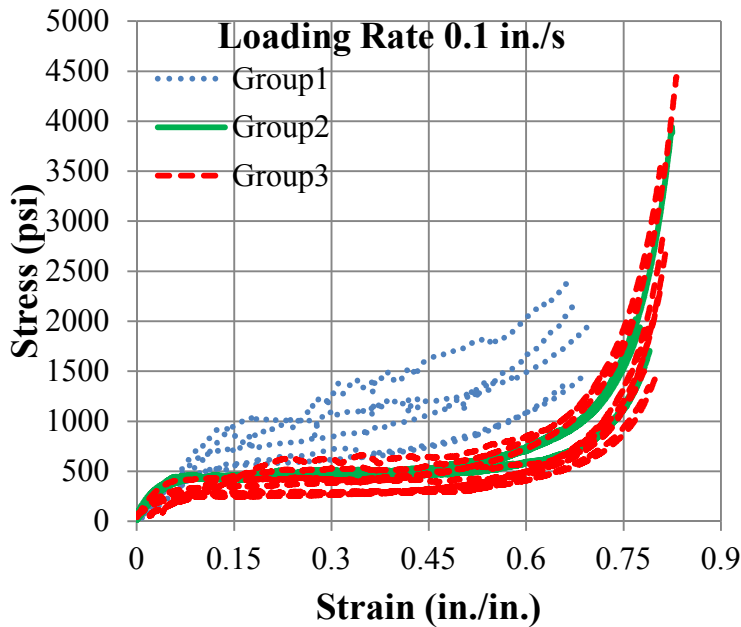


Figure 6.10 Engineering Stress-Strain Curve of PU Foam Cubes under Monotonic Compression Loads at 0.1 in./s

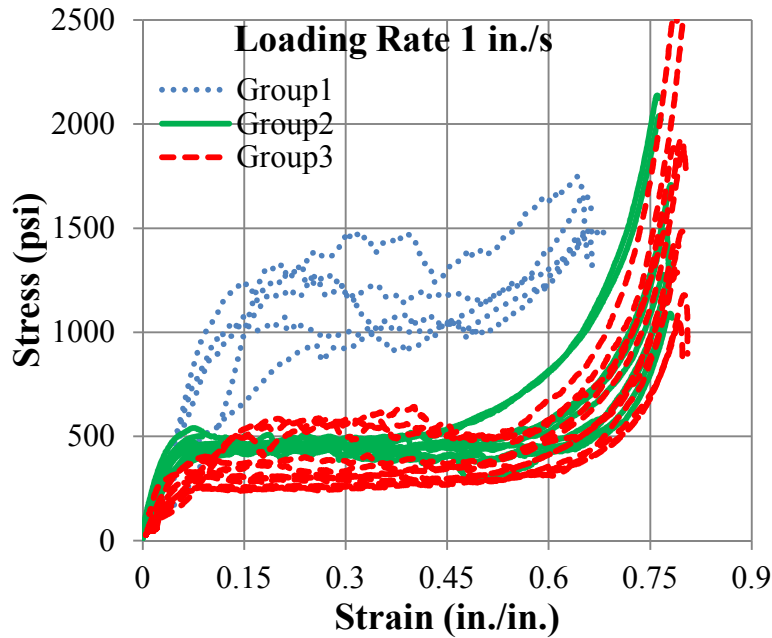


Figure 6.11 Engineering Stress-Strain Curve of PU Foam Cubes under Monotonic Compression Loads at 1 in./s

As shown in Figure 6.9 through Figure 6.11, under different loading rates, yield stress and stress at different strain levels in Group 1 are generally larger than that of other samples in Group 2 and Group 3 indicating the mechanical properties of the samples are affected by ambient temperature when mixing, curing and human factors such as manufacture quality, temperature and non-homogeneity of the material (Subhash et al., 2006). However, the yield stress and elastic modulus in Group 2 and Group 3 are fairly consistent.

On average, the initial linear behavior terminates at approximately the 0.05 strain level for all loading rates. The linear elastic behavior of samples in Group 1 is sustained to larger strain levels, up to 0.15 at the loading rate 1 in./sec. The respective average elastic modulus is 7920 psi, 6920 psi and 7790 psi with standard deviations of 4280 psi, 2500 psi and 2700 psi for samples tested at loading rates of 0.01 in./s, 0.1 in./s and 1 in./s as shown in Figure 6.12. The average yield stress of all the samples is 380 psi, 390 psi and 400 psi with standard deviations of 210 psi, 190 psi and 230 psi with increasing loading rates as shown in Figure 6.13. The average yield stress of the samples increases slightly with increasing loading rate which is attributable to the fact that under dynamic loads, the inertia of the porous cells in the PU foam can resist the deformation leading to slightly larger stress achieved compared to static loads.

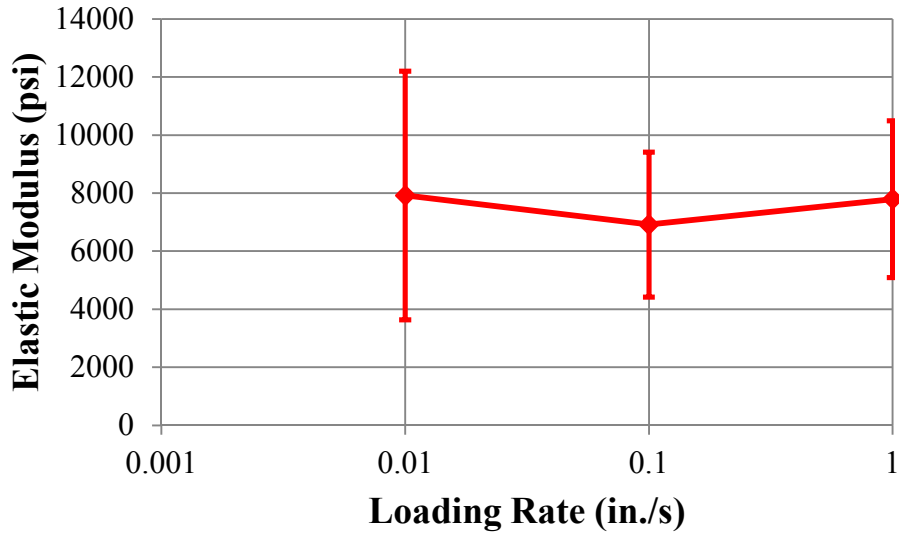


Figure 6.12 Average Elastic Modulus with Standard Deviation at Different Loading Rates

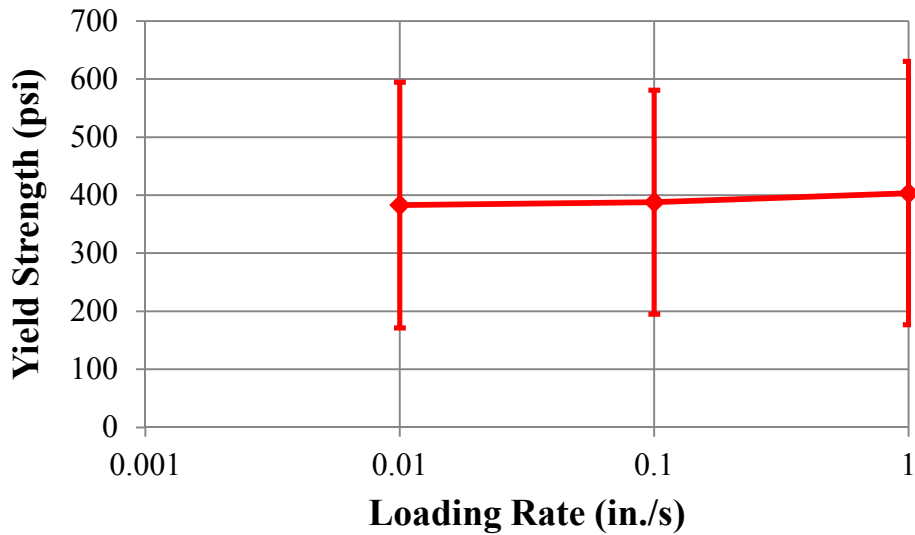


Figure 6.13 Average Yield Stress with Standard Deviation at Different Loading Rates

The elastic modulus and yield stress have significant scatter as shown in Table 6.3. In Figure 6.12 and Figure 6.13, error bars indicate one standard deviation of each parameter among the specimens. The large scatter in the material properties of Group 1 through Group 3 necessitates more study on the potential factors that can affect the mechanical properties of the foam since a good prediction of mechanical behavior is required for its application in structural engineering. The fairly consistent material data in Group 2 and Group 3 shows the standard deviation for yield

strength is only 85 psi, 60 psi and 70 ksi at increasing loading rates, respectively. This finding suggests care should be taken when mixing the foam material to obtain consistent material properties.

Figure 6.14 plots the stress at each strain level which suggests at small strain levels, stress is insensitive to loading rates while at large strains, stress increases with decreasing loading rates. As a result of foam consolidation, stress at large strains increases from around 500 psi up to 960 psi at the 0.01 in./s loading rate. On average, an increase in loading rate will lead to a slight increase in the compressive yield strength. However, at larger strain levels when consolidation begins, the stress measured at slower loading rates is slightly larger than that at faster loading rates. These findings suggest that at small strain level (strain less than 0.4), 16 lb PU foam is rate independent in terms of compressive yield strength and stress measured at each strain level whereas at large strain levels, loading rate should be considered. In the void fill application, 16 lb PU foam can be considered as insensitive to loading rate since strain levels should be relatively small under seismic loads compared with the large strains applied in these tests.

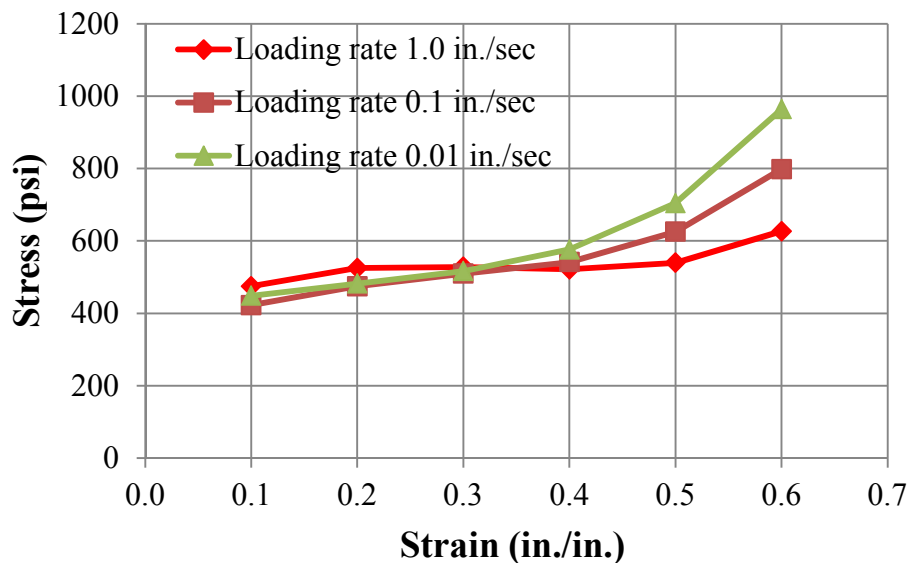


Figure 6.14 Stress at Different Strain Levels

The findings from the tests of the polymer foam under monotonic compressive loads suggest that there is at least a minor loading rate effect in regards to how the foam's voids collapse and consolidate. However, the loading rate effects on the elastic modulus, yield strength, and stress at

small strain levels (i.e. less than 40% strain) are negligible since the discrepancy is fairly small compared to their standard deviation. Significant variation between samples for all of these properties is observed as a result of the non-homogeneity of the material and manufacturing variables.

Table 6.3 Elastic Modulus and Yield Strength of 16 lb PU Foam under Monotonic Compression

Loading Rate (in./s)	Average of Elastic Modulus (psi)	Standard Deviation of Elastic Modulus (psi)	Average Yield Strength (psi)	Standard Deviation of Yield Strength (psi)
0.01	7920	4280	380	210
0.1	6920	2500	390	190
1	7790	2700	400	230

6.4.4 Poisson’s Ratio Test

Poisson’s ratio represents the ratio of transverse strain to axial strain which serves as the basis for stress and strain analysis. Since PU foam has more complex material characteristics which are quite different from metals, traditional methods such as extensometers, speckle interferometry, and holography methods for measurement of Poisson’s ratio of metals cannot obtain accurate results (Zhao & Jin, 1996). To characterize the Poisson’s ratio for the PU foam, digital image correlation (DIC), which applies tracking and digital images to measure deformation, displacement, and strain in 2D or 3D, is utilized. The theoretical background of DIC can be found in Schreier et al. (2009). Generally speaking, DIC correlates two images of the foam specimen before and after loading to obtain its deformation. It has been proven an effective and accurate method for deformation analysis owing to developments in computer technology and high-resolution digital cameras. However, DIC measurement of strain for rigid PU foam under large deformations is not applicable due to localized damage in the foam leading to irregular speckle patterns.

6.4.4.1 Test Setup

The experimental test setup for the DIC consists of a digital camera, light sources, computer to record data and 22 kips capacity MTS uniaxial frame to apply the compressive load. Five of the cube specimens manufactured in Group 1 are tested under monotonic compression tests at 0.01

in./s only up to a 10% strain level since large deformation may lead to inaccurate results owing to the occurrence of an irregular speckle pattern as the PU foam crushes. Before the tests, all the surfaces of specimens are free from visible flaws and then coated with a speckle pattern to provide the necessary contrast in the images (Figure 6.15). Then, the digital camera is aligned with the center of the specimen. A high resolution 8.1 megapixels progressive scan digital camera (Prosilica GX3300 4/3" with 18.1 mm by 13.6 sensing area) is used to capture digital images and monitor deformation of the specimens during loading. Images of the undeformed specimen provide a reference picture before load is applied. During loading, images are taken at a constant time interval of 0.1 seconds.

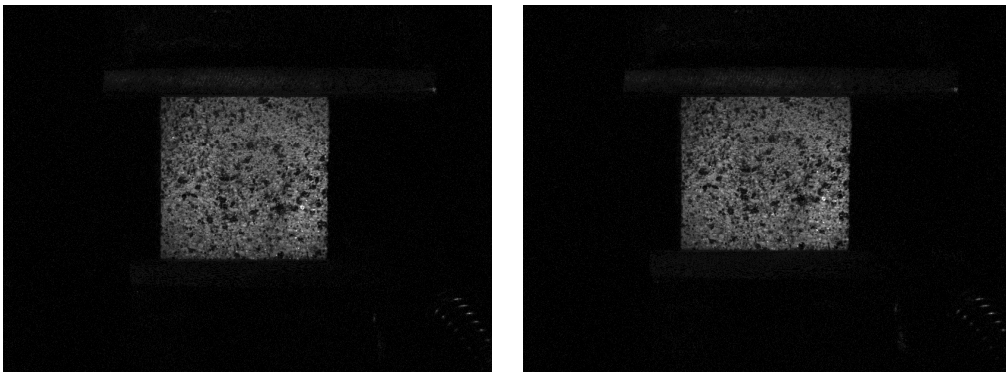


Figure 6.15 Speckle Pattern before and after Compressive Loading (Image size is 3296 by 2472 pixels)

6.4.1.2 Test Result

The undeformed and deformed images of the foam specimens are correlated and analyzed using Vic-2D digital image correlation software from Correlated Solution Inc. (2009). This software is accurate and fast which allows measurement of full field in-plane displacements. The area of interest is selected at the center of the specimen as shown in Figure 6.16. A step size of 2 is used to analyze all points in each direction for fine data analysis. Once the analysis starts, it shows strain or displacement contour as illustrated in Figure 6.17 and Figure 6.18. Computation of strain utilizes mean strain of the area at each time point and the Poisson's ratio is calculated following Equation 6.4. The the data points at the beginning and the end of the tests are removed since at small deformation, strain in the x direction is fairly negligible and the measurement is not very accurate and at the end of the test confidence in the analysis is low owing to crushing of the foam. Figure 6.19 plots the Poisson's ratio measured with respect to image number over time

which indicates that the Poisson's ratio is consistent over time under small deformation. The mean value of the Poisson's ratio and its standard deviation are computed as shown in Table 6.4. The small standard deviation indicates that for each specimen, the Poisson's ratio is almost constant. The average Poisson's ratio is 0.32 with standard deviation of 0.16 for the five specimens. It ranges from 0.08 to 0.47 which is typical for polymer foam and the scatter is attributable to the non-homogeneity of the material.

$$\nu = -\frac{\varepsilon_x}{\varepsilon_y} \quad (\text{Loading in } y \text{ direction}) \quad \text{Equation 6.4}$$

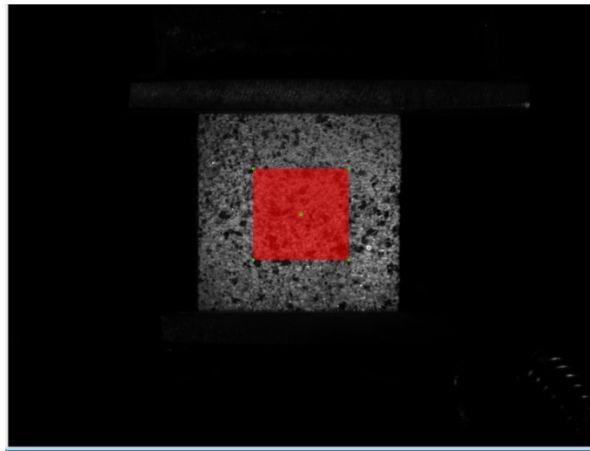


Figure 6.16 Selection of Area of Interest

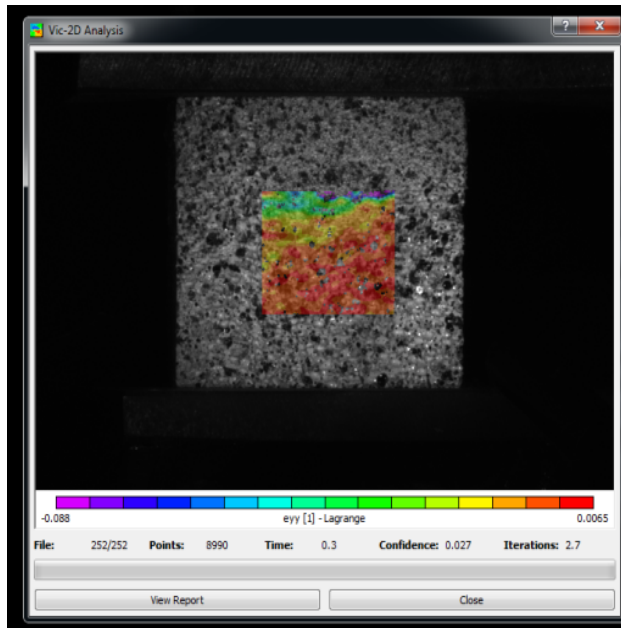


Figure 6.17 Strain Contour during Data Analysis

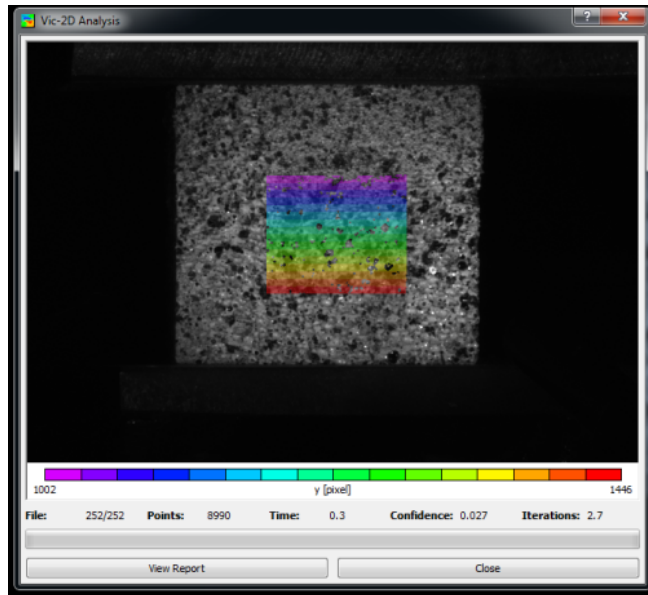


Figure 6.18 Displacement Contour during Data Analysis

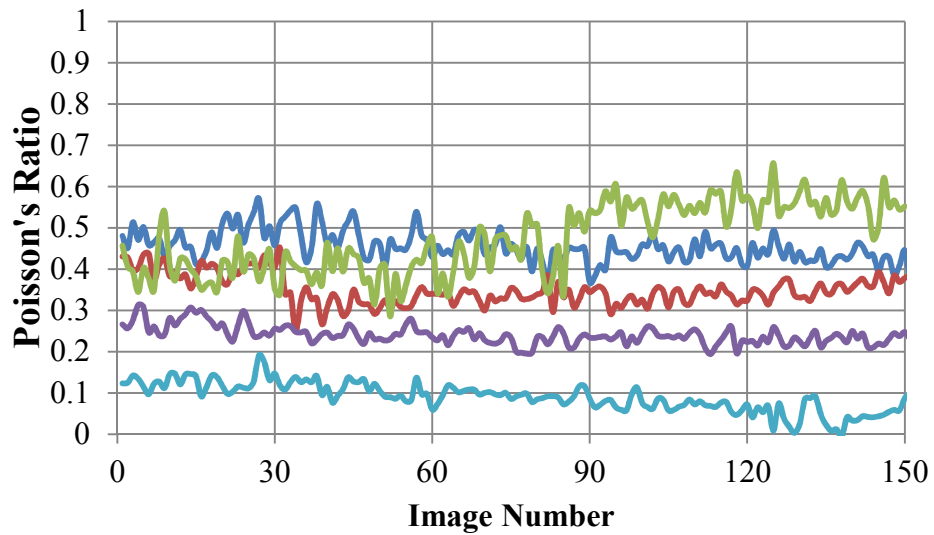


Figure 6.19 Poisson's Ratio at Different Time Points for Five Specimens

Table 6.4 Poisson's Ratio of Each Specimen

Specimen No.	Mean Value	Standard deviation
80	0.08	0.03
52	0.24	0.02
88	0.47	0.09
60	0.36	0.04
108	0.44	0.05

6.4.5 Cyclic Compression Test Result

To characterize the cyclic behavior of the PU foam under seismic loads, increasing cyclic compression tests are carried out to evaluate its performance in terms of ultimate stress at each strain level, energy dissipation capacity, and secant stiffness degradation. The loading protocol is illustrated in Figure 6.8. Crosshead displacement does not correlate with deformation and strain in the polymer foam cube during the unloading and reloading cycles due to the fact that the PU foam is rigid and shows residual deformation under compression loads. As a result of residual deformation, the cube top surface separates from the top platform during unloading to zero deformation. This behavior is accounted for in developing the stress-strain relationship. Stress is calculated as the load from the actuator divided by the average cross-sectional area of each specimen measured at three different locations along its height. The strain is calculated as crosshead displacement divided by the original height of the specimen when the platforms are in contact with the foam. All data points when the loading platforms are separate from the polymer foam are removed. As with the monotonic loading tests, three different loading rates, 0.01 in./s, 0.1 in./s, and 1 in./s (equivalent to strain rates of 0.007, 0.07 and 0.7) are considered to evaluate rate sensitivity of the polymer foam under cyclic compression loads. Two sets of samples are created using the same batch of liquid. The samples are created from the same material from Group 1 and Group 2 in the monotonic compression tests. The cyclic compression stress-strain relationship of 11, 12, and 11 specimens is shown in Figure 6.20 through Figure 6.22 under increasing loading rates, respectively. In those figures, blue dotted lines are the stress-strain curves for Group 1 and green solid lines represent stress-strain curves for specimens in Group 2. The discrepancy between Group 1 and Group 2 in stress-strain relationship is large due to the non-homogeneity of the material, but remains consistent with observations during the monotonic tests.

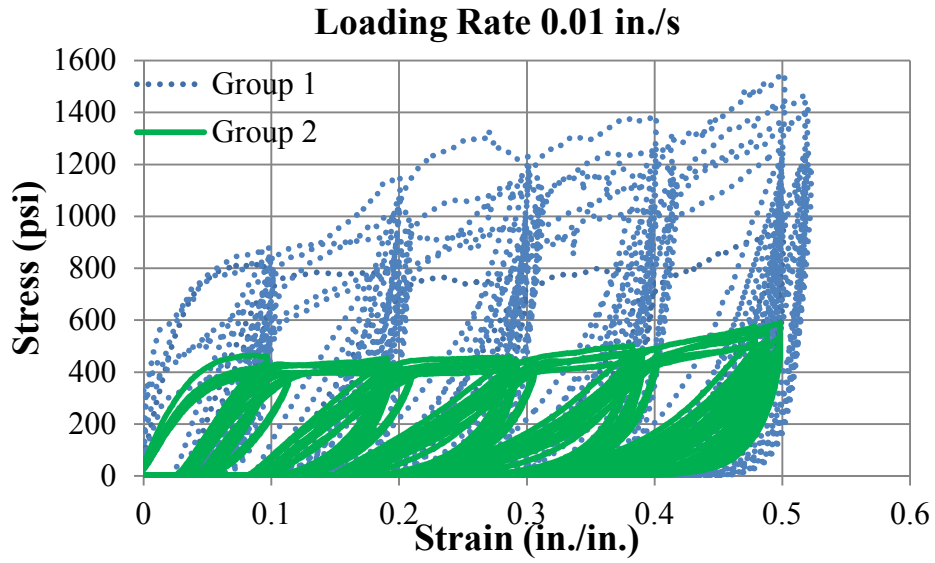


Figure 6.20 Stress Strain Curves at Loading Rate 0.01 in./s under Cyclic Compression Load

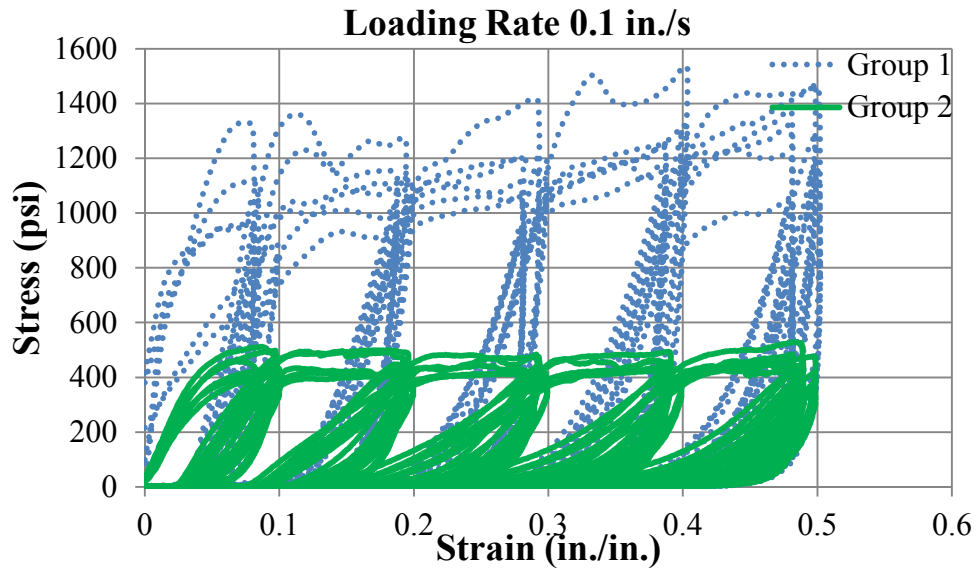


Figure 6.21 Stress Strain Curves at Loading Rate 0.1 in./s under Cyclic Compression Load

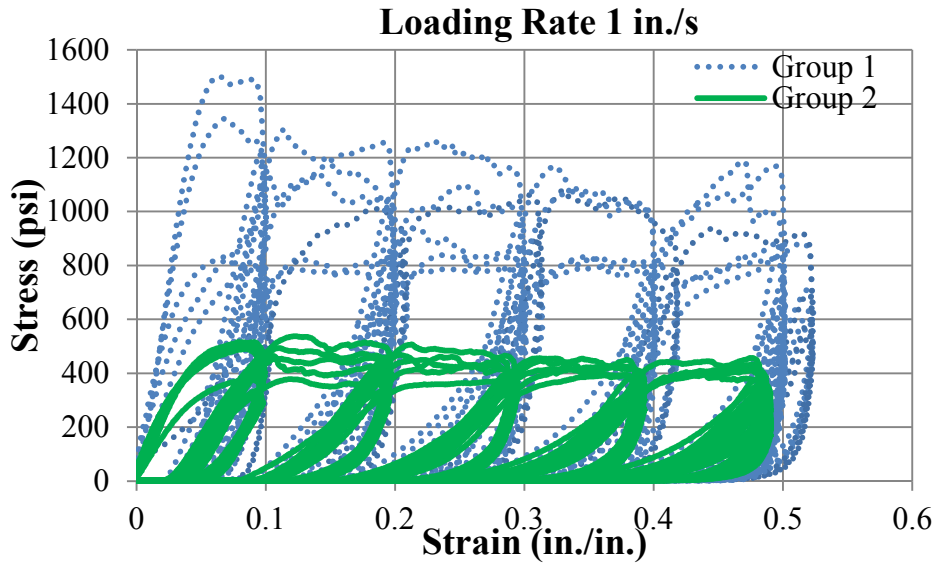


Figure 6.22 Stress Strain Curves at Loading Rate 1 in./s under Cyclic Compression Load

All of the specimens tested exhibit a similar behavior with a large full hysteresis loop during the first cycle to each strain level followed by a much smaller hysteresis loop to the same deformation level due to residual deformation in the foam. Generally, these second cycles show lower maximum stress levels than the first cycle at a given deformation level. For the 0.01 in./s loading rate, the average maximum stress during a cycle increases with increasing strain levels for the first and second cycle of a given deformation level whereas for the 0.1 in./s loading rate, the average maximum stress remains constant. For the fastest loading rate, the maximum cycle stress decreases with increasing deformation level as shown in Figure 6.23 and Figure 6.24. The error bars in these two plots represent one standard deviation for the mean maximum cyclic stress for all specimens at a given loading rate. This maximum cyclic stress level comes much earlier for the fastest loading rate as compared to the two lower loading rates. The average maximum stress ranges from 590 psi to 980 psi, 720 psi to 900 psi, and 730 psi to 780 psi for the first cycle of each strain level under increasing loading rates, respectively. The average maximum stress ranges from 560 psi to 860 psi, 620 psi to 720 psi, and 540 psi to 660 psi for the second cycle of each strain level under increasing load rates, respectively. In the last four cycles which are all at a strain of 0.5, the average maximum cyclic stress decreases significantly for all the loading rates due to the foam crushing. The maximum stress of the samples in Group 1 is significantly larger than that of the samples in Group 2 at a specific strain level. As a result, the standard deviation of maximum cyclic stress at each strain level is approximately 0.4 times the

average value which suggest large scatter is observed in the maximum cyclic stress of each deformation level.

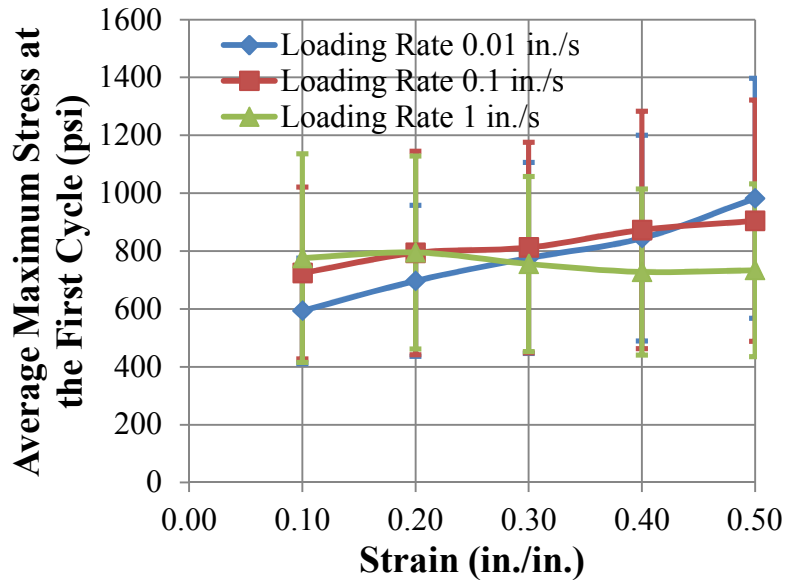


Figure 6.23 Average Maximum Cycle Stress at the First Cycle of Each Strain Level

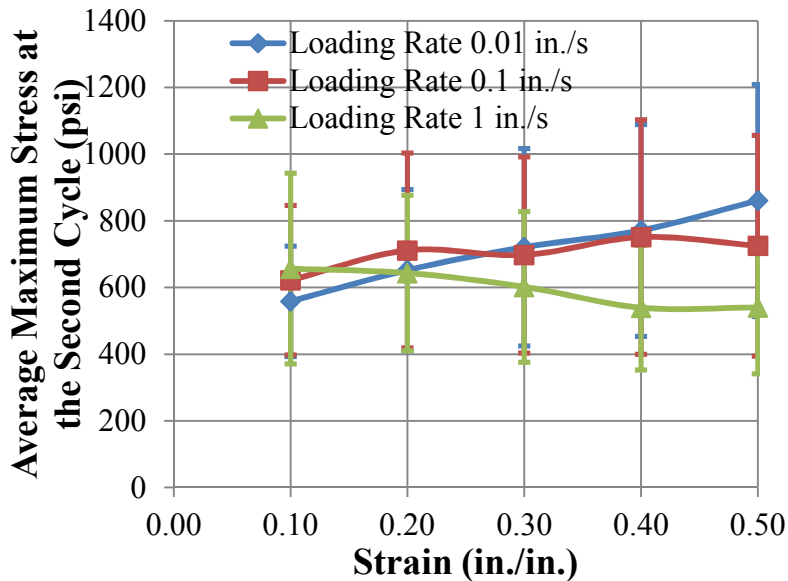


Figure 6.24 Average Maximum Cycle Stress at the Second Cycle of Each Strain Level

The secant stiffness of each cycle is computed as the load at maximum deformation divided by the maximum deformation of that cycle. Secant stiffness decreases with increasing strain levels and secant stiffness in Group 1 is higher than that of specimens in Group 2. At the same strain

level, secant stiffness in the later cycle is lower and the stiffness deterioration is attributable to foam crushing. The secant stiffness of the first cycle of a given deformation level is plotted in the Figure 6.25 through Figure 6.27 for the three different loading rates. At the loading rate of 0.01 in./s, the average secant stiffness ranges from 2940 lbf/in. to 8640 lbf/in. for the first cycle of each strain level. At the loading rate 0.1 in./s, the secant stiffness varies from 2600 lbf/in. to 11740 lbf/in., whereas at the fastest loading rate, secant stiffness ranges from 1520 lbf/in. to 8810 lbf/in. at the first cycle of a given deformation level. The average maximum stress in the highest strain level decreases with increasing loading rates suggesting capacity degradation is more severe at faster loading rates. At faster loading rates, the secant stiffness suddenly drops since low density foam tends to crush in a brittle manner especially under dynamic loads (Subhash et al., 2006). A large scatter is still observed in secant stiffness between specimens in Group 1 and Group 2. This suggests more studies on the variability of the 16 lb PU foam are necessary.

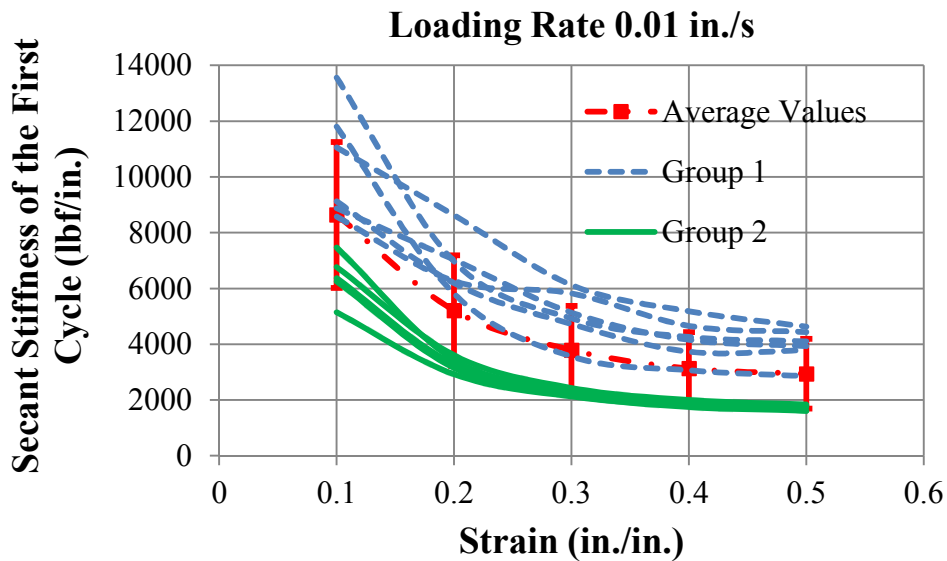


Figure 6.25 Secant Stiffness of the First Cycle at Each Strain Level at Loading Rate of 0.01 in./s

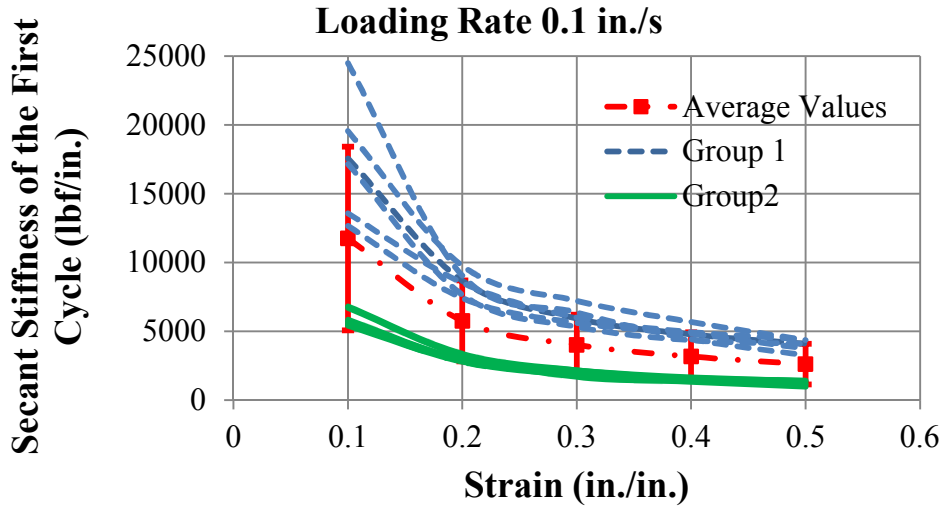


Figure 6.26 Secant Stiffness of the First Cycle at Each Strain Level at Loading Rate of 0.1 in./s

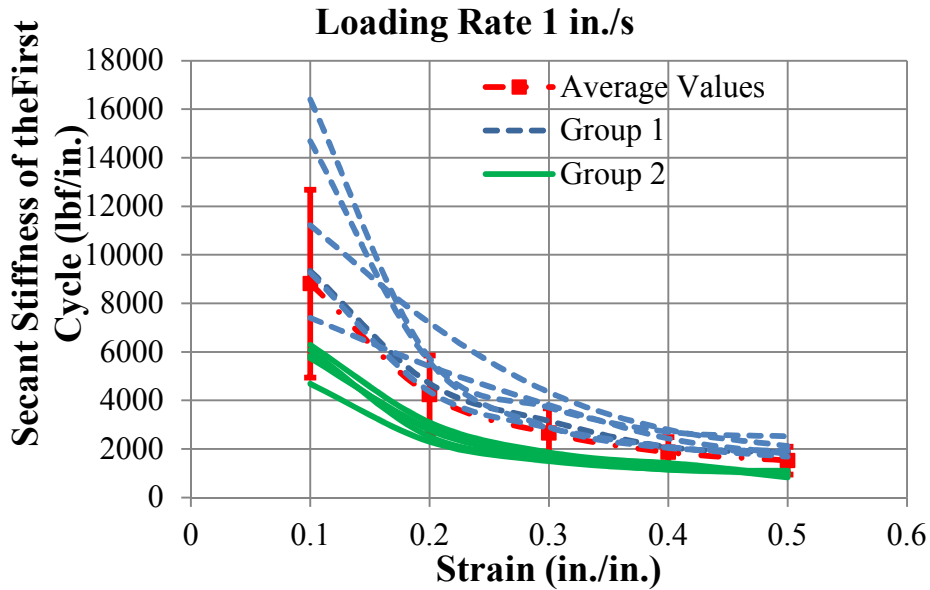


Figure 6.27 Secant Stiffness of the First Cycle at Each Strain Level at Loading Rate of 1 in./s

Energy dissipated in each cycle is calculated by the area enclosed by the load displacement curves as illustrated in Figure 6.28 and 6.29. At the same strain level, the energy dissipated in the first cycle is much higher than that in the later cycle since residual deformation after the first cycle is large thus inelastic deformation is minimal in the second cycle. A relatively large discrepancy in energy dissipation capacities exists between specimens in Group 1 and Group 2,

where Group 1 always dissipates more energy due to the higher stress achieved by the samples in Group 1 at the same strain level. In Figure 6.28 at the first cycle of a given deformation level, energy dissipated increases quickly at strain levels of 0.1 and 0.2 and energy dissipation capacity is similar at the three loading rates. When strain is larger than 0.2 at the largest loading rate, dissipated energy per cycle slightly decreases whereas it increases slowly at loading rates of 0.01 in./s and 0.1 in./s. A similar trend is also observed in the second cycle of each strain level indicating energy dissipation capacity is higher at lower loading rates under larger deformation. This observation is due to the fact that the maximum stress achieved by the PU foam decreases quickly at faster loading rates as a result of foam crushing as seen in Figure 6.23 and 6.24. The cumulative energy dissipated in the first cycle is 1290 lbf-in, 1350 lbf-in and 1260 lbf-in at increasing loading rates whereas in the second cycle it is 390 lbf-in, 360 lbf-in and 300 lbf-in for loading rate 0.01 in./s, 0.1 in./s and 1 in./s, respectively. This suggests energy dissipation capacity is insensitive to the loading rates since the difference is minimal. The energy dissipated in the second cycle of a given strain level decreases significantly compared to that in the first cycle which suggests the effects of 16 lb PU foam on mitigation of local buckling and improvement of energy dissipation capacity could be limited when subject constant loading amplitude or cyclic decreasing loads once foam consolidates.

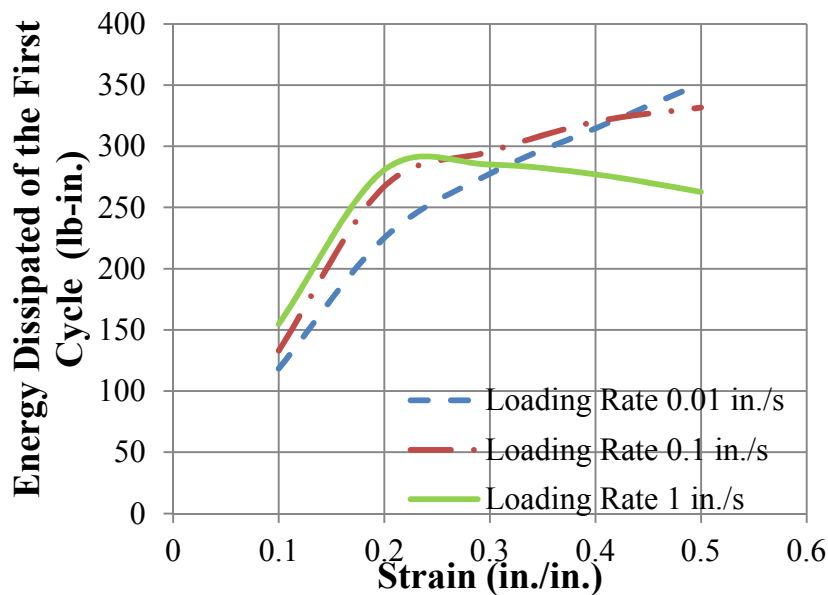


Figure 6.28 Average Energy Dissipation during the First Cycle at Each Strain Level

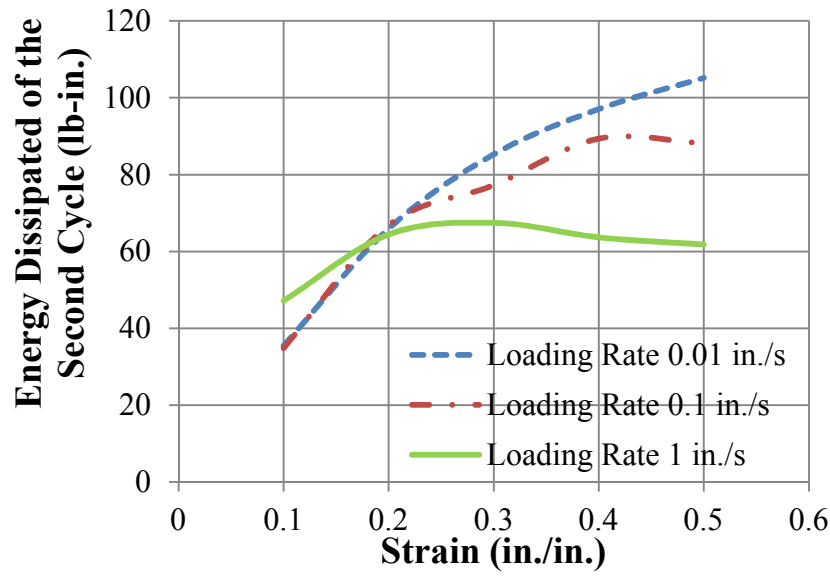


Figure 6.29 Average Energy Dissipation during the Second Cycle at Each Strain Level

The 16 lb PU foam is a rigid and brittle material exhibiting large residual deformation subject to cyclic loads. Localized damage due to foam crushing is also observed during testing. Although overall performance shows 16 lb PU foam is relatively insensitive to loading rate, cyclic increasing loads at faster loading rates can lead to larger strength and stiffness degradation.

6.6 Conclusion

An extensive study of suitable fill material has been carried out which consists of 11 filled and empty HSS beams subject to monotonic bending loads. Based on the test results, 16 lb PU foam has been selected due to its ability in postpone local buckling as well as improve moment capacity stability. To better understand the basic mechanical properties of this fill material, monotonic compression tests are conducted to study its elastic modulus, yield strength, stress at different strain levels and Poisson's ratio at three different loading rates. To further study the material properties under cyclic loading conditions, cyclic compression tests are performed to investigate maximum stress, secant stiffness and energy dissipated at each strain level. The conclusions are as follows:

1. During three-point and four-point monotonic bending tests, 16 lb PU foam shows better performance compared to 8 lb PU foam, 4 lb PU foam and urethane rubber in terms of when local buckling occurs, secant stiffness after the occurrence of local buckling and cumulative energy dissipation.
2. 16 lb PU foam is a non homogeneous material and material properties are scattered. For monotonic compression tests, the average elastic modulus is 7920 psi, 6920 psi and 7790 psi, respectively, at a loading rate of 0.01 in./s, 0.1 in./s and 1 in./s. The average yield stress of all the samples is 380 psi, 390 psi and 400 psi, respectively, at the increasing loading rates.
3. Poisson ratio for the 16 lb PU foam has an average of 0.32 and standard deviation of 0.16.
4. Under monotonic compression loads at small strain levels, an increase in loading rate leads to a slight increase in the compressive yield strength. However at large strain levels, the stress measured at slower loading rates is slightly larger. Influence of loading rate is negligible since discrepancy among specimens between different loading rates is small compared to the difference caused by human factors, ambient conditions and nonhomogeneity of the material.
5. During cyclic compression tests, the average maximum stress ranges from 590 psi to 980 psi, 720 psi to 900 psi, and 730 psi to 780 psi at the first cycle of each strain level under increasing load rates, respectively. Average secant stiffness ranges from 2940 lbf/in. to 8640 lbf/in., 2600 lbf/in. to 11740 lbf/in. and 1520 lbf/in. to 8810 lbf/in. at the first cycle of a given deformation level at 0.01 in./s, 0.1 in./s and 1 in./s, respectively.
6. The cumulative energy dissipated at the first cycle is always larger than that in the second cycle of each strain level, which is 1290 and 390 lbf-in., 1350 and 360 lbf-in., 1260 and 300 lbf-in. under increasing loading rates, respectively. The energy dissipated at the second cycle of a specific strain level is substantially smaller than that of the first cycle due to plastic deformation in the PU foam. This finding suggests the fill material effects on mitigation of local buckling and enhancement of energy dissipation capacity in the later cycles may be minimal once foam crushing occurs.
7. Large scatter between samples with respect to strength, elastic modulus under monotonic and cyclic loading conditions and Poisson's ratio can result in difficulty in predicting its

performance in void fill applications which requires further exploration of the stability of its mechanical properties and evaluation of feasibility of its application in structural and earthquake engineering.

CHAPTER 7 STUDY ON CYCLIC BEHAVIOR OF PU FOAM FILLED HSS BEAM

7.1 Introduction

Previous experimental tests of HSS based moment connections subject to cyclic loads showed HSS beams are susceptible to cracks initiating at their corners after the onset of local buckling under cyclic loads which leads to significant strength and stiffness losses. To prevent local buckling as well as provide added energy dissipation capacity, fill materials are considered in the voids of HSS beams. Numerous studies have focused on the cyclic performance of concrete filled tube (CFT) due to popularity of HSS member as braces, columns and beams in composite structures. Liu and Goel (1988) experimentally investigated the cyclic behavior of CFT braces and concluded that presence of concrete can mitigate local buckling, delay occurrence of crack initiation and increase energy dissipation. Elchalakani et al. (2004) studied cyclic inelastic flexural behavior of CFT subject to constant amplitude pure bending loads which demonstrated that the presence of concrete can improve the ultimate strength of an HSS by 15% to 24% and enhance fracture life by at least 1.5 times. Prion and Boehme (1994) performed cyclic loading tests of 26 specimens consisting of high strength concrete filled steel tubes which indicated they can be successfully applied where high strength is required with a ductile behavior. Hajjar and Gourley (1997) developed a cyclic nonlinear model for CFT which was calibrated with experimental test results and the findings suggested the model was suitable for CFT subject to monotonic static, cyclic static, or transient dynamic analysis in unbraced frame structures (Hajjar et al., 1997). These studies demonstrated effectiveness of the fill material (i.e. concrete) in mitigating local buckling as well as enhancement of strength and fracture life for seismic applications. However, concrete provides a significant increase in mass along with coordination between different trades during construction. Alternatively, few studies have considered lightweight and high energy absorption materials, such as polymer foam, as the fill material in HSS members overlooking the foams potential and benefits for seismic applications such as increasing energy dissipation capacity and postponing local buckling.

Polymer foam has been utilized as sandwich core in composite beams subject to static loads and dynamic loads in mechanical and aerospace engineering. Compston et al. (2006) conducted impact tests of polymer foam and an aluminum core sandwich structure which showed similar energy dissipation capacity, but the polymer foam structure exhibited localized damage. Hazizan and Cantwell (2002) experimentally studied failure modes of foam cored sandwich structures subject to low velocity impact response and suggested impact response can be modelled using material properties determined at quasi-static rates of strain. Sharma et al. (2004) experimentally and analytically investigated low velocity impact response of PU foam cored sandwich structures which exhibited excellent performance in terms of energy dissipation capacity. Studies and applications of polymer foam as energy absorption materials in sandwich structures show its potential for seismic application when used in the voids of HSS beams, but further exploration is still needed.

In this chapter, a parametric study of 14 filled and 14 empty HSS cantilever beams considering different beam width thickness and depth thickness ratios is carried out to evaluate the effectiveness of 16 lb PU foam fill to mitigate local buckling and enhance of energy dissipation capacity. Based on the parametric study results, minimum beam width thickness ratio and depth thickness ratio limits for the filled HSS beams can be derived based on SMF requirements.

7.2 Parametric Study on Fill HSS Beam via FE Analysis

FE models are developed in Abaqus/Explicit 6.14-1 to further study the seismic performance of filled HSS beams subject to cyclic bending. The FE models are calibrated and validated based on the mechanical behavior tests of the PU foam (Chapter 6) and against experimental tests of empty cantilever HSS members. These models then are used for a parametric study to consider beams with different width thickness (b/t) and depth thickness (d/t) ratios in order to fully capture the influence of the fill material on the beams' seismic performance.

7.2.1 Configuration and Details

The HSS beams considered in the parametric study are cantilevered to provide a means of evaluating the seismic performance of both filled and empty HSS beams subject to cyclic

bending loads. The model of the cantilevered HSS beam configuration is exactly the same with previously tested HSS beams (Fadden & McCormick, 2011) which allows for calibration and validation of the FE models against experimental test results. The length of the HSS beam is 60.5 in. The geometry of each section, including the width, depth, and thickness, is taken as that specified in the AISC Manual of Steel Construction (AISC, 2010c) for the studied HSS sizes. The corner radius is taken as twice the thickness of the beam section. Boundary conditions of the cantilevered beam are simulated with both ends having rigid endplates tied to the beam with tie constraints. One of the rigid plates is held fixed and the other one is cyclically displaced. This model configuration represents a cantilever beam with one fixed end and one free end where cyclic displacements are applied to the free end. The fill length is taken as 1.5 times the plastic hinge length for all specimens since local buckling tends to induce out of plane inelastic deformation in this region. The loading protocol increases from 0.00375 rad. to 0.07 rad. with two repeated cycles at each rotation level as shown in Figure 7.1.

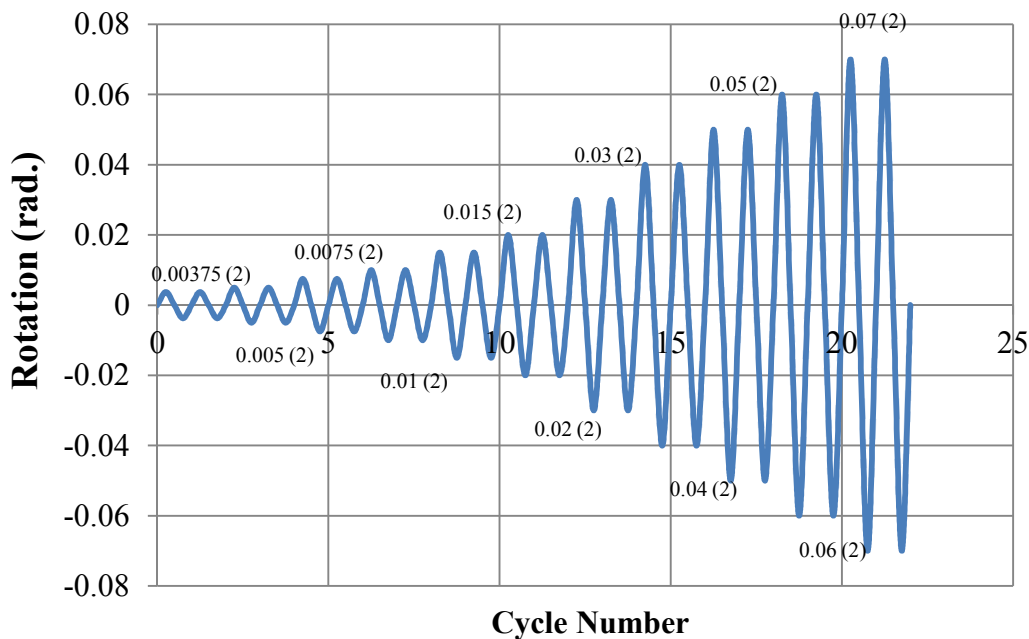


Figure 7.1 Loading History for FE Models

The explicit solution in Abaqus is a true dynamic procedure, but it can be used to solve certain types of quasi-static problems more effectively, especially for models with complicated contact situations. Special considerations are required to apply an explicit solution to quasi-static

problems. Static loads are accelerated, but inertial forces should remain insignificant. Mass scaling is an effective way to reduce solution time without artificially increase loading speed. However, increasing loading rate by utilization of mass scaling can induce dynamic effects which should be avoided in obtaining a static solution. Thus the mass scaling factor and loading speed are crucial for accuracy and efficiency of the FE model. A parametric study of the mass scaling factor and loading rate is conducted and the results are evaluated based on energy history. Kinematic energy and internal energy histories are shown in Figure 7.2 for the model with a mass scaling factor of 100 combined with a loading rate of 0.1 in./sec. The results illustrate that the kinematic energy is only a small fraction (less than 5%) of the internal energy throughout the loading history. This indicates inertial effects are negligible and the models are able to yield reliable and relatively accurate results. Thus when using an explicit solution for the FE models a mass scaling factor of 100 combined with a loading rate of 0.1 in./sec is employed to provide accurate results with less computational expense.

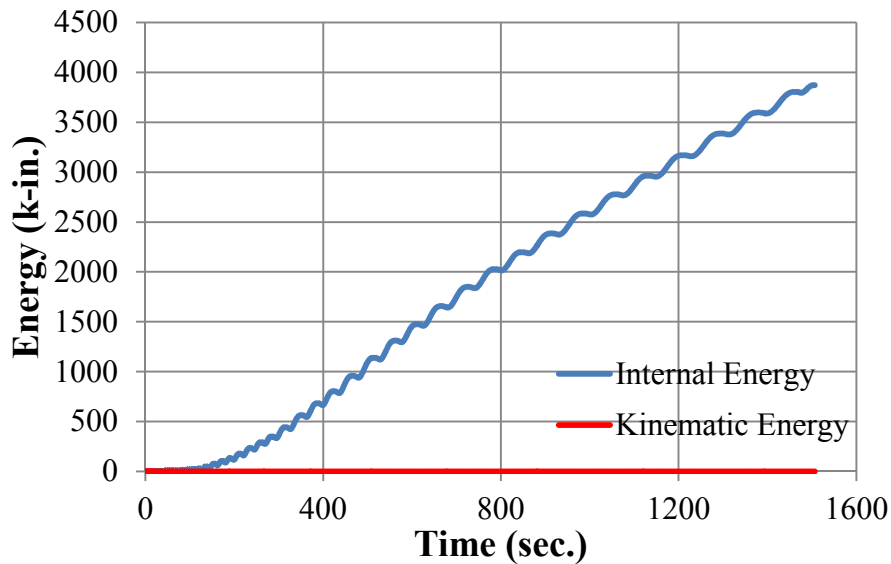


Figure 7.2 Energy History for the HSS 8×6×1/4 Beam with Mass Scaling of 100 and Loading Rate of 0.1 in./sec

As shown in Figure 7.3, the FE model mesh size is 0.5 in. square and element types are shell S4R for the HSS beam and solid C3D8R for the PU foam in the explicit library. The interface between the foam and the HSS beam’s internal surface uses tie constraints since the bond between the two remains intact throughout loading. Debonding was not observed even at

locations where local buckling occurred in the prior tests of the small scale filled beams (Chapter 6).

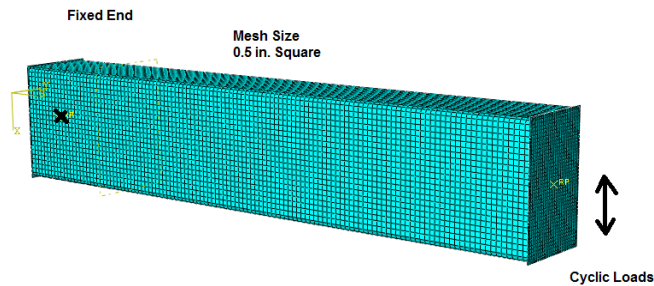


Figure 7.3 Mesh Size for the Cantilever Beam

7.2.2 Material Properties

Material properties from tensile coupon tests of the HSS 8×6×1/4 that was previously tested by Fadden and McCormick (2011) are applied to the flats and corners of the HSS models. A combined isotropic-kinematic hardening law with no strain rate effects is applied to the steel material model to more accurately capture the Bauschinger effect during cyclic loading conditions. The yield strength (F_y) and ultimate strength (F_u) are 54.0 ksi and 68.4 ksi for the HSS flats and 73.7 ksi and 81.0 ksi for the HSS corners, respectively. True stress and true strain curves converted from engineering stress and engineering strain are input into Abaqus' metal plasticity model as shown in Figure 7.4.

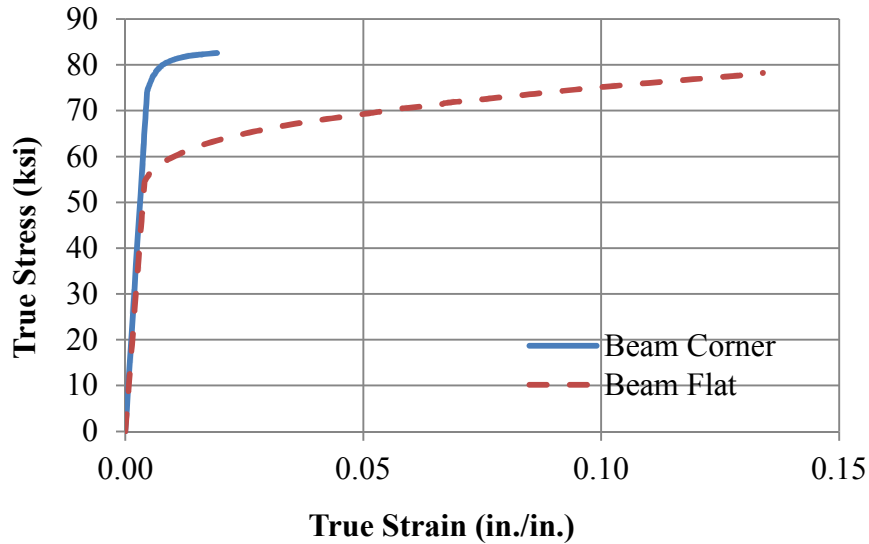


Figure 7.4 True Stress-Strain Plots for the Beam Corners and Flats

In the Abaqus material library (Abaqus, 2014), there are several models suitable for polymer foam including hyperfoam, hyperelastic, viscouelastic and crushable foam models. The most suitable model for the 16 lb PU foam is the crushable foam material model since it exhibits large plastic behavior and residual deformation subject to cyclic loading conditions as described in Chapter 6. One of the material tests from the Group 3 specimens under monotonic compression loads at a loading rate of 0.01 in./sec is selected as the representative behavior of the foam where the elastic modulus is 3.7 ksi and yield strength is 0.42 ksi. The selected material model represents the average strength of all the tested specimens. The Poisson's ratio for 16 lb PU foam is 0.32 based on the average compression tests presented in Chapter 6. A volumetric hardening model is utilized to better predict the hysteretic behavior of the foam since a volumetric hardening model assumes a perfectly plastic behavior while an isotropic hardening model predicts the same behavior in both hydrostatic tension and hydrostatic compression. The engineering stress and engineering strain relationship from the monotonic compression test is converted to true stress and true strain values utilizing Equation 7.1 and Equation 7.2.

$$\sigma = s(1 - e) \quad \text{Equation 7.1}$$

$$\varepsilon = -\ln(1 - e) \quad \text{Equation 7.2}$$

where e and s are engineering strain and engineering stress, respectively, and ε and σ are true strain and true stress, respectively.

The hardening curve describing the uniaxial compression yield stress as a function of corresponding plastic strain is utilized. A compression yield stress ratio (k) of 1 is utilized assuming the ratio of initial yield stress in uniaxial compression to initial yield stress in hydrostatic compression is 1 and the hydrostatic yield stress ratio (k_t) of 0.1 is selected assuming the ratio of yield stress in hydrostatic tension to initial yield stress in hydrostatic compression is 0.1. These input values are typical for PU foam (Schembri & Lewis, 2014) and based on a parametric study of a filled HSS beam considering various compression yield stress ratios and hydrostatic yield stress ratios. The parametric study shows that these parameters have little effects on the cyclic behavior of the filled beam.



Figure 7.5 True Stress-Strain Curve for the 16 lb PU Foam

7.2.3 FE Model Validation

The validation of the FE model aims to provide information on the accuracy of the FE model prior to conducting a larger parametric study of filled HSS beams. The FE models of the HSS beam member and PU foam are validated separately. The modeling approach for the HSS member is compared to previously tested unfilled HSS beams (Fadden & McCormick, 2011) in terms of moment capacity, secant stiffness and moment degradation. The moment-rotation

hysteresis curves of an empty HSS 8×6×1/4 beam from the FE model described above and experimental test conducted by Fadden and McCormick (2011) are shown in Figure 7.6. The FE model slightly overestimates the moment capacity of the beam by 6%. Secant stiffness is defined as the applied force at the first 0.01 rad. cycle divided by the corresponding displacement. The secant stiffness measured from test and FE model are almost the same with values of 19.7 k/in. and 19.4 k/in., respectively. The moment degradation as shown in Figure 7.6 indicates the FE results show a good agreement with the experimental tests. Thus the described explicit solution used with the FE model is able to accurately predict the cyclic behavior of an unfilled HSS beam.

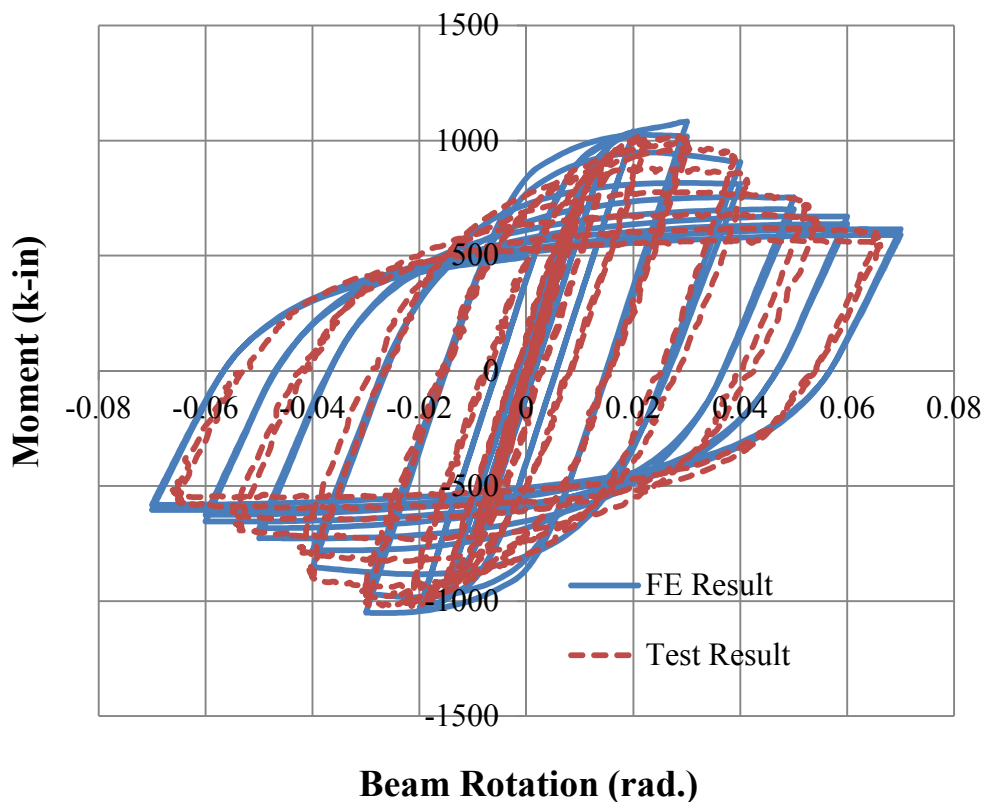


Figure 7.6 Comparison of Moment-Beam Rotation Relationship of a Cantilevered HSS 8×6×1/4 Beam from FEM and Experimental Testing

PU foam monotonic compression test results are also compared with an FE analysis to better assess the accuracy of the crushable foam model in Abaqus 6.14-1/Explicit and validate its ability to replicate the behavior of the 16 lb PU foam. Two rigid plates are utilized in the FE model to simulate the top and bottom platforms used in the compression tests as described in Chapter 6 (Figure 7.7). The boundary condition of the bottom steel plate is fixed and vertical

displacement is applied at the top plate. The dimension of the PU foam specimen is 1.5 in. cube which is the same as the experimental test specimen. The foam is compressed up to 80% of the original height. The measured engineering stress-strain from the FE model is compared with the input material model obtained from the monotonic compression test of the specimen in Group 3. The FE results show a slightly smaller plateau slope and the foam densification starts at larger strain levels. Figure 7.8 shows a good agreement with the test result indicating the FE result can accurately capture the behavior of the cube specimen under compression tests. As a result, the crushable foam material model is utilized in the parametric study to represent the PU foam fill.

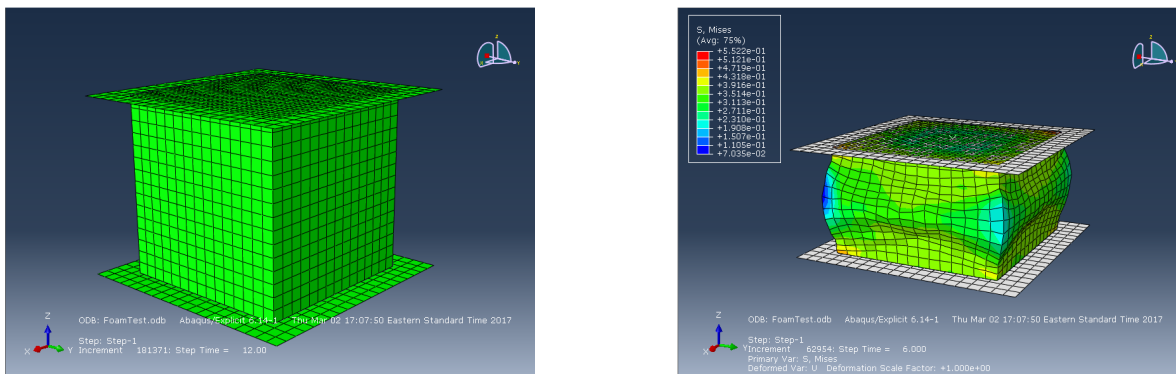


Figure 7.7 FE Model of the PU Foam Compression Test

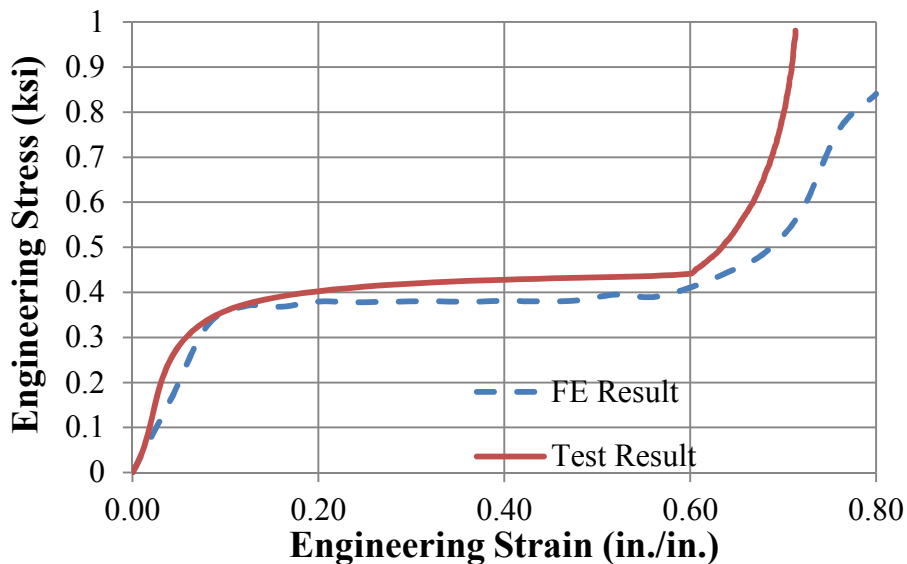


Figure 7.8 Engineering Stress-Strain Relationship from the FE model and Compression Test

7.2.4 Parametric Study Specimens

To better understand seismic performance of filled HSS beams under cyclic loads, FE models of fourteen PU foam filled HSS are developed and compared with fourteen equivalent empty HSS beams with the same geometry and material properties. Their behavior is evaluated in terms of hysteretic behavior, secant stiffness and energy dissipation capacity. The selection of the HSS beams is based on the width thickness (b/t) and depth thickness (d/t) ratio limits previously proposed by Fadden and McCormick (2014a) based on an empty HSS's ability to maintain 80% of its moment capacity to 0.04 rad. under a simulated far field earthquake protocol. These two limits are provided in Equation 7.3 and 7.4 and are based on the elastic modulus and yield strength of the HSS beam. The width thickness and depth thickness ratios to ensure that SMF criteria can be met are 10.9 and 25.0, respectively based on actual material properties applied in FE models.

$$\frac{b}{t} = 0.48 \sqrt{\frac{E}{F_y}} \quad \text{Equation 7.3}$$

$$\frac{d}{t} = 1.13 \sqrt{\frac{E}{F_y}} \quad \text{Equation 7.4}$$

To evaluate the effectiveness of the PU foam to inhibit local buckling and increase energy dissipation during cycling, the fourteen HSS sizes selected were distributed above and below these values resulting in four groups as shown in Figure 7.9. In Group 1, all of the beams have b/t and d/t ratios less than the proposed limits for empty HSS under cyclic bending suggesting these members will be able to meet SMF requirements even without the foam fill. For Group 2 and Group 3, one of the element slenderness ratios exceeds the proposed limit allowing for an evaluation of whether the proposed limits can be increased when PU foam fill is present. Group 4 exceeds both proposed limits and allows for evaluation of the extent of which the PU foam fill can improve the behavior of HSS under cyclic bending.

The HSS beams' section properties and fill length is provided in Table 7.1. The consideration of a wide range of specimens leads to a better understanding of limiting parameters for stable plastic hinge formation and moment degradation of the filled HSS beams subject to continued cyclic loads. Thus, suitability of the fill material in seismic applications can be assessed.

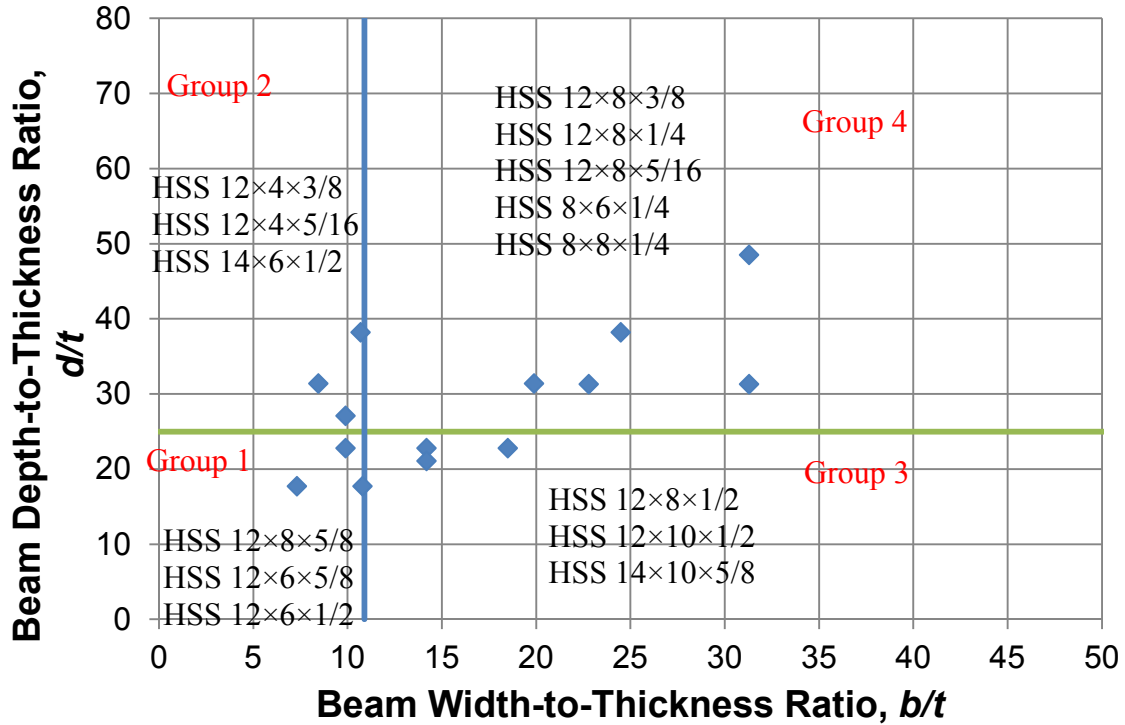


Figure 7.9 Distribution of Parametric Study Specimens with respect to b/t and d/t Ratios

Table 7.1 HSS Beam Properties and Fill Length

HSS Beam	d/t	b/t	Elastic Modulus S_x (in ⁴)	Plastic Modulus Z_x (in ³)	Fill Length (in.)	Plastic Moment Capacity M_p (k-in.)
HSS 12×4×3/8	31.4	8.46	28	36.7	22	1990
HSS 12×4×5/16	38.2	10.7	24.1	31.3	21	1697
HSS 14×6×1/2	27.1	9.9	57.4	73.6	20	3991
HSS 12×8×5/8	17.7	10.8	66.1	82.1	18	4451
HSS 12×6×5/8	17.7	7.33	53.4	68.8	20	3730
HSS 12×6×1/2	22.8	9.9	45.2	57.4	20	3112
HSS 12×8×1/2	22.8	14.2	55.6	68.1	17	3692
HSS 12×10×1/2	22.8	18.5	65.9	78.8	15	4273
HSS 14×10×5/8	21.1	14.2	98.2	120	17	6506
HSS 12×8×3/8	31.4	19.9	43.7	53	16	2874
HSS 12×8×1/4	48.5	31.3	30.6	36.6	15	1984
HSS 12×8×5/16	38.2	24.5	37.4	44.9	16	2434
HSS 8×8×1/4	31.3	31.3	17.7	20.5	13	1112
HSS 8×6×1/4	31.3	22.8	14.2	16.9	15	916

7.2.5 FE Study Results

The FE results provide a means of quantifying the effects of the fill material on the hysteretic behavior of HSS beams undergoing cyclic bending with respect to different b/t and d/t ratios. The overall performance of the HSS beams is evaluated in terms of moment-rotation relationship, secant stiffness, energy dissipation capacity and moment degradation at the 0.04 rad. cycle since SMF require the beam to maintain at least 80% of its moment capacity at 0.04 rad. of rotation. The findings also allow for new b/t and d/t limits to be developed for PU foam filled HSS based on SMF requirements. Thus the limiting parameters of b/t and d/t ratios of filled HSS beams which satisfy SMF requirement in AISC 340-10 (2010a) are presented.

7.3.5.1 Hysteretic Behavior

The moment-rotation behavior is considered for all fourteen sections with presented results focusing on representative moment-rotation curves from each group as seen in Figure 7.10 to Figure 7.13. The moment is normalized by the plastic moment capacity, M_p , of the HSS beam which is calculated as the yield strength of the beam flat applied in the FE models multiplied by the theoretical plastic section modulus of the HSS section without considering the fill since the fill has limited strength compared to the HSS member.

For the HSS beams in Group 1, the maximum normalized moments of the empty and filled beams range from 1.35 to 1.39 and 1.37 to 1.40. These results show only a minor increase in capacity which is the aim of the fill application so as not to need to change construction and detailing practices. The comparison of the moment-rotation hysteretic curves for the empty and filled HSS 12×6×1/2 ($b/t=9.9$ and $d/t=22.8$) is shown in Figure 7.10. The results from the FE analyses show that the filled beam produces slightly more stable hysteretic behavior, particularly at larger rotation levels. At the 0.07 rad. cycle, the moment degradation of the empty beam is approximately 15% which is induced by plastic hinge formation while the moment capacity of the filled HSS beam keeps increasing indicating that the PU foam can effectively postpone the occurrence of local buckling and potentially increase energy dissipation.

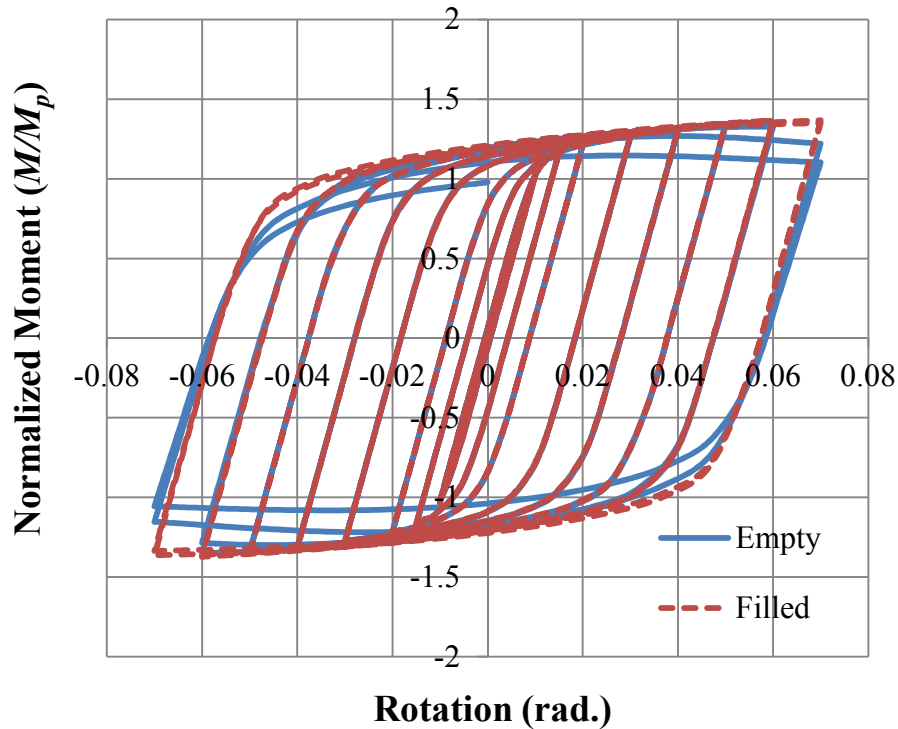


Figure 7.10 Normalized Moment versus Beam Rotation for HSS 12×6×1/2

For the HSS beams considered in Group 2 where the depth thickness ratio limits exceeded, the maximum normalized moment of the empty and filled beams vary from 1.25 to 1.34 and from 1.30 to 1.38, respectively. The representative moment-rotation relationship for an empty and filled HSS 12×4×5/16 ($b/t=10.7$ and $d/t=38.2$) is illustrated in Figure 7.11. The maximum moment of the empty and filled beam is achieved at the 0.04 rad. and 0.05 rad. cycle, respectively, indicating the effects of the PU foam on delaying local buckling. After local buckling occurs in both the empty and filled HSS beams, the maximum moment reached at the 0.07 rad. cycle is almost identical regardless of the presence of the fill material which is attributable to the fact that excessive inelastic deformation in the plastic hinge region leads to foam plastification and crushing. However, the presence of the foam does appear to extend the rotation level at which degradation occurs until the very large rotation level of 0.07 rad. The results suggest a slight increase in energy dissipation and a benefit in terms of local buckling when using the foam for this group of members.

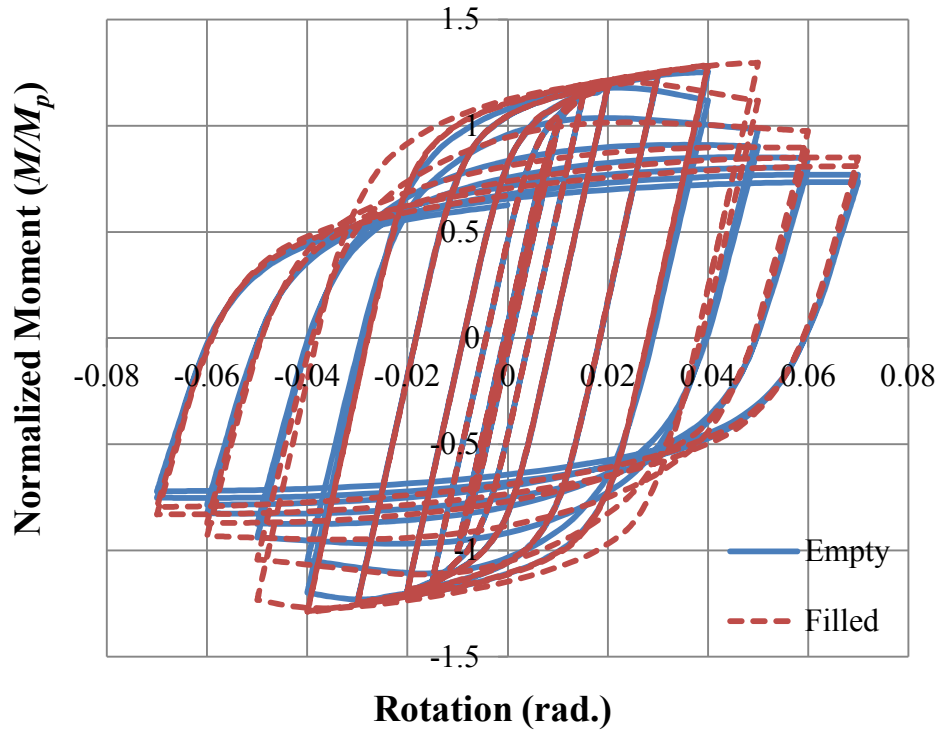


Figure 7.11 Normalized Moment versus Beam Rotation for HSS 12×4×5/16

For the HSS beams studied in Group 3 where the width thickness limit is exceeded, the maximum normalized moment of the empty and filled beams vary from 1.31 to 1.41 and from 1.33 to 1.46, respectively. As shown in Figure 7.12, the filled HSS 12×10×1/2 ($b/t=18.5$ and $d/t=22.8$) produces more stable hysteretic behavior, although both empty and filled beams reach their maximum moment at around the 0.03 rad. cycle. The filled HSS beam shows a much slower degradation in the moment capacity which indicates the fill material is effective in mitigation of local buckling.

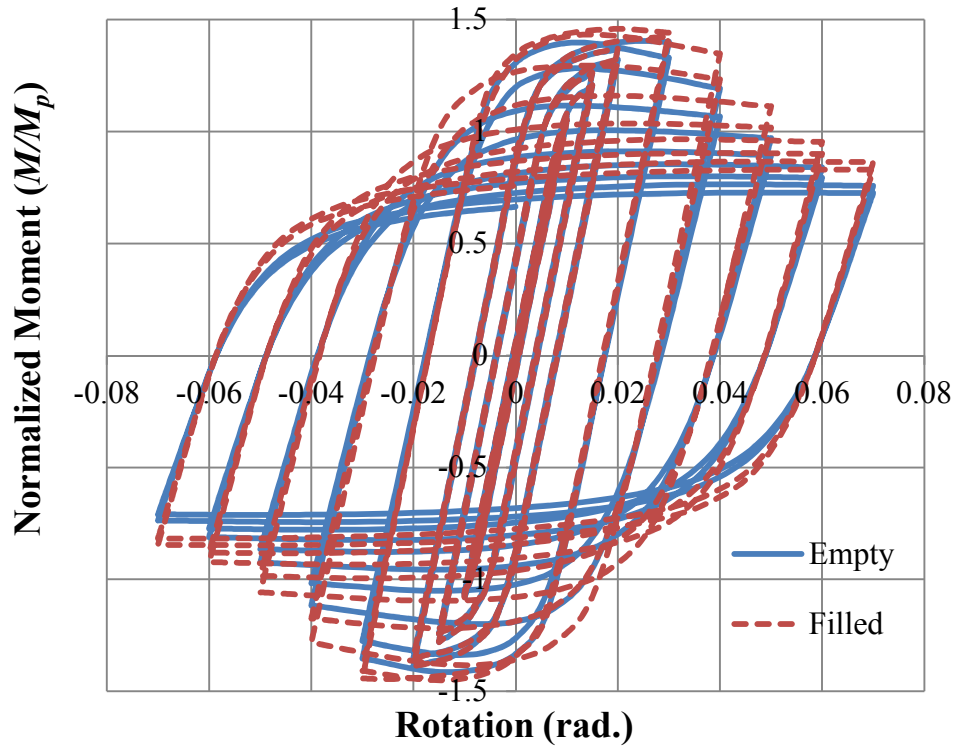


Figure 7.12 Normalized Moment versus Beam Rotation for HSS 12×10×1/2

For the HSS beams considered in Group 4, the maximum normalized moment of the empty and filled beams vary from 1.11 to 1.19 and from 1.13 to 1.26, respectively. The hysteretic behavior of the empty and filled HSS 12×8×1/4 is compared as seen in Figure 7.13. The filled HSS 12×8×1/4 ($b/t=31.3$ and $d/t=48.5$) exhibits a fuller hysteresis loop with significantly less moment degradation at larger rotation levels. The empty and filled beams reach their maximum moment at 0.015 rad. and 0.02 rad., respectively. The moment degradation at the 0.07 rad. cycle is approximately 63% and 42% for the empty and filled HSS 12×8×1/4, respectively. The results suggest that the foam fill has a more significant impact as the width thickness and depth thickness ratio increases.

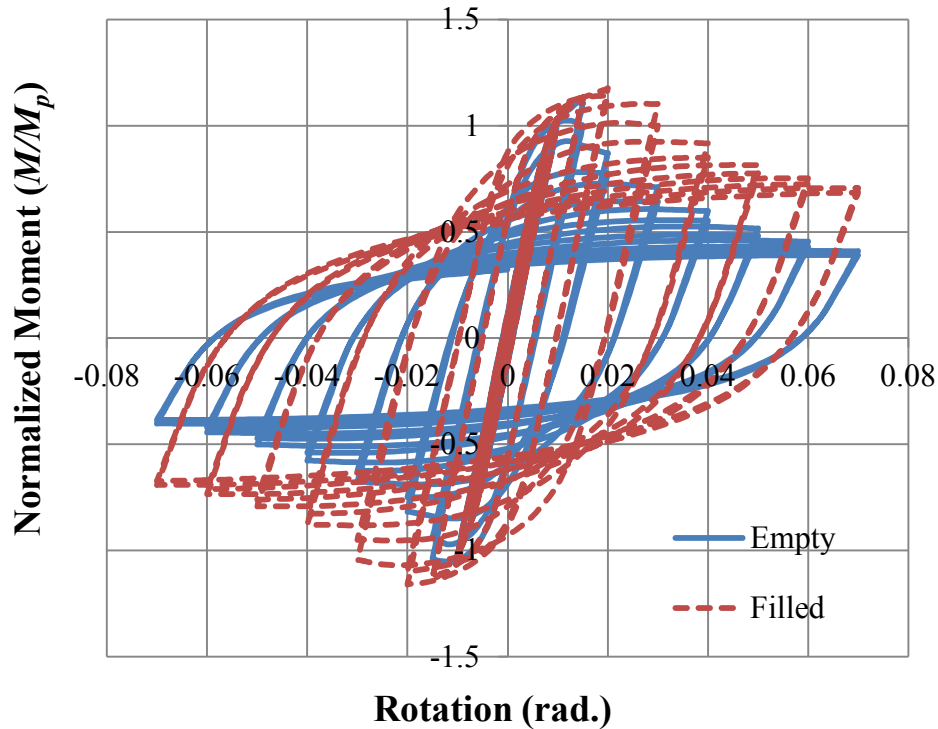


Figure 7.13 Normalized Moment versus Beam Rotation for HSS 12×8×1/4

The presence of the fill material is able to postpone occurrence of local buckling and produce more stable plastic hinge formation in almost all the specimens. At the larger rotation levels, discrepancy between the moment capacity of the filled and empty beam gradually diminishes due to foam crushing. The effects of the fill material on mitigation of local buckling are more significant for HSS beams with larger b/t and d/t ratios.

7.3.5.2 Secant Stiffness

Secant stiffness for the first cycle to each rotation level is computed as the applied force at the maximum cycle displacement divided by the maximum displacement as seen in Figure 7.14 to Figure 7.17 for the four HSS groups.

In Group 1, empty and filled beams produce almost the same values in regards to secant stiffness at each rotation level indicating that the PU foam has minor effects on secant stiffness for sections that meet the proposed width thickness and depth thickness limit requirements. The secant stiffness starts to decrease at 0.015 rad. due to inelastic deformation in the HSS beams.

Secant stiffness degradation at 0.04 rad. for all the filled and empty beams is approximately 70% of the initial value of the early cycles.

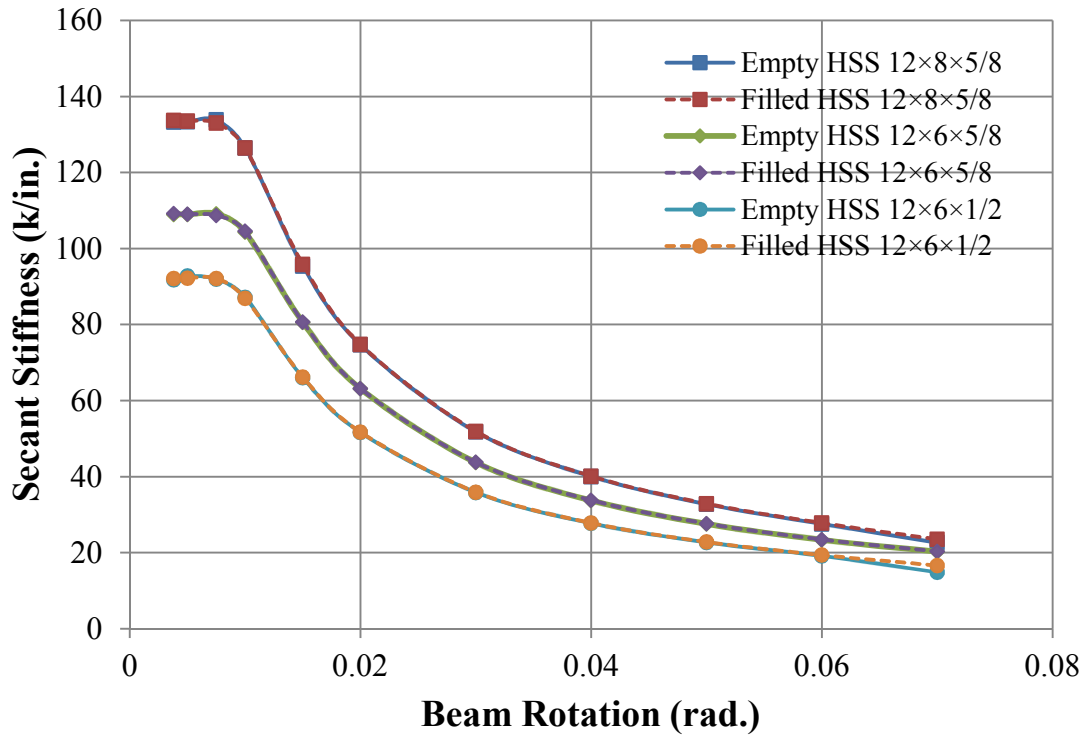


Figure 7.14 Secant Stiffness versus Beam Rotation for HSS Beams in Group 1

In Group 2 where the beam's d/t ratio exceeds the limit presented in Equation 7.4, the secant stiffness of the empty and filled beams is almost the same at the smaller rotation levels. When rotations are larger than 0.05 rad., the filled beams show slightly larger secant stiffness since moment degradation of the filled beams is smaller than that of the empty beams. Secant stiffness degradation at the 0.07 rad. cycles for all the filled and empty beams are approximately 85% and 90% of the secant stiffness at the 0.01 rad. cycle, respectively.

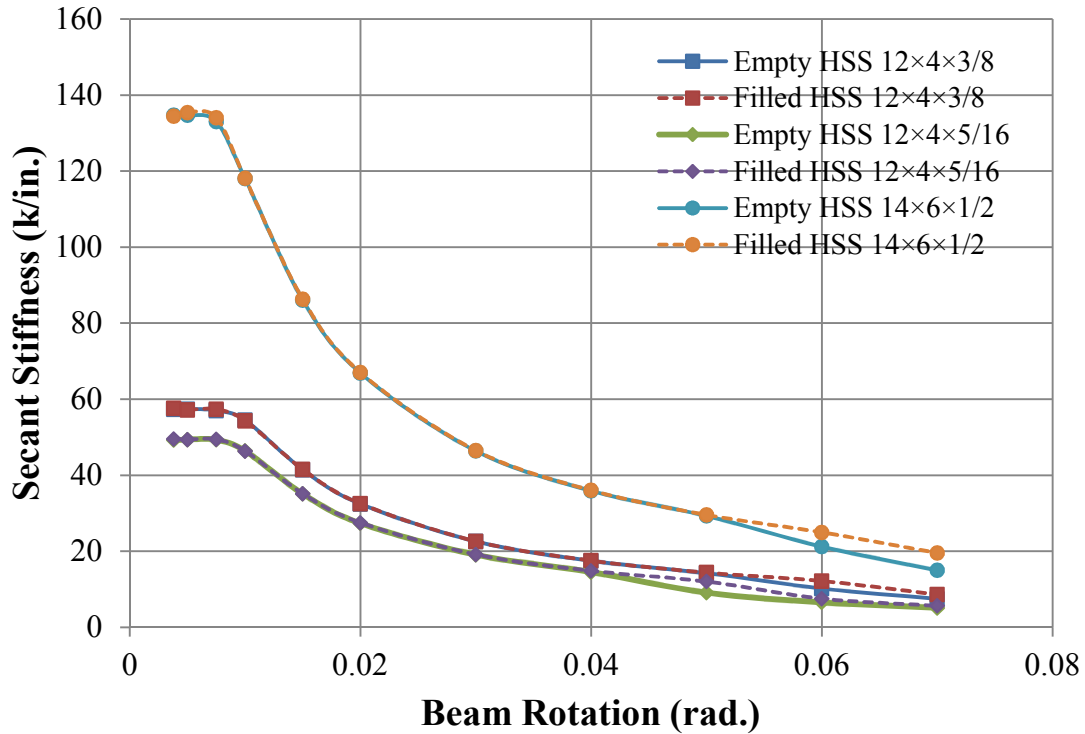


Figure 7.15 Secant Stiffness versus Beam Rotation for HSS Beams in Group 2

For Group 3 where the beam's b/t ratio exceeds the limit in Equation 7.3, the secant stiffness of filled beams is slightly larger when the beam's rotation is larger than 0.04 rad. since the fill material postpones occurrence of local buckling. Secant stiffness degradation at the 0.04 rad. cycle for all the filled and empty beams is approximately 75% of the secant stiffness measured at the 0.01 rad. cycle. While the deterioration of secant stiffness for empty and filled beams at the 0.07 rad. cycle is approximately 90% and 85% of the secant stiffness at 0.01 rad. suggesting the effect of the fill material is minor on the enhancement of secant stiffness after local buckling occurs in the beam plastic hinge region.

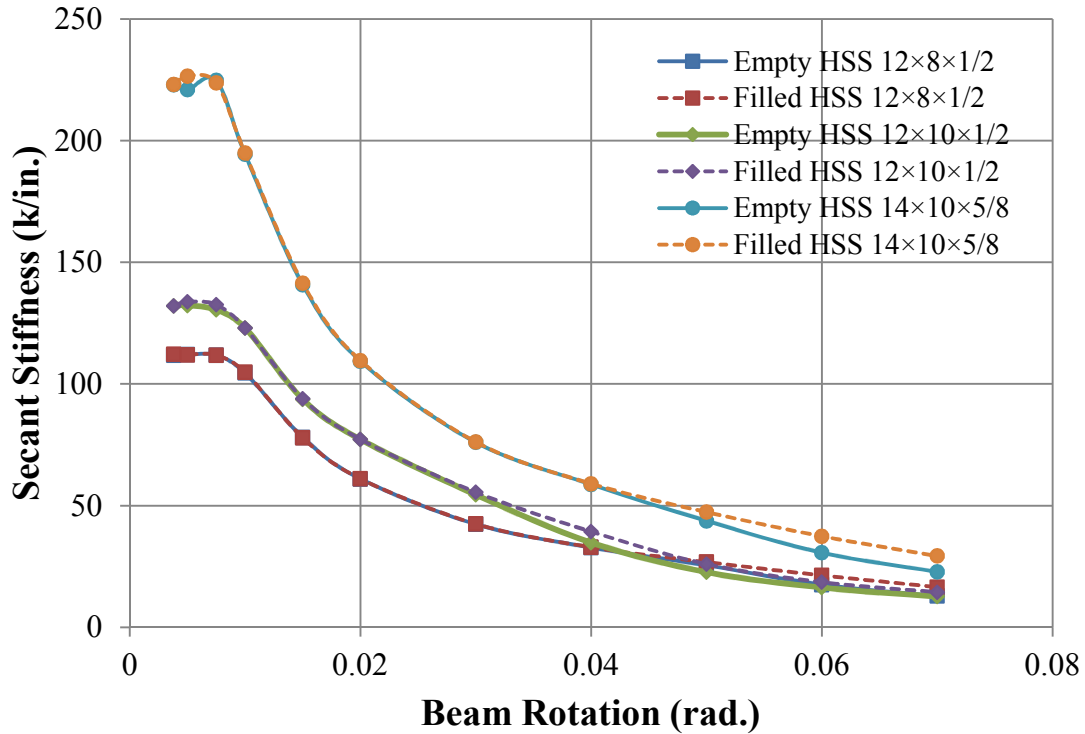


Figure 7.16 Secant Stiffness versus Beam Rotation for HSS Beams in Group 3

In Group 4, where both the b/t and d/t ratios exceed the limits in Equation 7.3 and Equation 7.4, the secant stiffnesses of the filled beams are slightly larger when the beam's rotation is larger than 0.03 rad. or even 0.02 rad. for the beam with the largest b/t and d/t ratios (i.e. HSS 12x8x1/4). The influence of the fill material on the secant stiffness is observed at smaller rotation levels compared with beams in other groups due to the earlier onset of local buckling in the HSS beams with larger d/t and b/t ratios. At the 0.04 rad. cycle, the fill material is able to decrease secant stiffness degradation by approximately 5% for all the beams in Group 4; while at the 0.07 rad. cycle, the degradation of the secant stiffness of the filled beams is only 2% less than that of empty HSS beams. This result is due to the fact that excessive inelastic deformation in the beam plastic hinge region occurs at large rotation levels leading to foam plastification and crushing.

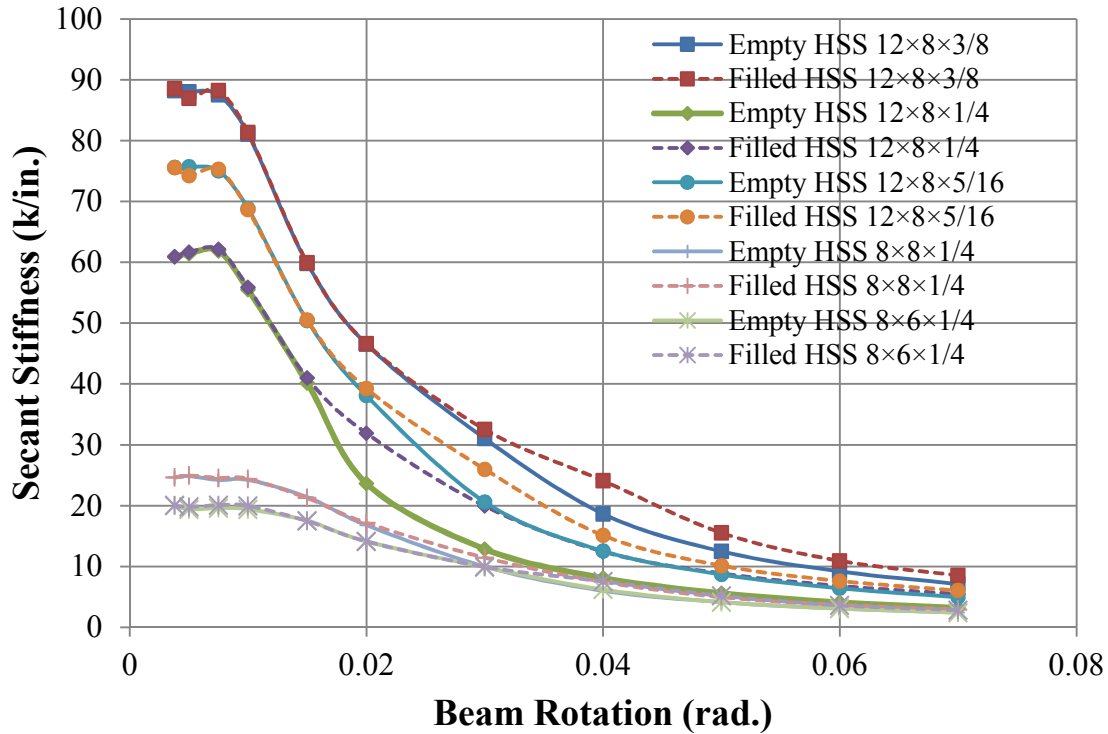


Figure 7.17 Secant Stiffness versus Beam Rotation for HSS Beams in Group 4

The effects of the PU foam on secant stiffness are insignificant especially for the HSS beams with smaller b/t and d/t ratios. The secant stiffness degradation of the filled HSS beam is approximately 5% less than that of empty HSS beams when local buckling initiates. At larger cycles, the discrepancies between secant stiffness degradation of the filled and empty HSS beams diminish since continued deformation after buckling leads to crushing and damage to the foam.

7.3.5.3 Energy Dissipation Capacity

The cumulative energy dissipated is obtained by summing the area enclosed by load-displacement curves at the increasing rotation levels as shown in Figure 7.18 to Figure 7.21. In Group 1 with most compact HSS beams, cumulative energy dissipated in the filled and empty HSS beams is almost identical throughout the loading history. In Group 2 and Group 3, the filled beams dissipate 10% more energy compared to empty beams over the course of the loading protocol. In Group 4, the filled beams show an increase in cumulative energy dissipated at approximately the 0.03 rad. cycle. At the final cycle, all the filled beams, but the HSS 12×8×1/4 ($b/t=31.3$ and $d/t=48.5$) exhibit 15% more energy dissipation. The beam with the largest b/t and

d/t ratios (i.e. HSS 12×8×1/4) shows 45% enhancement in cumulative energy dissipated throughout the loading history.

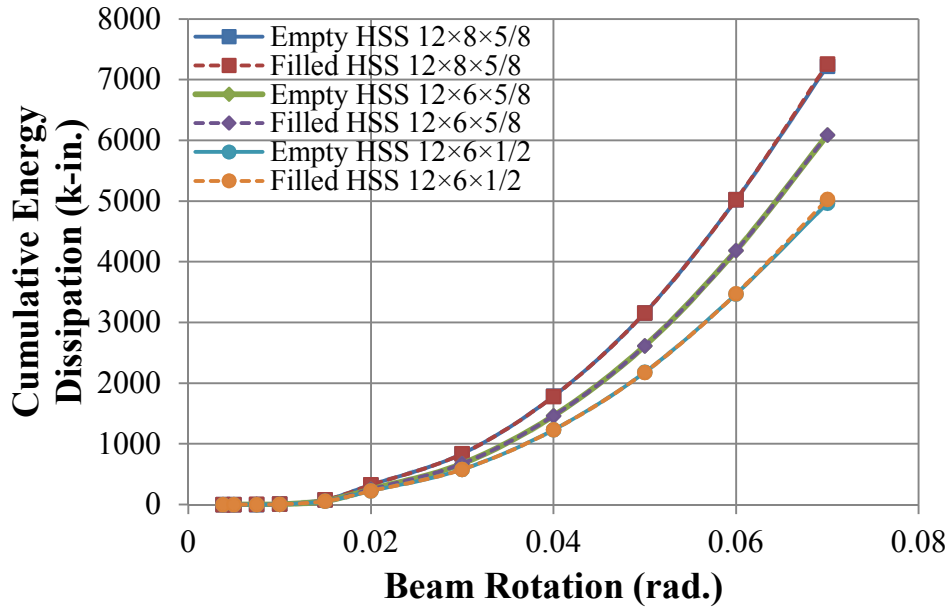


Figure 7.18 Cumulative Energy Dissipation versus Beam Rotation for HSS Beams in Group 1

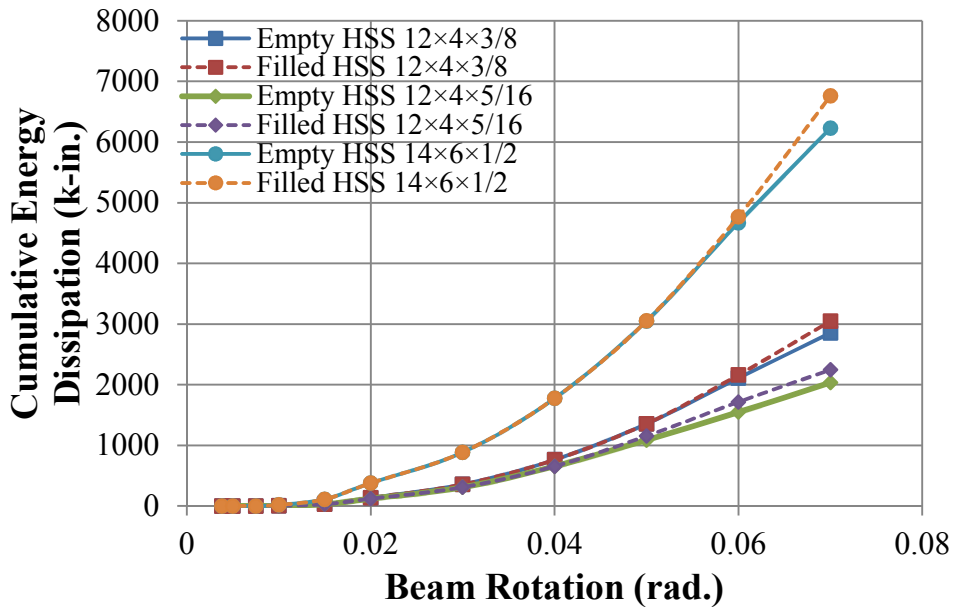


Figure 7.19 Cumulative Energy Dissipation versus Beam Rotation for HSS Beams in Group 2

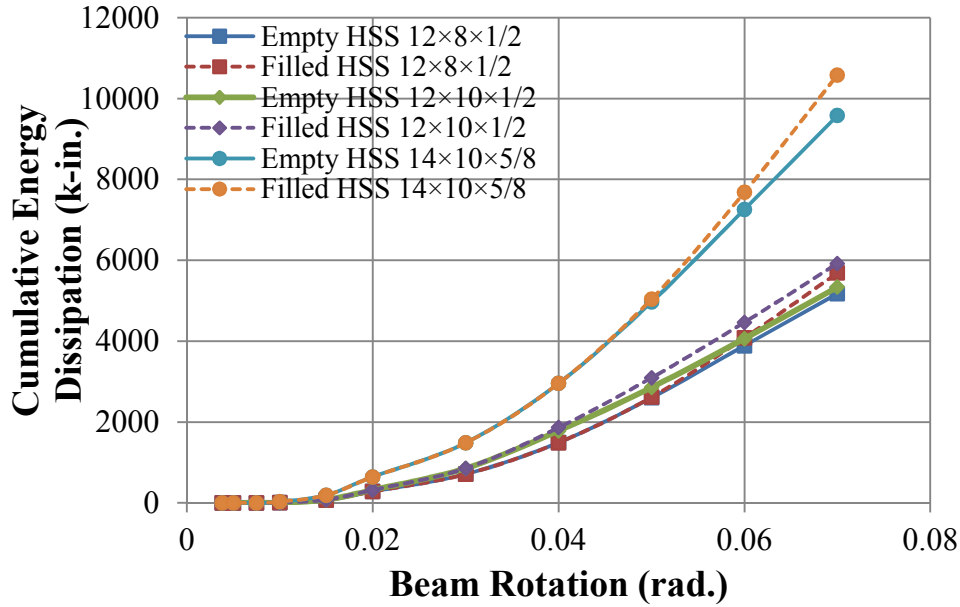


Figure 7.20 Cumulative Energy Dissipation versus Beam Rotation for HSS Beams in Group 3

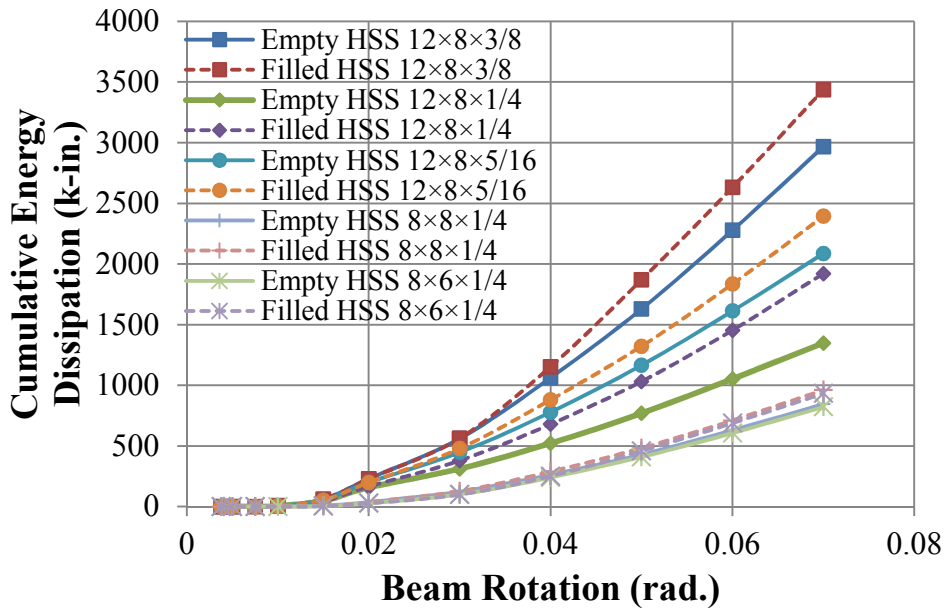


Figure 7.21 Cumulative Energy Dissipation versus Beam Rotation for HSS Beams in Group 4

The effects of the PU foam on energy dissipation capacity is negligible for HSS beam with b/t and d/t ratios smaller than the two limits provided in Equation 7.3 and Equation 7.4. For HSS beams with larger b/t and d/t ratios, enhancement of energy dissipation capacity ranges from 15% to 45% due to the presence of the fill material suggesting a positive impact on the HSS beam behavior.

7.3.5.4 Cycling Effects

The moment at the first cycle of each rotation level is evaluated to better characterize the cycling effects on moment degradation for both empty and filled HSS beams. The normalized moment-rotation backbone curves are shown in Figure 7.22 to Figure 7.25. For the beams with the smallest b/t and d/t ratios, the effects of the PU foam are minimal since local buckling is unlikely to occur or only occurs at larger rotation levels after the formation of a plastic hinge. As seen in Figure 7.22, little moment degradation for the filled HSS beams is observed compared to the maximum moment degradation of 15% in the empty HSS $12 \times 6 \times 1/2$ at the 0.07 rad. cycle as a result of the onset of local buckling. With an increase in the beams' b/t and d/t ratios, moment degradation starts at an earlier cycle and the effects of the PU foam fill are more significant in terms of mitigation of local buckling resulting in more stable and ductile behavior. As shown in Figure 7.23 to Figure 7.25, the filled beams are able to achieve slightly larger moment capacity at the larger rotation levels. After the onset of local buckling, filled beams exhibit much slower moment deterioration which is desirable for seismic applications and meeting SMF requirements. The filled beams in Group 2 to Group 4 achieve a maximum moment capacity at the cycle 0.01 rad. larger than that of the empty beams suggesting the fill material can effectively postpone local buckling to a 0.01 rad. larger cycle .

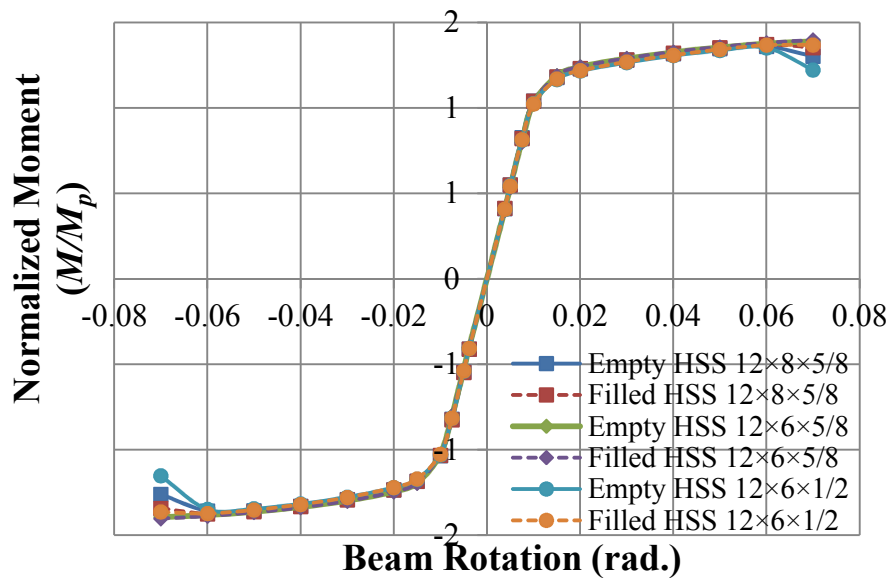


Figure 7.22 Normalized Moment at Each Rotation Level versus Beam Rotation Backbone Curves for Beams in Group 1

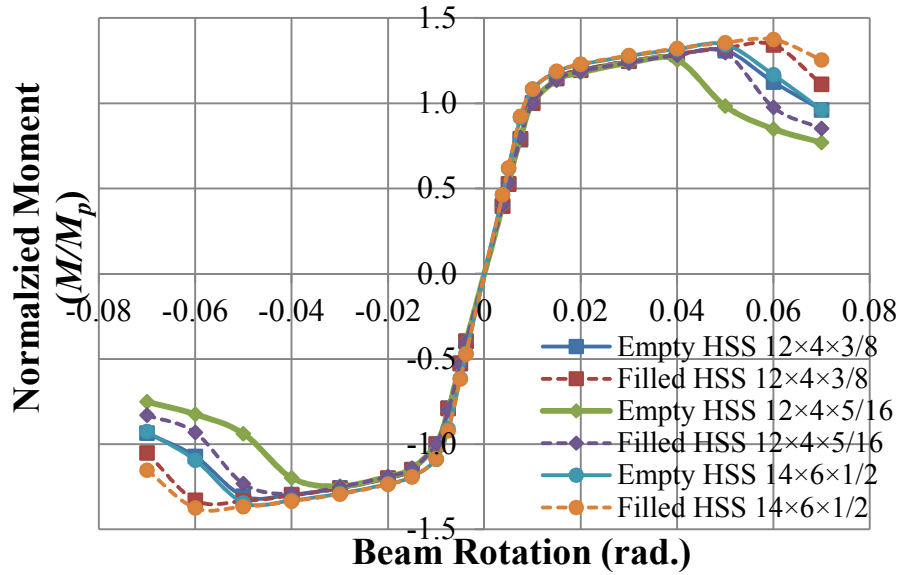


Figure 7.23 Normalized Moment at Each Rotation Level versus Beam Rotation Backbone Curves for Beams in Group 2

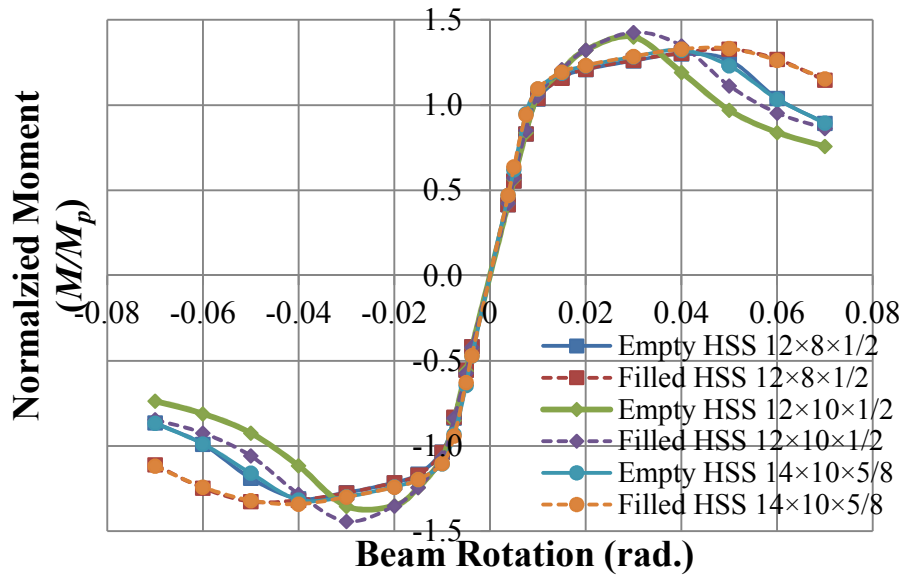


Figure 7.24 Normalized Moment at Each Rotation Level versus Beam Rotation Backbone Curves for Beams in Group 3

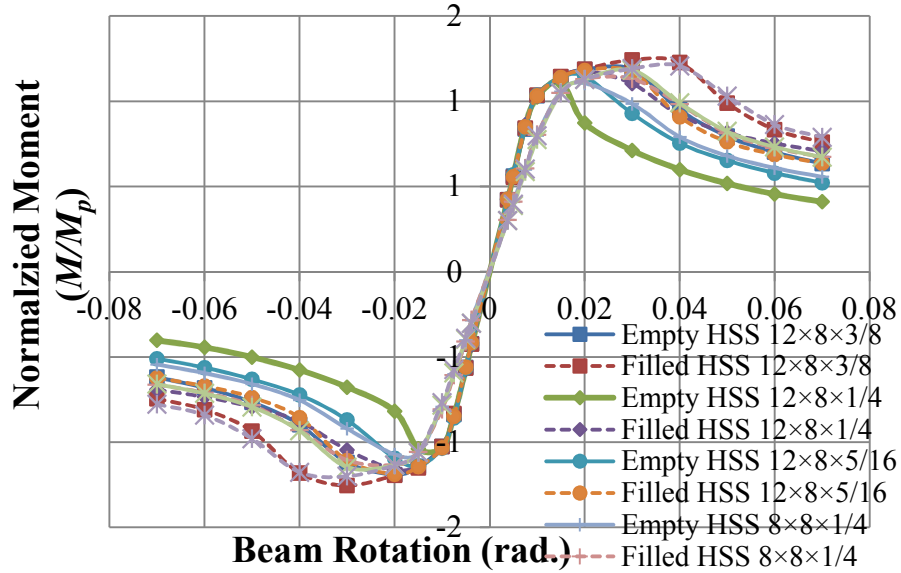


Figure 7.25 Normalized Moment at Each Rotation Level versus Beam Rotation Backbone Curves for Beams in Group 4

Since significant improvement in moment degradation at the 0.04 rad. rotation level is observed in the HSS 12×8×1/4 beam, stress contours of the filled and empty beams are shown in Figure 7.26 and 7.27. The stress distribution of both beams is similar at the first 0.02 rad. cycle. However, local buckling in the plastic hinge region is more apparent in the empty beam compared to the filled beam suggesting the fill material can effectively mitigate the occurrence of local buckling.

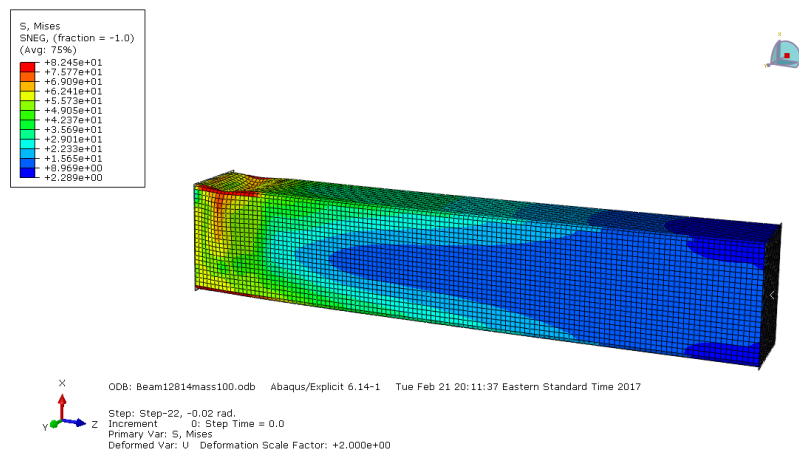


Figure 7.26 Stress Contour in Empty HSS 12×8×1/4 at the 0.02 rad. Cycle

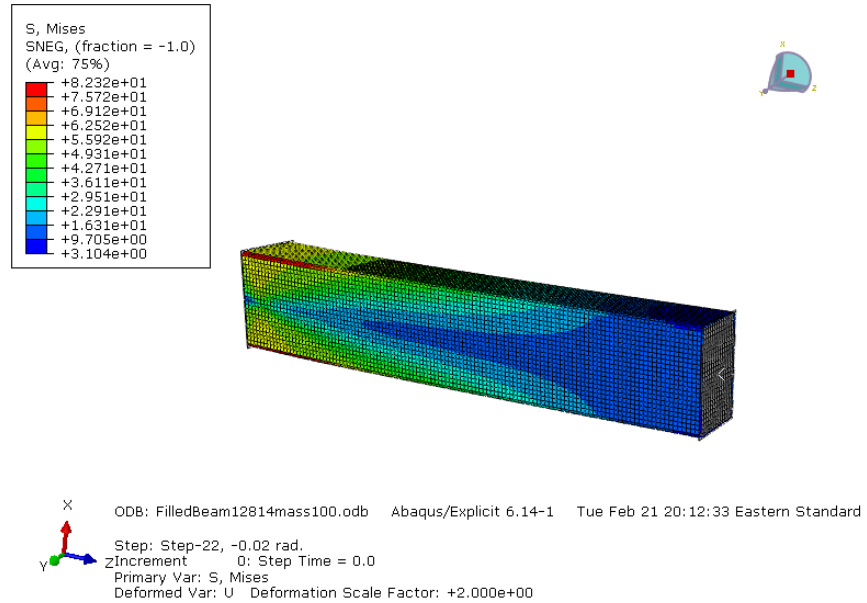


Figure 7.27 Stress Contour in Filled HSS 12×8×1/4 at the 0.02 rad. Cycle

7.3 Design Implication

The percent degradation of the maximum moment of the HSS beam at 0.04 rad. cycle is evaluated with respect to b/t and d/t ratios as shown in Figure 7.28 and Figure 7.29. The PU foam material can reduce the percent degradation of the maximum moment by 7% to 22% compared to the empty beams. A linear regression analysis is conducted for the fourteen specimens to relate the b/t and d/t ratios to the percent degradation of maximum moment at the 0.04 rad. cycle and the findings are shown in Equation 7.5 and Equation 7.6 for the empty HSS beams and Equation 7.7 and Equation 7.8 for the filled HSS beams, respectively. The larger slope in Equation 7.5 and Equation 7.7 indicates that degradation of moment capacity is more dependent on the b/t ratio. Based on the linear regression results, the b/t and d/t ratio limits for the empty HSS beam are 18.3 and 30.8, respectively, to ensure the beam’s ability to sustain 80% of its maximum moment under cyclic loads. These limits are larger than the values computed from Equation 7.3 and Equation 7.4 because the proposed equations by Fadden and McCormick (2014a) considered one standard deviation away from the mean. Also a much larger parametric study was conducted to obtain these limits. However, the results are able to provide a good comparison between the empty HSS and filled HSS beams. For the filled HSS beams, the b/t and

d/t ratio limits are 24.2 and 40.1 to maintain 80% of moment capacity which is much larger than those of the empty beams. The presence of the fill material allows consideration of HSS beams with less stringent requirements on b/t and d/t ratios in seismic applications thus reducing cost and seismic mass.

$$Deg_{0.04} \left(\frac{b}{t} \right) = 0.021 \left(\frac{b}{t} \right) - 0.19 \quad \text{for } 7.3 \leq \frac{b}{t} \leq 31.3 \quad \text{Equation 7.5}$$

$$Deg_{0.04} \left(\frac{d}{t} \right) = 0.016 \left(\frac{d}{t} \right) - 0.30 \quad \text{for } 17.7 \leq \frac{d}{t} \leq 48.5 \quad \text{Equation 7.6}$$

$$Deg_{0.04} \left(\frac{b}{t} \right) = 0.014 \left(\frac{b}{t} \right) - 0.14 \quad \text{for } 7.3 \leq \frac{b}{t} \leq 31.3 \quad \text{Equation 7.7}$$

$$Deg_{0.04} \left(\frac{d}{t} \right) = 0.009 \left(\frac{d}{t} \right) - 0.17 \quad \text{for } 17.7 \leq \frac{d}{t} \leq 48.5 \quad \text{Equation 7.8}$$

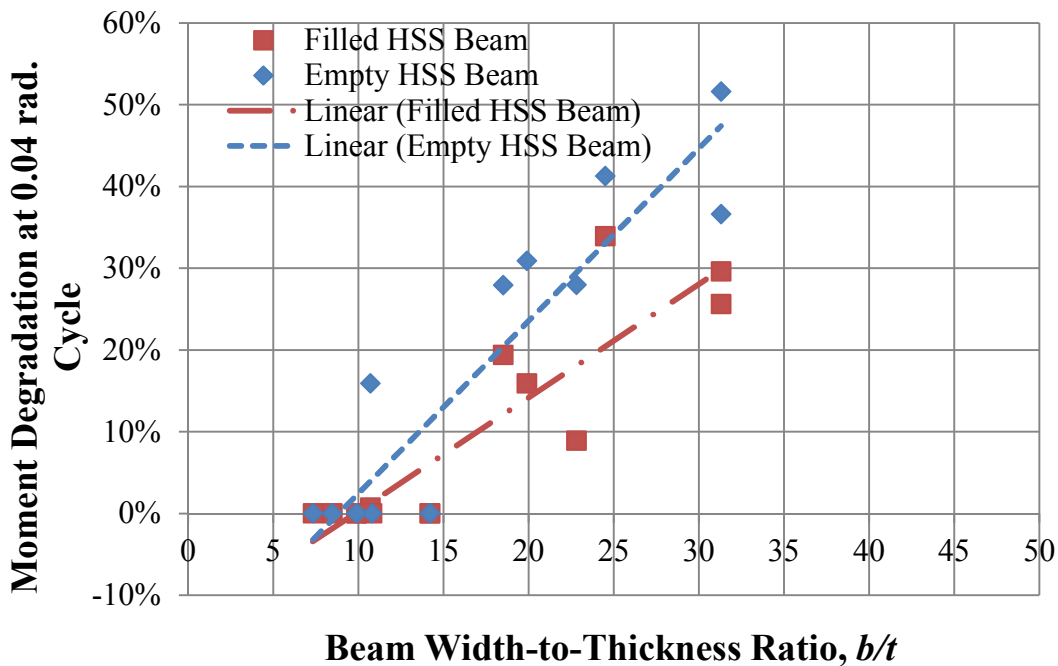


Figure 7.28 Effect of b/t Ratio on the Percent Degradation of Moment Capacity at 0.04 rad.

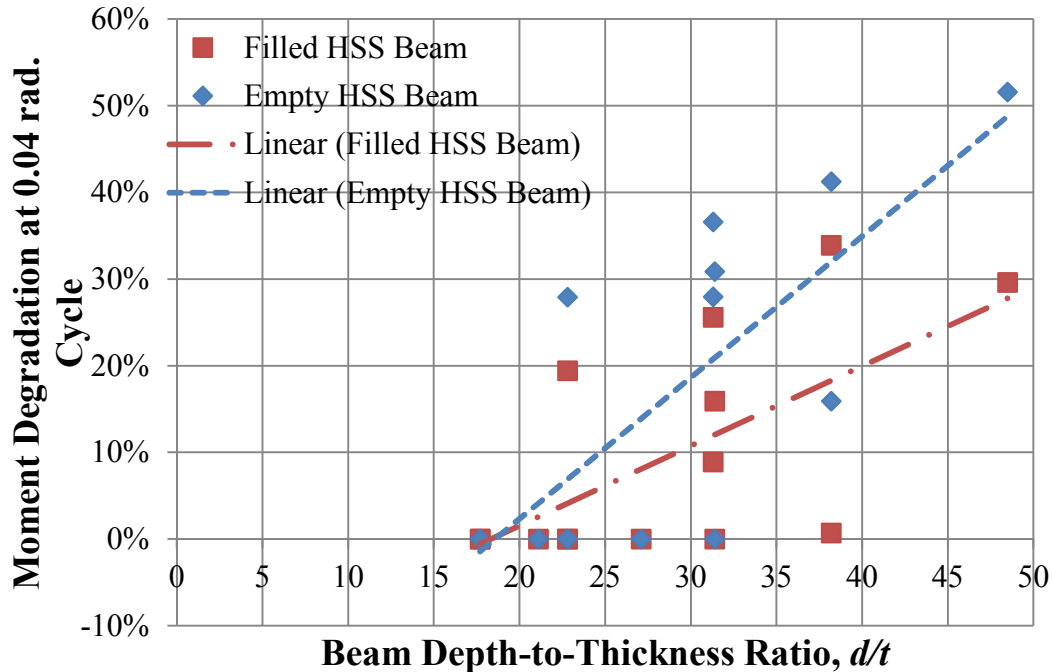


Figure 7.29 Effect of d/t Ratio on the Percent Degradation of Moment Capacity at 0.04 rad.

7.4 Conclusions

To further evaluate the feasibility of the fill materials in the seismic fill application, an FE model is validated to experimental results of an empty HSS beam and foam cubes. The validated model is then used to conduct a parametric study of empty and filled HSS beams subject to increasing cyclic bending loading. The parametric study considers 14 different sections distributed into four regions based on their b/t and d/t ratios. The b/t and d/t ratios of the HSS beams vary from 7.3 to 31.3 and 17.7 to 48.5, respectively. The effect of the fill material on the hysteretic behavior of the HSS beams is investigated with a focus on the moment degradation at 0.04 rad., cumulative energy dissipation capacity, secant stiffness, and when local buckling occurs. The key conclusions from this work are summarized as follows:

1. Comparison of an FE model and experimental test results of an empty HSS beam shows that the explicit solution from Abaqus is sufficient to accurately simulate the bending behavior of HSS beams subject to cyclic loads. The hysteretic behavior of empty HSS

beams from FE analyses show good correlation with experimental tests with only 6% difference in moment capacity.

2. The parametric study indicates that filled beams reach their moment capacity at larger rotation levels compared with empty beams especially for HSS with larger b/t and d/t ratios which indicates their ability to postpone local buckling.
3. For the HSS beams with larger b/t and d/t ratios, secant stiffness increases slightly at larger rotation levels by incorporation of the PU foam as the fill material due to mitigation of local buckling in the filled beams leading to larger moments achieved at the same rotation level after occurrence of local buckling. However, with continued deformation, the foam starts to enter its plastic plateau causing the secant stiffness of the filled and empty HSS beams to be almost identical.
4. In the most compact HSS beam sections, cumulative energy dissipated in the filled HSS beams is almost the same as the empty beams throughout the loading history. For the HSS beams with larger b/t and d/t ratios, cumulative energy dissipation capacity improves by 15% to 45% over the empty beams by incorporation of the PU foam.
5. The percent moment degradation of the filled HSS beams at 0.04 rad. is 7% to 22% less than that of the empty HSS beams. A linear regression analysis that relates the b/t and d/t ratios to the percent moment degradation at 0.04 rad. indicates b/t and d/t ratio limits for empty beams are 18.3 and 30.8 for their ability to sustain 80% moment capacity at 0.04 rad; while the b/t and d/t ratio limits for filled beams are 24.2 and 40.1 suggesting the fill material is able to produce more stable hysteretic behavior thus allowing more HSS beam sizes when filled to be utilized in seismic bending applications.
6. Effects of the fill material on the hysteretic behavior, secant stiffness, energy dissipation capacity and moment degradation is more significant for HSS beams with increasing b/t and d/t ratios since these beams are more susceptible to local buckling prior to establishing a stable plastic hinge.
7. 16 lb PU foam is an effective fill material in HSS beams in terms of mitigation of local buckling and increasing energy dissipation capacity especially for beams with larger b/t and d/t ratios.

CHAPTER 8 SUMMARY AND CONCLUSIONS

8.1 Summary

Hollow structural sections (HSS) have been widely used in onshore and offshore structural engineering as truss members, braces, towers, masts, and columns due to their excellent properties: high strength-to-weight ratio; and excellent compression, bending and torsional resistance. Research on HSS members and connections in structural applications has mainly focused on the behavior of HSS as columns, axially loaded braces and truss members. Only a few studies have considered the cyclic bending behavior of HSS members leading to limited applications of HSS based moment connections in seismic moment frames. Due to the lack of the understanding of the seismic performance of HSS based moment connections, these alternative connection configurations, which can potentially lead to a more resilient and robust seismic moment frame system subject to seismic loads, have been overlooked. Previous studies (Fadden & McCormick, 2011; Fadden et al., 2014) show that HSS based moment connections are feasible in seismic applications provided that the connection configuration enables the HSS beams to develop stable plastic hinges and avoid brittle failure subject to cyclic loads. However, detailing for these HSS based moment connections requires significant field welding leading to increased construction costs and more susceptibility to poor quality welds associated with the field welding. Fairly stringent width-thickness and depth-thickness requirements are needed to prevent local buckling prior to the formation of the plastic hinge. As a result, *the goal of this project is to experimentally and analytically characterize the seismic performance of an innovative HSS-to-HSS beam-to-column connection configuration that utilizes collars and limits the need for significant welding. To address local buckling constraints, the feasibility of lightweight, non-traditional civil engineering material filled HSS beams are evaluated in terms of the effects of the fill in mitigating local buckling and increasing energy dissipation when subject to increasing cyclic bending loads.*

The approach that has been taken here to accomplish the goal includes both experimental and analytical work in two phases. The first phase has experimentally and numerically evaluates the seismic performance of welded HSS based collar connections subject to large cyclic loads. The second phase focuses on experimental and analytical studies of the mechanical properties of non-traditional fill material (i.e. 16 lb PU foam) and the effectiveness of the fill to improve the cyclic behavior of HSS beams subject to seismic loads and widen the range of HSS applicable for seismic applications.

8.1.1 Summary of HSS based Seismic Moment Connection Study

A study of the feasibility and configuration requirements of HSS based moment connections was completed to evaluate and improve the seismic performance of welded HSS-to-HSS beam-to-column connections and to explore detailing requirements to ensure the ability of the moment connections to develop the beam plastic moment capacity with minor moment degradation with continued cycling. Previous studies showed unreinforced HSS based moment connections were not viable in seismic applications due to brittle failure at the toe of the welds and excessive inelastic deformation concentrated in the column face (Fadden et al., 2014). Meanwhile, increasing popularity of HSS members in seismic moment frames necessitates research on new configurations and detailing requirements of HSS based moment connections. The study of HSS based moment connections subject to cyclic loads was divided into three main phases: (1) experimental testing of two reinforced connections based on which the HSS leading to further development of an innovative HSS based moment connection configuration for ease of construction (2) an experimental study of two HSS based collar connections under large cyclic loads to better characterize their hysteretic behavior, load transfer mechanism and failure mode and (3) use of advanced finite element models for a parametric study of the collar connections to determine future design recommendations.

The first phase of the HSS based moment connection study considered the viability of reinforced HSS-to-HSS beam-to-column moment connections in seismic applications through experimental tests. The two reinforced HSS based moment connections showed promise for tube based seismic moment frames since they exhibited stable hysteretic behavior in a ductile manner. However, large amounts of field welding for these reinforced connection configurations

increases construction costs and potential for unanticipated behavior due to poor weld quality. As a result, the welded HSS collar based connection concept was explored. The design approach for the collar connections was developed based on the assumption that the beam is able to develop its moment capacity and weld failure does not occur prior to the formation of the beam plastic hinge. A preliminary parametric study of 12 different FE models considering the effects of endplate thickness, collar thickness, collar depth and use of endplate stiffeners on seismic performance of HSS based collar connections was conducted. Based on the developed design approach and preliminary parametric study results, two experimental HSS collar connections were designed, fabricated and tested.

During the second phase of the HSS based moment connection study, quasi-static cyclic tests of two full-scale HSS based collar connections were conducted to experimentally assess their capability of meeting seismic requirements. The seismic performance of the collar connections was evaluated in terms of hysteretic behavior, sources of plastic rotation, secant stiffness, energy dissipation capacity and distribution of strain. The limit state and load transfer mechanism of the collar connection subject to large cyclic loads were observed up to initiation of fracture in the HSS beams at rotation levels of 0.07 rad.

The final phase of the HSS based moment connection study calibrated and validated FE models against the experimental results. The validated FE models were incorporated in a parametric study of 28 HSS based collar connections with various beam depth thickness ratios, beam width thickness ratios, beam-to-column width ratios, thicknesses of the endplate and thicknesses of the collars to better understand their influences on the moment capacity, secant stiffness and energy dissipation capacity of the connections. Based on both the experimental testing and parametric study results, potential improvements were presented for future design.

8.1.2 Summary of a Lightweight, Non-Traditional Material Filled HSS Beam Study

The filled HSS beam study was performed to determine the suitability of lightweight, non-traditional civil engineering material as fill material in seismic application via experimental testing and finite element analyses. The work consisted of two phases: (1) preliminary experimental study for the selection of the most suitable fill material and experimental testing of the mechanical properties of the selected fill material (i.e. 16 lb PU Foam) and (2) a parametric

study of filled HSS beams subject to continued increasing cyclic loads to determine the influence of the fill on seismic performance and the ability to shift current width thickness and depth thickness requirements.

During the first phase of the filled HSS beam study, three types of PU foam and one type of rubber were considered as fill materials for HSS beams under monotonic bending loads to assess their performance in terms of inhibiting local buckling and improving the energy dissipation capacity of the member. The most suitable fill material was selected (16 lb PU foam) and the material properties were determined through monotonic and cyclic compression tests at the three different loading rates to better capture the 16 lb foam's mechanical behavior under cyclic loading conditions and provide necessary information for properly modeling the behavior in the finite element analyses. The mechanical properties considered included yield strength, elastic modulus, Poisson's ratio, stresses at different strain levels, cumulative energy dissipated and secant stiffness at different strain levels.

During the second phase of the filled HSS beam study, an FE model of one empty cantilever HSS beam subject to cyclic loads and the FE model of a PU foam cube under compression loads was validated against experimental test results. The FE model for the HSS member was compared with a previously tested empty HSS beam (Fadden & McCormick, 2011) whereas the FE model for the PU foam cube under compression was compared to the result of one of the PU foam specimens tested in monotonic compression. A parametric study of 14 filled and 14 empty cantilever HSS beams was then conducted considering the effects of various beam width thickness and depth thickness ratios. The numerical study results were utilized to further evaluate the benefits of filled HSS beams in seismic applications.

8.2 Conclusions

1. The full-scale quasi-static cyclic tests of the reinforced HSS-to-HSS beam-to-column moment connections demonstrated HSS based moment connections are viable for use in seismic applications. Both connections exhibited desirable ductile plastic hinging of the HSS beam with the majority of inelastic deformation concentrated in the HSS beam which meets current design requirements. However, the two welded reinforced HSS based moment

connections could be improved by incorporating other components into the inelastic response and reducing the amounts of field welds.

2. The HSS based collar connection concept was presented to reduce welding requirements and increase construction speeds. A parametric study showed these connections are able to develop the beam's plastic moment capacity in a ductile manner which is desirable for seismic applications.
3. A preliminary finite element parametric study considered effects of collar depth, stiffeners, and collar and endplate thicknesses on the performance of the collar connection. The results indicated that with an HSS 12×8×3/8 beam, the endplate thickness has the most influence on seismic behavior and stiffeners can effectively move the plastic deformation away from the column face.
4. A design approach was developed for welded collar connections based on the analysis of the load transfer mechanism. The approach used the beam moment capacity as the required connection moment and assumed beam plastic hinging and collar yielding occur simultaneously prior to weld failure to avoid brittle failure of the connection while achieving an economic design.
5. Two HSS based collar connections representing two exterior moment connections were cyclically tested to failure. Moment degradation was shown to start at around the 0.06 rad. rotation level which would meet current SMF requirements. The experimental results showed both collar connections are suitable for seismic application since they exhibited stable hysteretic behavior and achieved the beam plastic moment capacity with minor moment degradation prior to fracture initiation at the HSS beam corners. Almost all of the inelastic deformation was concentrated in the HSS beams indicating both collar connections satisfy current seismic design requirements. However, the performance of the collar connections can be improved by sharing the inelastic deformation with other structural components.
6. Stiffeners effectively moved the plastic deformation away from the column face with almost all the inelastic deformation concentrated in the beam. However, the presence of stiffeners did not exhibit a significant advantage in regards to behavior over the collar connection

without stiffeners.

7. Calibration of finite element models of the collar connections utilizing the same connection configuration as the test specimens, measured material properties, and geometric perturbation showed less than 10% discrepancies in the moment capacity and secant stiffness indicating the FE analyses can accurately capture the cyclic behavior of these connections.
8. A larger parametric study of HSS based collar connections considering beam depth thickness ratio, beam width thickness ratio, beam-to-column width ratio, and collar and endplate thickness was conducted. Twenty-four out of 28 collar connections are able to develop the beam plastic moment capacity which further indicated the collar connections are feasible for seismic applications.
9. The parametric study of the collar connections also indicated the moment capacity and secant stiffness of the collar connection increased with increasing endplate thickness due to the thicker, stiffer endplate allowing other components to be involved in the inelastic deformation. Decreasing the beam width thickness ratio (b/t) led to an increase in the moment capacity and secant stiffness since the collar connections with larger b/t are more susceptible to local buckling prior to the formation of the beam plastic hinge. However, the connections with the smallest b/t were not able to develop the beam moment capacity due to the fact that the limit state of the connection was controlled by collar yielding. Cumulative energy dissipation was inversely proportional to beam width thickness and depth thickness ratios due to the early onset of local buckling. Based on these results, the collar connections with larger b/t and d/t will exhibit more stable hysteretic behavior with larger energy dissipated under cyclic loads provided that endplate and collar yielding do not occur prior to development of the beam plastic moment capacity.
10. According to the experimental tests and parametric study of the collar connections, the welding configuration limited engagement of other structural components in accommodating the inelastic deformation. The improvement method for HSS based seismic moment connections were presented by removing the transverse welds along the endplate at the column face and transverse welds along the collar plates on the endplate. As a result, fillet welds along the endplate on the column face only transfer shear, and bending moments are

transmitted to the collars through endplate deformation. Thus, the collars are more effectively utilized.

11. Sixteen lb/ft³ polyurethane foam was found to be most suitable for seismic applications among three different densities of PU foam and one rubber material in terms of ability to improve local buckling behavior and the moment capacity of the beam. Monotonic bending tests of the empty HSS beams and filled HSS beams showed that 16 lb PU foam can effectively postpone the rotation level at which the maximum moment was achieved by 0.01 rad., increase the post buckling stiffness by 64% at 0.03 rad. and improve energy dissipation by 30% at 0.03 rad.
12. Material properties of 16 lb PU foam were obtained under monotonic and cyclic compression loads. The results indicated large scatter among samples in terms of elastic modulus, yield strength and Poisson's ratio which needs to be accounted for to ensure reliable performance. The loading rate had little effect on the material properties compared to the scatter due to the material nonhomogeneity, the ambient temperature during fabrication and human factors. Under cyclic compression loads, the PU foam showed large residual deformation suggesting plastic, unrecoverable deformation in seismic applications.
13. Calibration of the finite element models of an empty HSS beam subject to cyclic loads and the PU foam cube subject to monotonic compression loads showed a good correlation with experimental test results. A parametric study of 14 filled HSS beams and 14 empty HSS beams considering different beam width thickness and depth thickness ratios was conducted. The FE models of the filled HSS beam exhibited slower moment degradation, more cumulative energy dissipation, and larger secant stiffness at intermediate rotation levels indicating the effects of the fill material in mitigating local buckling and increasing energy dissipation capacity were positive.
14. The FE analyses indicated the effects of 16 lb PU foam on the hysteretic behavior, secant stiffness, energy dissipation capacity and moment degradation was more significant for the HSS beams with larger b/t and d/t ratios since they are more susceptible to local buckling.
15. Linear regression analyses for the filled HSS beams and empty HSS beams were conducted

based their moment degradation at the 0.04 rad. rotation level which provided a means of evaluating the suitability of these HSS beams for SMF. Based on the parametric study results, in order to meet the SMF requirement that at least 80% of the moment capacity is sustained at 0.04 rad., the b/t and d/t ratio limits are 18.3 and 30.8 for the empty HSS beam and 24.2 and 40.1 for the filled HSS beam, respectively. The increased b/t and d/t ratios in the filled HSS beams allow for more HSS beam sizes to be considered in seismic design thus reducing cost and seismic mass.

8.3 Research Impact

1. Experimental tests of the two reinforced HSS based moment connections showed HSS based moment connections are feasible for seismic application provided they exhibited stable hysteretic behavior with a majority of inelastic deformation concentrated in the HSS beam. However, the significant amounts of field welding required can lead to uneconomic connection configurations and potential poor failure due to weld quality.
2. The optimization of the HSS based moment connection was presented from the perspective of construction ease. As a result, the welded collar connection was presented and the design approach was provided that allows for development of the HSS beam plastic moment capacity when subject to seismic loads. Since welds connecting the HSS beam to the endplate and connecting the lower collar to the HSS column can be completed in the shop, only fillet welds along the endplate at the column face and around the upper collar are required in the field. Compared to the CJP welds needed in the reinforced connections, the amounts of field welds are reduced.
3. Experimental testing of the HSS based collar connections showed that these connections are suitable for seismic applications, but limited inelastic deformation is observed outside the beam member indicating further detailing improvements may lead to a more economic connection.
4. Analysis of finite element models of the collar connections showed that the utilization of welded collar connection was feasible for developing beam moment capacity provided collar

yielding does not occur prior to the formation of the beam plastic hinge.

5. The findings from the parametric study of the collar connections indicated the potential limit states of the collar connections include collar yielding and beam plastic hinging. To ensure the connection's ability to develop its plastic moment capacity, endplate and collar yielding should not occur prior to the formation of the beam plastic hinge. The collar connections with larger b/t and d/t exhibited larger moment degradation which is attributable to earlier onset of local buckling. The beam-to-column width ratio has little effect on the cyclic behavior of the collar connections which is due to the fact that load is transferred from the beam endplate to the column sidewall directly.
6. Based on the performance of the collar connections in both the experimental and analytical studies, optimization methods for improvement of the seismic performance of the HSS based moment connection were presented.
7. Experimental tests of filled HSS beams under monotonic bending showed that lightweight, non-traditional civil engineering material can effectively postpone local buckling and increase energy dissipation capacity.
8. Mechanical properties of the selected fill material, 16 lb PU foam, indicated the mechanical properties of the material were susceptible to influences from ambient temperature, humidity and human factors when fabricated. Loading rate had minor effect on the mechanical properties.
9. The parametric study of the PU foam filled HSS beams and empty HSS beams showed the promise of the fill material in seismic applications since it was effective in mitigating local buckling and increasing energy dissipation capacity.
10. The linear regression analyses from the parametric study results provided b/t and d/t ratio limits for the filled HSS beams which exceeded those required for empty HSS beams. The utilization of the fill material allows for a wider selection of HSS beams for SMF applications thereby reducing cost and seismic weight.
11. The results from this study allowed for a more effective utilization of HSS based moment

connections under cyclic loading conditions.

8.4 Recommendations for Future Research

This research focus on two enhancement methods for seismic moment frames by utilization of hollow structural sections and lightweight, non-traditional civil engineering materials. However, further work is needed for better characterization of seismic performance of welded HSS based moment connections and filled HSS members under increasing cyclic loading conditions. The recommendations for continued research are as follows:

- 1 Both analytical and experimental research on different HSS-to-HSS beam-to-column moment connection configurations that are likely suitable for seismic application is recommended. The optimization method presented for the HSS based collar moment connection reduces the amount of fillet welds, allows for rapid or modular construction and also more efficiently utilizes structural components with a more explicit load transfer path.
- 2 More mechanical tests are needed for better understanding of the PU foams performance in seismic application. The possible tests include foam in-plane shear, uni-axial tension, foam and steel adhesion tests, biaxial or even tri-axial tests.
- 3 Cyclic tests of 16 lb PU foam filled HSS beams are recommended to evaluate the effects of fill material for various beam depth thickness and width thickness ratios. These test results will be important for further calibration and validation of FE results.
- 4 Further research on lightweight, non-traditional civil engineering materials should consider more potential fill materials such as metal foam, honeycomb material and high damping rubber materials. Characterization of mechanical properties of these materials and cyclic behavior of filled HSS beams is needed in the search for the most suitable lightweight materials for the HSS fill application.

REFERENCE

- Abambres, M., Camotim, D., & Silvestre, N. (2012). *First order elastoplastic GBT analysis of tubular beams*. Paper presented at the Proceedings of the 14th Int. Symposium on Tubular Structures, London (UK).
- Abaqus, V. (2014). 6.14 Documentation. *Dassault Systemes Simulia Corporation*.
- AISC. (2010a). *Seismic provisions for structural steel buildings*: American Institute of Steel Construction.
- AISC. (2010b). *Specification for Structural Steel Buildings*. Chicago.
- AISC. (2010c). *Steel Construction Manual*; American Institute of Steel Construction. *Inc.*–.
- Amin, A., Wiraguna, S., Bhuiyan, A., & Okui, Y. (2006). Hyperelasticity model for finite element analysis of natural and high damping rubbers in compression and shear. *Journal of engineering mechanics*, 132(1), 54-64.
- Anderson, J., Gourley, B., Green, M., Hajjar, J., Johnston, R., Leon, R., et al. (1995). Case studies of steel moment frame building performance in the Northridge earthquake of January 17, 1994. *Report no. SAC, 95(07)*.
- Arruda, E. M., & Boyce, M. C. (1993). A three-dimensional constitutive model for the large stretch behavior of rubber elastic materials. *Journal of the Mechanics and Physics of Solids*, 41(2), 389-412.
- Ashby, M. F., Evans, T., Fleck, N. A., Hutchinson, J., Wadley, H., & Gibson, L. (2000). *Metal foams: a design guide*: Elsevier.
- ASTM. (2009). *Standard Test Method for Tensile and Tensile Adhesion Properties of Rigid Cellular Plastics*. , *Designation: D1623-09*. . ASTM International.
- ASTM. (2010). *Standard Test Method for Compressive Properties of Rigid Plastics*: ASTM International.
- ASTM. (2013). *ASTM A500/A500M-13, Standard Specification for Cold-formed Welded and Seamless Carbon Steel Structural Tubing in Rounds and Shapes*. Conshohocken, PA: ASTM International.
- ASTM. (2014). *Standard Test Method for Tensile Properties of Polymer Matrix Composite Materials*.: American Society for Testing and Materials.

- ASTM. (2016). Standard Test Methods for Flexible Cellular Materials-Slab, Bonded, and Molded Urethane Foams, *Designation: D3574-16*. : ASTM International.
- Bergström, J., & Boyce, M. (1998). Constitutive modeling of the large strain time-dependent behavior of elastomers. *Journal of the Mechanics and Physics of Solids*, 46(5), 931-954.
- Bergström, J., & Boyce, M. (2001). Constitutive modeling of the time-dependent and cyclic loading of elastomers and application to soft biological tissues. *Mechanics of materials*, 33(9), 523-530.
- Bertero, V. V., Uang, C.-M., Llopiz, C. R., & Igarashi, K. (1989). Earthquake simulator testing of concentric braced dual system. *Journal of Structural Engineering*, 115(8), 1877-1894.
- Bešević, M. (2014). Load bearing capacities of cold formed steel sections subjected to axial load. *Materials and structures*, 47(1-2), 367-379.
- Bjorhovde, R. (1977). Strength and behavior of cold-formed HSS columns.
- Bjorhovde, R., & Birkemoe, P. C. (1979). Limit states design of HSS columns. *Canadian Journal of Civil Engineering*, 6(2), 276-291.
- Brescia, M., Landolfo, R., Mammana, O., Iannone, F., Piluso, V., & Rizzano, G. (2009). Preliminary results of an experimental program on the cyclic response and rotation capacity of steel members. *Proceedings of behavior of steel structures in seismic areas*, 971-976.
- Brezny, R., & Green, D. J. (1990). The effect of cell size on the mechanical behavior of cellular materials. *Acta metallurgica et materialia*, 38(12), 2517-2526.
- Buckle, I. G. (2000). Passive control of structures for seismic loads. *Bulletin of the New Zealand Society for Earthquake Engineering*, 33(3), 209-221.
- Chan, S. L. (1989). Inelastic post-buckling analysis of tubular beam-columns and frames. *Engineering Structures*, 11(1), 23-30.
- Chan, S. L., Kitipornchai, S., & Al-Bermani, F. G. (1991). Elasto-plastic analysis of box-beam-columns including local buckling effects. *Journal of Structural Engineering*, 117(7), 1946-1962.
- Chen, C.-C., Chen, S.-W., Chung, M.-D., & Lin, M.-C. (2005). Cyclic behaviour of unreinforced and rib-reinforced moment connections. *Journal of Constructional Steel Research*, 61(1), 1-21.
- Chen, C.-C., Lin, C.-C., & Tsai, C.-L. (2004). Evaluation of reinforced connections between steel beams and box columns. *Engineering structures*, 26(13), 1889-1904.

- Chiew, S.-P., Lee, C.-K., Lie, S.-T., & Ji, H.-L. (2007). Fatigue behaviors of square-to-square hollow section T-joint with corner crack. I: Experimental studies. *Engineering fracture mechanics*, 74(5), 703-720.
- Christopoulos, C., Filiatrault, A., & Bertero, V. V. (2006). *Principles of passive supplemental damping and seismic isolation*: Iuss Press.
- Compston, P., Styles, M., & Kalyanasundaram, S. (2006). Low energy impact damage modes in aluminum foam and polymer foam sandwich structures. *Journal of Sandwich Structures & Materials*, 8(5), 365-379.
- Corona, E., & Vaze, S. P. (1996). Buckling of elastic—plastic square tubes under bending. *International Journal of Mechanical Sciences*, 38(7), 753-775.
- Correlated Solutions (2009). *Vic-2D Testing Guide*. available at <http://correlatedsolutions.com>.
- Davison, T., & Birkemoe, P. (1983). Column behaviour of cold-formed hollow structural steel shapes. *Canadian Journal of Civil Engineering*, 10(1), 125-141.
- Dawe, J., & Grondin, G. (1990). W-shape beam to RHS column connections. *Canadian Journal of Civil Engineering*, 17(5), 788-797.
- Dawe, J. L., Elgabty, A. A., & Grondin, G. Y. (1985). Local buckling of hollow structural sections. *Journal of Structural Engineering*, 111(5), 1101-1112.
- Dorfmann, A., & Ogden, R. W. (2004). A constitutive model for the Mullins effect with permanent set in particle-reinforced rubber. *International Journal of Solids and Structures*, 41(7), 1855-1878.
- Eidinger, J. M., & Kelly, J. M. (1978). *Experimental results of an earthquake isolation system using natural rubber bearings*: Earthquake Engineering Research Center.
- Elchalakani, M., Zhao, X.-L., & Grzebieta, R. (2003). Tests of cold-formed circular tubular braces under cyclic axial loading. *Journal of Structural Engineering*, 129(4), 507-514.
- Elchalakani, M., Zhao, X.-L., & Grzebieta, R. (2004). Concrete-filled steel circular tubes subjected to constant amplitude cyclic pure bending. *Engineering structures*, 26(14), 2125-2135.
- EN, C. (2005). 1-1-Eurocode 3: Design of steel structures-Part 1-1: General rules and rules for buildings. *European Committee for Standardization*.
- Engelhardt, M. D., & Sabol, T. A. (1997). Seismic - resistant steel moment connections: developments since the 1994 Northridge earthquake. *Progress in Structural Engineering and Materials*, 1(1), 68-77.
- Engelhardt, M. D., & Sabol, T. A. (1998). Reinforcing of steel moment connections with cover plates: benefits and limitations. *Engineering Structures*, 20(4-6), 510-520.

- Engelhardt, M. D., Winneberger, T., Zekany, A. J., & Potyraj, T. J. (1996). The dogbone connection: Part II. *Modern Steel Construction*, 36(8), 46-55.
- Fadden, M., & McCormick, J. (2011). Cyclic quasi-static testing of hollow structural section beam members. *Journal of Structural Engineering*, 138(5), 561-570.
- Fadden, M., & McCormick, J. (2014a). Finite element model of the cyclic bending behavior of hollow structural sections. *Journal of Constructional Steel Research*, 94, 64-75.
- Fadden, M., & McCormick, J. (2014b). HSS-to-HSS seismic moment connection performance and design. *Journal of Constructional Steel Research*, 101, 373-384.
- Fadden, M., Wei, D., & McCormick, J. (2014). Cyclic Testing of Welded HSS-to-HSS Moment Connections for Seismic Applications. *Journal of Structural Engineering*, 141(2), 04014109.
- Fadden, M. F. (2013). *Cyclic bending behavior of hollow structural sections and their application in seismic moment frame systems*. University of Michigan.
- Fan, F.-G., Ahmadi, G., Mostaghel, N., & Tadjbakhsh, I. (1991). Performance analysis of aseismic base isolation systems for a multi-story building. *Soil Dynamics and Earthquake Engineering*, 10(3), 152-171.
- FEMA. (2000a). *Recommended Postearthquake Evaluation and Repair Criteria for Welded Steel Moment-frame Buildings* (Vol. 352): Fema.
- FEMA. (2000b). *Recommended seismic evaluation and upgrade criteria for existing welded steel moment-frame buildings*: Fema.
- Fisher, J. W., Dexter, R. J., & Kaufmann, E. J. (1997). Fracture mechanics of welded structural steel connections. *Report No. SAC*, 95-09.
- Fogarty, J., & El-Tawil, S. (2014). Collapse behavior of steel columns under combined axial and lateral loading. In *Proceedings, Tenth US National Conference on Earthquake Engineering (10NCEE)*.
- Foutch, D. A., Goel, S. C., & Roeder, C. W. (1987). Seismic testing of full-scale steel building—Part I. *Journal of Structural Engineering*, 113(11), 2111-2129.
- Frater, G. S., & Packer, J. A. (1992). Modelling of hollow structural section trusses. *Canadian Journal of Civil Engineering*, 19(6), 947-959.
- Fujita, S. (1992). *Development of high damping rubber damper for vibration attenuation of high-rise building*.
- Fujita, S., Fujita, T., Furuya, O., Morikawa, S., Suizu, Y., Teramoto, T., et al. (1992). *Development of high damping rubber damper for vibration attenuation of high-rise building*.

- Fukuta, T., Nishiyama, I., Yamanouchi, H., & Kato, B. (1989). Seismic performance of steel frames with inverted V braces. *Journal of Structural Engineering*, 115(8), 2016-2028.
- Ghobarah, A., Mourad, S., & Korol, R. (1996). Moment-rotation relationship of blind bolted connections for HSS columns. *Journal of Constructional Steel Research*, 40(1), 63-91.
- Gibson, L. J., & Ashby, M. F. (1999). *Cellular solids: structure and properties*: Cambridge university press.
- Giroux, Y.-M., & Picard, A. (1977). Rigid framing connections for tubular columns. *Canadian Journal of Civil Engineering*, 4(2), 134-144.
- Goggins, J., Broderick, B., Elghazouli, A., & Lucas, A. (2005). Experimental cyclic response of cold-formed hollow steel bracing members. *Engineering Structures*, 27(7), 977-989.
- Goggins, J., Broderick, B. M., Elghazouli, A., & Lucas, A. (2006). Behaviour of tubular steel members under cyclic axial loading. *Journal of Constructional Steel Research*, 62(1), 121-131.
- Gong, Y. (2008). Double-angle shear connections with small hollow structural section columns. *Journal of Constructional Steel Research*, 64(5), 539-549.
- Guerrero, N., Marante, M. E., Picón, R., & Flórez-López, J. (2007). Model of local buckling in steel hollow structural elements subjected to biaxial bending. *Journal of Constructional Steel Research*, 63(6), 779-790.
- Haddad, M., Brown, T., & Shrive, N. (2010). Experimental cyclic loading of concentric HSS braces. *Canadian Journal of Civil Engineering*, 38(1), 110-123.
- Hajjar, J. F., & Gourley, B. C. (1997). A cyclic nonlinear model for concrete-filled tubes. I: Formulation. *Journal of structural Engineering*, 123(6), 736-744.
- Hajjar, J. F., Gourley, B. C., & Olson, M. C. (1997). A cyclic nonlinear model for concrete-filled tubes. II: Verification. *Journal of Structural Engineering*, 123(6), 745-754.
- Han, D., & Chen, W. (1983). Buckling and cyclic inelastic analysis of steel tubular beam-columns. *Engineering Structures*, 5(2), 119-132.
- Hancock, G., & Rasmussen, K. (1998). Recent research on thin-walled beam-columns. *Thin-Walled Structures*, 32(1), 3-18.
- Hancock, G. J., & Zhao, X.-L. (1992). Research into the strength of cold-formed tubular sections. *Journal of Constructional Steel Research*, 23(1-3), 55-72.
- Haque, T., & Packer, J. A. (2012). Elliptical hollow section T and X connections. *Canadian Journal of Civil Engineering*, 39(8), 925-936.

- Hassan, O. F. (1991). *Modeling of bracing members and seismic behavior of concentrically braced steel structures*.
- Hazizan, M. A., & Cantwell, W. (2002). The low velocity impact response of foam-based sandwich structures. *Composites Part B: Engineering*, 33(3), 193-204.
- Huang, Y. (2009). Simulating the inelastic seismic behavior of steel braced frames including the effects of low-cycle fatigue.
- Ikeda, K., & Mahin, S. (1986). Cyclic response of steel braces. *Journal of Structural Engineering*, 112(2), 342-361.
- Jin, J., & El-Tawil, S. (2003). Inelastic cyclic model for steel braces. *Journal of Engineering Mechanics*, 129(5), 548-557.
- Ju, M., Jmal, H., Dupuis, R., & Aubry, E. (2015). Visco - hyperelastic constitutive model for modeling the quasi - static behavior of polyurethane foam in large deformation. *Polymer Engineering & Science*, 55(8), 1795-1804.
- Jubb, J., & Redwood, R. (1966). *Design of joints to box sections*. Paper presented at the Conference on Industrial Building and the Structural Engineer.
- Kelly, J., & Hodder, S. (1982). Experimental study of lead and elastomeric dampers for base isolation systems in laminated neoprene bearings. *Bulletin of the New Zealand National Society for Earthquake Engineering*, 15(2), 53-67.
- Kelly, J. M. (1986). Aseismic base isolation: review and bibliography. *Soil Dynamics and Earthquake Engineering*, 5(4), 202-216.
- Key, P. W., & Hancock, G. J. (1993). A theoretical investigation of the column behaviour of cold-formed square hollow sections. *Thin-Walled Structures*, 16(1-4), 31-64.
- Key, P. W., Hasan, S. W., & Hancock, G. J. (1988). Column behavior of cold-formed hollow sections. *Journal of Structural Engineering*, 114(2), 390-407.
- Kim, T., Stojadinovic, B., & Whittaker, A. S. (2002). Behavior of steel moment connections between a wide-flange beam and a box column. In *Proceedings, Seventh US National Conference on Earthquake Engineering (7NCEE)*.
- Kim, T., Whittaker, A., Gilani, A., Bertero, V., & Takhirov, S. (2002). Cover-plate and flange-plate steel moment-resisting connections. *Journal of Structural Engineering*, 128(4), 474-482.
- Kinki, A. (1997). Full-scale test on plastic rotation capacity of steel wide-flange beams connected with square tube steel columns. *Committee on Steel Building Structures. The Kinki Branch of the Architectural Institute of Japan, Osaka*.

- Kircher, C. A., Reitherman, R. K., Whitman, R. V., & Arnold, C. (1997). Estimation of earthquake losses to buildings. *Earthquake spectra*, 13(4), 703-720.
- Korol, R., El-Zanaty, M., & Brady, F. (1977). Unequal width connections of square hollow sections in Vierendeel trusses. *Canadian Journal of Civil Engineering*, 4(2), 190-201.
- Korol, R. M., & Mirza, F. A. (1982). Finite element analysis of RHS T-joints. *Journal of the Structural Division*, 108(9), 2081-2098.
- Korol, R. M., Mirza, F. A., & Chiu, E. T.-C. (1983). An experimental investigation of double chord HSS trusses. *Canadian Journal of Civil Engineering*, 10(2), 248-260.
- Korol, R. M., Mitri, H. S., & Mirza, F. A. (1989). Finite Element Model for RHS Double Chord K-Joints. *Journal of Structural Engineering*, 115(5), 1038-1053.
- Kozy, B. (2005). *Chord bearing capacity in long-span tubular trusses*. University of Pittsburgh.
- Kumar, S. S., & Rao, D. P. (2006). RHS beam-to-column connection with web opening—experimental study and finite element modelling. *Journal of Constructional Steel Research*, 62(8), 739-746.
- Kurobane, Y. (2004). *Design guide for structural hollow section column connections*: Verlag TUV Rheinland.
- Kurobane, Y., Makino, Y., Miura, K., Tokutome, Y., & Tanaka, M. (2001). *Testing of new RHS column-to-beam connections with U-shaped welded joints*. Paper presented at the Ninth International Symposium on Tubular Structures.
- Lakes, R. S. (1983). Size effects and micromechanics of a porous solid. *Journal of materials science*, 18(9), 2572-2580.
- Lee, J., Goldsworthy, H., & Gad, E. (2010). Blind bolted T-stub connections to unfilled hollow section columns in low rise structures. *Journal of Constructional Steel Research*, 66(8), 981-992.
- Lee, L. J., Zeng, C., Cao, X., Han, X., Shen, J., & Xu, G. (2005). Polymer nanocomposite foams. *Composites science and technology*, 65(15), 2344-2363.
- Lee, S., & Goel, S. C. (1987). *Seismic behavior of hollow and concrete-filled square tubular bracing members*. University of Michigan Ann Arbor, MI.
- Lee, S., Ting, L., & Shanmugam, N. (1993). Use of external T-stiffeners in box-column to I-beam connections. *Journal of Constructional Steel Research*, 26(2-3), 77-98.
- Liew, J. R., Shanmugam, N., & Lee, S. (1989). Behavior of thin-walled steel box columns under biaxial loading. *Journal of Structural Engineering*, 115(12), 3076-3094.

- Lignos, D. G., Hikino, T., Matsuoka, Y., & Nakashima, M. (2012). Collapse assessment of steel moment frames based on E-Defense full-scale shake table collapse tests. *Journal of Structural Engineering*, 139(1), 120-132.
- Lignos, D. G., & Krawinkler, H. (2010). *A steel database for component deterioration of tubular hollow square steel columns under varying axial load for collapse assessment of steel structures under earthquakes*. Paper presented at the Proc. 7th Int. Conf. on Urban Earthquake Engineering (7CUEE).
- Lim, T. S., Lee, C. S., & Lee, D. G. (2004). Failure modes of foam core sandwich beams under static and impact loads. *Journal of Composite Materials*, 38(18), 1639-1662.
- Linul, E., Marsavina, L., Voiconi, T., & Sadowski, T. (2013). *Study of factors influencing the mechanical properties of polyurethane foams under dynamic compression*. Paper presented at the Journal of Physics: Conference Series.
- Liu, Z., & Goel, S. C. (1988). Cyclic load behavior of concrete-filled tubular braces. *Journal of Structural Engineering*, 114(7), 1488-1506.
- Mahendran, M., & Murray, N. (1990). Ultimate load behaviour of box-columns under combined loading of axial compression and torsion. *Thin-Walled Structures*, 9(1-4), 91-120.
- Mahin, S. A. (1998). Lessons from damage to steel buildings during the Northridge earthquake. *Engineering structures*, 20(4-6), 261-270.
- Mamaghani, I. (2010). Seismic performance evaluation of steel tubular columns under cyclic bidirectional loading. *Tubular Structures XIII*, 133.
- McCormack, T., Miller, R., Kesler, O., & Gibson, L. (2001). Failure of sandwich beams with metallic foam cores. *International Journal of Solids and Structures*, 38(28), 4901-4920.
- Miller, D. K. (1998). Lessons learned from the Northridge earthquake. *Engineering structures*, 20(4-6), 249-260.
- Mills, N. (2007). *Polymer foams handbook: engineering and biomechanics applications and design guide*: Butterworth-Heinemann.
- Mirghaderi, S. R., Torabian, S., & Keshavarzi, F. (2010). I-beam to box-column connection by a vertical plate passing through the column. *Engineering Structures*, 32(8), 2034-2048.
- Miura, K., Makino, Y., Obukuro, Y., Kurobane, Y., Van Der Vegte, G., Tanaka, M., et al. (2002). Testing of beam-to-RHS column connections without weld-access holes. *International Journal of Offshore and Polar Engineering*, 12(03).
- Morgan, T. A., & Mahin, S. A. (2011). *The use of base isolation systems to achieve complex seismic performance objectives*: Pacific Earthquake Engineering Research Center.

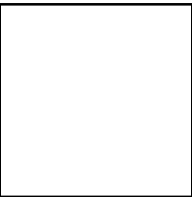
- Mourad, S., Ghobarah, A., & Korol, R. (1995). Dynamic response of hollow section frames with bolted moment connections. *Engineering structures*, 17(10), 737-748.
- Mullins, L. (1948). Effect of stretching on the properties of rubber. *Rubber Chemistry and Technology*, 21(2), 281-300.
- Naeim, F., & Kelly, J. M. (1999). *Design of seismic isolated structures: from theory to practice*: John Wiley & Sons.
- Nagarajaiah, S., & Sun, X. (2000). Response of base-isolated USC hospital building in Northridge earthquake. *Journal of structural engineering*, 126(10), 1177-1186.
- Nakashima, M., Inoue, K., & Tada, M. (1998). Classification of damage to steel buildings observed in the 1995 Hyogoken-Nanbu earthquake. *Engineering Structures*, 20(4-6), 271-281.
- Nakashima, M., Roeder, C. W., & Maruoka, Y. (2000). Steel moment frames for earthquakes in United States and Japan. *Journal of Structural Engineering*, 126(8), 861-868.
- Narayanaswamy, K., Vidyasagar, H., & Reddy, N. R. (2014). Bending Characteristics of Open Cell Polymer Foam Sandwich Structure. *Procedia Materials Science*, 5, 1906-1914.
- Nip, K., Gardner, L., & Elghazouli, A. (2010). Cyclic testing and numerical modelling of carbon steel and stainless steel tubular bracing members. *Engineering Structures*, 32(2), 424-441.
- Ogden, R., & Roxburgh, D. (1999). *A pseudo-elastic model for the Mullins effect in filled rubber*. Paper presented at the Proceedings of the Royal Society of London A: Mathematical, Physical and Engineering Sciences.
- Packer, J. A., & Cassidy, C. E. (1995). Effective weld length for HSS T, Y, and X connections. *Journal of Structural Engineering*, 121(10), 1402-1408.
- Packer, J. A., & Henderson, J. (1997). *Hollow structural section connections and trusses: a design guide*: Willowdale, Ont.: Canadian Institute of Steel Construction.
- Packer, J. A., Wardenier, J., Zhao, X. L., van der Vegte, J., & Kurobane, Y. (2009). *Design guide for rectangular hollow section (RHS) joints under predominantly static loading*: Verlag TÜV Rheinland.
- Palmer, K. D., Roeder, C. W., Lehman, D. E., Okazaki, T., Shield, C. K., & Powell, J. (2012). Concentric X-braced frames with HSS bracing. *International Journal of Steel Structures*, 12(3), 443-459.
- Pan, J., Oh, S., Wang, D.-A., Chien, W.-Y., Pan, T., & Wang, J. (2003). *Failure mechanisms of sandwich specimens with epoxy foam cores under bending conditions* (No. 0148-7191): SAE Technical Paper.

- Payne, A. R. (1962). The dynamic properties of carbon black - loaded natural rubber vulcanizates. Part I. *Journal of applied polymer science*, 6(19), 57-63.
- Picard, A., & Giroux, Y.-M. (1976). Moment connections between wide flange beams and square tubular columns. *Canadian Journal of Civil Engineering*, 3(2), 174-185.
- Pillai, S. U., & Kurian, V. (1977). Tests on hollow structural section beam columns. *Canadian Journal of Civil Engineering*, 4(2), 257-262.
- Pollien, A., Conde, Y., Pambaguian, L., & Mortensen, A. (2005). Graded open-cell aluminium foam core sandwich beams. *Materials Science and Engineering: A*, 404(1), 9-18.
- PONS, H. F. (1997). *Dynamic behavior of tubular bracing members with single plate concentric connections*. University of Toronto.
- Popov, E. P., & Blondet, M. (1996). *Behavior of large steel beam-column connections*. Paper presented at the Proc. 11th WCEE, World Conf. Earthq. Engrg., Acapulco, Mexico, August, Elsevier Science Ltd., Paper.
- Prion, H. G., & Boehme, J. (1994). Beam-column behaviour of steel tubes filled with high strength concrete. *Canadian Journal of Civil Engineering*, 21(2), 207-218.
- Rao, D. P., & Kumar, S. S. (2006). RHS beam-to-column connection with web opening—parametric study and design guidelines. *Journal of constructional steel research*, 62(8), 747-756.
- Rehkopf, J. D., McNeice, G. M., Brodland, G. W., Kuczynski, E. T., & Kerman, M. (1994). *Dynamic behaviour of an automotive polyurethane foam under multiple compression cycles* (No. 0148-7191): SAE Technical Paper.
- Rizov, V. (2009). Indentation of foam-based polymer composite sandwich beams and panels under static loading. *Journal of materials engineering and performance*, 18(4), 351.
- Roeder, C. (2000). *Performance of Moment-Resisting Connections*. Paper presented at the 12th World Conference on Earthquake Engineering, Auckland, NEW Zealand.
- Roeder, C. W., Carpenter, J. E., & Taniguchi, H. (1989). Predicted ductility demands for steel moment resisting frames. *Earthquake spectra*, 5(2), 409-427.
- Roeder, C. W., Foutch, D. A., & Goel, S. C. (1987). Seismic testing of full-scale steel building—part II. *Journal of Structural Engineering*, 113(11), 2130-2145.
- Sabol, T. A. (2001). Seismic Design Criteria for New Steel Moment Frame Buildings *Structures 2001: A Structural Engineering Odyssey* (pp. 1-8).
- SAC. (1997). *Protocol for fabrication, inspection, testing, and documentation of beam-column connection tests and other experimental specimens*.

- Schembri, P. E., & Lewis, M. W. (2014). *Calibrating the Abaqus Crushable Foam Material Model using UNM Data*: Los Alamos National Laboratory (LANL), Los Alamos, NM (United States).
- Schreier, H., Orteu, J.-J., & Sutton, M. A. (2009). *Image correlation for shape, motion and deformation measurements*: Springer US.
- Shanmugam, N., Liew, J. R., & Lee, S. (1993). Ultimate strength design of biaxially loaded steel box beam-columns. *Journal of Constructional Steel Research*, 26(2-3), 99-123.
- Shanmugam, N., Ting, L., & Lee, S. (1994). Non-linear analysis of I-beam to box-column connections. *Journal of Constructional Steel Research*, 28(3), 257-278.
- Shanmugam, N., & Ting, L. (1995). Welded interior box-column to I-beam connections. *Journal of Structural Engineering*, 121(5), 824-830.
- Shanmugam, N., Ting, L., & Lee, S. (1991). Behaviour of I-beam to box-column connections stiffened externally and subjected to fluctuating loads. *Journal of Constructional Steel Research*, 20(2), 129-148.
- Sharma, S., Narasimha Murthy, H., & Krishna, M. (2004). Low-velocity impact response of polyurethane foam composite sandwich structures. *Journal of reinforced plastics and composites*, 23(17), 1869-1882.
- Sivertsen, K. (2007). Polymer foams. *Polymer Physics*, 1(17).
- Smolka, A., & Rauch, E. (1996). *The earthquake of northridge 1994 and Kobe 1995-Lessons for risk assessment and loss prevention with special reference to earthquake insurance*. Paper presented at the 11 th World Conference on Earthquake Engineering.
- Sohal, I., & Chen, W.-F. (1988). Local buckling and inelastic cyclic behavior of tubular sections. *Thin-Walled Structures*, 6(1), 63-80.
- Soong, T., & Spencer, B. (2002). Supplemental energy dissipation: state-of-the-art and state-of-the-practice. *Engineering structures*, 24(3), 243-259.
- Spencer Jr, B., & Nagarajaiah, S. (2003). State of the art of structural control. *Journal of structural engineering*, 129(7), 845-856.
- Steel Tube Institute, A. (2003). *Hollow structural sections dimensions and sectionproperties-HSS: technical brochure*.
- Subhash, G., Liu, Q., & Gao, X.-L. (2006). Quasistatic and high strain rate uniaxial compressive response of polymeric structural foams. *International Journal of Impact Engineering*, 32(7), 1113-1126.
- Sully, R. M., & Hancock, G. J. (1996). Behavior of cold-formed SHS beam-columns. *Journal of Structural Engineering*, 122(3), 326-336.

- Sun, M. (2014). *Mechanical Behaviour of Cold-Formed Hollow Structural Section Material*. University of Toronto.
- Tan, Z., Luo, H., Long, W., & Han, X. (2013). Dynamic response of clamped sandwich beam with aluminium alloy foam core subjected to impact loading. *Composites Part B: Engineering*, 46, 39-45.
- Tang, X., & Goel, S. C. (1989). Brace fractures and analysis of phase I structure. *Journal of Structural Engineering*, 115(8), 1960-1976.
- Tani, T., Yoshitomi, S., Tsuji, M., & Takewaki, I. (2009). High - performance control of wind - induced vibration of high - rise building via innovative high - hardness rubber damper. *The Structural Design of Tall and Special Buildings*, 18(7), 705-728.
- Ting, L., Shanmugam, N., & Lee, S. (1991). Box-column to I-beam connections with external stiffeners. *Journal of Constructional Steel Research*, 18(3), 209-226.
- Toma, S., & Chen, W. F. (1983). Post-buckling behavior of tubular beam-columns. *Journal of Structural Engineering*, 109(8), 1918-1932.
- Tremblay, R. (2002). Inelastic seismic response of steel bracing members. *Journal of Constructional Steel Research*, 58(5), 665-701.
- Tremblay, R., Archambault, M.-H., & Filiatrault, A. (2003). Seismic response of concentrically braced steel frames made with rectangular hollow bracing members. *Journal of Structural Engineering*, 129(12), 1626-1636.
- Tremblay, R., Filiatrault, A., Timler, P., & Bruneau, M. (1995). Performance of steel structures during the 1994 Northridge earthquake. *Canadian Journal of Civil Engineering*, 22(2), 338-360.
- Tremblay, R., Haddad, M., Martinez, G., Richard, J., & Moffatt, K. (2008). *Inelastic cyclic testing of large size steel bracing members*. Paper presented at the 14th World Conference on Earthquake Engineering October.
- Triantafillou, T. C., & Gibson, L. J. (1987). Failure mode maps for foam core sandwich beams. *Materials Science and Engineering*, 95, 37-53.
- Uang, C.-M., Yu, Q.-S. K., Noel, S., & Gross, J. (2000). Cyclic testing of steel moment connections rehabilitated with RBS or welded haunch. *Journal of Structural Engineering*, 126(1), 57-68.
- Uriz, P., Filippou, F. C., & Mahin, S. A. (2008). Model for cyclic inelastic buckling of steel braces. *Journal of structural engineering*, 134(4), 619-628.
- Vaze, S. P., & Corona, E. (1998). Degradation and collapse of square tubes under cyclic bending. *Thin-Walled Structures*, 31(4), 325-341.

- Vegte, G. v. d., Wardenier, J., & Puthli, R. S. (2010). FE analysis for welded hollow-section joints and bolted joints. *Proceedings of the Institution of Civil Engineers-Structures and Buildings*, 163(6), 427-437.
- Wang, T., McCormick, J., Yoshitake, N., Pan, P., Murata, Y., & Nakashima, M. (2008). Collapse simulation of a four - story steel moment frame by a distributed online hybrid test. *Earthquake Engineering & Structural Dynamics*, 37(6), 955-974.
- Wang, W., Fang, C., Chen, Y., & Wang, M. (2016). Seismic performance of steel H-beam to SHS-column cast modular panel zone joints. *Engineering Structures*, 117, 145-160.
- Wardenier, J. (1982). *Hollow section joints*. TU Delft, Delft University of Technology.
- Wardenier, J., Kurobane, Y., Packer, J. A., van der Vegte, G. J., & Zhao, X. L. (2008). *Design guide for circular hollow section (CHS) joints under predominantly static loading*: Verlag TUV Rheinland.
- Wardenier, J., Packer, J., Zhao, X., & Van der Vegte, G. (2002). *Hollow sections in structural applications*: Bouwen met Staal Rotterdam,, The Netherlands.
- Wardenier, J., Packer, J., Zhao, X.-L., & van der Vegte, G. (2010). HOLLOW SECTIONS IN STRUCTURAL APPLICATIONS.
- Warn, G. P., & Ryan, K. L. (2012). A review of seismic isolation for buildings: historical development and research needs. *Buildings*, 2(3), 300-325.
- Warren, W., & Kraynik, A. (1991). The nonlinear elastic behavior of open-cell foams. *Journal of Applied Mechanics*, 58(2), 376-381.
- Wheeler, A., Clarke, M., & Hancock, G. (1998). Finite element modelling of bolted moment end plate connections in tubular members. *A. A. Balkema Publishers, Tubular Structures VIII(USA)*, 549-558.
- Wheeler, A., Clarke, M., & Hancock, G. (2000). FE modeling of four-bolt, tubular moment end-plate connections. *Journal of Structural Engineering*, 126(7), 816-822.
- Wilkinson, T., & Hancock, G. J. (1998). Tests to examine compact web slenderness of cold-formed RHS. *Journal of Structural Engineering*, 124(10), 1166-1174.
- Woghiren, C., & Brennan, F. P. (2009). Weld toe stress concentrations in multi-planar stiffened tubular KK joints. *International Journal of Fatigue*, 31(1), 164-172.
- Yoshida, J., Abe, M., & Fujino, Y. (2004). Constitutive model of high-damping rubber materials. *Journal of Engineering Mechanics*, 130(2), 129-141.
- Yu, Q.-S. K., Uang, C.-M., & Gross, J. (2000). Seismic rehabilitation design of steel moment connection with welded haunch. *Journal of Structural Engineering*, 126(1), 69-78.



Zenkert, D., & Burman, M. (2009). Tension, compression and shear fatigue of a closed cell polymer foam. *Composites Science and Technology*, 69(6), 785-792.

Zhao, R., Huang, R., Khoo, H., & Cheng, J. (2007). Experimental study on slotted rectangular and square hollow structural section (HSS) tension connections. *Canadian Journal of Civil Engineering*, 35(11), 1318-1330.

Zhao, W., & Jin, G. (1996). An experimental study on measurement of Poisson's ratio with digital correlation method. *Journal of applied polymer science*, 60(8), 1083-1088.

Zhao, X.-L., Grzebieta, R., & Lee, C. (2002). Void-filled cold-formed rectangular hollow section braces subjected to large deformation cyclic axial loading. *Journal of Structural Engineering*, 128(6), 746-753.

Zhao, X.-L., & Hancock, G. J. (1992). Square and rectangular hollow sections subject to combined actions. *Journal of structural engineering*, 118(3), 648-667.